Imbibition, Crystallization, and Dynamics of Polymers and Water under Nanometer Confinement

Dissertation zur Erlangung des Grades

'Doktor der Naturwissenschaften (Dr. rer. nat)'

im Promotionsfach Physikalische Chemie

am Fachbereich Chemie, Pharmazie, und Geowissenschaften

der Johannes Gutenberg-Universität, Mainz

vorgelegt von

Yang Yao

Geboren in Anshan, China

Mainz 2018

Abstract

The way polymers penetrate into thin pores is of fundamental interest and importance for many applications in nanotechnology. In this Thesis we first investigate how polymer melts penetrate into self-ordered nanoporous alumina (AAO). The results for the imbibition height deviate from the theoretical Lucas-Washburn equation. The deviation is explained by a competition between the adsorption of polymer chains on the pore walls and the reptation of free chains under a pressure gradient. In addition, motivated by the different imbibition speeds between shorter and longer chains, we study the imbibition of homogeneous polymer blends and find an enrichment of shorter chains inside nanopores. In a second area we investigate the effect of chain topology on the imbibition, crystallization, and dynamics of polymers under confinement. Poly(ethylene oxide) (PEO) based polymers are employed including star PEOs, hyperbranched (*hb*) PEOs, and diblock copolymers of poly(isoprene-*b*-ethylene oxide) (PI-*b*-PEO). Despite the non-linear structure, these polymers (*hb*PEOs) can be infiltrated into AAO, albeit with a slower filling speed than theoretically predicted. Surprisingly, PI-*b*-PEO can be successfully infiltrated from an ordered state. Subsequently, we investigate polymer crystallization under confinement. Mainly homogeneous nucleation is observed. The homogeneous nucleation temperature of the non-linear topologies is identical to that of linear PEO, provided that the arm, branched, or the block molecular weight is used instead of the total molecular weight. In addition, the segmental dynamics speed-up reflecting a reduction in glass temperature. Lastly, motivated by earlier studies in our lab, we investigate the crystallization and dynamics of water under confinement. We use two confining media; one with a moderate confinement (hollow silica spheres) and one where confinement is severe (mesoporous silica). We establish the phase diagram (*T vs*. 1/*d*) of confined water over a broad area of pore sizes. The dependence of the heterogeneous and the homogeneous nucleation temperatures on pore diameter is obtained. The two lines coincide at a pore diameter of ~ 2.6 nm below which crystallization is not possible. By employing both dielectric spectroscopy and solid state nuclear magnetic resonance techniques we investigate the dynamics of ice and water within mesoporous silica. Both techniques identify -for the first time – two different states of *liquid* water under confinement and their dynamics is explored.

Zusammenfassung

Die Art und Weise, wie Polymere in dünne Poren eindringen, ist für viele Anwendungen in der Nanotechnologie von fundamentalem Interesse und Bedeutung. In dieser Doktorarbeit untersuchen wir, wie Polymerschmelzen in selbstgeordnetes nanoporöses Aluminiumoxid (AAO) eindringen. Die Ergebnisse weichen von der theoretischen Lucas-Washburn-Gleichung (LWE) ab. Die Abweichung erklärt sich durch eine Konkurrenz zwischen der Adsorption von Polymerketten an den Porenwänden und der Reptation freier Ketten unter einem Druckgradienten. Darüber hinaus untersuchen wir, angeregt durch die unterschiedlichen Aufsauggeschwindigkeiten zwischen kürzeren und längeren Ketten, die Einlagerung von Polymerblends und finden eine Anreicherung von kürzeren Ketten in Nanoporen. In einem zweiten Teil untersuchen wir den Effekt der Kettentopologie auf die Imbibition, Kristallisation und Dynamik von Polymeren unter räumlicher Einschränkung. Polymere auf Poly(ethylenoxid) (PEO)-Basis werden verwendet, einschließlich Sternverzweigter-PEO, hyperverzweigter (*hb*) PEO, und Poly(Isopren-*b*-Ethylenoxid) (PI-*b*-PEO)-Diblockcopolymere. Trotz der nichtlinearen Struktur können *hb*PEO in AAO infiltriert werden, wenn auch mit einer langsameren Füllgeschwindigkeit als theoretisch vorhergesagt. Überraschenderweise kann PI-*b*-PEO erfolgreich aus einem geordneten Zustand in AAO infiltriert werden. Anschließend untersuchen wir die Polymerkristallisation unter räumlicher Einschränkung. Hauptsächlich wird eine homogene Keimbildung beobachtet. Die homogene Keimbildungstemperatur der nichtlinearen Topologien ist identisch mit der von linearem PEO, vorausgesetzt, dass das Arm-, Verzweigungs- oder Blockmolekulargewicht anstelle des Gesamtmolekulargewichts verwendet wird. Zudem beschleunigt sich die Segmentdynamik durch eine Absenkung der Glastemperatur. Schließlich, motiviert durch frühere Studien in unserem Labor, untersuchen wir die Kristallisation und Dynamik von Wasser unter räumlicher Einschränkung. Wir verwenden zwei begrenzende Medien; eines mit mäßigem Einschluss (hohle Silikakugeln) und eines mit starkem Einschluss (mesoporöses Silika). Wir erstellen das Phasendiagramm (T vs. $1/d$) von räumlich eingeschränktem Wasser über einen weiten Bereich von Porengrößen. Die Abhängigkeit der heterogenen und der homogenen Keimbildungstemperaturen vom Porendurchmesser wird erhalten. Die beiden Linien fallen bei einem Porendurchmesser von ~ 2,6 nm zusammen, unterhalb dessen eine Kristallisation nicht möglich ist. Durch den Einsatz von dielektrischer Spektroskopie und Festkörper-NMR-Methoden untersuchen wir die Eis- und Wasserdynamik in mesoporösem Siliciumdioxid. Beide Techniken identifizieren - zum ersten Mal

- zwei Zustände von räumlich eingeschränktem, *flüssigem* Wasser und ihre Dynamik wird erforscht.

Contents

Chapter 1. Introduction

1.1. Dynamic imbibition of polymer melts

1.1.1. Motivation and earlier knowledge

The way that polymers penetrate into fine pores is of fundamental interest and importance for many fields including engineering, biotechnology, and nanotechnology.[1-4] For example, in applications including lab-on-chip and related nanofluidic devices, or the flow of fluid through channels in biomembranes, an essential process is the ability of fluids to penetrate thin pores. In addition, filling nanoporous membranes with polymers opens new possibilities in fabricating 1D to 3D nanosized materials with enhanced physical properties.[5-7] As a model 2D confining medium, herein, we employ self-ordered anodic alumina oxide (AAO). AAOs were first fabricated by Masuda and Fukuda[8-10] *via* electrochemical oxidation of aluminum. AAO templates contain isolated, parallel, cylindrical nanopores that are uniform in length (up to 100 μm) and diameter (from 25 to 400 nm). Figure 1 shows the morphology of AAO templates used in this thesis. The diameter and length are precisely controlled by adjusting the anodization parameters, including anodization voltage, current, and temperatures.[11]

Unlike small molecules, polymer imbibition into nanosized pores needs to be considered in detail because of the longer times and different lengthscales involved with polymers. It turns out that polymer imbibition is a highly non-trivial process, especially when the coil size approaches the pore radius ($2R_g \approx d$). In most cases, polymer melts can be smoothly infiltrated into nanopores as shown in Figure 2a. The figure depicts AAOs with a 2D hexagonal structure fully infiltrated by a polymer (isotactic polypropylene (iPP) in this case). Figure 2b depicts that released nanorods that are fairly uniform being exact replicas of the pore bottoms.[12] However, in some cases instabilities are observed during polymer flow, which result in some unexpected structures (e.g. the helical structure in Figure 2c and the bridge structure in Figure 2d). These considerations, as well as earlier knowledge, motivated us to investigate the imbibition process of polymer melts in nanopores in more detail.

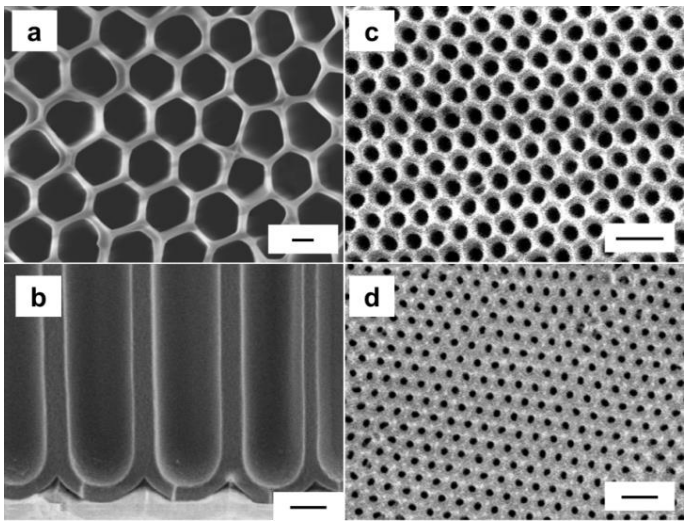

Figure 1. Scanning electron microscopy images of self-ordered AAOs. a. Top view of AAO with pore diameter of 400 nm. b. Cross section of AAO with diameter of 400 nm. c, d. Top view of AAO with pore diameter of 65 nm and 35 nm, respectively. Scale bar indicates 200 nm.

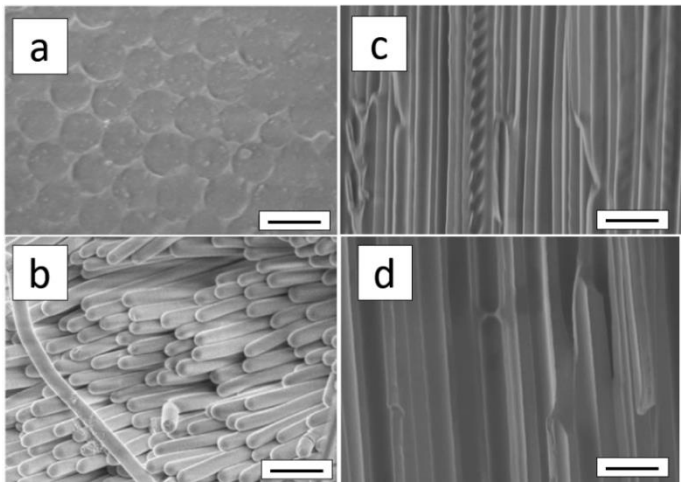

Figure 2. Scanning electron microscopy images of polymers infiltrated in self-ordered AAO. a. Top view of iPP in AAO with diameter of 380 nm. b. Released iPP nanorods from AAO templates.[12] c and d. Cross section of star-PEO in AAO with diameter of 400 nm. Scale bar indicates 500 nm.

Nearly 100 years ago, Lucas and Washburn derived what is known as the Lucas-Washburn equation (LWE) for Newtonian liquids penetrating a cylindrical capillary of radius *R*.[13,14] A brief

derivation of the LWE is as follows. We consider a cylindrical pore of radius *R*, where one end of the pore is inserted into a Newtonian fluid bath. The capillary force will drag the fluid into the pore, as shown in Figure 3.

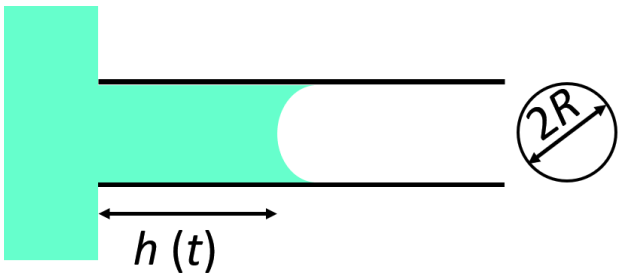

Figure 3. A sketch of capillary penetration of a fluid into a cylindrical pore.

Two opposite forces are acting on the fluid within the capillary: (i) the capillary force and (ii) the viscous force. The capillary force, F_c, can be expressed as:

$$F_C = 2\pi R\,(\gamma_{SV} - \gamma_{SL}) \tag{1}$$

where γ_{SL}, γ_{SV}, and γ are the interfacial tension between solid/liquid, solid/vapor, and liquid/vapor, respectively. The three interfacial tensions are related by Young's equation to the equilibrium contact angle, θ_E, as,

$$\gamma_{SV} - \gamma_{SL} = \gamma cos\theta_E \tag{2}$$

The viscous force, providing friction against imbibition, can be expressed as:

$$F_V = 8\pi\eta_0 hv \tag{3}$$

where η_0 is the bulk viscosity of the fluid, $v = dh/dt$ is the filling speed, and h is the penetration length of the liquid meniscus. The balance between the capillary force and viscous force results in the evolution equation:

$$2\pi R\gamma cos\theta_E = 8\pi\eta_0 hv \quad \Rightarrow \quad v = \frac{R\gamma cos\theta_E}{4\eta_0 h} \tag{4}$$

The solution of equation 4 is the celebrated LWE:

$$h^2(t) = \frac{\gamma R cos\theta}{2\eta_0} t \quad \Rightarrow \quad h(t) = \left(\frac{\gamma R cos\theta}{2\eta_0}\right)^{1/2}\sqrt{t} \tag{5}$$

The quantity, $\frac{\gamma R cos\theta}{2\eta_0}$, measures the penetrating power of a liquid and is known as the coefficient of penetrance or the penetrability.[13,14]

Several studies indicated that the LWE is generally applicable for Newtonian liquids in macroscopic capillaries when taking into account the dynamic contact angle, friction effect *etc*.[13, 15,16] For example in Figure 4a, the height rise of the meniscus for PDMS oil in a ~mm capillary follows a modified LWE when considering intrinsic friction.[15] The height rise of castor oil in a spider silk channel and in a PVA-templated channel also follows the LWE (Figure 4b).[16] However, as already stated by Washburn,[14] *this equation will probably not apply for pores having diameters approaching the molecular dimensions of the liquid*.

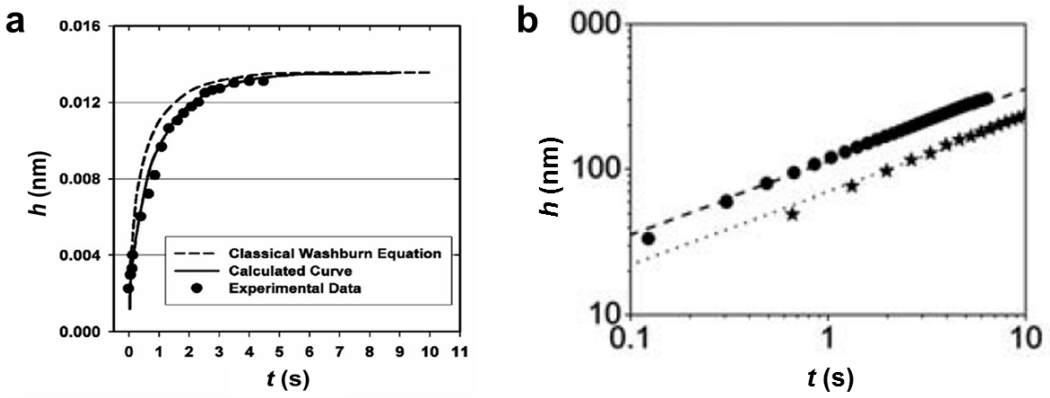

Figure 4. a. Experimental results for capillary rise of PDMS oils and the curve calculated using classical LWE (dash line) and modified LWE (solid line).[15] b. Filling distance of castor oil in a spider silk channel (radius, r = 650 ± 50 nm, circles) and in a PVA-templated channel (r = 250 ± 50 nm, stars). The lines show the corresponding theoretical values according to LWE.[16]

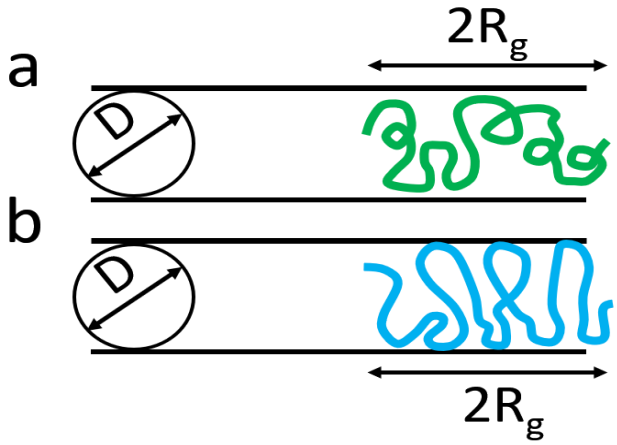

Figure 5. a. An ideal chain trapped in a tube with diameter of *D*. b. A chain in a tube under adsorption situation. Figure reproduced from ref [3].

Based on the theory of de Gennes[3], polymer chains resist entering in narrow spaces because of the reduced entropy inside nanopores as compared to the bulk. If we consider an ideal chain trapped in a tube without adsorption to the tube wall (Figure 5a), the corresponding free energy per chain is: $\mathrm{F} = \mathrm{T}\frac{\mathrm{R_g^2}}{\mathrm{D^2}}$. If we further consider the adsorption of the chain to the tube walls[17](Figure 5b), the corresponding free energy per chain is:

$$F = T\frac{R_g^2}{D^2} - T\delta f_b N \tag{6}$$

Here, the first term is the confinement energy and the second term describes the contact interactions with the surface. $T\delta$ is the effective attraction seen by a monomer adsorbed at the surface, f_b, is the fraction of adsorbed monomers and N is the number of repeat units.

Although there is a reduction in entropy when polymer chains enter a thin tube, the capillary force is strong enough and drags the chains into nanopores. The complex dynamics of polymers challenges the applicability of LWE for polymer melts in nanopores, especially when the R_g is comparable to tube diameter. Indeed, recent experiments on polymer fluids in nanopores have shown some deviations from LWE when nanopores were infiltrated with entangled polymer melts. Shin *et al.*[18] investigated the imbibition of high molecular weight polystyrenes (PS) (M_w from 115 kg/mol to 1210 kg/mol, M_e (PS)~ 20 kg/mol) in AAO with a single pore diameter of 15 nm (hence, exploring the $2R_g/d$ parameter space from 1.6 to 3.2). The capillary rise in this case was detected by a relatively indirect method, on the basis of changes in the X-ray scattering invariant during the capillary flow. They suggested an enhanced mobility of confined polymer chains compared to the bulk. The dependence of the viscosity on the molecular weight changed from $\eta \sim N^3$ in the bulk to $\eta \sim N^{1.4}$ under confinement. The enhanced mobility of polymers was discussed in terms of the reduction of the entanglement density under confinement.[19] Cao *et al.*[20] employed polyethylene (PE) and studied its penetration into commercially available disordered AAO filters (Whatman Anodisc). Figure 6 shows the SEM images of the template used his study with a nominal pore diameter of 20 nm (which is the pore diameter of a thin size-selective layer on top of a thick support layer with pore diameters scattered about 200 nm)[21]. Despite the porous template being not uniform, they found that the capillary rise of PE melts was faster than predicted by the LWE. The faster infiltration was explained in terms of the effect of shear rate on the polymer viscosity during capillary flow.

The fluid dynamics of polymer melts in thin tubes were also studied by theory and simulations. Binder *et al.*[22] used molecular dynamics simulations to investigate the capillary rise of both small molecule fluids and polymer melts in nanotubes. They found that the meniscus rise followed $t^{1/2}$ law; however, the description of the imbibition process in nanotubes was only possible upon modification of LWE taking into account the slip length (δ), suggesting a modified LWE

$$h(t) = \left[\frac{\gamma_{LV}(R+\delta)^2 cos\theta}{2R\eta}\right]^{1/2} \sqrt{\mathrm{t}} \tag{7}$$

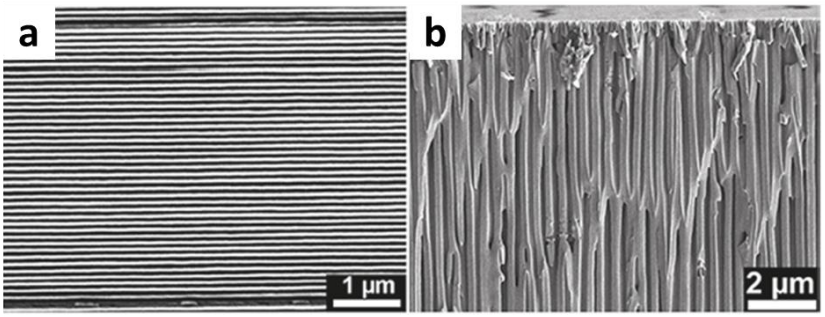

Figure 6. (a) SEM images of self-ordered AAO anodized with anodized with oxalic acid. (b) SEM image of commercially available disordered AAO (Whatman Anodisc), nominal pore diameter is 20 nm. Whatman Anodisc membranes are designed as filters having a thin size-selective layer (on the top) with narrow pores supported by a thick layer with larger pores having diameters scattering about 200 nm in order to reduce flow resistance in the course of separation processes. The pore size distributions are broad; the pores are partially interconnected. Figure is taken from ref [21].

Despite recent work in capillary rise of polymer in nanopores,[19,23,24] there are still several aspects that have not been addressed. In this thesis, we investigate the imbibition of polyethylene oxide (PEO) melts as a function of molecular weight (from 50 kg/mol to 1000 kg/mol, $\overline{M}$ /$\overline{M}_e$ ranging from 25 to 500, $\overline{M}_e$ (PEO) ~ 2 kg/mol), and pore diameters (from 400 nm to 25 nm) by experiment, simulation, and theory. With this range of M_ws and pore diameters we explore a broad range of $2R_g$/d from 0.06 to 3 which have not been explored before. We show that capillary imbibition is much richer than in earlier reports. In contradiction to earlier studies we found a reversal in dynamics of capillary filling with increasing polymer molecular weight. The complex imbibition can be explained by the competition between two mechanisms (see below). In addition, motivated by the large difference in imbibition speeds for the longer and shorter chains, we study the imbibition of polymer blends in AAO. We explore the idea that the different imbibition speeds

might suggest a new method in separating long/short chains in a poly-dispersed polymer melt and in the absence of solvent. As a result, experiment and SCFT calculations demonstrate an enrichment of pores by the short chains.

1.1.2. Sample characteristics

Poly(ethylene oxide)s (PEO) with five different molecular weights (PEO 50 kg/mol, PEO 100 kg/mol, PEO 280 kg/mol, PEO 500 kg/mol, PEO 1000 kg/mol) were employed in the present investigation. Their molecular characteristics and properties including surface tension, contact angle, and viscosity are shown in Table 1. PEO 50k, PEO 100k and PEO 280k were synthesized and characterized by T. Wagner and J. Thiel (MPI-P). PEO 500k and PEO 1000k were purchased from Polymer Standards Service. All samples were synthesized *via* anionic polymerization techniques with tert-butyl ether and hydroxyl end groups. The weight fractions and values used for LWE parameters of PEO mixtures were also included in Table 1.

Table 1. Molecular weight, surface tension, contact angle, and bulk viscosity of PEOs and PEO mixtures used in the present study

Homopolymer	$\overline{M}_w$ (g/mol)	$\overline{M}_n$ (g/mol)	PDI	γ ($\times 10^{-3}$ N/m)	θ_e (deg)	η_0 (Pa·s)
PEO 50k	53090	44510	1.19	29.1	44.0	4.3×10^{2}
PEO 100k	92930	83370	1.11	27.8	44.5	3.9×10^{3}
PEO 280k	273600	335900	1.23	28.0	44.0	1.5×10^{5}
PEO 500k	480000	398000	1.21	28.1	40.7	4.6×10^{5}
PEO 1000k	1020000	884000	1.15	28.0	47.7	2.7×10^{6}
PEO Mixture	PEO50k/PEO500k			γ ($\times 10^{-3}$ N/m)	θ_e (deg)	η_0 (Pa·s)
Mixture S1	75/25			28.9	42	1.7×10^{4}
Mixture S2	50/50			28.6	42	8.5×10^{4}
Mixture S3	25/75			28.4	42	2.2×10^{5}

1.1.3. Main findings

a. Dynamic imbibition of homopolymers[25]

To test the applicability of LWE on imbibition of polymer melts in nanopores, we used PEO melts. All parameters entering in the LWE were evaluated separately for each polymer. Figure 7 shows an example of a measurement of the dynamic contact angle of PEO 100 kg/mol as a function of contact line velocity on the electro-polished Al disk coated by a thin native oxide layer (the latter comprises a flat model surface that mimics AAO surface). To get the best estimation of 'static' advancing contact angle, the measured values were extrapolated to zero velocity.

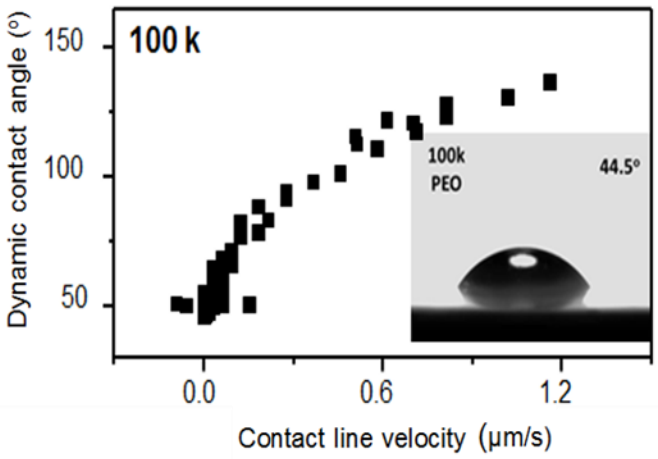

Figure 7. Dynamic contact angle of the PEO 100k. The quasi-static advancing contact angle is estimated from the lowest contact line velocity image showed as inset.

Figure 8. Reflection microscopy images of PEO 500k located inside 65 nm AAO infiltrated for different times as indicated. Scale bar indicates 10 μm.

Representative reflection microscopy images of capillary filling of PEO 500k in 65 nm AAO are shown in Figure 8. Images depict the rise of the imbibition front within AAOs with time. The results with respect to the imbibition height, h, as a function of $t^{1/2}$ for PEO 100k and PEO 500k

are summarized in Figure 9. In general, the $t^{1/2}$ dependence in LWE is approximately valid for all samples expect short time imbibitions (less than 15 min). For PEO 100k in 400 nm, the theoretical LWE describes the measured imbibition lengths well. However, in the smaller pores, capillary rise is slower than theoretically predicted (Figure 9 left). The situation for the imbibition length in PEO 500k is distinctly different. A faster capillary rise is observed for all the pore diameters (Figure 9 right). The reversal in dynamics of capillary imbibition between low and high molecular weights is discussed in Figure 10 in terms of the effective viscosity. Effective viscosities calculated from the slope of imbibition height are plotted as a function of $2R_g/d$ (R_g is the radius of gyration of the polymer). At a fixed value of confinement, e.g., $2R_g/d = 1$ (red frame in Figure 10), the effective viscosity has a weak dependence on N ($\eta_{eff} \sim N^{0.9\pm0.1}$) as opposed to the dynamics of reptating chains in the bulk ($\eta_{eff} \sim N^{3.4}$) (green frame in Figure 10).

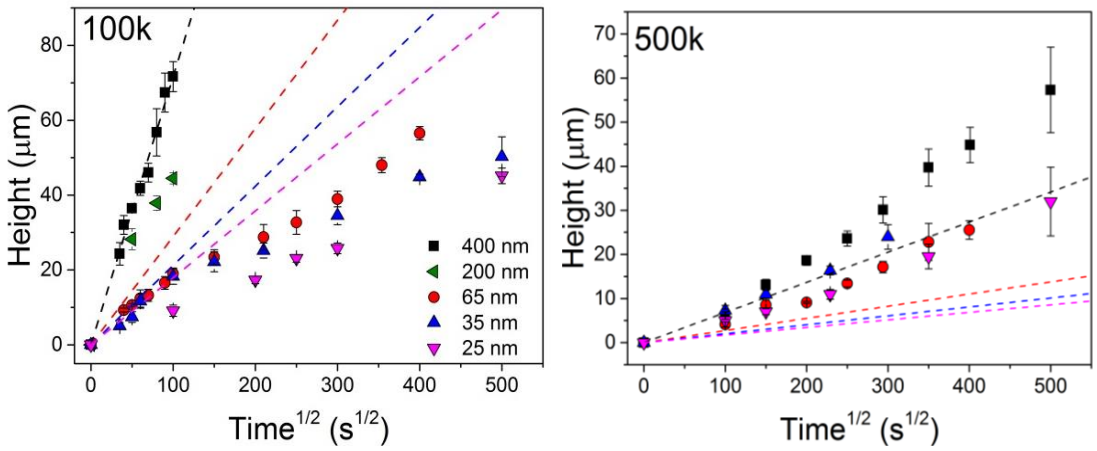

Figure 9. Imbibition height, h, as a function of $t^{1/2}$ for PEO 100k (left) and PEO 500k (right). Dash lines give the prediction of the LWE.

In summary, capillary imbibition of entangled PEO melts within AAO nanopores follows an approximate $t^{1/2}$ behavior according to LWE. However, a reversal in dynamic of capillary filling is found with increasing polymer molecular weight. Polymer chains with 50 entanglements or less show a slower imbibition than theoretically predicted, indicating a higher effective viscosity. For longer chains with more entanglements, the imbibition is faster than the theory and the effective viscosity is much lower than the bulk. Next we present the theoretical framework of polymer imbibition in nanopores and the comparison to the experiment.

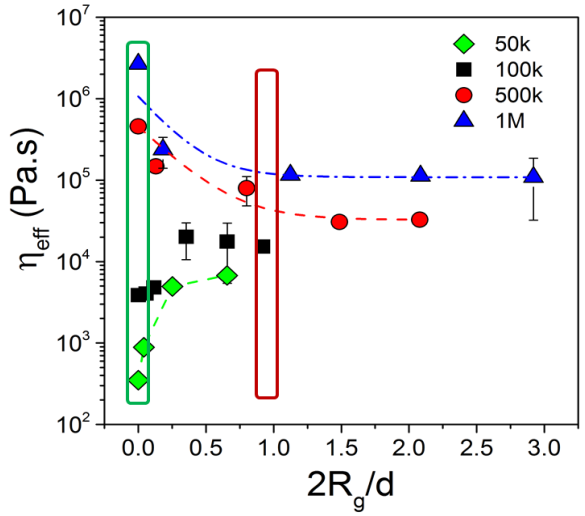

Figure 10. Effective viscosity (calculated from the slopes in Figure 9) as a function of $2R_g/d$ for the four PEO samples infiltrated in AAO. The green and red frames indicates the bulk and $2R_g/d = 1$ cases, respectively.

b. Theory on capillary imbibition of polymer melts in nanopores[26]

The unusual effective viscosities for PEO melts in AAO can be discussed by the competition of two mechanisms: one is the standard hydrodynamic flow, resulting in a parabolic flow profile. When the inner wall has a strong attraction to the polymer, a layer of immobile chains is created, resulting in an increase of the effective viscosity (slower imbibition). The other one is the reptation model proposed by Johner *et al.*[23], which leads to a plug flow profile and reduction in the effective viscosity (faster imbibition). Figure 11 shows the motion of the wetting front by the reptation of free chains through the network.

According to the first mechanism, polymer chains near the inner wall are strongly adsorbed and create a "dead zone" with thickness ΔR. An effective pore radius can be defined as $R_{eff} = R - \Delta R$. Outside the dead zone, the polymer melt exhibits a macroscopic flow with the usual parabolic profile. We rewrite equation 4 in term of pressure:

$$v = \frac{R^2}{8\eta_0 h}\Delta P,\ \Delta P = \frac{2\gamma cos\theta_E}{R} \tag{8}$$

where, ΔP, is the Laplace pressure that drives the imbibition. This term remains unchanged when the dead zone is considered, but we have to replace R^2 in the numerator by R_{eff}^2. Since only R_{eff}^2 / R^2 portion of the polymer contributes to the flow, the fluid front advances at the rate:

$$\dot{h} = v_{flow}\frac{R_{eff}^2}{R^2} = \frac{\gamma cos\theta\, R_{eff}^4}{4\eta_o h R^3} \tag{9}$$

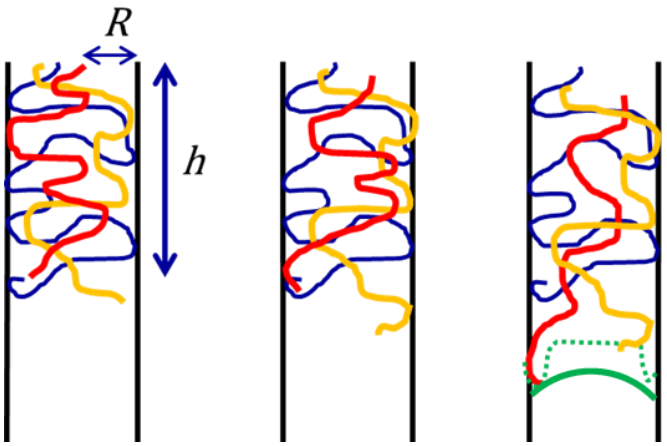

Figure 11. Schematic of the motion of the wetting front during polymer imbibition in nanopores. The wetting front moves by adsorption of chains to the pore wall and subsequent reptation of chains through the gel-like network.

As the pore radius is reduced and becomes comparable to the thickness of the dead zone, the macroscopic flow is nearly stopped. In this case, the material transport under very strong confinement is achieved mainly by the reptation of free polymer chains in a network driven by the pressure gradient. Johner *et al.*[23] have developed a theoretic framework for this scenario. A polymer chain is constrained by other chains due to the entanglements, and it can only move along the "reptation tube". Each free polymer chain experiences a driving force due to the pressure difference along the chain as follows:

$$[-p(x + R_x) + p(x)]l^2 = -l^2 R_x \frac{dp}{dx} \tag{10}$$

where l^2 is the cross section and R_x is the x-component of the end-to-end vector. The friction to the free chain is given by $N\zeta v_c$, where, N, is number of segments, ζ, is the friction constant for one Kuhn segment, and v_c is the chain's velocity along the reptation tube. The balance between the pressure gradient and the frictional force gives:

$$v_c = -\frac{l^2}{\zeta N} R_x \frac{dp}{dx} \tag{11}$$

The averaged velocity for the center of mass of the polymer is:

$$\langle v_g \rangle = \langle \frac{R_x}{L} v_c \rangle = -\frac{l^2 a_t}{3\zeta N}\frac{dp}{dx} \tag{12}$$

where, L, is the contour length of the tube, given by $L = (N/N_e)a_t$, N_e is the entanglement length, and $a_t = N_e^{1/2}b$ is the tube diameter. The average of R_x^2 is assumed to be ideal $\langle R_x^2 \rangle = (1/3)\, Nb^2$.

If the fraction of polymer chains participating the reptation is,φ, the filling speed is then given by:

$$\dot{h} = \varphi \langle v_g \rangle = \varphi \frac{l^2 a_t}{3\zeta N} \frac{2\gamma \cos\theta}{hR} \tag{13}$$

In the case of $R_g << R$, the dead-zone effect is dominant and the filling dynamics is given by equation 9. In the other limit, $R_g >> R$, the reptation mode is more important and the filling dynamics is governed by equation 13. A simple formula to interpolate these two limits is:

$$\dot{h} = \frac{\gamma cos\theta\, R_{eff}^4}{4\eta_o h R^3} + \varphi \frac{l^2 a_t}{3\zeta N} \frac{2\gamma \cos\theta}{hR} = \left[\frac{R_{eff}^4}{8\eta_o R^2} + \varphi \frac{N_e^{\alpha} b^3}{3\zeta N} \right] \frac{2\gamma \cos\theta}{hR} \tag{14}$$

Within the context of the LWE, we can define an effective viscosity, η_{eff}, by:

$$\dot{h} = \frac{\gamma \cos\theta R}{4\eta_{eff} h} = \frac{R^2}{8\eta_{eff}} \frac{2\gamma \cos\theta}{hR} \tag{15}$$

Comparing equation 14 with equation 15, we obtain:

$$\frac{\eta_{eff}}{\eta_0} = \left[\left(\frac{R_{eff}}{R} \right)^4 + \varphi \frac{8 N_e^{\alpha} b^3 \eta_0}{3\zeta N R^2} \right]^{-1}, \; \eta_0 \approx \frac{\zeta b^2}{V_0} \frac{N^3}{N_e^2} \tag{16}$$

The effective viscosity in equation 16 can be written as:

$$\frac{\eta_{eff}}{\eta_0} = [f(\Delta R, R) + g(\phi, N, R)]^{-1} \tag{17}$$

where the first function, f, is related to the dead-zone,

$$f(\Delta R, R) = \begin{cases} \left(1 - \frac{\Delta R}{R}\right)^4 & if\ R > \Delta R \\ 0 & if\ R < \Delta R \end{cases} \tag{18}$$

The second function, g, is from the reptation model,

$$g(\phi, N, R) = \varphi \frac{8 N_e^{\alpha} b^3 \eta_0}{3\zeta N R^2} = \varphi \frac{8 N_e^{\alpha - 2} b^5}{3 V_0} \frac{N^2}{R^2} = \phi \frac{N^2}{R^2} \tag{19}$$

Figure 12 shows the theoretical predictions in terms of the separate influence of (a) the fraction of free chains (ϕ), (b) the molecular weight (N), and (c) the dead zone thickness (ΔR) in the dependence of η_{eff}/η_0 *vs.* $1/R$. All plots show a non-monotonic behavior. Decreasing fraction of

free chains ϕ, N, or dead-zone thickness all shift the η_{eff}/η_0 maximum to larger $1/R$, *i.e.* to smaller pore diameters.

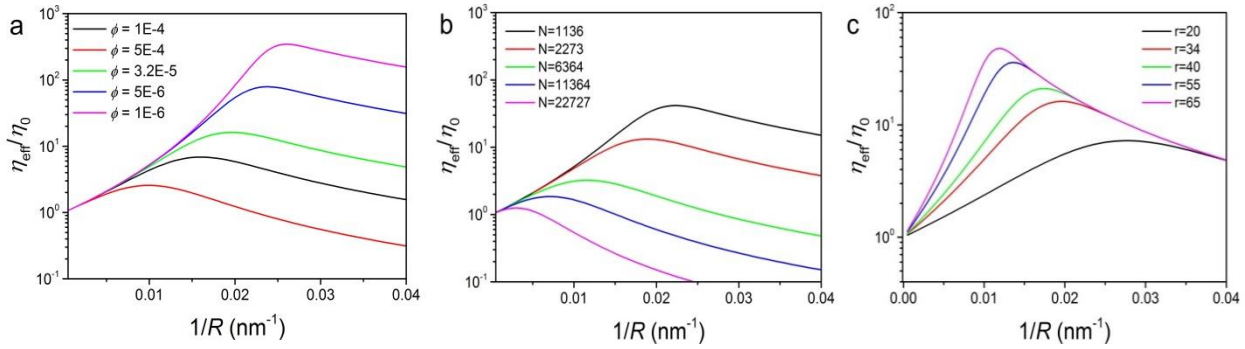

Figure 12. Simulation of the ratio η_{eff}/η_0 as a function of $1/R$ based on theory, showing the influence of (a) the fraction of free chains, ϕ, (b) the molecular weight, N, and (c) the dead-zone, ΔR.

Figure 13 shows the comparison between the experiment and theory, in a plot of the η_{eff}/η_0 as a function of $1/R$. The fitting parameters were obtained by global fitting to equation 17 resulting to ΔR = 34.3 nm, $\phi = 3.21\times10^{-5}$ nm^2. Notwithstanding the large ΔR value, the theoretical prediction is in qualitative agreement with the experimental data. Most importantly, the theory has captured the non-monotonic variation in the effective viscosity. The main reason for the non-monotonic behavior is that functions f and g vary differently with respect to $1/R$. In the large pore limit, these two functions $f \rightarrow 1$ while $g \rightarrow 0$, and the effective viscosity approaches the bulk value, $\eta_{eff} \rightarrow \eta_0$. As the pore radius decreases ($1/R$ increases), the effect of the dead zone becomes important and eventually stops the macroscopic flow. Accordingly, function f decreases. On the other hand, for small pores the reptation motion of the entangled polymer becomes effective and function g increases. It is the opposite trends in the functions f and g that lead to the non-monotonic variation of the effective viscosity as observed experimentally.

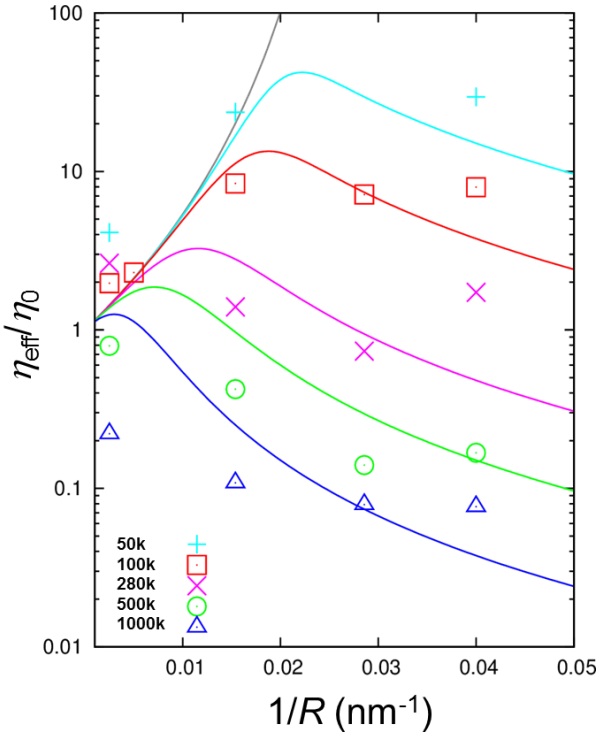

Figure 13. Comparison between the experiments (symbols) and theory (lines) for PEO melts.

c. Dynamics of imbibition of polymer mixtures[27]

Here we explore the possibility of separating long from short polymer chains, e.g. in a bimodal dispersed mixture by taking advantage of the differences in their imbibition speeds. Capillary imbibition of bimodal mixtures follows approximately $t^{1/2}$ dependence but contradicts the predictions of the classical LWE because of the prefactor in the equation (Figure 14). Results from both reflection microscopy and self-consistent field theory (SCFT) calculations demonstrate the faster imbibition for the shorter chains. On top of that, SCFT shows an enrichment of the short chains near the pore surface. These results taken together suggest a way of separating long from short polymer chains in the absence of solvent, namely, by the difference in imbibition speeds within narrow pores.

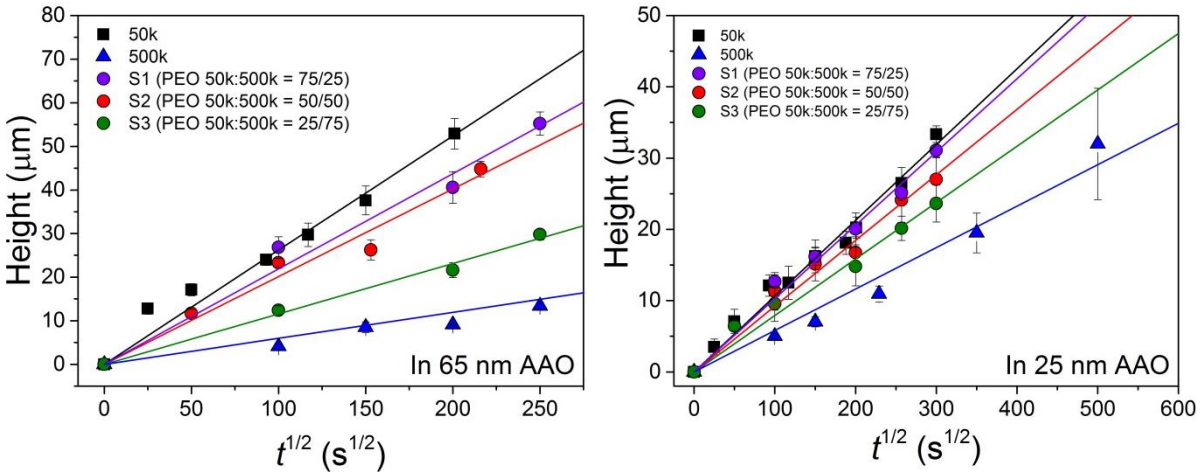

Figure 14. Imbibition length, *h*, as a function of $t^{1/2}$ for two PEO homopolymers with molecular weights of 50k (squares) with 500k (triangles) and their mixtures with compositions: 50/50 (red spheres), 75/25 (magenta spheres), and 25/75 (green spheres) located inside AAO with pore diameters of (left) 65 nm and (right) 25 nm. Lines represent the result of a linear fit to the homopolymers and their mixtures.

1.1.4. Outlook

Reflection optical microscopy (ROM) is an easily approachable method to study the imbibition of the polymers with high molecular weight. However, because of the limitation in short time imbibition, this method is not applicable for studying the imbibition of liquid samples, oligomer, or polymers with lower molecular weights (especially when $M \leq M_e$). Other methods, such as optical interferometric microscopy (OIM) might be a better candidate to study polymer imbibition. OIM is based on the difference in refractive index between the liquid filled part and the empty alumina. It can be used for short imbibition times ($t_{min} \approx 1$ s). Table 2 makes a comparison of the advantages and limitations between the two methods.

Table 2. Comparison between ROM and OIM

	Advantages	Limitations
ROM	-relatively easy to achieve -possible to study long time imbibition (t > 30^2 s) of importance to high M_w polymers	-ex-situ method -short time imbibition for low M_ws polymers
OIM	-in-situ method -possible to study short time imbibition ($t_{min} \approx$ 1 s) for low M_w polymers	-long time imbibition -calibration with reference liquids is necessary

1.2. Effect of chain topology on polymer crystallization under confinement

1.2.1. Polymer crystallization

Crystallization is a process where a solid of highly organized atoms or molecules is formed from solution, melt, or the gas phase. Nucleation is the first activated process in crystallization; the growing nucleus of the new phase must overcome a barrier, created by the balance of a surface free energy term and a volume free energy term (Figure 15). There are two mechanisms of nucleation: heterogeneous nucleation and homogeneous nucleation. Homogeneous nucleation occurs when nuclei form uniformly throughout the phase at large supercooling, overcoming a large energy barrier. On the other hand, the existence of impurities (e.g. remaining catalyst, rough surfaces, additives, bubbles *etc*.) can largely decrease the energy barrier and initiate heterogeneous nucleation at low supercooling. Given that impurities are almost unavoidable in conventional environments, most materials crystallize *via* heterogeneous nucleation in bulk.

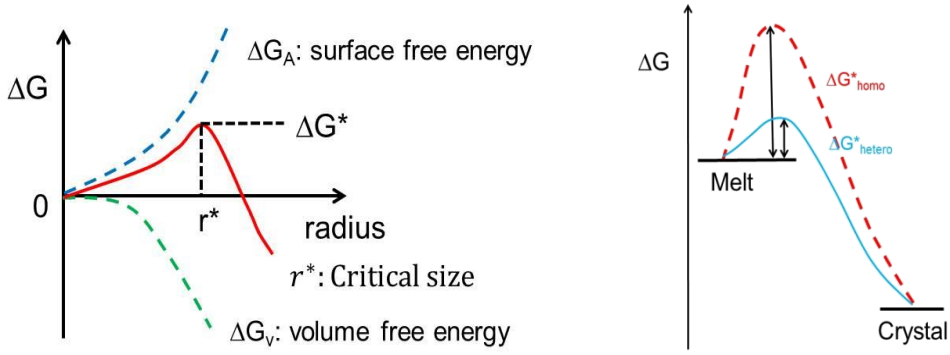

Figure 15. (left) Schematic of the energy barrier during the nucleation. (right) Schematic of the different energy barriers for heterogeneous nucleation and homogeneous nucleation.

In general, polymers can be divided into two main classes: fully amorphous and semicrystalline (about 70% of all polymers). The latter possesses structures over three different length scales. The first length scale is the unit cell (typically ~nm). Figure 16a presents as an example the unit cell structure of polyethylene (PE).[28,29] The second length scale is the lamellar structure (typically ~10 nm) (Figure 16b). The stacks of layer-like crystallites are interrupted by amorphous configurations of chains giving rise to the long period, *d*, measured by small angle X-ray scattering (SAXS) or

SEM/TEM. By applying Bragg's law (equation 20), one can derive the long period from the peak position, q_{max}, in SAXS as[29]:

$$d = \frac{2\pi}{q_{max}} \tag{20}$$

The third length scale is the supermolecular structure (e.g. spherulites, axialites, *etc.*) with sizes from 0.5 μm to several centimeters. The supermolecular structures are typically observed by polarized optical microscopy (POM). Figure 16c shows a spherulite of star-PEO obtained by POM.

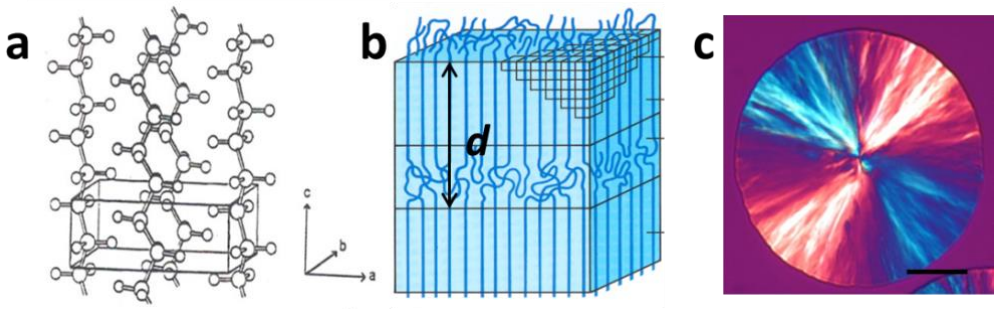

Figure 16. a. Unit cell of PE crystallites: Orthorhombic symmetry, a = 7.42 Å, b = 4.95 Å, c = 2.55 Å. Structure determinination by Bunn[28] b. Schematic of lamellar crystals with the long period, d. c. POM image of a spherulite corresponding to a star PEO. The scale bar indicates 50 μm.

Polymer crystallization involves both the formation of stable nuclei (nucleation) and the diffusion of units to the crystal front (growth). Lauritzen and Hoffman (1960) established a growth theory (known as LH theory)[30] which has been dominant in polymer crystallization for decades. The LH theory provides expressions for the linear growth rate as a function of supercooling ($\Delta T = T_m^0 - T_C$), where T_m^0 is the equilibrium melting temperature and T_C is the crystallization temperature. Figure 17 shows a model of growing crystal lamellar according to the LH theory. It is assumed that the macroscopically observed linear growth rate is the same as that of crystal growth front.

Figure 17. A growing crystal lamellar according to the LH theory[30]

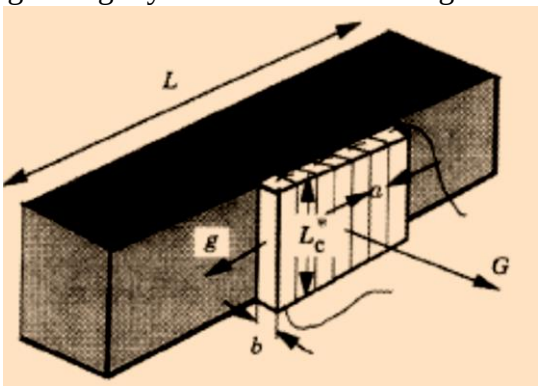

Based on the LH theory, the overall crystallization rate can be described according to:

$$u = u_0 \exp\left(-\frac{U*}{R(T_c - T_\infty)}\right)\exp\left(-\frac{K_g}{T_c(T_m^0 - T_c)}\right) \quad (21)$$

here u_0 is a rate constant that depends on the segmental flexibility, U^* is the activation energy, T_m^0 is the equilibrium melting temperature, T_c is the crystallization temperature, T_∞ is the "ideal" glass temperature at which segmental motility is practically frozen, and K_g is a kinetic constant. In equation 21, the first term expresses the temperature dependence of the segmental mobility of the melt, whereas, the second term indicates the free energy of activation associated with the placement of a secondary nucleus on the growth face (growth). The melting point of a crystal with thickness L_c in Figure 17 is given by the Gibbs-Thomson equation as:

$$T(L_C) \simeq T_m^o - \frac{2\sigma_e T_m^o}{\Delta h_f}\frac{1}{L_C} \quad (22)$$

Here, σ_e, is the excess free energy of the fold surfaces and Δh_f is the heat of fusion. Equation 22 suggests a reduction in melting temperature relative to an ideal crystal (T_m^o) because of the finite size of crystal, L_c. For a crystallization temperature, T, the Hoffman-Lauritzen predicts a thickness of the growing crystals of

$$L_c = \frac{2\sigma_e T_m^o}{\Delta h_f (T_m^o - T)} - \delta \quad (23)$$

δ is a minor excess for providing a driving force.

The kinetic crystallization theory of Lauritzen and Hoffman has been accepted and used for a few decades. However, recent experimental findings contradicted some of the basic assumptions of the theory.[31-35] In 2009, Strobl[36] proposed a modified theory including an intermediate metastable state in the process of polymer crystallization. He suggested that polymer crystallization and melting are controlled by three characteristic temperatures, T_m^0 , T_c^0, and T_{zg}

(zero growth temperature). They are arranged as $T_{zg} < T_m^0 < T_c^0$. He suggested the growth rate of polymer crystallites increases exponentially with the supercooling below T_{zg} instead of T_m^0:

$$u = u_0 \exp\left(-\frac{u^*}{R(T_c - T_\infty)}\right) \exp\left(-\frac{K_g}{T_c(T_{zg} - T_c)}\right) \quad (24)$$

1.2.2. Effect of topology in the melt state

There are many possible polymer topologies, such as star, branched, comb, ring, block copolymer *etc.* (Figure 18). Polymer topology influences the structure, packing, and dynamics of chains. For instance, short-chain branching tends to reduce the degree of crystallinity, whereas long-chain branching affects the rheological properties.[37,38] In addition, ring polymers, in the absence of entanglements, have more compact structure and faster diffusion in the melt. In general, rings form more easily into extended equilibrium configurations and as a result have higher equilibrium melting temperatures.[39]

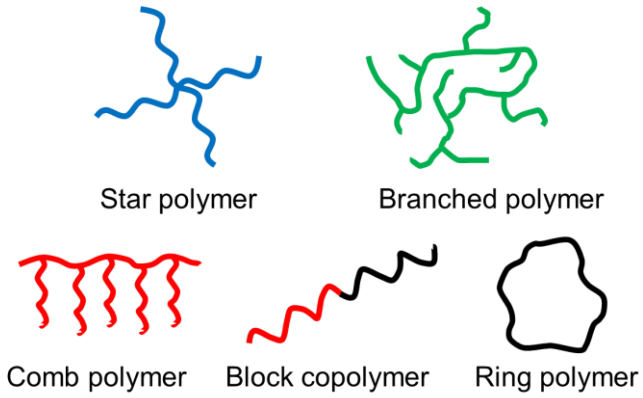

Figure 18. Various polymer architectures

In the melt, the chain topology strongly affects the chain dynamics, especially for highly entangled polymers. For instance, the chain motion of entangled flexible linear polymers can be described by the tube model[40], where the polymer chain is confined in a tube-like fixed network of obstacles, as shown in Figure 19. Based on the tube model, the terminal relaxation time can be expressed as

$$\tau = \zeta_0 b N^3 / (k_B T N_e) \quad (25)$$

where ζ_0 is the friction constant, b is constant length, and N_e is the entangled molecular weight.

Figure 19. Schematic of tube model for flexible linear polymer chain (reproduced from ref [40])

However, chain dynamics can be quite different for polymers with non-linear topologies, e.g. star-shaped polymers. In the latter, contour length fluctuations play an essential role. Simple reptation is not possible and the polymer can only change its conformation by utilizing contour length fluctuation. In this case, relaxation is only possible by arm-retraction (Figure 18), *i.e.* a mechanism where the polymer withdraws an arm down the tube to the branching point, followed by release of the arm to a different tube. The probability distribution of contour length, L_a, at equilibrium is given by

$$\Psi_{eq}(L_a) \propto e^{\left[-\frac{3}{2N_a b^2}{L_a}^2\right]} \tag{26}$$

where N_a is the arm molecular weight.

The terminal relaxation time of the arm, τ_{arm}, is given by

$$\tau_{\mathrm{arm}} \propto \tau_0 e^{\left[\frac{3}{2}\mathrm{N_a}\left(\frac{\mathrm{b}}{\mathrm{a}}\right)^2\right]} \tag{27}$$

Here, the prefactor, τ_0, depends weakly on L, and a is the step length.

Equation (26) predicts that τ_{arm} increases exponentially with the arm length, N_a, which makes the star chains difficult to relax. This result was first predicted by de Gennes[40,41], and then confirmed by computer simulation and experiments.[42,43] As we will see here, these effects play also a role in confined polymer crystallization.

Figure 20. A star polymer in the network of obstacles (reproduced from ref [40]).

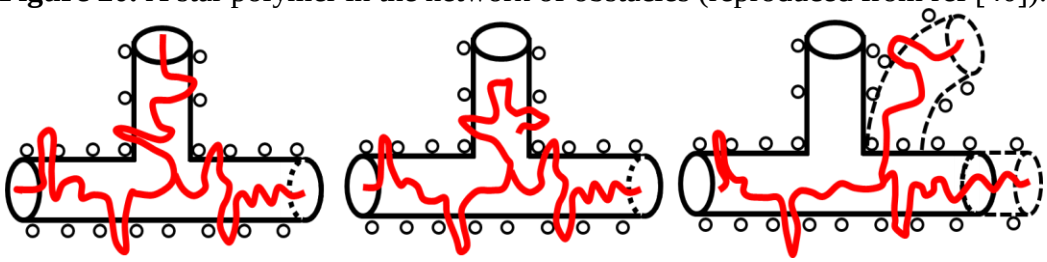

1.2.3. Effect of confinement on polymer crystallization

Polymers under nanoscale confinement have important applications in materials science. For example, the fabrication of polymeric materials with predetermined crystallinity can provide devices with controlled mechanical and optical properties. In the last decade, a variety of linear polymers have been investigated under 1D, 2D, and 3D confinement.[44-47] Recent concerted efforts in this field have focused on the 2D confinement provided by AAO for reasons that were already explained in Chapter 1.1.[8-10]

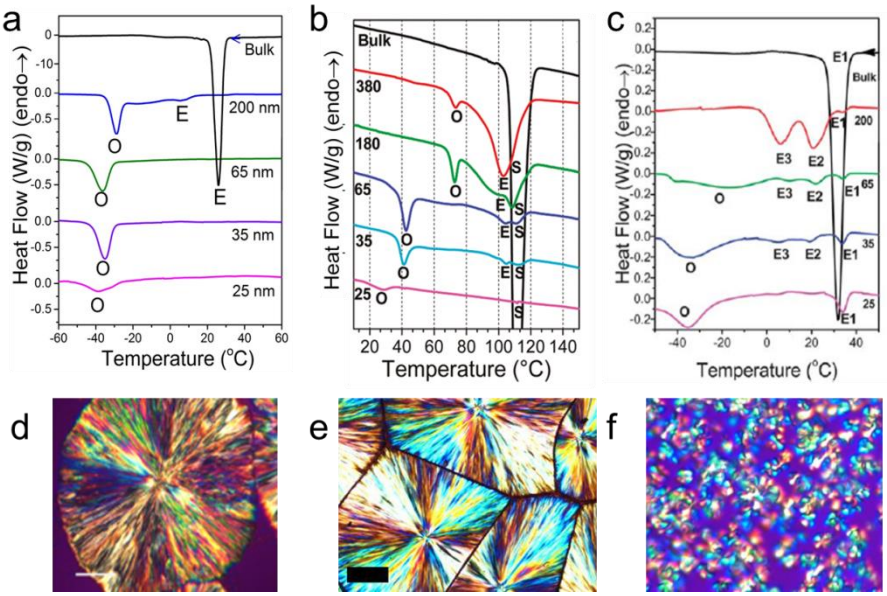

Figure 21. DSC cooling curves of bulk and of samples located inside self-ordered AAO for PEO-1070[48] (a), iPP[12] (b), PCL-7700[49] (c). POM image of a PEO-1070[48] (d), iPP (e), and PCL-7700[49] (f) spherulites in the bulk.

The effect of confinement lies in (i) the nucleation mechanism, (ii) the crystal orientation, and (iii) the segmental dynamics of polymers. First, the effect of confinement on the nucleation mechanism can be discussed in terms of the nucleation density in the bulk. Figure 21 summarizes the earlier studies from our group for the crystallization of iPP, PCL, and PEO confined within

AAO.[12,48,49] The nucleation density can be obtained from polarized optical microscopy (POM). A typical PEO spherulite has a diameter of ~ 300 μm (Figure 21d), suggesting that the volume per impurity/nucleus is ~ 10^{-2} mm^3 in bulk. Within self-ordered AAO, the PEO is located in discrete cylindrical pore. Therefore, crystallization has to be initiated separately in each AAO pore. The volumes of 100 μm deep AAO pores range from ~ 4×10^{-11} mm^3 (25 nm) to ~ 3×10^{-9} mm^3 (400 nm). Since the pore volumes are many orders of magnitude smaller than the volume per heterogeneous nucleus in bulk PEO, only a small portion of AAO pores contain heterogeneous nuclei and the crystallization initiated by these heterogeneous nuclei are restricted to the volumes of the pores. Hence, the volume fraction of crystallization initiated by heterogeneous nucleation is negligible under confinement.[48] On the other hand, the polymer in the vast majority of AAO pores in the absence of heterogeneous nucleus crystallizes via homogeneous nucleation (peak O in Figure 21). However, for samples containing more heterogeneous nucleus in bulk, e.g. iPP or PCL, more nanopores contain heterogeneous nuclei as compared to PEO. Thus, a small fraction of crystallization initiated by heterogeneous nucleation could be observed even in nanopores with a diameter of 35 nm (peak E in Figure 21b and c).

In addition, the homogeneous nucleation temperature depends on both the confining volume and on the polymer molecular weight. Earlier important contributions on linear PEO crystallization under confinement have employed different confining media including droplets[50,51], spherical nanodomains of block copolymers[52], and AAO[48,53]. Figure 22 provides a summary of the homogeneous nucleation temperatures as a function of domain/droplet volume.[54] Linear PEOs crystallized *via* homogeneous nucleation in all confining media. Figure 22 depicts an additional dependence of the homogeneous nucleation temperature to polymer molecular weight.

The second interesting effect of confinement lies in the possibility of inducing a preferential crystal orientation. The majority of studies indicated that the crystal growth direction is along the nanopore axis[55,56] though few studies argued that random orientations were not entirely excluded[57,58]. The representative results and scenarios on crystal orientation under confinement are summarized in Figure 23. First, Steinhart *et al.*[55] studied the crystal orientation of polyvinylidene fluoride (PVDF) in AAO with pore diameter of 35 nm with and without an interconnecting surface layer. In the absent of surface layer, the preferred orientation of the corresponding lattice planes was parallel to the surface of the template, *i.e.* <*hk0*>. The crystal

orientations along <*hkl*> directions with non-zero *l* index were suppressed by the pore wall (Figure 23a, d). Shin *et al*[56] studied the PE crystal orientation within AAOs (from 15 nm to 110 nm). Based on the X-ray diffraction patterns, they found that the *c*- and *a*-axes of orthorhombic PE crystals were preferentially aligned perpendicular to the long axis of nanopores, while the *b*-axis was parallel to it (Figure 21b, e). The preferred chain orientation perpendicular to the pore direction was confirmed by most of the present studies[59,60], including linear PEO in AAO,[61] although few studies suggested coexisting orientation along other directions. Wu *et al*.[57] studied

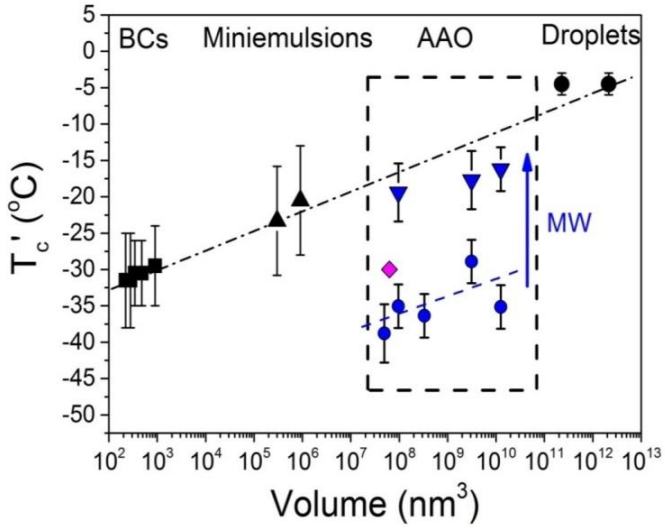

Figure 22. Dependence of the crystallization temperature, T_c', of crystallization processes initiated *via* homogeneous nucleation of PEO within droplets (black rhombi), in miniemulsions (up triangles) and within the spherical domains of block copolymers (squares). The dash-dotted line is a guide for the eye. Data on PEO homogeneous crystallization within AAO templates are included for two molecular weights: $\overline{M_n}$=1070 g/mol (blue spheres) and $\overline{M_n}$=10^5 g/mol (down triangles). The blue dashed line is a guide to the eye for the lower molecular weight PEO. Another PEO sample from literature ($\overline{M_n}$=41000 g/mol)[53], is also shown (magenta rhombus). The vertical arrow shows the dependence of homogeneous nucleation temperature on polymer molecular weight.

the orientation of syndiotactic polystyrene (sPS) crystal in AAO by FTIR spectroscopy. First, they found that the c- axis of the β' crystals preferentially oriented perpendicular to the axis of pores, which agreed with previous studies (Figure 23c). In addition, they found that the degree of orientation decreased with the decrease in pore diameter. They suggested that the decrease in perpendicular orientation (A direction in Figure 23f) was because of the formation of nuclei that

was parallel at the pore wall (B direction in Figure 23f). They further attributed this hypothesis to the role of wall surface on the crystallization of polymer inside AAO.

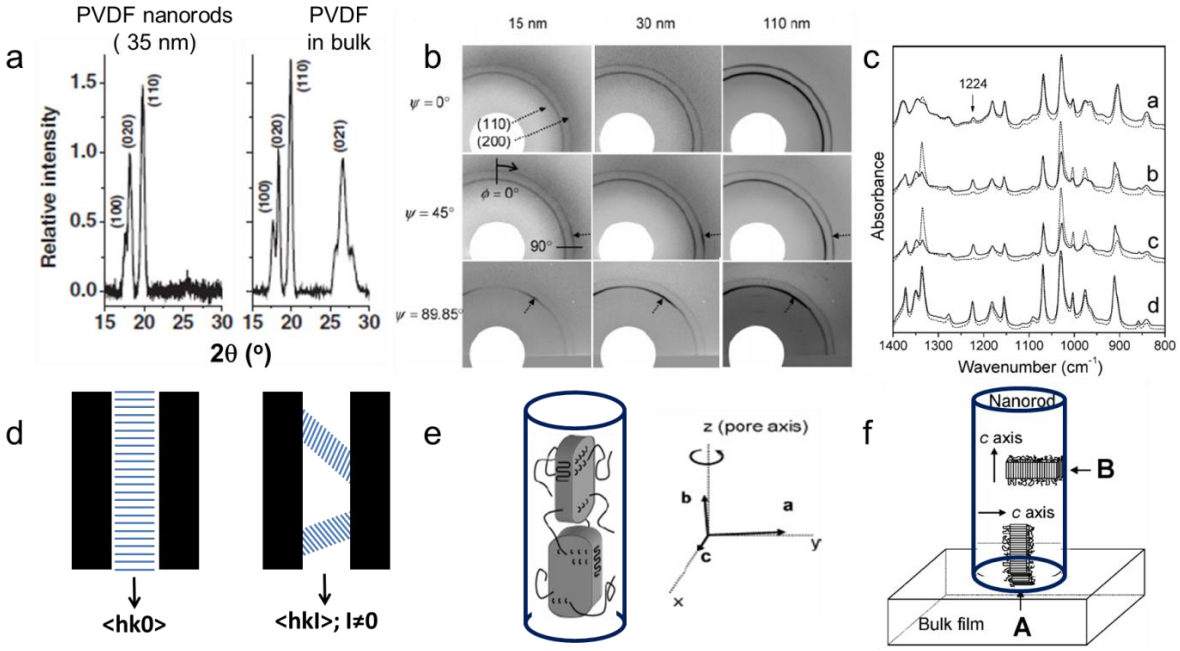

Figure 23. (a) XRD analysis of PVDF in 35 nm AAO compared with the bulk spectra.[55] (b) X-ray patterns for linear PE in AAO with different pore diameter.[56] (c) Polarized infrared spectra of the sPS nanorods with different diameter compared with the bulk.[57] (d), (e), and (f) are the schematics used in the discussion of corresponding results in (a), (b), and (c), respectively. Figure is reproduced from ref[55-57].

Another effect of confinement is on the polymer segmental dynamics. Previous studies from our group have shown that the segmental dynamics of linear PEO[48] and PCL[49] became faster under confinement within AAO, which was reflected on the reduction of the liquid-to-glass temperature (T_g). A recent work from Alexandris *et al.*[62] investigated the dynamics of a series of amorphous polymers (including poly(phenylmethylsiloxane) (PMPS), poly(vinyl acetate) (PVAc), 1,4-polybutadiene (PB), oligostyrene (PS), and poly(dimethylsiloxane) (PDMS)) with different T_g and polymer/substrate interfacial energies (γ_{SL}) by dielectric spectroscopy (DS). The interfacial energy was found to play a significant role in controlling the segmental dynamics of polymer under confinement. There was a trend for decreasing T_g relative to the bulk with increasing interfacial energy (Figure 24).

Figure 24. Dependence of $\Delta T_g = T_g^{AAO} - T_g^{bulk}$ on interfacial energy obtained at 290 K.[62]

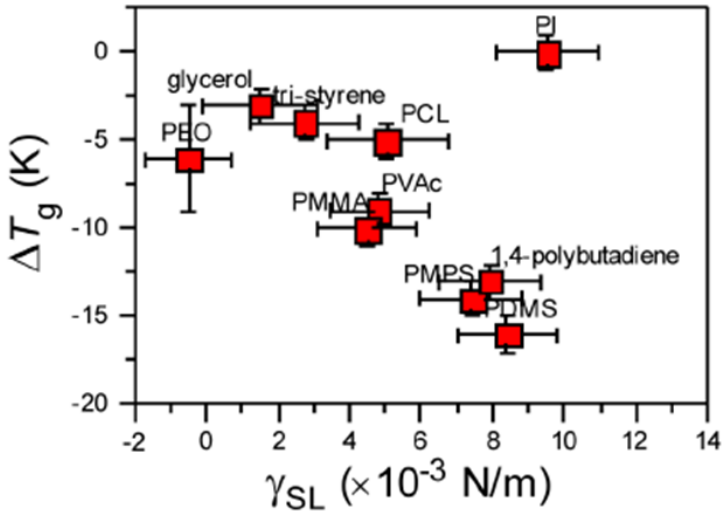

Currently most of the studies on polymer crystallizations under confinement have focused on linear polymers. In this thesis, we employ non-linear polymers with three different chain topologies, star[54], branched (hyperbranched PEOs, *hb*PEOs)[63], and a block copolymer, poly(isoprene-*b*-ethylene oxide) (PI-*b*-PEO), to study the effect of topology on the imbibition, crystallization, and segmental dynamics under confinement. First, despite the non-linear topologies of the samples, we show that all topologies can be successfully infiltrated into AAO. The imbibition of *hb*PEO within AAO follows the $t^{1/2}$ dependence but is slower than the LWE prediction. Surprisingly, imbibition of PI_{79}-*b*-PEO_{465} is achieved at a temperature far below the order-to-disorder transition temperature, T_{ODT}, where hexagonally packed cylinders are formed in the bulk. Secondly, as with homopolymers, confinement mainly affects the nucleation mechanism, crystal orientation, and the segmental dynamics of the polymer. Homogeneous nucleation is also found for non-linear PEOs in nanopores (in the absence of catalyst). In addition, the homogeneous nucleation temperature of PEOs exhibits a dependence on molecular weight, that is reminiscent to the glass temperature (T_g) dependence (Fox-Flory). This suggests a strong correlation between homogeneous nucleation temperature to T_g. The molecular weight dependence of the homogeneous nucleation temperature for non-linear polymers is identical to that of linear ones provided that the arm (star), branched (*hb*PEO), or the block (PI-*b*-PEO) molecular weight is used, instead of the total molecular weight. It further suggests that the chain diffusion mechanism involved in the process of homogeneous nucleation is controlled by long-range motions, like arm

retraction and branched point fluctuations. Thirdly, the segmental dynamics of non-linear polymers with different topologies speed up on confinement, reflecting a reduction in glass temperature.

1.2.4. Sample information

Polymers with three topologies (star-, hyperbranched, block-copolymer) were used in the present investigation (Table 3). First, four star-PEOs with different end groups and molecular weights were provided by Prof. Dr. Takamasa Sakai (The University of Tokyo). Tetra-Amine-Terminated PEO (TAPEO) and Tetra-NHS-Glutarate-Terminated PEO (TNPEO) were prepared from Tetrahydroxyl-Terminated PEO (THPEO) as described elsewhere in detail.[64,65] TNPEO has bulkier end group compared with TAPEO (Table 3). TAPEO sample contains remaining catalyst. Star THPEO was synthesized by successive anionic polymerization reaction of ethylene oxide from sodium alkoxide of pentaerythritol. Secondly, hyperbranched PEOs (*hb*PEOs) were provided by the group of Prof. Dr. Holger Frey (JGU Mainz)[66]. The synthesis was carried out in one step by random anionic copolymerization of ethylene oxide and glycidol using a partially deprotonated trifunctional core molecule and dimethyl sulfoxide as a solvent. Thirdly, diblock copolymers of PI-*b*-PEOs were synthesized and characterized by Wagner and Thiel (MPI-P).

Table 3. Molecular weights and schematics of star-PEOs, *hb*PEOs, and PI-*b*-PEOs

Star-PEOs	$\overline{M}_w$ (g/mol)	PDI	X_c (%)	T_m^o (^{o}C)	Molecular structure
TA PEO 10k	9620	1.05	62	66	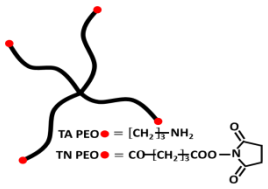
TA PEO 20k	20444	1.04	65	70	
TN PEO 10k	11100	1.01	43	54	
TN PEO 20k	19389	1.04	54	62	

***hb* PEOs**	$\overline{M}_n$ (g/mol)	PDI	Glycidol fraction	Degree of branching	$M_{branched}$	T_m^o (^{o}C)	Molecular Structure
G4 *hb*PEO	2980	2.1	0.04	0.08	396	23	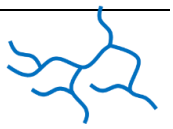
G9 *hb*PEO	2630	1.9	0.09	0.11	264	0	

BCPs	$\overline{M}_{n,PI}$ (g/mol)	$\overline{M}_{n,PEO}$ g/mol)	$\overline{M}_{total}$ g/mol)	N_{total}	f_{PEO}	X_c (%)	Molecular structure
PI_{79}-*b*-PEO_{84}	5360	3700	9060	163	0.36	0.67	
PI_{79}-*b*-PEO_{127}	5360	5600	11000	207	0.45	0.76	
PI_{47}-*b*-PEO_{234}	3200	10300	13460	281	0.72	0.83	
PI_{79}-*b*-PEO_{465}	5360	20450	25820	544	0.75	0.70	

1.2.5. Main findings

a. Star-PEOs in AAO[54]

First, we study the effect of confinement on the nucleation mechanism of star-PEOs. The melting and crystallization of star-PEOs (TAPEO and TNPEO) in confinement of AAO can be summarized with respect to a phase diagram shown in Figure 25. The melting temperature for both TAPEO and TNPEO show a pore size dependence according to the Gibbs-Thompson (GT) equation. On the other hand, the crystallization of the TAPEO and TNPEO shows distinctly different mechanism. TAPEO crystallizes *via* heterogeneous nucleation in confinement initiated by the remaining catalyst in the system. However, in the absence of impurities, TNPEO crystallized *via* homogeneous nucleation in confinement at much larger supercooling.

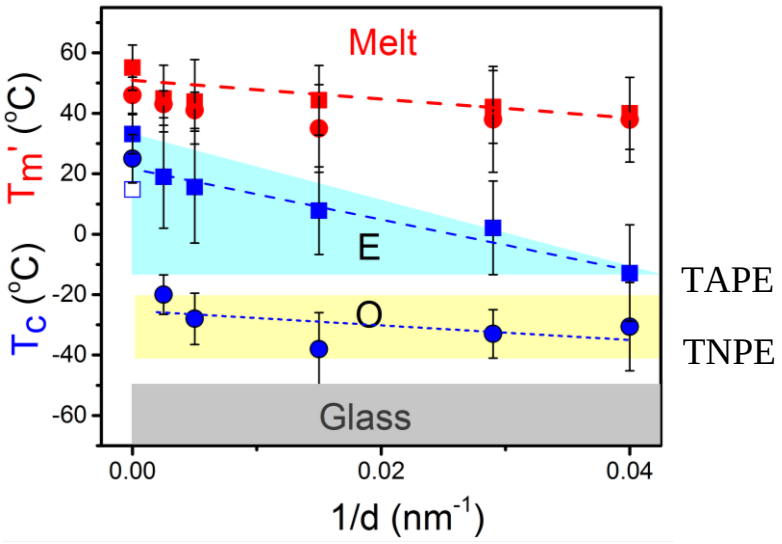

Figure 25. Apparent melting (red symbols) and crystallization temperatures (blue symbols) of TAPEO 10k (squares) and TNPEO 10k (circles) located inside AAO as a function of inverse pore diameter. The vertical bars do not indicate uncertainties but the temperature range corresponding to each crystallization/melting peak. Lines represent linear fits. Shadded areas indicate the (approximate) regions of heterogeneous nucleation (E), homogeneous nucleation (O) and glassy states.

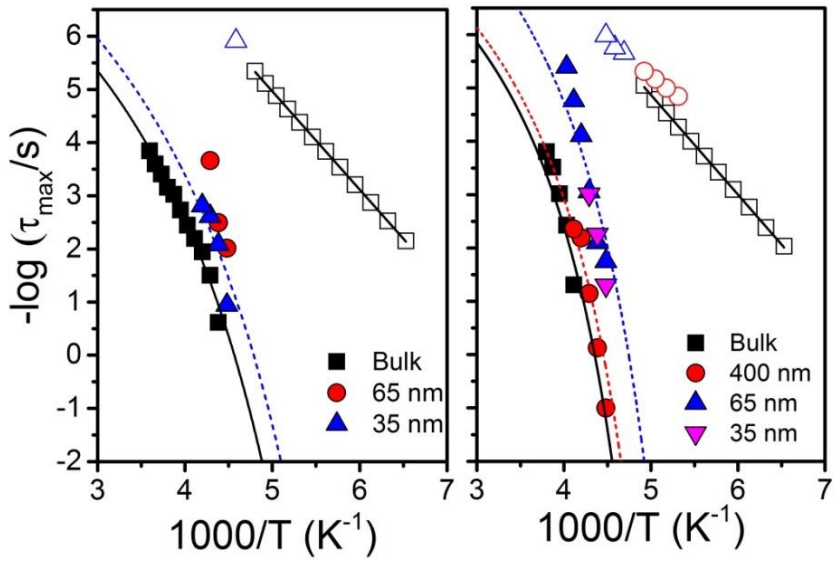

Figure 26. Relaxation times at maximum loss corresponding to the α-(filled symbol) and β- (open symbols) processes of TAPEO 20k (left) and TNPEO 20k (right) located inside self-ordered AAO pores with pore diameters ranging from 400 to 35 nm. Lines are fits to the VFT and Arrhenius equations.

Next we investigate the effect of confinement on the segmental dynamics by DS. The relaxation times obtained are depicted in Figure 26. For both TAPEO and TNPEO, the segmental relaxation

become faster on confinement, that is anticipated from the earlier studies of linear PEO within the same AAOs.[48-49] The speed-up of segmental dynamics reflects a reduction in glass temperature by confinement.[62]

b. Hyperbranched PEOs (*hb*PEOs) in AAO[63]

There are only few studies of homopolymer imbibition but absolutely no knowledge of how non-linear polymers penetrate into pores. In this thesis we present the results of such studies. We first show the imbibition process for hyperbranched PEOs. The imbibition heights of two *hb*PEOs as a function of $t^{1/2}$ are shown in Figure 27. The theoretical the LWE lines for different samples are shown with the dash lines. The imbibition speed of *hb*PEOs follows $t^{1/2}$ dependence but is slower than LWE prediction. Insets in Figure 27 demonstrate successful infiltration of AAO nanopores by the complex hyperbranched polymers. This facilitates the first investigation of the effect of confinement on the crystallization process for a highly nonlinear (hyperbranched) topology.

Next we compare the phase behavior of the different non-linear topologies. The crystallization and melting of G4 *hb*PEOs in confinement of AAO are compared with linear PEO and star-TNPEO in the same AAOs with respect to the phase diagram shown in Figure 28. Starting from higher temperatures, the apparent melting temperatures show a dependence on pore size according to the GT equation, as T_m' (^oC)= -500/d +27 (d in nm). In all cases, PEO crystallization within the smaller pores proceeds *via* homogeneous nucleation in sharp contrast to the bulk. Furthermore, homogeneous nucleation temperature has a weak dependence on confining volume as anticipated from earlier studies[53,54]. Notably, homogeneous nucleation temperatures appear in the following sequence $T_{\text{linear PEO}} > T_{\text{star PEO}} > T_{\text{G4 } hb\text{PEO}}$. At no surprise, homogeneous nucleation temperatures are in the vicinity of the glass temperatures of confined G4 *hb*PEO.

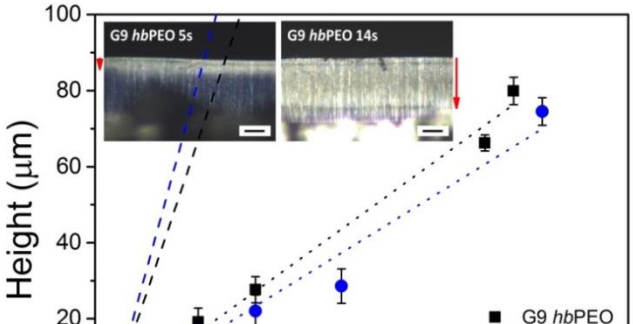

Figure 27. Imbibition length, *h*, as a function of $t^{1/2}$ for G4 *hb*PEO and G9 *hb*PEO within self-ordered AAOs with a pore diameter of 65 nm. Dashed lines give the predictions of the LWE equation. Dotted lines are the results of a linear fit to the experimental data. The inset shows reflection microscopy images of G9 *hb*PEO located inside 65 nm AAO infiltrated for 5 s (left) and for 14 s (right) (scale bar is 20 μm). Vertical arrows indicate respective imbibition lengths.

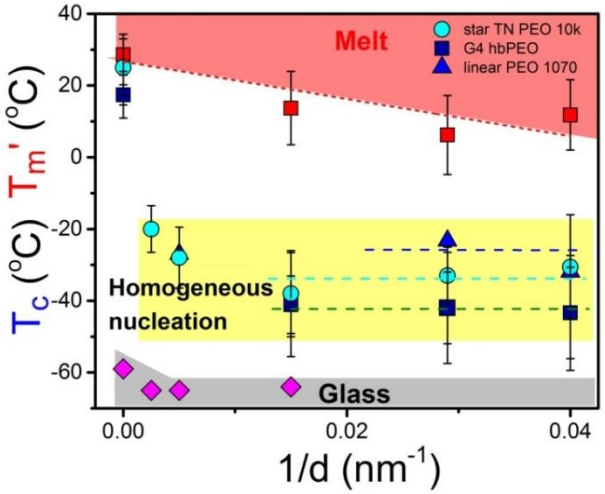

Figure 28. Apparent melting (red symbols) and crystallization temperatures (blue symbols) of star PEO 10000 g/mol (circles), G4 *hb*PEO (squares), and linear PEO (with molecular weight of 1070 g/mol) (triangles) located inside AAO as a function of inverse pore diameter. Glass temperatures from DS are shown with rhombi. The vertical bars indicate the temperature range corresponding to each crystallization/melting peak. Shadded areas indicate the (approximate) regions of melt state (red), homogeneous nucleation (yellow), and glass state (grey). Dashed lines are guides to the eye.

Lastly we investigate the effect of confinement on the segmental dynamics for *hb*PEOs. The segmental dynamics of G4 *hb*PEO confined within self-ordered AAOs were investigated with DS and the relaxation times are shown in Figure 29. The β-process, with an activation energy of E = 31±1 kJ/mol, is unaffected by the confinement as indicated by the $\tau(T)$ dependence. In the contrary,

the α-process speeds-up in confinement, which is in agreement with earlier studies of linear PEOs in AAO.[48] From the speed-up of segmental dynamics one can obtain that the T_g reduces from a bulk value of -50 ºC to -64 ºC within AAO with 65 nm pores. A slower process, known as the Maxwell-Wagner-Sillars (MWS) polarization, appears due to the heterogeneous nature of the material (alumina and polymers).

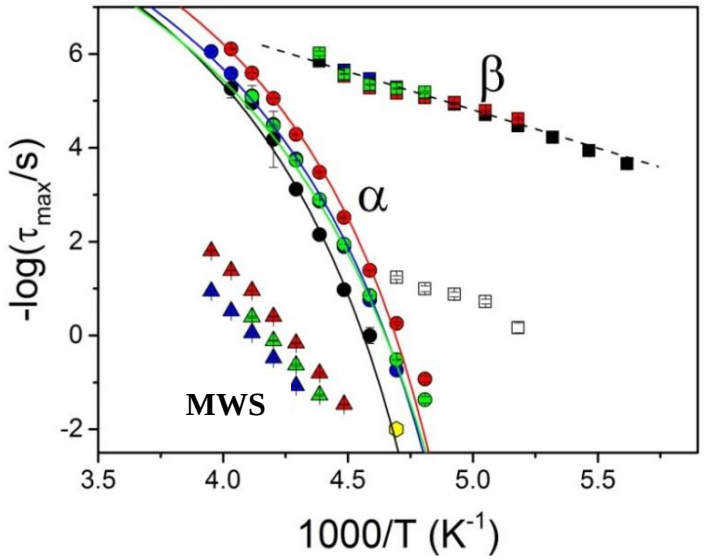

Figure 29. Relaxation times at maximum loss corresponding to the *α*-(filled circles) and *β*- (filled squares) and MWS (filled triangles) processes of bulk G4 *hb*PEO (black symbols) and G4 *hb*PEO located inside self-ordered AAO pores with pore diameters; 400 nm (red), 200 nm (blue) and 65 nm (green). Solid and dashed lines are fits to the VFT and Arrhenius equations, respectively. Open squares show the contribution of a small amount of water in the bulk sample. The yellow hexagon is the bulk T_g (obtained from DSC).

c. Block-copolymer (PI-*b*-PEO) in AAO

The third topology investigated in this thesis is a diblock copolymer (BCP), poly(isoprene-*b*-ethylene oxide) (PI-*b*-PEOs), within AAO. In principle, the imbibition process for block copolymer can be affected by the phase state of the copolymer at the temperature of imbibition. An earlier study[67] on a double crystalline diblock copolymer has shown the successful infiltration within AAO at a temperature above the T_{ODT}. Russell *et al.*[68,69] have shown in experiments that BCP can form into various morphologies under cylindrical confinement at equilibrium state based on both the surface interaction[70] and volume fraction of blocks, which was later confirmed by simulation studies[71]. On the other hand, the crystallizable block within BCP experiences two types of confinement within AAO (i) by the nanodomain of the BCP and (ii) by AAO nanopores. The specific system, PI-*b*-PEOs, is chosen here because of its high value of the interaction parameter (χ) (χ =65/T+0.125). These block copolymers can be strongly segregated even at low M_w. Both imbibition and crystallization study under confinement is interesting because of the nanodomain morphology of PI-*b*-PEOs.

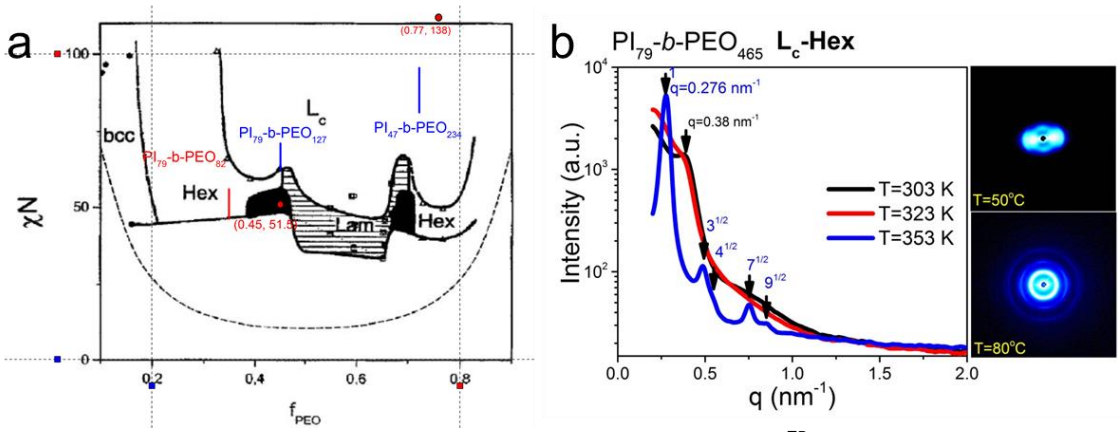

Figure 30. (a) Phase diagram of PI-*b*-PEO copied from ref[72]. The phase notation is as follows: Lc, crystalline lamellar, Lam, amorphous lamellar, Hex, hexagonal packed cylinders. The values of χN were obtained by using χ = 65/T+0.125. (b) (left) SAXS spectra for PI_{79}-*b*-PEO_{465} shown at different temperatures. Arrows indicate positions of the main and higher order peaks. (right) 2D SAXS patterns obtained at 50 °C (top) and 80 °C (bottom).

First, we study the imbibition of PI_{79}-*b*-PEO_{465} (total molecular weight is ~26 kg/mol) into AAO (pore diameter 65 nm, 35 nm, and 25 nm) at 80 °C, a temperature much below its T_{ODT} ≈ 300 °C. Based on the phase diagram[72] and SAXS results (Figure 30), the morphology of PI_{79}-*b*-PEO_{465} in the bulk is hexagonally packed cylinders (domain spacing of ~22.8 nm) at the imbibition temperature. Interestingly, the sample can be successfully infiltrated into AAO nanopores despite

the cylindrical nanodomains morphology and the high viscosity in the bulk. For the first time, we followed the imbibition of an ordered block copolymer in AAO nanopores and demonstrated a reversal of the imbibition speeds depending on the pore diameter. The imbibition of PI_{79}-*b*-PEO_{465} in 35 nm and 25 nm AAO pores is similar to that of linear PEO 50k (e.g. a linear PEO with twice the block copolymer M_W). However, in 65 nm pores, the imbibition speed of PI_{79}-*b*-PEO_{465} is much faster than that of a linear PEO 35k (e.g. linear PEO of approximately the same M_W as in the block copolymer) (Figure 31).

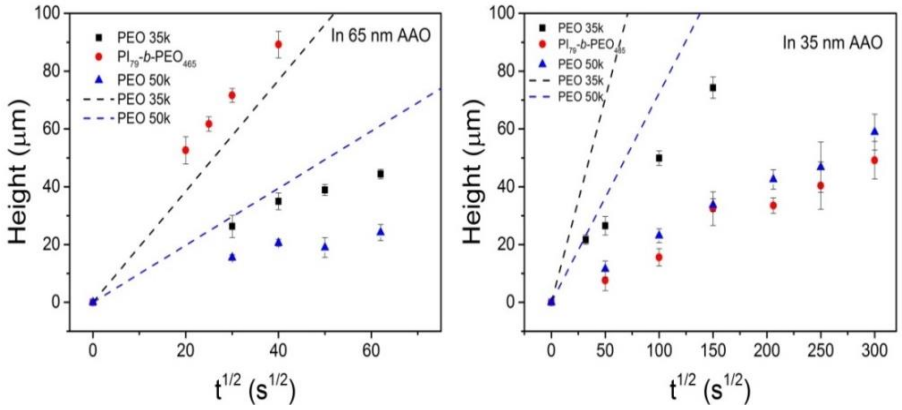

Figure 31. Imbibition length, *h*, as a function of $t^{1/2}$ for PI_{79}-*b*-PEO_{465} within self-ordered AAOs with a pore diameter of 65 nm (left) and 35 nm (right). Dashed lines give the predictions of the LWE equation for linear PEO 35k and 50k, respectively.

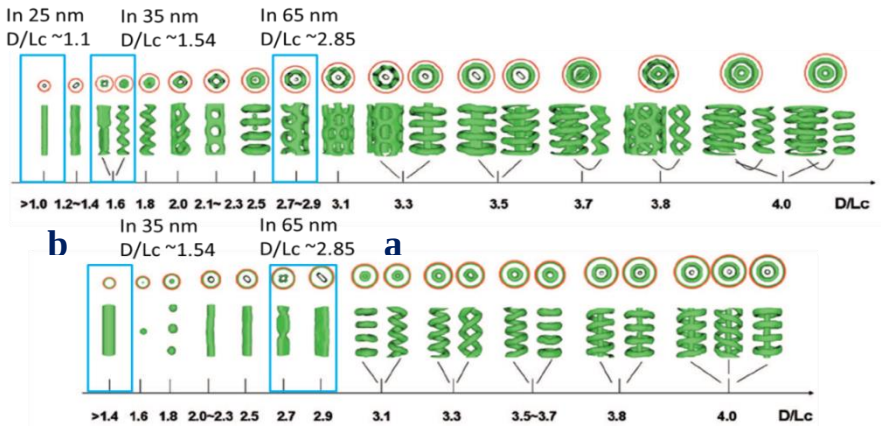

Figure 32. Self-assembled morphologies for asymmetric diblock copolymers with f_A=1/4 as a function of D/L_C. Only the *A* blocks are shown. The outermost red circle in each top view indicates the surface of the cylindrical pore. (top) α= −1.0 and (bottom) α =1.0. Figure reproduced from ref[71].

The reversal in imbibition for PI_{79}-*b*-PEO_{465} for the different pore diameters is at presently not well understood. The variable imbibition speeds for the different pore diameters could be discussed with the help of simulations of block copolymers within nanopores. Simulations[71] considered the effect of pore diameter, D, with respect to the domain spacing, L_c, as well as the type of surface/polymer interactions the latter given by the surface preference parameter α (α=1.0 strongly preferential for block *A*, α=0.1 nearly neutral and α=-1.0 strongly attractive to the majority block, *B* in this case, as f_A=1/4). In the case of PI_{79}-*b*-PEO_{465} (f_{PI}~1/4), the possible α value is 1.0 and the possible morphologies in 65 nm and 35 nm are depicted as a and b, respectively, based on simulation (Figure 32).

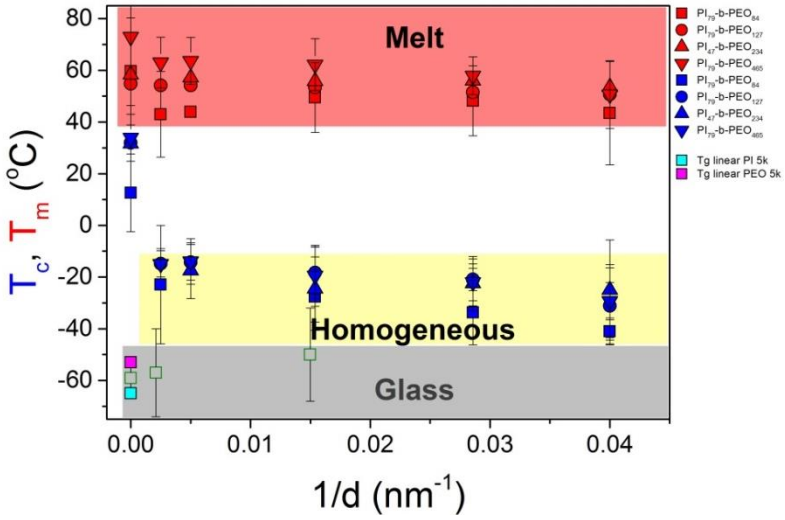

Figure 33. Apparent melting (red symbols) and crystallization temperatures (blue symbols) of PI-*b*-PEOs located inside AAO as a function of inverse pore diameter. Glass temperatures from DS are shown with squares. The vertical bars indicate the temperature range corresponding to each crystallization/melting peak. Shadded areas indicate the (approximate) regions of melt state (red), homogeneous nucleation (yellow), and glass state (grey).

The melting, crystallization and glass temperatures for PI-*b*-PEOs with different PEO fractions are summarized in a phase diagram, T vs 1/d, shown in Figure 33. The apparent melting temperature has a dependence on pore diameter according to GT equation. On the other hand, in AAO nanopores all the PI-*b*-PEOs crystallize at lower temperatures *via* homogeneous nucleation. Both melting temperatures (T_m) and crystallization temperatures (T_c) show dependence on

molecular weight of PEO block. PI_{79}-b-PEO_{84} has lower T_m and T_c than PI_{79}-*b*-PEO_{465} in all the pore sizes.

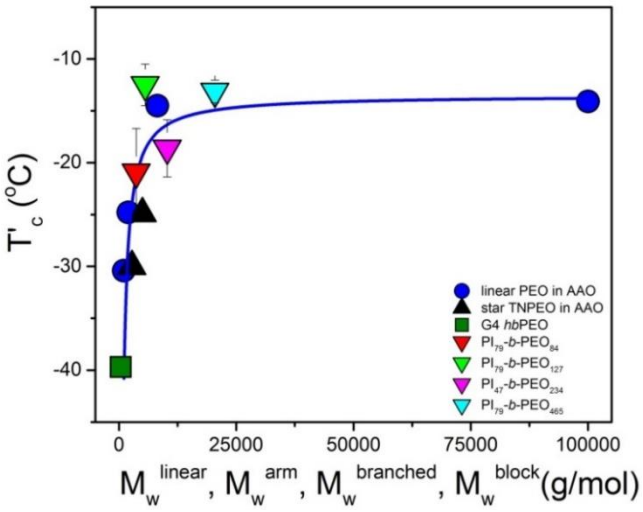

Figure 34. Dependence of the crystallization temperature T_c' initiated by homogeneous nucleation on the molecular weight of PEO in the limit $d \rightarrow \infty$ (d = AAO pore diameter). Spheres: the $T_c'(d)$ profiles were obtained from DSC scans of linear PEO inside AAO at a cooling rate of 10 K/min. Triangles: star-shaped PEOs (in the limit $d \rightarrow \infty$) obtained from DSC at a cooling rate of 10 K/min. Square: G4 *hb*PEO (in the limit $d \rightarrow \infty$) obtained from DSC at a cooling rate of 2 K/min. Inverted triangles: PI-*b*-PEOs (in the limit $d \rightarrow \infty$) obtained from DSC at a cooling rate of 10 K/min. The solid line is a fit using the Fox−Flory equation for linear PEOs located within self-ordered AAO templates.

A common feature of confined crystallization for the different PEO topologies is that all can be discussed on the basis of a single diagram: T_c' vs. PEO arm, PEO branch, or block molecular weight. The dependence of homogeneous nucleation temperature on polymer architecture is summarized in Figure 34. As with T_g, the dependence of homogeneous nucleation temperature on molecular weight for linear PEOs was found to follow similar Fox-Flory equation: [48,54]

$$T_C^{hom} = T_C^{\infty} - \frac{A}{M_w} \tag{28}$$

where T_C^{∞} is the apparent crystallization temperature via homogeneous nucleation in the limit of very high molecular weight. The homogeneous nucleation temperatures in the different polymer architectures (linear, star, branched, block) can be discussed by comparing the arm (star), branched (*hb*PEO), or the block (PI-*b*-PEO) molecular weight, instead of the total molecular weight. Figure 34 reveals a single Fox-Flory dependence for the different PEO architectures. It further suggests

that long-range motions, like arm retraction and branched point fluctuations, are controlling the chain diffusion mechanism involved in the process of homogeneous nucleation.

1.2.6. Outlook

We clearly know that a block copolymer can be infiltrated in nanopores in its disordered phase (PCL-*b*-PEO), but surprisingly, also in its ordered phase (cylindrical PI-*b*-PEO with a cylinderical morphology). However, the precise mechanism remains unclear. Further experiments in this direction could address the following remaining issues: (a) the role of nanodomain spacing, L_c, (b) of nanodomain morphology, and (c) of surface interaction between polymer and pore wall. On another issue, (e) could it be possible to infiltrate a semicrystalline polymer and, if so, what are the requirements of crystallinity, nucleation density, lamellar thickness with respect to the pore diameter, *i.e.*, can we make a crystal to flow? Lastly, (f) can we infiltrate a polymer at a temperature close to or slightly above its T_g, *i.e.*, can we make a glass to flow?

1.3. Effect of confinement on the crystallization and dynamics of water

1.3.1. Motivation and earlier knowledge

Water, one of the most important substances on the earth, exhibits a number of anomalies as compared to normal liquids. Two most known anomalies are (i) the volume increase upon freezing, and (ii) the density maximum at 4 ºC. Figure 35 provides a schematic of the temperature areas where water exists in its amorphous state at atmospheric pressure. Below 0 ºC, water can exist either in a crystal form or in the glassy state under certain conditions. According to Mishama *et al.* there are at least two distinct amorphous forms of water, high-density amorphous (HDA) water and low-density amorphous (LDA) water.[73] The first-order transition between HDA and LDA water suggests the existence of two liquid states in water. However, the critical point of liquid-liquid transition (LLT) for water is nearly experimentally inaccessible since it takes place in the region known as "no man's land" (from -120 ºC to -45 ºC), where water crystallizes.[74,75]

Figure 35. Schematic of different areas of amorphous water at atmospheric pressure. The

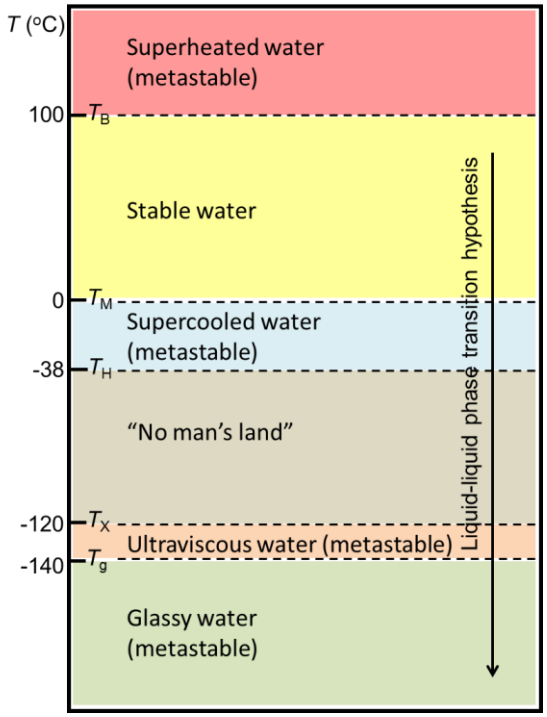

temperature ranging from -45 ºC to -120 ºC is known as "no man's land". Figure is reproduced from ref [74].

One strategy to study the hidden physical nature of water is by confinement into nanometer size pores. In fact, understanding water in confinement in itself is of fundamental importance in science and nanotechnology since confined water is frequently found in biological and geological systems. To this end, water has been confined in disordered porous materials such as silica hydrogels[76], Vycor glasses[77], graphite oxide[78] *etc*. More ordered confining media like AAO (hundreds of nm) and mesoporous silica (2~12 nm) have also been employed. Suzuki *et al.*[79] studied water in confinement AAOs with pore diameter ranging from 400 nm to 25 nm. In smaller pores (35 nm and 25 nm), the heterogeneities were filtered out. Thus, water crystallization - as with polymer crystallization - was initiated by homogeneous nucleation. In larger pores (400 nm and 200 nm) the majority of pores contain impurities which initiate crystallization *via* heterogeneous nucleation. This is shown in a phase diagram for confined water in Figure 36.

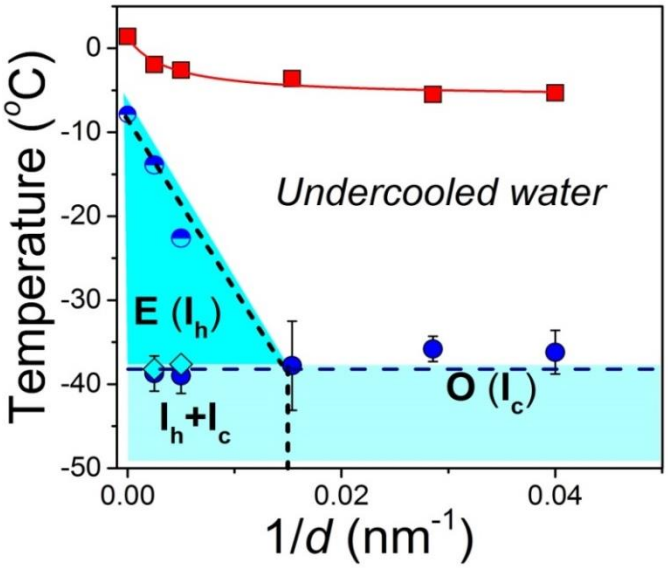

Figure 36. Phase diagram of water located inside self-ordered AAO. The squares indicate the melting temperatures as a function of inverse pore diameter. The red line is the result of a fit to the Gibbs−Thomson equation. The half-filled circles indicate heterogeneous nucleation whereas the completely filled circles homogeneous nucleation as obtained from dielectric spectroscopy. Light blue and cyan areas correspond to ice formation *via* homogeneous (O) and heterogeneous (E) nucleation, respectively. I_h indicates hexagonal ice, I_c predominantly cubic ice, whereas I_h + I_c indicates predominantly hexagonal ice. Figure is reproduced from ref [79].

Subsequently, the kinetics of ice nucleation in AAO was investigated.[80] Both heterogeneous and homogeneous nucleation was proved to be stochastic in nature, involving variable degrees of metastability (~4 ^{o}C and 0.4 ^{o}C for heterogeneous and homogeneous nucleation, respectively). To understand the kinetics of nucleation, the possible coupling of all pores through a heat wave and a sound wave were examined with the latter being the more realistic scenario.[80] In addition, the dynamics of water confined in AAO was studied with DS and infrared spectroscopy (IR).[81] The effects of confinement on water dynamics were manifested in (a) the bimodal relaxation, (b) the broadening of relaxation spectra, (c) the slower dipolar dynamics, and (d) the weaker dipolar orientation correlations. Two relaxation processes were revealed for confined water, which were attributed to ice and supercooled water relaxation, respectively.

Besides AAO, water has also been studied in narrower confining media, e.g. mesoporous silica (MPS). MPS, including MCM-41, SBA-15, and SBA-16, exhibit nanopores with defined and tunable diameters in the range from 2 nm to 12 nm. Several experimental studies have focused on the freezing/melting of confined water by means of differential scanning calorimetry (DSC) and solid-state nuclear magnetic resonance (NMR) with partially or completely filled pores.[82-84] In general, crystallization of water in confinement was suppressed below the bulk freezing temperature. The melting process of ice in MPS in most cases could be represented by a modified Gibbs-Thompson (GT) equation that took into account the existence of a surface layer of unfrozen water of thickness t (t value from 0.3 nm to 0.6 nm).[83,85,86]

$$T_m = T_m^{\infty}\left(1 - \frac{2\sigma}{\rho\Delta H}\frac{1}{R-t}\right) \tag{29}$$

Here, T_m^{∞}, is the melting point of bulk ice, T_m, is the melting point of confined ice, σ, is the interfacial free energy, ρ, is the density of water, ΔH, is the heat of fusion, and t is the thickness of non-freezable water layer. In addition, the minimum pore size (D*) for the first-order transition (melting/freezing) of water to take place was also discussed based on the thermal hysteresis between freezing/ melting of confined water. D* = 2.8 ± 0.1 nm was indicated as a limiting pore diameter for the existence of crystallization in confinement.[83,87] Clearly, smaller pores disrupt the hydrogen bonding network of ice that is required for crystallization.

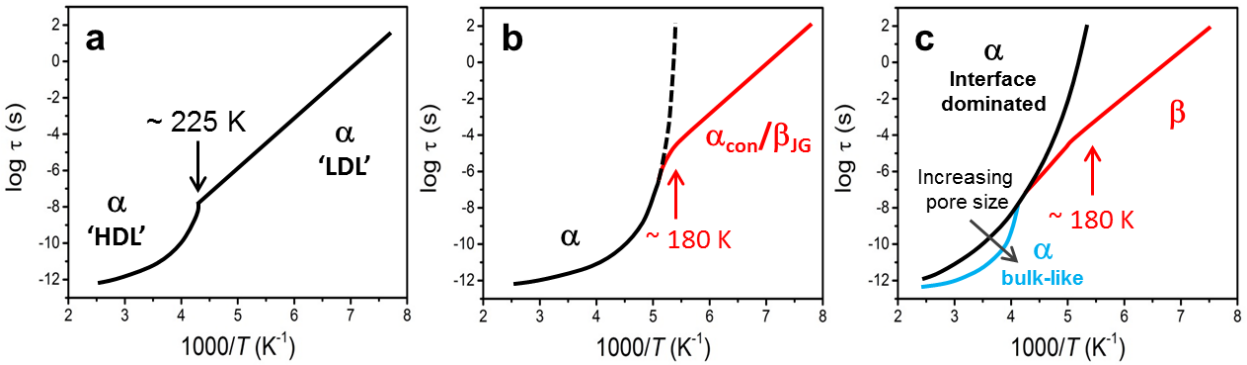

Figure 37. Schematic diagram at ambient pressure of different scenarios for the dynamical behavior of supercooled confined water. α_{conf} indicate confined α-relaxation, and β_{JG} means Johari−Goldstein β-relaxation. Figure is reproduced from ref [88].

Although there is consensus about the critical diameter needed for water to crystallize, much less is known about the dynamics of supercooled water and of ice under confinement. Earlier efforts studied the dynamics of confined water by solid-state NMR spectroscopy,[89-91] quasielastic neutron scattering (QENS),[92-94] and DS[95], however, their results and predictions were contradictory. A dynamic crossover for water in MPS was suggested at either 225 K or 180 K. The interpretation of the dynamic crossover is highly depended on the analysis of experimental data as well as the type of experiment. Three most commonly used relaxation scenarios for confined water exist that were summarized in a recent review (Figure 37).[88] In the first scenario (Figure 37a), a dynamic crossover at ~225 K from a non-Arrhenius dependence at high temperatures to an Arrhenius dependence at low temperatures was observed *via* NMR and QENS. Based on the LLT hypothesis, this dynamic crossover was assigned to a fragile-to-strong transition upon crossing the Widom line (Widom line is often regarded as an extension of the coexistence line into the ''one-phase region''[96]) in the vicinity of LLT[97,98]. The second scenario (Figure 37b), based on DS studies, suggest a change in the dynamics from a liquid-like behavior (Vogel-Fulcher-Tammann, VFT) to a localized motion (Arrhenius) at ~180 K.[94,95] A possible interpretation for the observed crossover is that the characteristic length scales of the dynamics of confined liquid approach the size of the confinement, which prevents its further growth. The third scenario (Figure 37c), based on solid-state ^{2}H NMR studies of heavy water in MPS, predicts two dynamic crossovers at ~ 225 K and ~ 185 K, respectively. A α-process-like dynamics was probed above 225 K whereas a β-process was observed below this temperature. In this case, the crossover was assigned to a

solidification of the inner water. The second crossover at 185 K was assigned to a glass-temperature of interfacial water.

Evidently, existing literature on the dynamics of supercooled confined water is anything but clear. More efforts are necessary with precisely controlled confining media. In this chapter, two model confining media are employed, namely, hollow silica (HS) spheres and MPS with precisely controlled pore diameters and pore volumes. In the former system, water is confined in hollow spheres with diameters ranging from 190 nm to 640 nm. Homogeneous nucleation is found inside the hollow spheres, whereas, water in the surrounding dispersion crystallizes *via* heterogeneous nucleation. In the latter system, water is confined in nanopores with diameter ranging from 2.1 nm to 5 nm. Water is able to crystallize only in MPS pores larger than 2.6 nm. The freezing/melting of water in MPS compared with those within AAO are presented in a phase diagram covering a broad range of pore diameters. A liquid-like surface layer with thickness 0.21 nm is obtained from the modified GT equation. Moreover, the dynamics of water in MPS are investigated by employing both DS and solid-state NMR in the same samples. Relaxation processes of two types of water molecules inside nanopores are observed with both techniques which correspond to inner viscous water and interfacial water, respectively.

1.3.2. Sample information

In this study, we employ two confining media (hollow silica (HS) spheres and mesoporous silica (MPS)) to study water crystallization and dynamics. HS spheres provide a moderate confinement with relatively large confining volume and sphere diameter (~ hundreds of nm). On the other hand, MPS provide a severe confinement with extremely small confining volume and pore diameter (few of nm).

HS spheres were provided by the group of Prof. Dr. Markus Retsch (University of Bayreuth). Briefly, the synthesis was made in three steps: (1) synthesis of polystyrene particles, (2) coating of polystyrene template particles with a silica shell *via* a Stöber condensation process, and (3) calcination of the core-shell particles to remove the polystyrene core. The TEM images of HS spheres demonstrate a nearly perfect uniformity (Table 4). These hierarchical materials exhibit structure over several length scales; they comprise micropores within the silica network (with a size of ~3 nm), which are then confined to a thin shell (~20 nm) of a hollow sphere (~190-640 nm). Herein we explore how these multiple length scales affect the nucleation mechanism of water.

MPS samples were synthesized in the group of Prof. Dr. Katharina Landfester (MPI-P) by Dr. Wei Huang. The synthetic procedure is described elsewhere in detail.[99] Because of the different synthetic procedure, MPS with pore diameter larger than 3 nm possesses straight pore channels, while MPS with pore diameter smaller than 2.6 nm show a twisted morphology (Table 4). The pore diameters, shell thicknesses, pore lengths, pore volumes, together with some representative images are provided in Table 4. The SEM images demonstrate the morphology of MPS particles. The TEM images of MPS show very uniform channels of nanopores.

Table 4. Summary of the confining media employed in this study (hollow silica spheres and mesoporous silica)

Hollow silica spheres	Diameter (nm)	Thickness (nm)	Pore Volume (nm^3)	S_{pore}/V_{pore} (nm^{-1})	TEM images
HS-185	185.1 ± 3.7	20.6 ± 1.3	$1.6 \cdot 10^6$	0.042	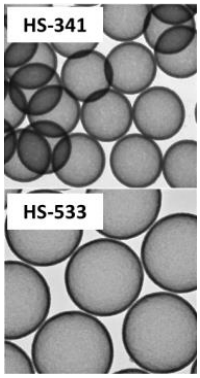
HS-257	256.2 ± 4.7	15.6 ± 1.0	$6.0 \cdot 10^6$	0.027	
HS-341	340.7 ± 7.5	20.1 ± 1.2	$1.4 \cdot 10^7$	0.020	
HS-533	533.4 ± 12.5	23.5 ± 1.6	$6.0 \cdot 10^7$	0.012	
HS-533-s	533.4 ± 12.5	23.5 ± 1.6	$6.0 \cdot 10^7$	0.012	
HS-533-l	533.4 ± 12.5	23.5 ± 1.6	$6.0 \cdot 10^7$	0.012	
HS-637	636.6 ± 13.4	21.9 ± 1.8	$1.1 \cdot 10^8$	0.010	

Mesoporous silica	Pore diameter (nm)	Channel length (μm)	Pore Volume (nm^3)	SEM images	TEM images
077C	2.0	0.55	1.7×10^3	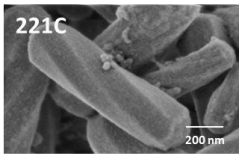	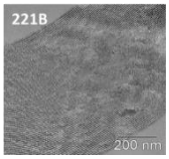
221C	2.5	1	4.9×10^3		
221F	2.6	0.7	3.7×10^3		
221G	3.0	0.9	6.5×10^3		
221D	3.8	--	--	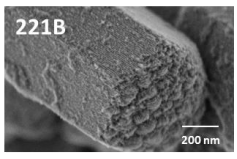	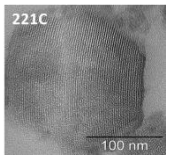
221A2	4.0	0.9	1.1×10^4		
221B	5.0	1.2	2.4×10^4		

1.3.3. Main findings

a. Crystallization of water under moderate confinement; water inside hollow silica spheres (HS spheres)[100]

The effect of confinement on water crystallization is studied in monodisperse HS spheres in an homogeneous aqueous phase (with concentration of 10 wt%). Both DSC and DS isochronal measurement are used in this study. As an example, DSC of ice formation in water/HS spheres (533 nm in diameter) shows two exothermic peaks (Figure 38a); a major one in the temperature range from -20 to -24 ^{o}C and a weaker one in the range from -36 to -41 ^{o}C. We assign the crystallization peaks at higher and lower temperatures to water crystallized outside/inside the HS spheres, respectively. Water outside the HS spheres is the majority component and crystallizes *via* heterogeneous nucleation at low supercooling. On the other hand, a fraction of water can penetrate through the thin channels (~3 nm) on the shell to the inside of hollow spheres. The thin channels filter out nearly all the impurities, thus, water inside HS spheres crystallizes at large supercooling *via* homogeneous nucleation, which contributes to the weak peak at low temperatures. Besides DSC measurement, isochronal measurements made by DS can also be employed to study water crystallization. Earlier studies have shown that the high dielectric permittivity of water (ε_{water} ~ 80, ε_{ice} ~ 3.4 at 1 MHz) and its temperature dependence can be employed as a fingerprint of the mechanism of ice nucleation (Figure 39). Figure 38b shows an example of the change in permittivity upon cooling. In agreement with the DSC result, we observed two steps on cooling, which are assigned to ice formation *via* heterogeneous and homogeneous nucleation, respectively.

The melting and crystallization temperatures of water in HS spheres are summarized in a phase diagram, in comparison with earlier results of water crystallization in AAO (Figure 40). The temperatures of homogeneous nucleation in the two different systems are in remarkable coincidence. In contrast, there is no heterogeneous nucleation inside HS spheres, implying that the ~3 nm channels on the shell of HS spheres filter away all heterogeneities and leave homogeneous nucleation as the sole nucleation mechanism. The assignment of the low temperature process in the smaller HS spheres to homogeneous nucleation (and of the low temperature feature of HS-637 to heterogeneous nucleation) becomes more evident by comparison with the onset of homogeneous ice nucleation in supercooled water microdroplets as a function of the droplet volume (Figure 40). Overall, our results support the notion that nucleation of ice is volume-dominated.[101]

Figure 38. (a) DSC curves of water/hollow silica spheres with diameter of 533 nm

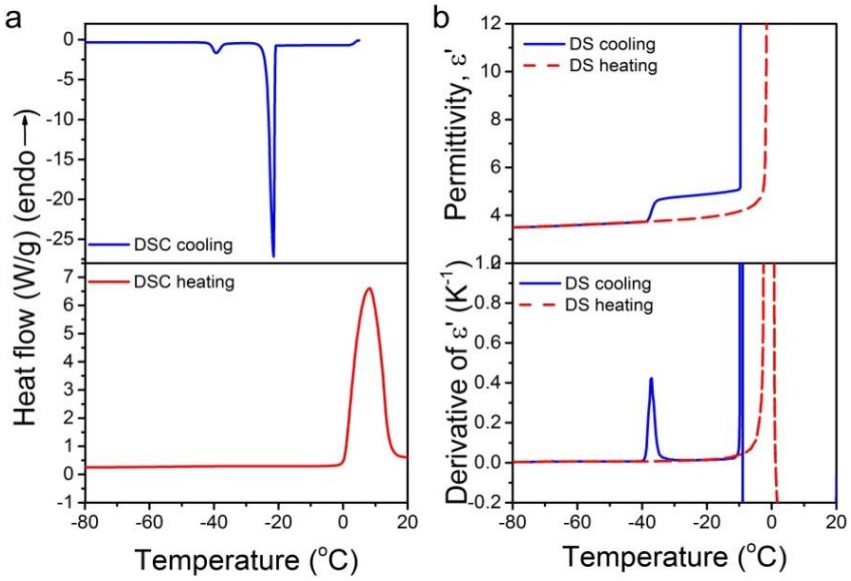

obtained on cooling (top) and heating (bottom) with a rate of 10 ºC/min. (b) Temperature dependence of the dielectric permittivity (top) and derivative of dielectric permittivity, dε'/dT, as a function of temperature of water/hollow silica spheres with diameter of 533 nm obtained on cooling and heating with a rate of 5 ºC/min.

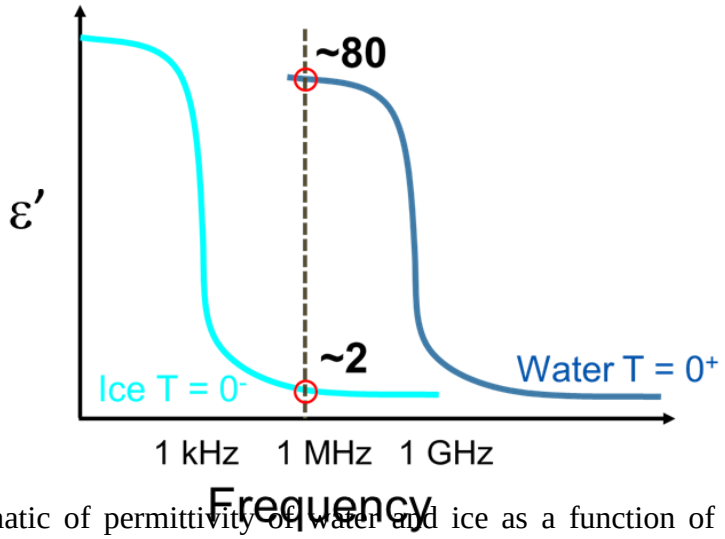

Figure 39. Schematic of permittivity of water and ice as a function of frequency at temperatures around freezing ($T=0^+$, $T=0^-$). The vertical line indicates the frequency used in the isochronal measurements (1 MHz).

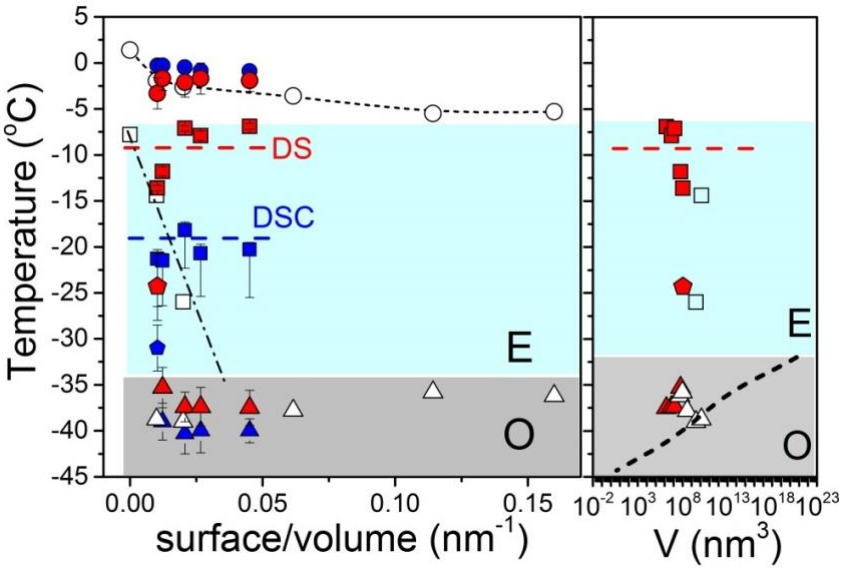

Figure 40. (Left) Phase diagram of water in hollow silica spheres (filled symbols) compared to water located inside self-ordered AAO (open symbols)[22] as a function of the surface to volume ratio. Magenta and blue symbols represent results from DS and DSC, respectively. The circles indicate the melting temperatures. The squares indicate the process of heterogeneous nucleation. The triangles indicate crystallization via homogeneous nucleation. Grey and blue areas correspond to ice formation via homogeneous (O) and heterogeneous (E) nucleation, respectively. The dash-dotted line gives the heterogeneous nucleation of ice in self-ordered AAOs.[22] The horizontal dashed line gives the temperature of heterogeneous nucleation in polystyrene-silica core-shell particles (CS-261) from DS (magenta) and DSC (blue). Note the agreement with the DS and DSC results in water/HS solutions. (Right) Dependence of the homogeneous nucleation temperature on volume. The black dashed line gives the reported lowest temperatures for homogeneous nucleation of water droplets as a function of their volume (cooling rate of ~1 ºC/min).[7] The symbols and shaded areas have the same meaning.

b. Crystallization and dynamics of water under severe confinement; water inside mesoposous silica (MPS)

Compared with other confining media, MPS contains nanopores with much smaller diameters and pore volumes. The crystallization of water located inside MPS was studied by DS and DSC. Here we concentrate only in two pore sizes. For water in 221B (d ~ 5 nm), there are three step-like decreases in permittivity as measured on cooling (Figure 41a), that can be better seen as peaks in the derivative representation, $d\varepsilon'/dT$ (Figure 41b). We assign the two peaks at higher and lower temperatures to the crystallization of water inside MPS initiated *via* heterogeneous and

homogeneous nucleation, respectively. In addition, both samples show a broad reversible peak ~ -67 °C. As we will discuss below, this peak corresponds to the relaxation of an interfacial water layer (process 4 in Figure 43, 44). For 221F (d ~ 2.6 nm) with the smaller pore diameter, only a broad peak ~ -67 °C is observed, indicating the complete absence of crystallization within this nanopores.

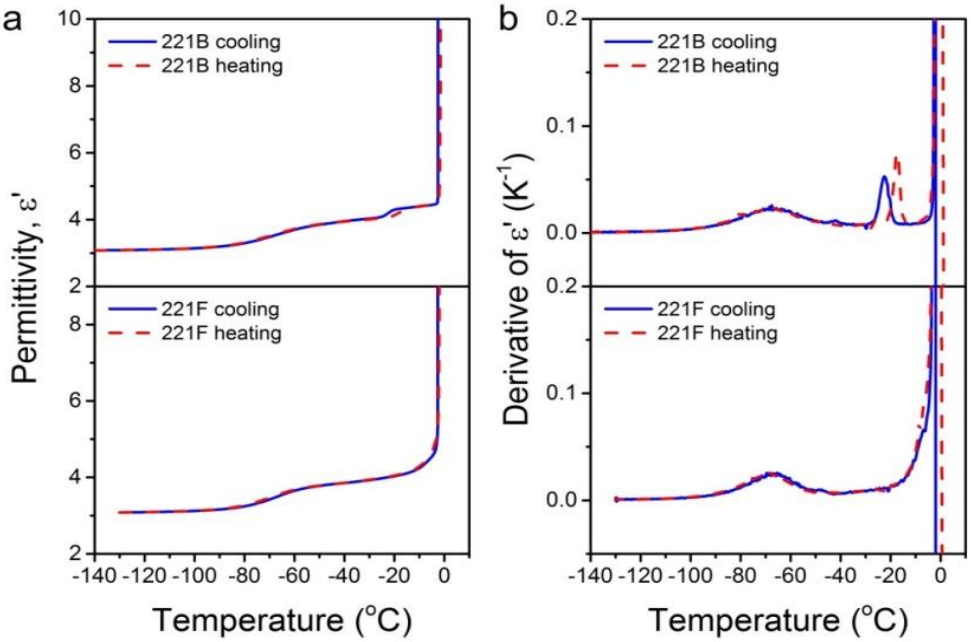

Figure 41. (a) Temperature dependence of the dielectric permittivity and (b) of the derivative of dielectric permittivity, dε'/dT, as a function of temperature for water/221B (top) and water/221F (bottom) obtained on cooling (solid line) and heating (dashed line) with a rate of 5 °C/min.

The freezing/melting of confined water in different media (AAO, SBA, MCM) with pore diameters from 400 nm down to 2.2 nm can be discussed with respect to the "phase diagram" shown in Figure 42. The melting and crystallization temperatures for water inside SBA-15 and MCM-41 are shown as diamonds and circles, respectively. First of all, a liquid like surface water layer (t = 0.3 nm) is obtained inside MPS from the T_m *vs*. d dependence according to the modified GT (equation 29). For water inside pores with diameter larger than 2.6 nm, the temperatures of homogeneous nucleation in the different systems are in remarkable coincidence. In pores with diameter smaller than 2.6 nm no crystallization of water was observed. The yellow points correspond to the relaxation of the supercooled water at low temperatures (obtained at a frequency of 1 MHz). The phase diagram indicates a large (T ~ 1/d) space where water remains in its

amorphous state (red area, MCM). Interestingly, at a diameter of ~2.6 nm below which no crystallization is obtained, the homogeneous and heterogeneous $T^{O,E}$ vs. $1/d$ lines meet.

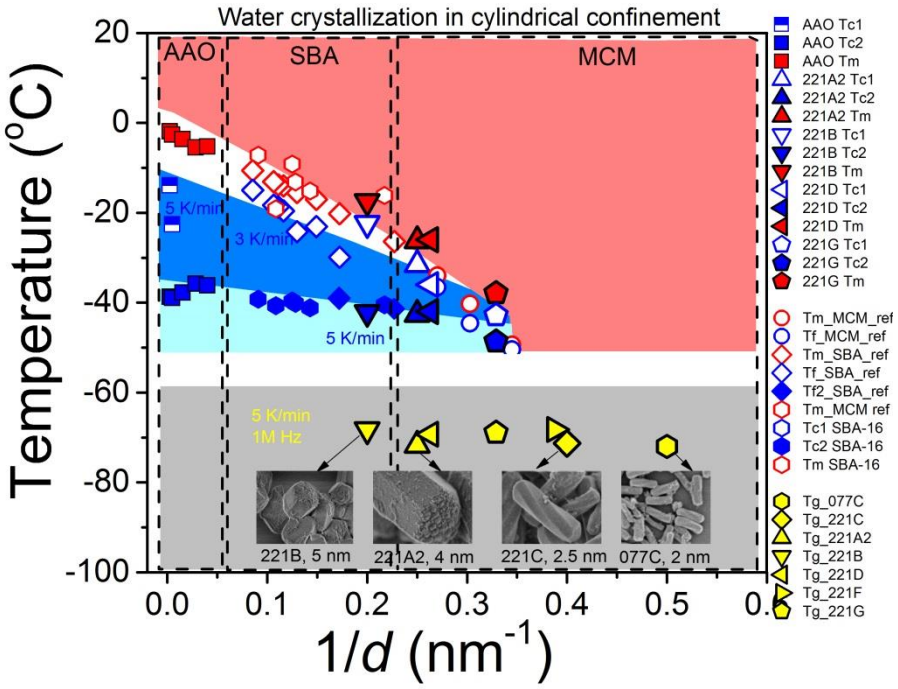

Figure 42. Phase diagram of water in mesoporous silica (larger symbols) compared to water located inside self-ordered AAO[79] (square symbols) and other MCM/SBA pores in literatures[83] as a function of the inverse of pore diameter. Red area corresponds to the melt. Blue and cyan areas correspond to ice formation *via* heterogeneous (E) and homogeneous (O) nucleation, respectively, grey area corresponds to the amorphous state.

As a next step we investigate the dynamics of confined water (and ice) with DS and NMR. We again employ two typical MPS nanopores (221B and 221F) for DS and NMR investigation. Four processes were detected from DS for D_2O confined in 221B below the homogeneous nucleation temperature (214 K) (Figure 43). Process 1 (olive triangle) and 2 (green triangle) have the highest intensities ($T\Delta\varepsilon$). Based on the weight contribution, process 2 is assigned to the relaxation of outside excess ice and process 1 is related to the relaxation of excess ice close to the pore wall. Because of the interaction of water molecule to the -OH groups on the wall, both processes are slightly slower than bulk ice dynamics (indicated by the solid line). Besides, we observe two dynamically distinguishable types of water coexisting at low temperatures, depicted as process 3 (magenta triangle) and process 4 (orange triangle). Based on the intensity and relaxation times, the

faster process 4 is assigned to the unfrozen interfacial water close to the pore wall. The slower process 3 is assigned to the inner water which is less mobile. The relaxation times of process 3 is similar to that of bulk ice, suggesting the inner water is crystallized at these temperatures, which agrees with the results from the isochronal DS measurements. Interestingly, relaxation times obtained from NMR stimulated echo measurement (blue and cyan spheres for fast and slower process, respectively) show similar temperature dependence as with DS and further confirm the assignment of the two processes as revealing relaxations from liquids water.

Figure 43. Relaxation times for different processed obtained from fitting DS spectra for

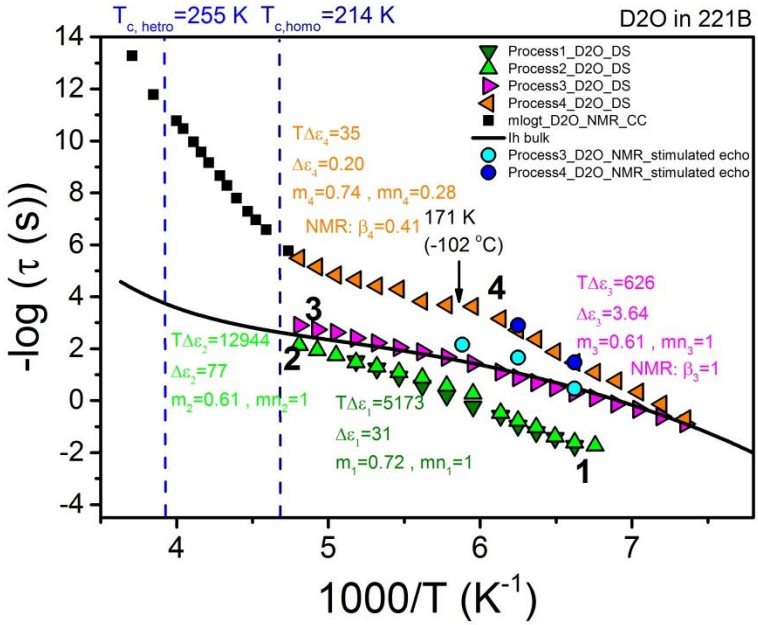

D_2O confined in 221B, compared with those obtained from NMR T_1 measurement, fitted with Cole-Cole function (filled squares), and stimulated echo. Solid line shows the relaxation of bulk ice[102]. The vertical dash lines show the crystallization temperature of D_2O *via* heterogeneous and homogeneous nucleation, respectively.

Figure 44 shows the dynamics of H_2O in 221F from DS measurements in comparison to that of D_2O from NMR. Again, four processes were detected from DS below despite the absence of freezing of water inside the pores. Based on the combined results from DS and NMR, both process 3 and 4 are assigned to the relaxation of unfrozen water. The relaxation times of process 3 in 221F are slightly faster than in bulk ice, suggesting the nature of inner water in 221F is very viscous. Process 4 in 221F has similar dielectric strength as with that of 221B ($T\Delta\varepsilon$ ~ 34 K).

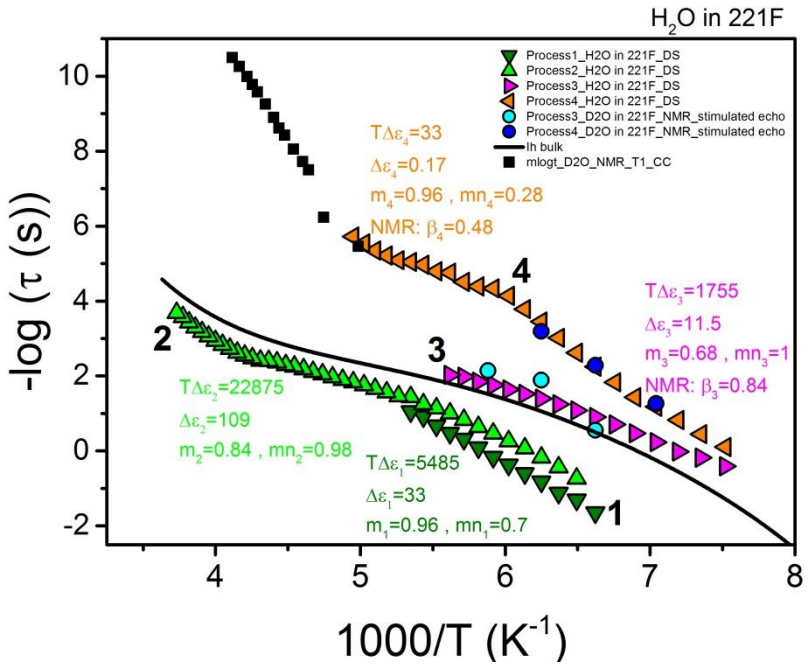

Figure 44. Relaxation times for different processed obtained from fitting DS spectra for H_2O confined in 221F, compared with those obtained from NMR T_1 measurement, fitted with Cole-Cole function (filled squares), and stimulated echo. Solid line shows the relaxation of bulk ice[102].

1.3.4. Outlook

We have established the phase diagram of confined water by employing a broad (*T vs.* 1/*d*) parameter size that includes confinement within nanoporous alumina (AAO), and SBA/MCM mesoporous silica. The *T vs.* 1/*d* dependence of the homogeneous and heterogeneous nucleation temperatures is established. The two lines coincide at a pore diameter of ~ 2.6 nm below which no crystallization could be obtained. This provides an estimate for the critical nucleus size required for ice formation to proceed.

By employing both DS and solid state NMR techniques we investigated the ice and water dynamics within mesoporous silica. Both techniques identified -for the first time- two states of liquid water under confinement and their dynamic features were explored.

In the future water can be studied in water/glycerol and water/LiCl mixtures where the V-shaped phase behavior is controlled by intensive variables of pressure and concentration. These

phase diagrams can be studied under AAO confinement, to establish the role of confinement on the possible breaking of local tetrahedral order.

1.4 References

1. Bruening, M.; Dotzauer, D., Polymer films: Just spray it. *Nature Materials* **2009,** *8* (6), 449.
2. Sakaue, T.; Raphaël, E., Polymer chains in confined spaces and flow-injection problems: some remarks. *Macromolecules* **2006,** *39* (7), 2621-2628.
3. De Gennes, P.-G.; Gennes, P.-G., *Scaling Concepts in Polymer Physics*. Cornell university press: 1979.
4. Kremer, F., *Dynamics in Geometrical Confinement*. Springer: 2016.
5. Beard, J. D.; Rouholamin, D.; Farmer, B. L.; Evans, K. E.; Ghita, O. R., Control and modelling of capillary flow of epoxy resin in aligned carbon nanotube forests. *RSC Advances* **2015,** *5* (49), 39433-39441.
6. Ugarte, D.; Chatelain, A.; De Heer, W., Nanocapillarity and chemistry in carbon nanotubes. *Science* **1996,** *274* (5294), 1897-1899.
7. Alvine, K. J.; Shpyrko, O. G.; Pershan, P. S.; Shin, K.; Russell, T. P., Capillary filling of anodized alumina nanopore arrays. *Physical Review Letters* **2006,** *97* (17), 175503.
8. Masuda, H.; Fukuda, K., Ordered metal nanohole arrays made by a two-step replication of honeycomb structures of anodic alumina. *Science* **1995,** *268* (5216), 1466-1468.
9. 9Masuda, H.; Hasegwa, F.; Ono, S., Self-Ordering of Cell Arrangement of Anodic Porous Alumina Formed in Sulfuric Acid Solution. *Journal of the Electrochemical Society* **1997,** *144* (5), L127-L130.
10. Masuda, H.; Yada, K.; Osaka, A., Self-ordering of cell configuration of anodic porous alumina with large-size pores in phosphoric acid solution. *Japanese Journal of Applied Physics* **1998,** *37* (11A), L1340.
11. Mijangos, C.; Hernandez, R.; Martin, J., A review on the progress of polymer nanostructures with modulated morphologies and properties, using nanoporous AAO templates. *Progress in Polymer Science* **2016,** *54*, 148-182.
12. Duran, H.; Steinhart, M.; Butt, H.-J. r.; Floudas, G., From heterogeneous to homogeneous nucleation of isotactic poly (propylene) confined to nanoporous alumina. *Nano Letters* **2011,** *11* (4), 1671-1675.
13. Lucas, R., Ueber das Zeitgesetz des kapillaren Aufstiegs von Flüssigkeiten. *Kolloid-Zeitschrift* **1918,** *23* (1), 15-22.
14. Washburn, E. W., The dynamics of capillary flow. *Physical Review* **1921,** *17* (3), 273.
15. Hamraoui, A.; Nylander, T., Analytical approach for the Lucas–Washburn equation. *Journal of Colloid and Interface Science* **2002,** *250* (2), 415-421.
16. Mammen, L.; Papadopoulos, P.; Friedemann, K.; Wanka, S.; Crespy, D.; Vollmer, D.; Butt, H.-J., Transparent and airtight silica nano-and microchannels with uniform tubular cross-section. *Soft Matter* **2013,** *9* (41), 9824-9832.
17. De Gennes, P., Scaling theory of polymer adsorption. *Journal de Physique* **1976,** *37* (12), 1445-1452.

18. Shin, K.; Obukhov, S.; Chen, J.-T.; Huh, J.; Hwang, Y.; Mok, S.; Dobriyal, P.; Thiyagarajan, P.; Russell, T. P., Enhanced mobility of confined polymers. *Nature Materials* **2007,** *6* (12), 961.
19. Ok, S.; Steinhart, M.; Şerbescu, A.; Franz, C.; Vaca Chávez, F. n.; Saalwächter, K., Confinement effects on chain dynamics and local chain order in entangled polymer melts. *Macromolecules* **2010,** *43* (10), 4429-4434.
20. Cao, B.-Y.; Yang, M.; Hu, G.-J., Capillary filling dynamics of polymer melts in nanopores: experiments and rheological modelling. *RSC Advances* **2016,** *6* (9), 7553-7559.
21. Grigoriadis, C.; Duran, H.; Steinhart, M.; Kappl, M.; Butt, H.-J. r.; Floudas, G., Suppression of phase transitions in a confined rodlike liquid crystal. *ACS Nano* **2011,** *5* (11), 9208-9215.
22. Dimitrov, D.; Milchev, A.; Binder, K., Capillary rise in nanopores: molecular dynamics evidence for the Lucas-Washburn equation. *Physical Review Letters* **2007,** *99* (5), 054501.
23. Johner, A.; Shin, K.; Obukhov, S., Nanofluidity of a polymer melt: Breakdown of Poiseuille's flow model. *EPL (Europhysics Letters)* **2010,** *91* (3), 38002.
24. Stroberg, W.; Keten, S.; Liu, W. K., Hydrodynamics of capillary imbibition under nanoconfinement. *Langmuir* **2012,** *28* (40), 14488-14495.
25. Yao, Y.; Alexandris, S.; Henrich, F.; Auernhammer, G.; Steinhart, M.; Butt, H.-J.; Floudas, G., Complex dynamics of capillary imbibition of poly (ethylene oxide) melts in nanoporous alumina. *The Journal of Chemical Physics* **2017,** *146* (20), 203320.
26. Yao, Y.; Butt, H. J.; Floudas, G.; Zhou, J.; Doi, M., Theory on capillary filling of polymer melts in nanopores. *Macromolecular Rapid Communications* **2018**, 1800087.
27. Yao, Y.; Butt, H.-J.; Zhou, J.; Doi, M.; Floudas, G., Capillary Imbibition of Polymer Mixtures in Nanopores. *Macromolecules* **2018**.
28. Bunn, C. W., The crystal structure of long-chain normal paraffin hydrocarbons. The "shape" of the CH2 group. *Transactions of the Faraday Society* **1939,** *35*, 482-491.
29. Strobl, G. R.; Strobl, G. R., *The Physics of Polymers*. Springer: 1997; Vol. 2.
30. Lauritzen, J.; Hoffman, J. D., Theory of formation of polymer crystals with folded chains in dilute solution. *J. Res. Natl. Bur. Stand. A* **1960,** *64* (1), 73102.
31. Rastogi, S.; Hikosaka, M.; Kawabata, H.; Keller, A., Role of mobile phases in the crystallization of polyethylene. Part 1. Metastability and lateral growth. *Macromolecules* **1991,** *24* (24), 6384-6391.
32. Keller, A.; Hikosaka, M.; Rastogi, S.; Toda, A.; Barham, P.; Goldbeck-Wood, G., An approach to the formation and growth of new phases with application to polymer crystallization: effect of finite size, metastability, and Ostwald's rule of stages. *Journal of Materials Science* **1994,** *29* (10), 2579-2604.
33. Imai, M.; Kaji, K.; Kanaya, T.; Sakai, Y., Ordering process in the induction period of crystallization of poly (ethylene terephthalate). *Physical Review B* **1995,** *52* (17), 12696.
34. Olmsted, P. D.; Poon, W. C.; McLeish, T.; Terrill, N.; Ryan, A., Spinodal-assisted crystallization in polymer melts. *Physical Review Letters* **1998,** *81* (2), 373.
35. Hauser, G.; Schmidtke, J.; Strobl, G., The role of co-units in polymer crystallization and melting: new insights from studies on syndiotactic poly (propene-co-octene). *Macromolecules* **1998,** *31* (18), 6250-6258.
36. Strobl, G., Colloquium: Laws controlling crystallization and melting in bulk polymers. *Reviews of Modern Physics* **2009,** *81* (3), 1287.

37. Gedde, U. W., *Polymer Physics*. Springer Science & Business Media: 2013.
38. Floudas, G.; Reiter, G.; Lambert, O.; Dumas, P., Structure and dynamics of structure formation in model triarm star block copolymers of polystyrene, poly (ethylene oxide), and poly (ε-caprolactone). *Macromolecules* **1998,** *31* (21), 7279-7290.
39. Zardalidis, G.; Mars, J.; Allgaier, J.; Mezger, M.; Richter, D.; Floudas, G., Influence of chain topology on polymer crystallization: poly (ethylene oxide)(PEO) rings vs. linear chains. *Soft Matter* **2016,** *12* (39), 8124-8134.
40. Doi, M.; Edwards, S. F., *The Theory of Polymer Dynamics*. oxford university press: 1988; Vol. 73.
41. De Gennes, P., Reptation of stars. *Journal de Physique* **1975,** *36* (12), 1199-1203.
42. Needs, R.; Edwards, S., Computer simulation of the dynamics of star molecules. *Macromolecules* **1983,** *16* (9), 1492-1495.
43. Klein, J.; Fletcher, D.; Fetters, L. J., Diffusional behaviour of entangled star polymers. *Nature* **1983,** *304* (5926), 526.
44. Loo, Y.-L.; Register, R. A.; Ryan, A. J.; Dee, G. T., Polymer crystallization confined in one, two, or three dimensions. *Macromolecules* **2001,** *34* (26), 8968-8977.
45. Montenegro, R.; Antonietti, M.; Mastai, Y.; Landfester, K., Crystallization in miniemulsion droplets. *The Journal of Physical Chemistry B* **2003,** *107* (21), 5088-5094.
46. Massa, M. V.; Dalnoki-Veress, K.; Forrest, J., Crystallization kinetics and crystal morphology in thin poly (ethylene oxide) films. *The European Physical Journal E* **2003,** *11* (2), 191-198.
47. Kageyama, K.; Tamazawa, J.-i.; Aida, T., Extrusion polymerization: catalyzed synthesis of crystalline linear polyethylene nanofibers within a mesoporous silica. *Science* **1999,** *285* (5436), 2113-2115.
48. Suzuki, Y.; Duran, H.; Steinhart, M.; Butt, H.-J.; Floudas, G., Homogeneous crystallization and local dynamics of poly (ethylene oxide)(PEO) confined to nanoporous alumina. *Soft Matter* **2013,** *9* (9), 2621-2628.
49. Suzuki, Y.; Duran, H.; Akram, W.; Steinhart, M.; Floudas, G.; Butt, H.-J., Multiple nucleation events and local dynamics of poly (ε-caprolactone)(PCL) confined to nanoporous alumina. *Soft Matter* **2013,** *9* (38), 9189-9198.
50. Massa, M. V.; Dalnoki-Veress, K., Homogeneous crystallization of poly (ethylene oxide) confined to droplets: the dependence of the crystal nucleation rate on length scale and temperature. *Physical Review Letters* **2004,** *92* (25), 255509.
51. Taden, A.; Landfester, K., Crystallization of poly (ethylene oxide) confined in miniemulsion droplets. *Macromolecules* **2003,** *36* (11), 4037-4041.
52. Chen, H.-L.; Hsiao, S.-C.; Lin, T.-L.; Yamauchi, K.; Hasegawa, H.; Hashimoto, T., Microdomain-tailored crystallization kinetics of block copolymers. *Macromolecules* **2001,** *34* (4), 671-674.
53. Müller, A. J.; Balsamo, V.; Arnal, M. L., Nucleation and crystallization in diblock and triblock copolymers. In *Block copolymers II*, Springer: 2005; pp 1-63.
54. Yao, Y.; Sakai, T.; Steinhart, M.; Butt, H.-J. r.; Floudas, G., Effect of poly (ethylene oxide) architecture on the bulk and confined crystallization within nanoporous alumina. *Macromolecules* **2016,** *49* (16), 5945-5954.

55. Steinhart, M.; Göring, P.; Dernaika, H.; Prabhukaran, M.; Gösele, U.; Hempel, E.; Thurn-Albrecht, T., Coherent kinetic control over crystal orientation in macroscopic ensembles of polymer nanorods and nanotubes. *Physical Review Letters* **2006,** *97* (2), 027801.
56. Shin, K.; Woo, E.; Jeong, Y. G.; Kim, C.; Huh, J.; Kim, K.-W., Crystalline structures, melting, and crystallization of linear polyethylene in cylindrical nanopores. *Macromolecules* **2007,** *40* (18), 6617-6623.
57. Wu, H.; Wang, W.; Huang, Y.; Su, Z., Orientation of syndiotactic polystyrene crystallized in cylindrical nanopores. *Macromolecular Rapid Communications* **2009,** *30* (3), 194-198.
58. Guan, Y.; Liu, G.; Gao, P.; Li, L.; Ding, G.; Wang, D., Manipulating crystal orientation of poly (ethylene oxide) by nanopores. *ACS Macro Letters* **2013,** *2* (3), 181-184.
59. García-Gutiérrez, M.-C.; Linares, A.; Hernández, J. J.; Rueda, D. R.; Ezquerra, T. A.; Poza, P.; Davies, R. J., Confinement-induced one-dimensional ferroelectric polymer arrays. *Nano Letters* **2010,** *10* (4), 1472-1476.
60. Shingne, N.; Geuss, M.; Hartmann-Azanza, B.; Steinhart, M.; Thurn-Albrecht, T., Formation, morphology and internal structure of one-dimensional nanostructures of the ferroelectric polymer P (VDF-TrFE). *Polymer* **2013,** *54* (11), 2737-2744.
61. Michell, R. M.; Lorenzo, A. T.; Müller, A. J.; Lin, M.-C.; Chen, H.-L.; Blaszczyk-Lezak, I.; Martin, J.; Mijangos, C., The crystallization of confined polymers and block copolymers infiltrated within alumina nanotube templates. *Macromolecules* **2012,** *45* (3), 1517-1528.
62. Alexandris, S.; Papadopoulos, P.; Sakellariou, G.; Steinhart, M.; Butt, H.-J. r.; Floudas, G., Interfacial energy and glass temperature of polymers confined to nanoporous alumina. *Macromolecules* **2016,** *49* (19), 7400-7414.
63. Yao, Y.; Suzuki, Y.; Seiwert, J.; Steinhart, M.; Frey, H.; Butt, H.-J. r.; Floudas, G., Capillary Imbibition, Crystallization, and Local Dynamics of Hyperbranched Poly (ethylene oxide) Confined to Nanoporous Alumina. *Macromolecules* **2017,** *50* (21), 8755-8764.
64. Sakai, T.; Matsunaga, T.; Yamamoto, Y.; Ito, C.; Yoshida, R.; Suzuki, S.; Sasaki, N.; Shibayama, M.; Chung, U.-i., Design and fabrication of a high-strength hydrogel with ideally homogeneous network structure from tetrahedron-like macromonomers. *Macromolecules* **2008,** *41* (14), 5379-5384.
65. Nomoto, Y.; Matsunaga, T.; Sakai, T.; Tosaka, M.; Shibayama, M., Structure and physical properties of dried Tetra-PEG gel. *Polymer* **2011,** *52* (18), 4123-4128.
66. Wilms, D.; Schömer, M.; Wurm, F.; Hermanns, M. I.; Kirkpatrick, C. J.; Frey, H., Hyperbranched PEG by random copolymerization of ethylene oxide and glycidol. *Macromolecular Rapid Communications* **2010,** *31* (20), 1811-1815.
67. Suzuki, Y.; Duran, H.; Steinhart, M.; Butt, H.-J.; Floudas, G., Suppression of Poly (ethylene oxide) Crystallization in Diblock Copolymers of Poly (ethylene oxide)-b-poly (ε-caprolactone) Confined to Nanoporous Alumina. *Macromolecules* **2014,** *47* (5), 1793-1800.
68. Xiang, H.; Shin, K.; Kim, T.; Moon, S. I.; McCarthy, T. J.; Russell, T. P., From cylinders to helices upon confinement. *Macromolecules* **2005,** *38* (4), 1055-1056.
69. Xiang, H.; Shin, K.; Kim, T.; Moon, S. I.; McCarthy, T. J.; Russell, T. P., Block copolymers under cylindrical confinement. *Macromolecules* **2004,** *37* (15), 5660-5664.

70. Kellogg, G.; Walton, D.; Mayes, A.; Lambooy, P.; Russell, T.; Gallagher, P.; Satija, S., Observed surface energy effects in confined diblock copolymers. *Physical Review Letters* **1996,** *76* (14), 2503.
71. Yu, B.; Sun, P.; Chen, T.; Jin, Q.; Ding, D.; Li, B.; Shi, A.-C., Self-assembly of diblock copolymers confined in cylindrical nanopores. *The Journal of Chemical Physics* **2007,** *127* (11), 114906.
72. Floudas, G.; Vazaiou, B.; Schipper, F.; Ulrich, R.; Wiesner, U.; Iatrou, H.; Hadjichristidis, N., Poly (ethylene oxide-b-isoprene) diblock copolymer phase diagram. *Macromolecules* **2001,** *34* (9), 2947-2957.
73. Mishima, O.; Calvert, L.; Whalley, E., An apparently first-order transition between two amorphous phases of ice induced by pressure. *Nature* **1985,** *314* (6006), 76.
74. Mishima, O.; Stanley, H. E., The relationship between liquid, supercooled and glassy water. *Nature* **1998,** *396* (6709), 329.
75. Murata, K.-i.; Tanaka, H., Liquid–liquid transition without macroscopic phase separation in a water–glycerol mixture. *Nature Materials* **2012,** *11* (5), 436.
76. Cammarata, M.; Levantino, M.; Cupane, A.; Longo, A.; Martorana, A.; Bruni, F., Structure and dynamics of water confined in silica hydrogels: X-ray scattering and dielectric spectroscopy studies. *The European Physical Journal E* **2003,** *12* (1), 63-66.
77. Zanotti, J.-M.; Bellissent-Funel, M.-C.; Chen, S.-H., Relaxational dynamics of supercooled water in porous glass. *Physical Review E* **1999,** *59* (3), 3084.
78. Cerveny, S.; Barroso-Bujans, F.; Alegria, A.; Colmenero, J., Dynamics of water intercalated in graphite oxide. *The Journal of Physical Chemistry C* **2010,** *114* (6), 2604-2612.
79. Suzuki, Y.; Duran, H.; Steinhart, M.; Kappl, M.; Butt, H.-J. r.; Floudas, G., Homogeneous nucleation of predominantly cubic ice confined in nanoporous alumina. *Nano Letters* **2015,** *15* (3), 1987-1992.
80. Suzuki, Y.; Steinhart, M.; Butt, H.-J. r.; Floudas, G., Kinetics of ice nucleation confined in nanoporous alumina. *The Journal of Physical Chemistry B* **2015,** *119* (35), 11960-11966.
81. Suzuki, Y.; Steinhart, M.; Graf, R.; Butt, H.-J. r.; Floudas, G., Dynamics of ice/water confined in nanoporous alumina. *The Journal of Physical Chemistry B* **2015,** *119* (46), 14814-14820.
82. Kittaka, S.; Ueda, Y.; Fujisaki, F.; Iiyama, T.; Yamaguchi, T., Mechanism of freezing of water in contact with mesoporous silicas MCM-41, SBA-15 and SBA-16: role of boundary water of pore outlets in freezing. *Physical Chemistry Chemical Physics* **2011,** *13* (38), 17222-17233.
83. Schreiber, A.; Ketelsen, I.; Findenegg, G. H., Melting and freezing of water in ordered mesoporous silica materials. *Physical Chemistry Chemical Physics* **2001,** *3* (7), 1185-1195.
84. Jähnert, S.; Chávez, F. V.; Schaumann, G.; Schreiber, A.; Schönhoff, M.; Findenegg, G., Melting and freezing of water in cylindrical silica nanopores. *Physical Chemistry Chemical Physics* **2008,** *10* (39), 6039-6051.
85. Brovchenko, I.; Oleinikova, A., *Interfacial and Confined Water*. Elsevier: 2008.
86. Jaroniec, M.; Solovyov, L. A., Improvement of the Kruk− Jaroniec− Sayari method for pore size analysis of ordered silicas with cylindrical mesopores. *Langmuir* **2006,** *22* (16), 6757-6760.

87. Findenegg, G. H.; Jähnert, S.; Akcakayiran, D.; Schreiber, A., Freezing and melting of water confined in silica nanopores. *ChemPhysChem* **2008,** *9* (18), 2651-2659.
88. Cerveny, S.; Mallamace, F.; Swenson, J.; Vogel, M.; Xu, L., Confined water as model of supercooled water. *Chemical Reviews* **2016,** *116* (13), 7608-7625.
89. Sattig, M.; Vogel, M., Dynamic crossovers and stepwise solidification of confined water: a 2H NMR study. *The Journal of Physical Chemistry Letters* **2013,** *5* (1), 174-178.
90. Sattig, M.; Reutter, S.; Fujara, F.; Werner, M.; Buntkowsky, G.; Vogel, M., NMR studies on the temperature-dependent dynamics of confined water. *Physical Chemistry Chemical Physics* **2014,** *16* (36), 19229-19240.
91. Grünberg, B.; Emmler, T.; Gedat, E.; Shenderovich, I.; Findenegg, G. H.; Limbach, H. H.; Buntkowsky, G., Hydrogen Bonding of Water Confined in Mesoporous Silica MCM-41 and SBA-15 Studied by 1H Solid-State NMR. *Chemistry-A European Journal* **2004,** *10* (22), 5689-5696.
92. Teixeira, J.; Bellissent-Funel, M.; Chen, S.; Dorner, B., Observation of new short-wavelength collective excitations in heavy water by coherent inelastic neutron scattering. *Physical Review Letters* **1985,** *54* (25), 2681.
93. Soper, A. K.; Ricci, M. A., Structures of high-density and low-density water. *Physical Review Letters* **2000,** *84* (13), 2881.
94. Liu, L.; Chen, S.-H.; Faraone, A.; Yen, C.-W.; Mou, C.-Y., Pressure dependence of fragile-to-strong transition and a possible second critical point in supercooled confined water. *Physical Review Letters* **2005,** *95* (11), 117802.
95. Sjöström, J.; Swenson, J.; Bergman, R.; Kittaka, S., Investigating hydration dependence of dynamics of confined water: Monolayer, hydration water and Maxwell–Wagner processes. *The Journal of Chemical Physics* **2008,** *128* (15), 154503.
96. Xu, L.; Kumar, P.; Buldyrev, S. V.; Chen, S.-H.; Poole, P. H.; Sciortino, F.; Stanley, H. E., Relation between the Widom line and the dynamic crossover in systems with a liquid–liquid phase transition. *Proceedings of the National Academy of Sciences of the United States of America* **2005,** *102* (46), 16558-16562.
97. Mallamace, F.; Broccio, M.; Corsaro, C.; Faraone, A.; Wanderlingh, U.; Liu, L.; Mou, C.-Y.; Chen, S.-H., The fragile-to-strong dynamic crossover transition in confined water: nuclear magnetic resonance results. AIP: 2006.
98. Giovambattista, N.; Rossky, P.; Debenedetti, P., Computational studies of pressure, temperature, and surface effects on the structure and thermodynamics of confined water. *Annual Review of Physical Chemistry* **2012,** *63*, 179-200.
99. Sayari, A.; Han, B.-H.; Yang, Y., Simple synthesis route to monodispersed SBA-15 silica rods. *Journal of the American Chemical Society* **2004,** *126* (44), 14348-14349.
100. Yao, Y.; Ruckdeschel, P.; Graf, R.; Butt, H.-J. r.; Retsch, M.; Floudas, G., Homogeneous nucleation of ice confined in hollow silica spheres. *The Journal of Physical Chemistry B* **2016,** *121* (1), 306-313.
101. Pruppacher, H., A new look at homogeneous ice nucleation in supercooled water drops. *Journal of the Atmospheric Sciences* **1995,** *52* (11), 1924-1933.
102. Johari, G.; Whalley, E., The dielectric properties of ice Ih in the range 272–133 K. *The Journal of Chemical Physics* **1981,** *75* (3), 1333-1340.
103. Chung-li, Y.; Goodwin, J. W.; Ottewill, R. H., Studies on the preparation of monodisperse polystyrene latices. **1976,** *60*, 163-165.

104. Stöber, W.; Fink, A.; Bohn, E., Controlled Growth of Monodisperse Silica Spheres in Micron Size Range. *J. Colloid Interface Sci.* **1968,** *26*, 62-69.

Chapter 2. Complex Dynamics of Capillary Imbibition of Poly(ethylene oxide) Melts in Nanoporous Alumina

This chapter has been published as a research paper in The Journal of Chemical Physics. It is reprinted here with kind permission of AIP Publishing.

Yang Yao, Stelios Alexandris, Franziska Henrich, Günter Auernhammer, Martin Steinhart, Hans-Jürgen Butt, and George Floudas

The Journal of Chemical Physics 146, 20, 203320 (2017)
DOI: 10.1063/1.4978298

Abstract

Capillary penetration of a series of entangled poly(ethylene oxide) (PEO) melts within nanopores of self-ordered alumina follows an approximate $t^{1/2}$ behavior according to the Lucas-Washburn equation (LWE); t is time. However, the dependence on the capillary diameter deviates from the predicted proportionality to $d^{1/2}$; d is the pore diameter. We observed a reversal in the dynamics of capillary rise with polymer molecular weight. Chains with 50 entanglements ($M_w \leq 100$ kg/mol) or less show a *slower* capillary rise than theoretically predicted as opposed to chains with more entanglements ($M_w \geq 500$ kg/mol) that display a *faster* capillary rise. Although a faster capillary rise has been predicted by theory and observed experimentally, it is the first time to our knowledge that a slower capillary rise is observed for an entangled polymer melt under conditions of strong confinement (with $2R_g/d=1$). These results are discussed in the light of theoretical predictions for the existence of a critical length scale that depends on the molecular weight and separates the microscopic ($d<d^*$) from the macroscopic ($d>d^*$) regime.

2.1. Introduction

The way that polymers penetrate into thin pores is of fundamental interest and importance for many applications.[1-5] For example, fabrication of nanocomposite materials with enhanced mechanical strength by nanomoulding is based on the flow behavior of polymers through nanochannels.[6] Of particular interest is the case of a confining medium with sizes being comparable to the molecular length scale.[1-6] When a polymer melt gets into contact with the opening of a thin pore the capillary force is strong and drags the chains into the pore. It is the purpose of the current investigation to follow the dynamics of capillary flow of polymer melts into nanopores.

Despite recent work in understanding capillary rise in nanopores by experiment,[7-13] theory[14] and simulation[15-18] there are still several aspects that have not been addressed. Nearly 100 years ago, Lucas and Washburn derived what is known as the Lucas-Washburn equation (LWE) for Newtonian liquids penetrating a cylindrical capillary of radius R:[7,8]

$$h(t) = (\frac{\gamma R cos\theta}{2\eta})^{1/2}\sqrt{t} \quad (1)$$

Here, $h(t)$ is the penetration length of the liquid meniscus, γ is the surface tension, θ is the advancing contact angle, η is the viscosity and t is the wetting time. In LWE the quantity, $\gamma\cos\theta/2\eta$, measures the penetrating power of a liquid and is termed the coefficient of penetrance or the penetrativity. It was already discussed by Lucas and Washburn that the term, $\cos\theta$, makes penetrability a function of the nature of the material comprising the capillary. Thus both γ and $\cos\theta$, need to be evaluated separately for each polymer on the same surface. According to LWE the degree of penetration is proportional to $t^{1/2}$ as well as to $(\gamma/\eta)^{1/2}$. In fact, the former dependence applies to any kind of process that starts fast and slows-down with time. These dependencies were tested for Newtonian fluids and a good agreement was found.[7] However, as already stated by Washburn,[8] *this equation will probably not apply for pores having diameters approaching the molecular dimensions of the liquid*. Indeed, recent experiments have shown deviations from the LWE when nanopores where infiltrated with entangled polystyrene (PS)[9] and polyethylene (PE).[12] In the former study,[9] made as a function of PS molecular weight for a single nanopore diameter, an enhanced mobility was concluded on the basis of changes in the X-ray scattering invariant during capillary flow resulting in a weak molecular weight dependence for the viscosity ($\eta \sim N^{1.4}$).

In the latter study,[12] deviations from the LWE for two nanopore diameters were attributed to the effect of shear rate on the polymer viscosity during capillary flow.

To test the applicability of the LWE we used poly(ethylene oxide) (PEO) melts with molecular weights in the range from M_w=5.3×10^4 g/mol to M_w=1.02×10^6 g/mol. As confining medium we employ self-ordered nanoporous aluminum oxide (AAO) that contains arrays of discrete-isolated, parallel, cylindrical nanopores that are uniform in length and diameter.[19-22] As such, they have been employed as *model* systems in studying the effect of 2-d confinement on the dynamics of amorphous[23,24] and semicrystalline polymers,[25-28] including PEO. More recently, we investigated the effect of interfacial energy on the segmental dynamics of several polymers located within the same AAOs. We found[24] that interfacial energy play a significant role on the segmental dynamics of confined polymers by controlling the liquid-to-glass temperature, T_g.

Our results as a function of pore diameter and polymer molecular weight show the breakdown of the classical LWE for polymer melts. Although a faster capillary rise has been reported earlier and predicted by theory, it is the first time to our knowledge that a slower capillary rise is observed for an entangled polymer melt under conditions of confinement where the molecular dimensions are comparable to the pore size ($2R_g/d$=1). These results are discussed in view of a recently proposed[14] microscopic mechanism for transport in a thin capillary based on the reptation model.

2.2. Experimental

2.2.1. Materials and method of infiltration

Poly(ethylene oxide)s (PEO) with four different molecular weights (PEO 50k, PEO 100k, PEO 500k, PEO 1M) were employed in the present investigation. Their molecular characteristics are shown in Table 1. All have molecular weights are much above the entanglement molecular weight (M_e^{PEO}=1620 g/mol[29]). PEO 100k was synthesized and characterized by T. Wagner and J. Thiel (MPIP-P). PEO 500k and PEO 1M were purchased from Polymer Standards Service. All three PEOs were synthesized via anionic polymerization techniques with *tert*-butyl ether and hydroxyl end groups. Additional PEOs with lower molecular weights (M_w=2×10^3 g/mol, M_w=5×10^3 g/mol and M_w=8×10^3 g/mol) were synthesized and employed in the surface tension measurements. AAO templates (pore depth of 100 μm; pore diameters of 400 nm, 200 nm, 65 nm, 35 nm, and 25 nm) were prepared following the method reported in the literature. Figure S1, Supplementary material,

gives representative images from scanning electron spectroscopy (SEM) of empty AAO templates indicating their uniformity, a property of paramount importance in this investigation.

Table 1. Molecular Weights of PEOs Used in the Present Investigation

Sample	M_w (g/mol)	M_n (g/mol)	PDI (M_w/M_n)
PEO 50k	53090	44510	1.19
PEO 100k	92930	83370	1.11
PEO 500k	480000	398000	1.21
PEO 1M	1020000	884000	1.15

Prior to infiltration, PEO films were prepared by hot-pressing at 100 ^oC. As shown in Figure S2, Supplementary material, within the oven, a polymer film with thickness from 100 μm to 300 μm was placed above the AAO template at a fixed distance maintained by four pillars made also of PEO with $M_w=5\times10^3$ g/mol. The pillars kept the polymer film at a close distance from the open end of AAO templates so as to keep the nanopores open before the application of vacuum. Subsequently, the oven was heated to 85 ^oC under vacuum. As pillars melted above the melting point of PEO (the equilibrium melting temperature of PEO is at 70 ^oC) they brought the polymer film smoothly in contact with the AAO surface. The polymer melt was then infiltrated into the nanopores by capillary force. The infiltration procedure was monitored for specific time intervals. Subsequently, the AAO templates were brought to ambient temperature. The distance penetrated by the melt under capillary pressure (*i.e.*, the imbibition length) was determined from cross sections by reflection microscopy (Zeiss Axiotech vario). The optical contrast originates from the change in the index of reflaction between the polymer infiltrated part and the empty nanopores. Although all results presented herein are based on reflection microscopy efforts were made to extract the imbibition length from scanning electron spectroscopy (SEM), as well. A representative image is shown in Figure S1 Supplementary material. It turned out that reflection microscopy is superior to SEM with respect to the determination of the imbibition lengths during capillary flow.

2.2.2. Surface tension

The Wilhelmy plate method[30] was employed to measure the surface tension of PEO melts. A rod-like platin-iridium plate (diameter of 1.2 mm) was vertically placed into the polymer melt (85 ^oC).

The polymer melt has a contact angle of around 0° on the platinium-iridium rod surface. The surface tension exerts a downward force (F), which is measured with a Tensionmeter (DCAT 11BC, Dataphysics). The surface tension (γ) can be calculated from $F = l\gamma$, where l is the circumference of the rod-like plate. To avoid the influence of viscoelasticity of the polymer, the rod plate was slowly (with velocity of 0.01 mm/s) moved out of the polymer melt up to the measurement point. All measurements were performed under dry nitrogen environment to avoid contamination from air (*e.g.* due to humidity).

2.2.3. Contact angle

The advancing contact angles of the solid polymers were measured by placing nearly spherical polymer particles of ~ 1mm diameter onto the substrate and heating to 85 ^{o}C. To form spherical particles, around 1 mg of PEO sample was placed on a soot-templated superamphiphobic surface. The sample was heated up and kept at 85 ^{o}C for 96 h under vacuum to form a spherical shape caused by the surface tension of the polymer.[31] Subsequently, the polymer sphere was slowly cooled below the melting temperature and transferred onto an electropolished Al disk coated by a thin native oxide layer. The latter comprises a flat model surface that mimics the AAO surface. The advancing contact angle of the polymer melt was measured during spreading onto the substrate at 85 ^{o}C with a commercial goniometer (OCA35, Dataphysics).

2.2.4. Rheology

The viscosities of the different PEO samples were measured by a shear rheometer (ARES). Measurements were made with the environmental test chamber as a function of temperature. Samples were prepared on the lower plate of the 8 and 25 mm diameter parallel plate geometry. The upper plate was brought into contact, the gap thickness was adjusted and the sample was cooled. The storage (G') and loss (G'') shear moduli were monitored in different types of experiments. The linear and nonlinear viscoelastic ranges were identified from strain sweep experiments by recording the strain amplitude dependence of the complex shear modulus $|G^*|$ at selected temperatures. In the subsequent experiment of frequency sweeps at selected temperatures strain amplitudes within the linear viscoelastic range were used. The complex viscosity (η^*) follows: $\eta^* = G''/\omega - iG'/\omega$, where ω is the angular velocity (in rad/s).

2.3. Results and discussion

Surface tension measurements were carried out for different PEO samples with molecular weights in the range from 2000 g/mol to 92930 g/mol (PEO 100k) at 85 ^{o}C. For PEO molecular weights below or somewhat above the entanglement molecular weight, the equilibrium value is rapidly obtained. However, for higher molecular weights, it took from few hundreds of seconds (M_w~8000 g/mol) to few hours (M_w=92930 g/mol) to reach equilibrium (Figure 1 and Figure S3, Supplementary material). Following an exponential fit to $\gamma(t)$, the characteristic relaxation time for attaining the equilibrium surface tension is found to be substantially longer than the terminal relaxation time. A simple dimensional analysis using the viscosity, the surface tension and the capillary length, l_c, ($l_c=(\gamma/g\rho)^{1/2}$, here g is the gravitational constant and ρ is the density) suggests a characteristic time that balances the capillary driving force and the dissipation due to the flow, as $\tau=\eta l_c/\gamma$. This time is within an order of magnitude from the experimental time. In the inset to Fig. 1, the obtained equilibrium

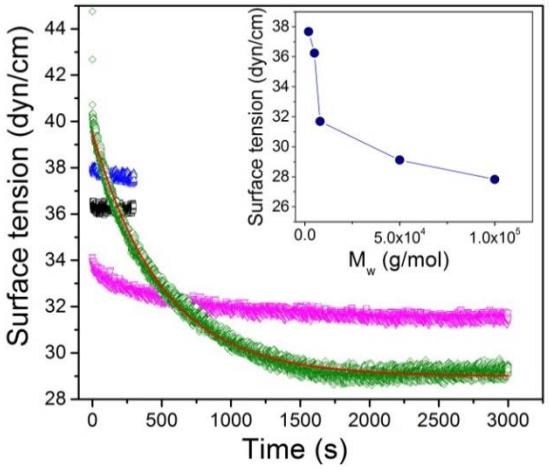

Figure 1. Surface tension as a function of time for different molecular weights of PEO all measured at 85 ^{o}C; (blue triangles): $M_w=2\times10^3$ g/mol, (black squares): $M_w=5\times10^3$ g/mol, (magenta down triangles): $M_w=8\times10^3$ g/mol and (green rhombi): $M_w=5.3\times10^4$ g/mol. The solid line is the result of a fit to an exponential function for the $M_w=5.3\times10^4$ g/mol data. In the inset the equilibrium values of surface tension are plotted as a function of PEO molecular weight. The line is a guide for the eye.

values of surface tension are plotted and reveal a decreasing function of molecular weight. For the PEO 500 and PEO 1M samples values of the equilibrium time of the surface tension were too long to measure the surface tension experimentally. In this case the values were obtained by

extrapolation from lower molecular weights (following the empirical equation $\gamma(M)=27.8+1724\ M^{-2/3}$).

Table 2. Parameters entering the LWE together with terminal relaxation times and characteristic times of surface tension relaxation, all measured at 85 °C.

Sample	γ ($\times10^{-3}$ N/m)	θ_e (°)	η_o (Pa·s)	$\tau_{terminal}$ (s)	τ_γ (s)
PEO 50k	29.1	44.0	4.3×10^{2}	9×10^{-3}	500
PEO 100k	27.8	44.5	3.9×10^{3}	0.2	1900
PEO 500k	28.1	40.7	4.6×10^{5}	7	-
PEO 1M	28.0	47.7	2.7×10^{6}	56	-

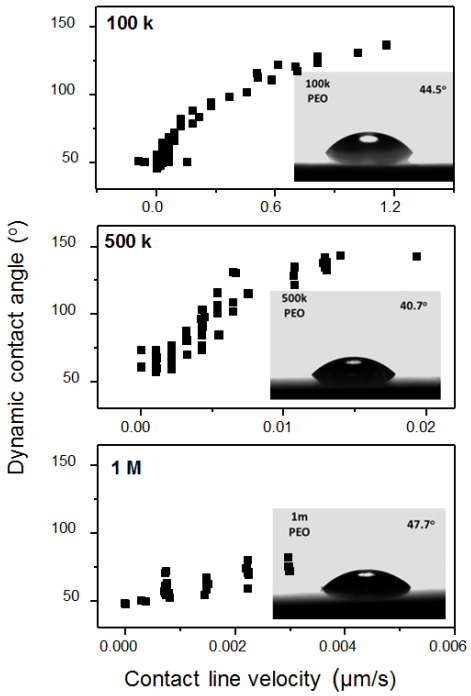

Figure 2. Dynamic contact angles of the three PEO polymers. The quasi-static advancing contact angle is estimated from the lowest contact line velocity images showed as insets.

Contact angles of highly viscous liquids need long times to equilibrate. Dynamic contact angles of all three samples were measured at 85 °C. The dynamic contact angles depend on the velocity of the three-phase contact line (Fig. 2). To get the best estimation of "static" advancing contact angles, the measured values were extrapolated to zero velocity. Note the slow contact angle

velocity with increasing PEO molecular weight. The values employed in subsequent calculations are summarized in Table 2. A video giving the evolution of contact angles is provided in the Supplementary materials section.

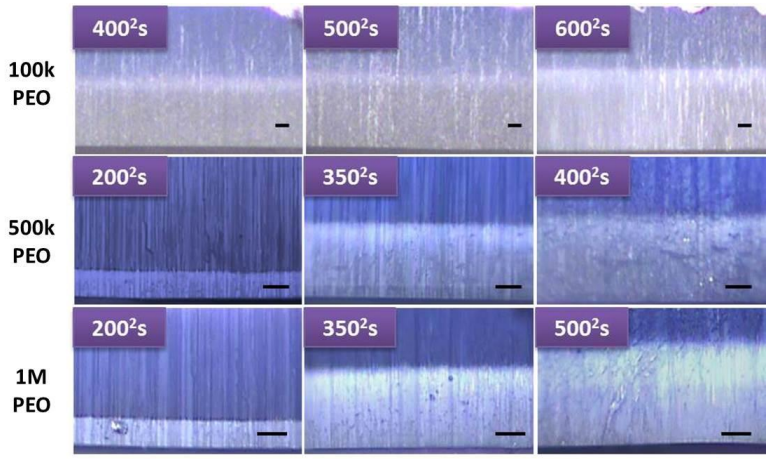

Figure 3. Reflection microscope images of PEO located inside AAO infiltrated for different times: (top) PEO 100k in 35 nm AAO; (middle) PEO 500k in 65 nm AAO; (bottom): PEO 1M in 65nm AAO. Scale bar indicates 10 μm.

Representative reflection microscopy images of the capillary filling process for each one of the three PEO samples are depicted in Figure 3. In general, images show the rise of the imbibition front within the AAO capillaries with time. In this process, gravity can be neglected as the pore length is much smaller than the capillary length. Evidently, the time scales involved in the different samples are quite different. The results with respect to the imbibition length, h, as a function of $t^{1/2}$ are summarized in Figure 4. These results are discussed separately with respect to PEO 100k and the two higher molecular weights. In general, the $t^{1/2}$ dependence is approximately valid for all samples. However, a careful examination especially for PEO 100k within self-ordered AAO with a pore diameter of 65 nm suggests deviations from linearity at longer times (the latter is shown in Supplementary material, Figure S4). In this case we have examined the effect of employing the shorter- and longer- time slopes as opposed to the whole time regime (symbols in Fig. 5). In both cases the effective viscosities are well within the error bars plotted in Fig. 5. Therefore, the particular choice of time interval does not affect the conclusions. For PEO 100k in self-ordered AAO with pore diameters of 400 nm and 200 nm the theoretical LWE (with measured parameters given in Table 2) describes the measured imbibition lengths well. Evidently, in the smaller pores, capillary rise is *slower* than theoretically predicted. This result is consistent with a recent dynamic

study- albeit in another polymer (1,4 polyisoprene) within the same AAO templates - where both segmental and chain dynamics could be studied dielectrically under nanometer confinement. There, chain dynamics where slowed down with respect to the bulk whereas the segmental dynamics were unaffected.[23] Figure 4d gives the imbibition length h, now normalized with respect to the pore radius $R^{1/2}$ as predicted by LWE. Should LWE be valid, all data would collapse to a single curve as shown by the dashed line. Figure 4d demonstrates the breakdown of LWE for entangled PEO.

The situation for the imbibition length in PEO 500k and PEO 1M are distinctly different. For PEO 500k, Figure 4b,e shows a *faster* capillary rise than theoretically predicted (Table 2) for all pore diameters. Similar results are shown for PEO 1M (with parameters from Table 2) (Figure 4 c,f). In all cases experimental imbibition lengths grow faster than the LWE predictions for all pore diameters. The dynamic imbibition reverses between the PEO 100k with 50 entanglements per chain, and the higher molecular weights with 244 and 542 entanglements per chain.

Next, the effect of employing the dynamic contact angle (DCA), θ_d, instead of the equilibrium one (ECA), θ_e, was examined. It is known that DCA depends on the velocity of the three-phase contact line, v, results in a modification to the LWE.[32-34] The exact form of the $\theta(v)$ dependence is still a point of debate, however, the thermodynamic theory proposed by Cox[35] has shown good agreement with experiment. The theory emphasizes the viscous energy dissipation in the bulk and removes the singularities at the triple line by employing a microscopic slip boundary length, δ, according to:

$$\theta_d = \left(\theta_e^3 + 9A\frac{\eta}{\gamma}v\right)^{1/3} \qquad (2)$$

where A=ln(R/δ), θ is expressed in radian and v in m/s. Representative fits to the DCA data for PEO 100k and PEO 500k are given in Figure S5, Supplementary material. The effect of employing the DCA instead of the ECA in the LWE is tested in Figure S6, Supplementary material by assuming v=dH/dt. Since $\theta_e > \theta_d$, the modified LWE invariably predicts a smaller capillary rise. Differences from the usual LWE are minor, hence DCAs, cannot account for the experimental observations in lower and higher molecular weight samples.

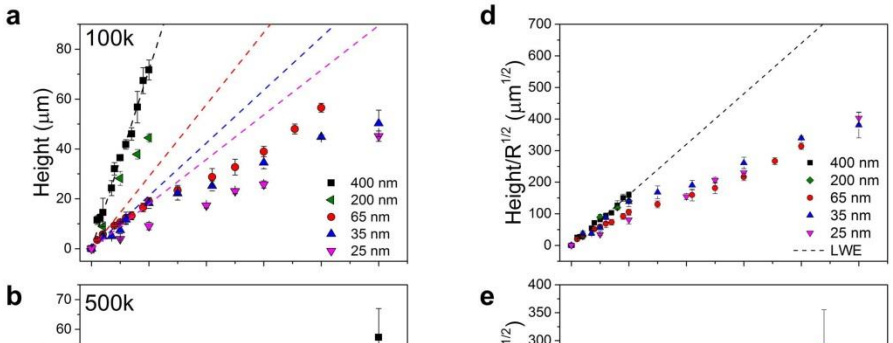

Figure 4. Imbibition length *h*, as a function of $t^{1/2}$ for (a) PEO 100k, (b) PEO 500k and (c) PEO 1M within self-ordered AAOs with different pore diameters; (squares) 400 nm, (left triangles): 200 nm, (spheres): 65 nm, (up triangles): 35 nm and (down triangles): 25 nm. The respective data normalized to the pore radii are shown in the right (d, e, f). Dashed lines give the predictions of the LWE equation.

A recent theoretical work[13] of the capillary rise of an entangled polymer in a thin tube created by the difference in hydrostatic pressure between the ends of the chain, considered two mechanisms of mass transfer. The first being the viscoelastic flow of the entangled mesh of constraints and the second, the flow of polymer chains with respect to this mesh of constraints. The model predicts the breakdown of macroscopic hydrodynamics as characterized by the bulk viscosity and proposed a new microscopic mechanism of transport along a thin capillary. For a pressure gradient p' along the chain ends and under stick boundary conditions, the total volume flux through a surface was shown to scale as $Q=p'b^2d^2/\eta_o(N/N_e)^{1.4}$ where b is the statistical segment length, d is the pore diameter, η_o is the local viscosity. As the apparent viscosity is inversely proportional the flux, a very weak molecular weight dependence ($\eta \sim N^{1.4}$) could be obtained as opposed to the bulk entangled case. In addition, a crossover capillary diameter was proposed separating the microscopic ($d<d^*$) from the macroscopic ($d>d^*$) regime that is proportional to N, as $d^*=bN/N_e^{1/2}$, the latter being of the order of some tens of nanometers and identical to the primitive path length.

These theoretical predictions can be tested against the experimental data. In the experiment, an effective viscosity is obtained from the slope of $h(t)$ vs $t^{1/2}$ dependence (Fig. 4) by assuming the LWE, whereas all other parameters (surface tension, contact angle) are measured independently. In Figure 5 we plot the effective viscosities as a function of $1/d$ and $2R_g/d$. We first note that at a fixed value of confinement, e.g., $2R_g/d=1$, the effective viscosity has a weak dependence on N ($\eta_{eff}\sim N^{0.9\pm0.1}$) as opposed to reptating chains in the bulk ($\eta_{eff}\sim N^{3.4}$). Similarly, when the comparison is made under a fixed pore diameter (d=25 nm) the effective viscosity scales as $\eta_{eff}\sim N^{0.83\pm0.14}$. Both cases suggest a Rouse type behavior for the effective viscosity ($\eta_{eff}\sim N^{1}$). However, scaling of the effective viscosity with $2R_g/d$ alone cannot explain the reversal of the effective viscosity in PEO 50k and PEO 100k in comparison to the higher molecular weights. This suggests that other length scales are involved. In the inset to Figure 5b we plot the effective viscosity normalized to its bulk value with respect to the proposed crossover length, $d^*=bN/N_e^{1/2}$, evaluated from b=0.68 nm and N_e (=37).[28] In accord with the theoretical predictions, there is a decrease in apparent viscosity for ($d^*/d\geq1$) marking the transition from microscopic to macroscopic flow. Despite capturing the general form of a decreasing effective viscosity at $d<d^*$, the theory cannot explain the distinctly different behavior of PEO 50k and PEO 100k. Furthermore, the macroscopic regime is only reached for PEO 100k at the larger pore diameters, whereas for all other samples this regime is not reached at any pore diameter. Figure S6, Supplementary material, compares the effective viscosity during imbibition for two polymers (PEO with the PS[9,11]) within AAO nanopores. Overall, the effective viscosity data display similar trends for the low[11] and higher[9] molecular weight samples, albeit the more steep dependence for polystyrenes with the higher molecular weights. These experimental findings, and especially the reversal in dynamics of capillary imbibition (Fig. 5), present a challenge to theory. Below we discuss other effects that can influence the capillary rise.

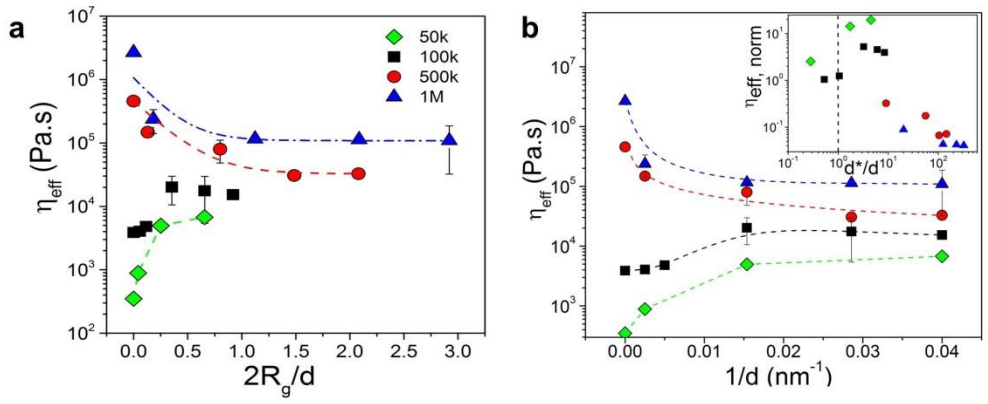

Figure 5. (a) Effective viscosities (calculated from the slopes of Fig.4) for PEO infiltrated within AAO as a function of the ratio of $2R_g/d$ for the four PEO samples. (b) Effective viscosities plotted as a function of inverse pore diameter. In all cases lines are guides for the eye. In the inset the effective viscosities normalized to the bulk are plotted as a function of the reduced length scale, d^*/d. The vertical line separates the microscopic regime from the macroscopic regime.

Additional effects, that could influence the capillary rise relate to the presence of (i) not completely stick boundary conditions, to (ii) adsorption effects, to (iii) surface roughness and (iv) segmental mobility (*i.e.*, confinement-induced changes in glass temperature). With respect to the boundary conditions (i), de Gennes treated the case of a mixed Poiseuille flow and plug flow that in the presence of a slip length resulted to d^4 and d^3 terms in the flux.[36] Depending on the scale of surface roughness the effective viscosities were predicted to vary from $\eta_{eff}{\sim}N^{1.4}$ to $\eta_{eff}{\sim}N^{3.4}$. Strong adsorption effects (ii) can influence the prefactor in the flux equation and in extreme cases even stop the flow. However, this apparently does not happen. It can be envisaged that a chain can have several contact points with the inner pore surface but of a limited lifetime. In addition, hydrogen bonding with the AAO surface can enhance this effect. Hydrogen bonding through the end-groups will be more effective in slowing down the shorter chains. Under these conditions imbibition will be dominated by chains located in the internal pore diameter. This provides a way to reconcile the measured imbibition lengths with the LWE equation for the shorter chains by assuming a dead layer of polymer chains next to the pore walls. The extracted dead layer thickness for PEO 100k is 24 nm (*i.e.*, $2R_g$, in the ideal Gaussian limit) for AAO with a pore diameter of 65 nm, and 11 nm and 9 nm (*i.e.*, of the order of R_g) for pore diameters of 35 and 25 nm, respectively. Similar results were obtained for PEO 50k. With respect to surface roughness (iii), the internal pore surface

roughness was recently evaluated by atomic force microscopy.[28] It was found to be smaller than 0.6 nm, *i.e.* of the order of the statistical segment length. This can affect the imbibition length as during the infiltration process certain repeat units can be entrapped within the corrugated surface and slow down capillary rise. In addition, the segmental dynamics (iv) of polymers located within the same AAOs are influenced by the interfacial energy. We have recently shown[24] that there is a trend for a decreasing glass temperature relative to the bulk with increasing interfacial energy. For PEO a reduction of the glass temperature by 6 K was reported by confining within AAO with pores having diameter of 65 nm. However, this reduction in glass temperature brings about a decrease in viscosity by a mere 15%. Hence a T_g - suppression *cannot* account for the large changes in effective viscosity under confinement for the shorter *or* for the longer chains. Other effects such as confinement-induced changes in the distribution of entanglements (intrachain vs interchain entanglements)[37,38] and a constrained release mechanism for the shorter chains may also play a role.

Lastly, we comment on the effect of shear rate on the effective viscosity. The effective shear rate during capillary rise can be calculated from the data shown in Fig. 4. The extracted range of shear rates – with the higher shear rates experienced during shorter times - is depicted in Figure S5, Supplementary material together with the measured viscosities for the three PEO samples at 85 ºC as a function of frequency. Evidently, for PEO 50k and PEO 100k all shear rates encountered in the imbibition process correspond to the zero shear rate viscosity plateau whereas for the PEO 1M the effective viscosity is reduced by a factor of two at the highest shear rate experienced by the polymer during flow. Thus shear rate effects *cannot* account neither for the magnitude of changes in viscosity nor for the sign of changes.

2.4 Conclusion

The imbibition of a series of entangled PEO melts (with 27, 50, 244 and 542 entanglements per chain) within self-ordered AAO nanopores display an approximate $t^{1/2}$ behavior as predicted by the LWE. However, the pore size dependence shows deviations from LWE. PEOs with 27 and 50 entanglements per chain penetrate *slower* while PEO with a higher number of entanglements penetrate *faster* than expected into AAO nanopores. Hence the reversal in the behavior of capillary imbibition occurs for PEO chains with 50 to 244 entanglements per chain. These results are only partially consistent with theoretical predictions for a critical length scale that depends on molecular

weight and separates the microscopic from the macroscopic regime. The theory can capture the decrease in effective viscosity within the microscopic regime for the higher molecular weights but not the reversal in the dynamics of imbibition for the lower molecular weights.

2.5 References

1. P.-G. De Gennes, Scaling concepts in polymer physics. (Cornell university press, Ithaca, 1979).
2. S. Granick, "Motions and relaxations of confined liquids," Science **253**, 1374 (1991).
3. T. Sakaue and E. Raphaël, "Polymer chains in confined spaces and flow-injection problems: some remarks," Macromolecules **39**, 2621 (2006).
4. M. Ediger and J. Forrest, "Dynamics near free surfaces and the glass transition in thin polymer films: a view to the future," Macromolecules **47**, 471 (2013).
5. F. Kremer (Ed.), Dynamics in Geometrical Confinement (Springer, Leipzig, 2014).
6. J.D. Beard, D. Rouholamin, B.L. Farmer, K.E. Evans, O.R. Ghita, "Control and modelling of capillary flow of epoxy resin in aligned carbon nanotube forests," RSC Adv. **5**, 39433 (2015).
7. R. Lucas, "Ueber das Zeitgesetz des Kapillaren Aufstiegs von Flüssigkeiten," Kolloid Z. **23**, 15 (1918).
8. E. W. Washburn, "The dynamics of capillary flow," Physical Review **17**, 273 (1921).
9. K. Shin, S. Obukhov, J.-T. Chen, J. Huh, Y. Hwang, S. Mok, P. Dobriyal, P. Thiyagarajan and T. P. Russell, "Enhanced mobility of confined polymers," Nature Materials **6**, 961 (2007).
10. S. Ok, M. Steinhart, A. Serbescu, C. Franz, F. n. Vaca Chávez and K. Saalwächter, "Confinement effects on chain dynamics and local chain order in entangled polymer melts," Macromolecules **43**, 4429 (2010).
11. A. Serghei, in Dynamics in Geometrical Confinement (Springer, Leipzig, 2014), pp. 165-170, F. Kremer (Ed.).
12. B.-Y. Cao, M. Yang and G.-J. Hu, "Capillary filling dynamics of polymer melts in nanopores: experiments and rheological modelling," RSC Advances **6**, 7553 (2016).
13. L. Mammen, P. Papadopoulos, K. Friedemann, S. Wanka, D. Crespy, D. Vollmer, H.-J. Butt, "Transparent and airtight silica nano- and microchannels with uniform tubular cross-section," Soft Matter **9**, 9824-9832 (2013).
14. A. Johner, K. Shin and S. Obukhov, "Nanofluidity of a polymer melt: Breakdown of Poiseuille's flow model," Europhysics Letters **91**, 38002 (2010).
15. S. Supple and N. Quirke, "Molecular dynamics of transient oil flows in nanopores I: Imbibition speeds for single wall carbon nanotubes," The Journal of Chemical Physics **121**, 8571 (2004).
16. S. Supple and N. Quirke, "Rapid imbibition of fluids in carbon nanotubes," Physical Review Letters **90**, 214501 (2003).
17. W. Stroberg, S. Keten and W. K. Liu, "Hydrodynamics of capillary imbibition under nanoconfinement," Langmuir **28**, 14488 (2012).

18. D. Dimitrov, A. Milchev and K. Binder, "Capillary rise in nanopores: molecular dynamics evidence for the Lucas-Washburn equation," Physical Review Letters **99**, 054501 (2007).
19. H. Masuda and K. Fukuda, "Ordered metal nanohole arrays made by a two-step replication of honeycomb structures of anodic alumina," Science **268**, 1466 (1995).
20. H. Masuda, F. Hasegwa and S. Ono, "Self-Ordering of Cell Arrangement of Anodic Porous Alumina Formed in Sulfuric Acid Solution," Journal of the Electrochemical Society **144**, L127 (1997).
21. H. Masuda, K. Yada and A. Osaka, "Self-ordering of cell configuration of anodic porous alumina with large-size pores in phosphoric acid solution," Japanese Journal of Applied Physics **37**, L1340 (1998).
22. M. Steinhart, Self-Assembled Nanomaterials II (Springer, Berlin, 2008), pp. 123-187.
23. S. Alexandris, G. Sakellariou, M. Steinhart and G. Floudas, "Dynamics of unentangled cis-1, 4-polyisoprene confined to nanoporous alumina," Macromolecules **47**, 3895 (2014).
24. S. Alexandris, P. Papadopoulos, G. Sakellariou, M. Steinhart, H.-J. r. Butt and G. Floudas, "Interfacial Energy and Glass Temperature of Polymers Confined to Nanoporous Alumina," Macromolecules **49**, 7400 (2016).
25. J. Martin, M. Krutyeva, M. Monkenbusch, A. Arbe, J. Allgaier, A. Radulescu, P. Falus, J. Maiz, C. Mijangos, J. Colmenero, D. Richter, "Direct observation of confined single chain dynamics by neutron scattering," Physical Review Letters **104**, 197801 (2010).
26. Y. Suzuki, H. Duran, M. Steinhart, H.-J. Butt and G. Floudas, " Suppression of Poly (ethylene oxide) Crystallization in Diblock Copolymers of Poly (ethylene oxide)-*b*-poly (ε-caprolactone) Confined to Nanoporous Alumina," Macromolecules **47**, 1793 (2014).
27. Y. Suzuki, H. Duran, M. Steinhart, H.-J. Butt and G. Floudas, "Homogeneous crystallization and local dynamics of poly(ethylene oxide)(PEO) confined to nanoporous alumina," Soft Matter **9**, 2621 (2013).
28. Y. Suzuki, M. Steinhart, M. Kappl, H.-J. Butt and G. Floudas, "Effects of polydispersity, additives, impurities and surfaces on the crystallization of poly (ethylene oxide)(PEO) confined to nanoporous alumina," Polymer **99**, 273 (2016).
29. L. Fetters, D. Lohse, D. Richter, T. Witten and A. Zirkel, "Connection between polymer molecular weight, density, chain dimensions, and melt viscoelastic properties," Macromolecules **27**, 4639 (1994).
30. S. Wu, "Interfacial and surface tensions of polymers," Journal of Macromolecular Science **10**, 1 (1974).
31. X. Deng, L. Mammen, H.-J. Butt and D. Vollmer, "Candle soot as a template for a transparent robust superamphiphobic coating," Science **335**, 67 (2012).
32. R.L. Hoffman, "A study of the advancing interface. I. Interface shape in liquid-gas systems," J. Colloid Interface Sci., **50**, 228 (1975).
33. M.N. Popescu, J. Ralston, R. Sedev, "Capillary rise with velocity-dependent dynamic contact angle," Langmuir **24**, 12710 (2008).
34. M. Yang, B.-Y. Cao, W. Wang, H.-M. Yun, B.-M. Chen, "Experimental study on capillary filling in nanochannels," Chem. Phys. Lett. **662**, 137 (2016).

35. R.G. Cox, "The dynamics of the spreading of liquids on a solid surface. Part 1. Viscous flow ," J. Fluid Mech. **168**, 169 (1986).
36. P.G. De Gennes, "Conjectures on the transition from Poiseuille to plug flow in suspensions, " Journal de Physique, **40**, 783 (1979).
37. L. Si, M.V. Massa, K. Dalnoki-Veress, H.R. Brown, R.A.L. Jones, "Chain entanglement in thin freestanding polymer films," Physical Review Letters **94**, 127801 (2005).
38. S. Rastogi, D.R. Lippits, G.W.M. Peters, R. Graf, Y. Yao, H.W. Spiess, "Heterogeneity in polymer melts from melting of polymer crystals," Nature Materials **4**, 635 (2005).

2.6 Supplementary material

See supplementary material for SEM characterization of empty and infiltrated pores, surface tension measurements, a video with contact lines and rheology measurements.

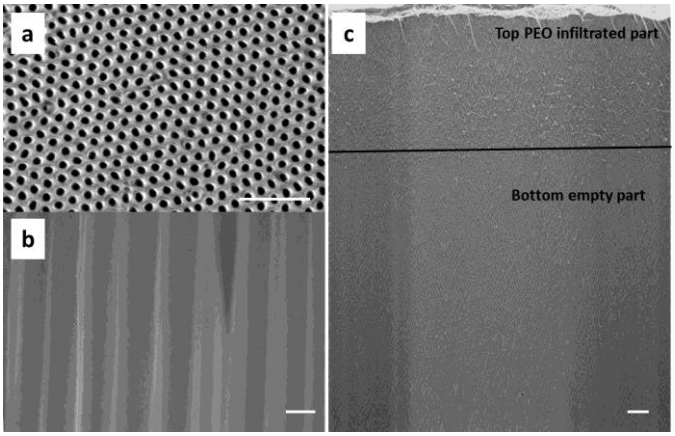

Figure S1. Scanning electron microscopy images of (a) top view of empty AAO with pore diameter of 65 nm (scale bar is 200 nm), (b) cross-section of empty AAO with pore diameter of 400 nm (scale bar is 200 nm), and (c) AAO with pore diameter of 65 nm infiltrated by PEO 100k for 100^2 s (scale bar is 2 μm).

Figure S2. Schematic of the infiltration method.

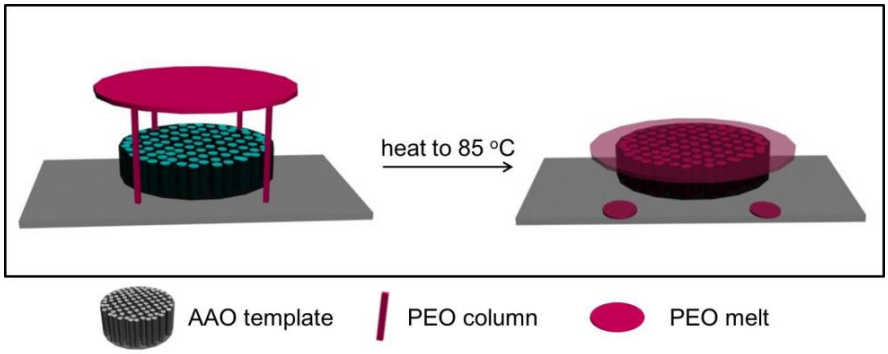

Figure S3. Surface tension as a function of time for PEO 100k. The solid line is the result from a fit to an exponential function.

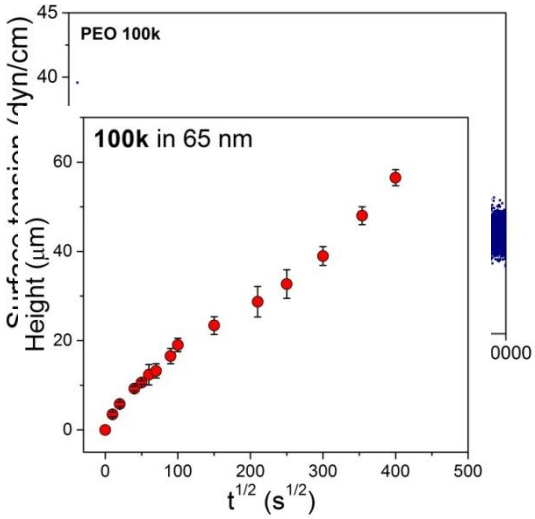

Figure S4. Imbibition length *h*, as a function of $t^{1/2}$ for PEO 100k within self-ordered AAOs with pore diameter of 65 nm.

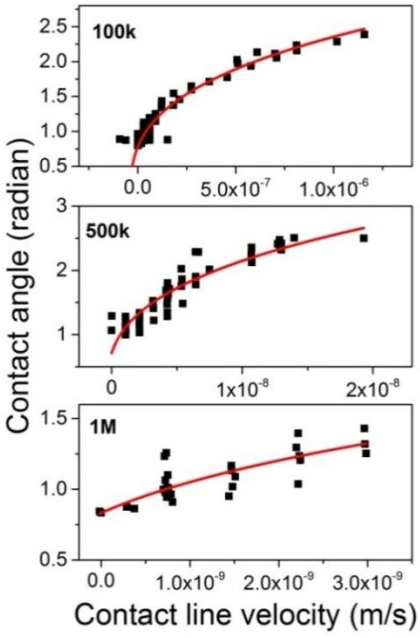

Figure S5. Dynamic contact angles for the three PEO polymers. Lines give the result of the fits according to the Cox equation.

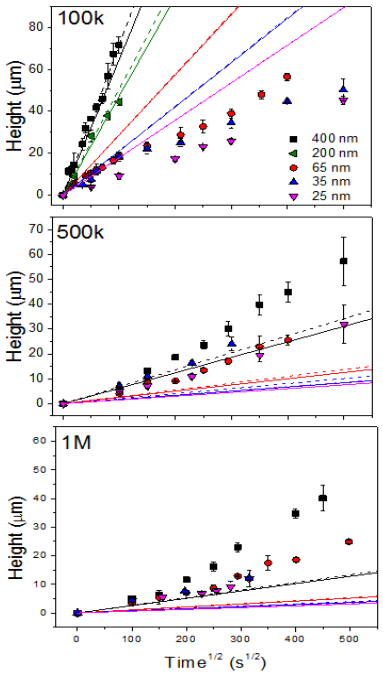

Figure S6. Imbibition length h, as a function of $t^{1/2}$ for (top) PEO 100k, (middle) PEO 500k and (bottom) PEO 1M within self-ordered AAOs with different pore diameters; (squares) 400 nm, (left triangles): 200 nm, (spheres): 65 nm, (up triangles): 35 nm and (down triangles): 25 nm. Dashed and solid lines give the predictions of LWE (Eq. 1) and modified LWE equation for the dynamic contact angle.

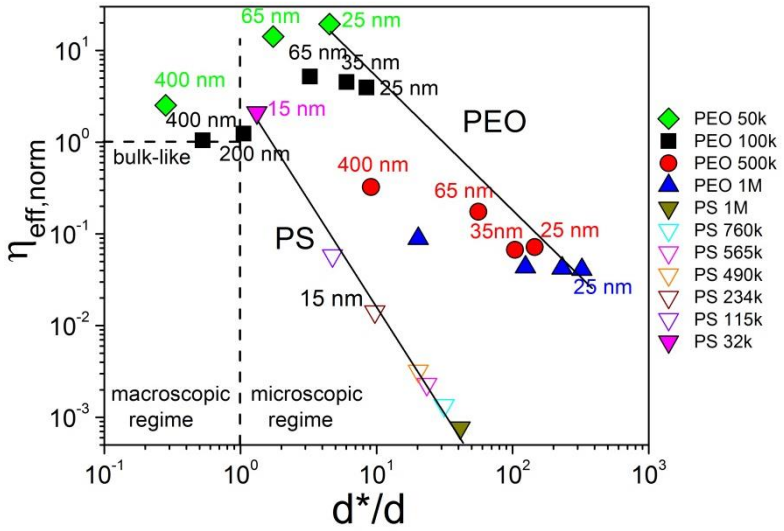

Figure S7. Comparison of results of the effective viscosity during imbibition for two polymers (PEO with the PS) within the same AAO nanopores: Effective viscosities normalized to the bulk as a function of the reduced length scale, d^*/d. For PS (down triangles) all measurements[8,10] refer to pores with a diameter of 15 nm. Notice the increase in effective viscosity relative to the bulk for the PS with M_w=35000 g/mol (green rhombus) with $d \sim d^*$. For the higher PS molecular weights and for $d^*/d>1$, a steeper reduction in effective viscosity is seen relative to PEO. Solid lines are guides for the eye. They refer to the PS within AAO with 15 nm pores and to PEO within AAO with 25 nm pores.

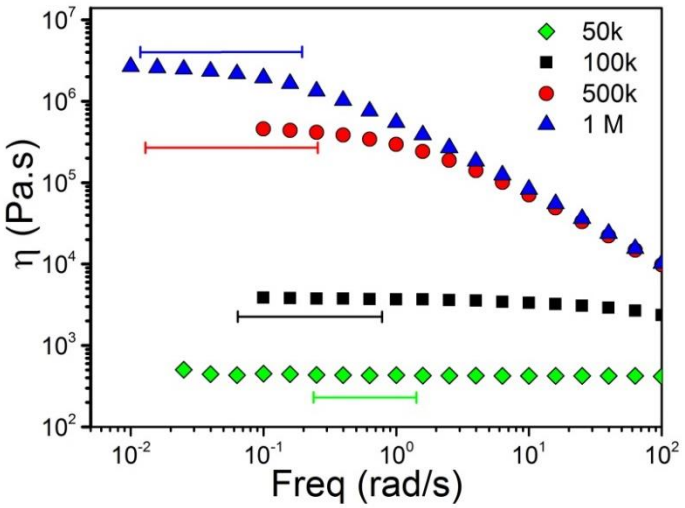

Figure S8. Measured viscosities for the four PEO samples investigated herein at 85 ºC as a function of frequency. The horizontal bars indicate the range of shear rates experienced by the polymers during the infiltration process.

Chapter 3. Theory on Capillary Imbibition of Polymer Melts in Nanopores

This chapter has been published as a research paper in Macromolecular Rapid Communications. It is reprinted here with kind permission of John Wiley and Sons.

Yang Yao, Hans-Jürgen Butt, George Floudas, Jiajia Zhou, and Masao Doi
Macromolecular rapid communications, 1800087 (2018)
DOI: 10.1002/marc.201800087

Abstract

A unified theory for the imbibition dynamics of entangled polymer melting into nanopores is presented. Experiments demonstrate the validity of $t^{1/2}$ dependence but contradict the predictions of the classical Lucas–Washburn equation because of the prefactor. A reversal in dynamics of capillary filling is reported with increasing polymer molecular weight. Polymer imbibition under nanometer confinement can be discussed by two mechanisms: one is the standard hydrodynamic flow, resulting in a parabolic flow profile. When the inner wall has a strong attraction to the polymer, a layer of immobile chains is created, resulting in an increase of the effective viscosity and to slower imbibition. The other is the reptation model proposed by Johner et al., leading to a plug flow profile and to the reduction in the effective viscosity (faster imbibition). The reversal in dynamics of polymer imbibition can be explained by the competition between these two mechanisms.

3.1. Introduction

Understanding fluid dynamics in a confined geometry is important in many different fields such as engineering, physics, chemistry, biotechnology, and nanotechnology. Successful applications include the development of inkjet printheads for commercial xerography, synthesis and production of various nanoparticles and polymeric materials on a lab-on-a-chip device, separation and manipulation of DNA or other bio-macromolecules, and on-the-spot medical diagnosis in clinical pathology. Under spatial confinement, the volume of the fluid reduces, and the surface-to-volume ratio increases. This leads to the fact that the interaction between the fluid and the surface, *i.e.*, the capillary effect, becomes the dominant factor among many other interactions. A canonical example is the fluid imbibition into a pore with hydrophilic inner surfaces. For Newtonian fluid, the standard model to describe the imbibition dynamics is the celebrated Lucas–Washburn equation (LWE)[1, 2].

$$h(t) = At^{1/2},\ h(t) = (\frac{\gamma R cos\theta}{2\eta_0})^{1/2}\sqrt{t}, \tag{1}$$

Here $h(t)$ is the imbibition length of the fluid inside the pore, R is the pore radius, γ is the surface tension of the fluid, θ_E is the equilibrium contact angle, and η_0 is the fluid viscosity in the bulk. The dynamical scaling of $t^{1/2}$ has been found in many phenomena involving capillarity and wetting.[3] Extensive studies by experiments,[4–7] theory,[8,9] and simulations[10–12] have advanced our understanding on the capillary filling, but there are still new avenues to be explored.[13,14]

An implicit assumption in the derivation of Lucas–Washburn equation is that the size of fluid particles should be an order of magnitude smaller than the pore radius. This is valid for simple fluids, for example, when water ($\approx 10^{-10}$ m) fills an μm-size glass pore. Experimentalists nowadays can probe the range where the two length scales are comparable: for example, when a polymer (radius of gyration $R_g \approx 10 - 100$ nm) penetrates into self-ordered nanoporous aluminum oxide (AAO) (also $R \approx 10 - 100$ nm).[13,14] Surprisingly, the dynamical scaling of $t^{1/2}$ is consistently observed in experiments and remains valid in the nanometer ranges. However, the prefactor A exhibits interesting behaviors even for simple liquids.[5] From the experimentally measured A value, one can deduce an effective viscosity

$$\eta_{eff} = \frac{R\gamma cos\theta_E}{2A^2} \tag{2}$$

The value of η_{eff} is in general different than the bulk value η_0.

Recent experiments have shown a complex behavior of the effective viscosity for capillary imbibition of polymer melts into nanoscale pores.[14] Capillary penetration of a series of entangled poly(ethylene oxide) (PEO) melts within nanopores of self-ordered alumina followed $h \sim t^{1/2}$ behavior according to the LWE. However, a reversal in dynamics of capillary filling has been observed with increasing polymer molecular weight. Polymer chains with 50 entanglements or less showed a slower capillary filling than theoretically predicted, indicating a higher effective viscosity. For longer chains with more entanglements, the capillary filling was faster than the theory and the effective viscosity was reduced as compared to bulk. In this article, we present a possible explanation for this unusual observation.

3.2. Theoretical considerations

We first present a brief derivation of the Lucas–Washburn equation. Let us consider a cylindrical pore of radius R (schematically shown in Figure 1). One end of the pore is in contact with a Newtonian fluid bath, and the fluid is drawn into the pore under capillarity. The dynamics of the filling can be described by $h(t)$, the length of the fluid inside the pore.

There are two opposite forces acting on the fluid

i) Capillary force

$$F_C = 2\pi R\,(\gamma_{SV} - \gamma_{SL}) = 2\pi R\gamma cos\theta_E \tag{3}$$

where γ_{SV}, γ_{SL}, and γ are the interfacial tension between solid/vapor, solid/fluid, and fluid/vapor, respectively. These three interfacial tensions are related by the Young's relation, $\gamma_{SV} - \gamma_{SL} = \gamma \cos\theta_E$, where θ_E is the equilibrium contract angle. Here we only consider a hydrophilic surface, *i.e.*, $\theta_E < 90°$. The capillary force drives the imbibition.

ii) Viscous force

$$F_V = 8\pi\eta_0 hv \tag{4}$$

where η_0 is the fluid viscosity and $v = dh/dt$ is the filling speed. The prefactor depends on the pore geometry, and for circular pore it equals to 8π. The viscous force provides the friction against the imbibition.

The balance between the capillary and viscous forces results in the evolution equation

$$2\pi R\gamma cos\theta_E = 8\pi\eta_0 hv \quad \Rightarrow \quad v = \frac{R\gamma cos\theta_E}{4\eta_0 h} \tag{5}$$

The solution to the above equation is

$$h^2(t) = \frac{\gamma R cos\theta}{2\eta_0} t \tag{6}$$

This is the classical Lucas–Washburn Equation (1) with $h \sim t^{1/2}$ scaling. We would like to point out some general requirements for systems to have the $t^{1/2}$ scaling. The left-hand side of the force balance Equation (5) is a thermodynamic force, which can be derived from conserved potential energy. This term must not depend on *h*. A counterexample is the capillary rising when gravity is important. In this case, the gravitational force is proportional to the mass of the fluid, and *h*(*t*) eventually approaches an asymptotic Jurin's height at long time. The right-hand side of the force balance Equation (5) is related to the energy dissipation. In the simplest form of Equation (4), the force is due to the viscous dissipation resulting from the parabolic flow profile. This term must be proportional to *h*. A counterexample is the dissipation in the meniscus at the fluid front. In this case, a friction force related to the meniscus has no *h*-dependency, and the resulting evolution of *h*(*t*) would notbe of the Lucas–Washburn type ($t^{1/2}$).

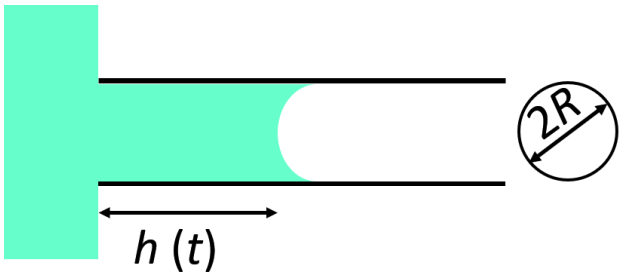

Figure 1. A sketch of capillary penetration of a fluid into a cylindrical pore.

In the following, we will consider the imbibition of polymericfluids into nanopores. We focus on the situation where the Lucas–Washburn scaling $t^{1/2}$ is valid, and consider various effects that may lead to different prefactors in a modified LWE.

3.2.1. Confinement effect

When the pore diameter is of the same order as the molecule size, as in our case of polymeric fluids, the conformation of the polymer chain is perturbed. In general, polymer chains have higher free energy in the pores than in the bulk. This reduces the driving force for the filling, and may be described by an effective surface tensionmay be described by an effective surface tension

$$\gamma_{eff} = \gamma cos\theta_E - \Delta f \frac{R}{2} \tag{8}$$

where Δf is the change in the free energy density of a polymer melt under confinement in comparison to the bulk.

We may evaluate Δf using the blob model.[15] The polymer chains are under biaxial confinement and can be viewed as a sequence of compression blobs of the pore diameter $2R$. For ideal chains, the number of monomer g in each compression blob is given by $g = (2R/b)^2$, where b is the statistical length of the monomer (Kuhn length). The number of blobs per chain is given by N/g, where N is the number of monomers per chain. The free energy penalty due to confinement is of the order of k_BT per compression blob, *i.e.*, $\Delta F = k_BTN/g = k_BTNb^2/(4R^2)$. To obtain the free energy density, we use the number density of the polymer chain $1/(v_0N)$, where v_0 is the monomer volume. The difference in the free energy density Δf is then given by

$$\Delta f = \frac{1}{v_0 N} \times k_B T \frac{Nb^2}{4R^2} = k_B T \frac{b^2}{4v_0 R^2} \tag{9}$$

We estimate the effect of confinement by comparing the two terms in Equation (8). The ratio between these two terms is

$$\frac{k_B T}{\gamma cos\theta_E} \frac{b^2}{8v_0 R} \tag{10}$$

Using the experiments of PEO in AAO pores as an example[14]: $v_0 = 6.04 \times 10^{-29}$ m^3, T = 358 K, $k_BT = 4.94 \times 10^{-21}$ J, $\gamma\cos\theta_E = 0.02$ Jm^{-2}, $b = 0.68$ nm, and $2R = 35$ nm, this results a ratio of 0.014. This is too small an effect to account for the increase in the effective viscosity. Note here we considered the confinement energy based on an isolated ideal chain. For the melt system, this energy is due to the fluctuation-induced long-range interaction and was shown to be even smaller (b/R of Equation (9)).[16,17]

3.2.2. Dead zone effect

For simple fluids, the flow profile inside the pore has a parabolic profile, a result of the Stokes equation and no-slip boundary condition on the wall. For polymeric fluids, the polymer chains near the inner wall can be strongly adsorbed. There exist experimental evidences for that from dielectric spectroscopy measurements for polymers confined to nanoporous alumina.[18] These immobile chains create a "dead zone" of thickness ΔR. We define an effective radius of the pore by $R_{eff} = R - \Delta R$, and consider the effect of dead zone on the imbibition speed.

Outside the dead zone, the polymer melts exhibit a macroscopic flow with the usual parabolic profile. We rewrite Equation (6) in term of a pressure

$$v = \frac{R^2}{8\eta_0 h}\Delta P,\ \Delta P = \frac{2\gamma cos\theta_E}{R} \tag{11}$$

where ΔP is the Laplace pressure that drives the imbibition. This term remains unchanged when the dead zone is considered, but we have to replace R^2 in the numerator by R_{eff}^2. Since only R_{eff}^2/R^2 portion of the polymer contributes to the flow, the fluid front advances at the rate

$$\dot{h} = v_{flow}\frac{R_{eff}^2}{R^2} = \frac{\gamma cos\theta\, R_{eff}^4}{4\eta_o h R^3} \tag{12}$$

Comparing the above equation to Equation (6) with η_0 replaced by an effective viscosity η_{eff}, defined by $\dot{h} = \frac{\gamma R cos\theta_E}{4\eta_{eff} h}$, we obtain the following expression for η_{eff}

$$\frac{\eta_{eff}}{\eta_0} = \left(\frac{R}{R_{eff}}\right)^4 \tag{13}$$

Since $R_{\text{eff}} < R$, we have $\eta_{\text{eff}} > \eta_0$. Also because of the fourth power, the effect of dead zone is quite substantial even for a small change in R_{eff}. This is the origin of the slow-down in the imbibition dynamics for shorter chains.

3.2.3. Reptation under confinement

As the pore radius is reduced and becomes comparable to the thickness of the dead zone, the macroscopic flow is nearly stopped. The material transport under very strong confinement is achieved mainly by the reptation of free polymer chains in a network driven by the pressure gradient. Johner *et al*. has developed a theoretic framework for this scenario.[8] Here we present their results for completeness, while also include the pore-size dependence of the pressure gradient.

Figure 2 shows one single free chain under a pressure gradient. A polymer chain is constrained by other chains due to entanglements, and as such it can only move along the "reptation tube". Each free polymer chain experiences a driving force due to the pressure difference along the chain $[-p(x+R_x) + p(x)]\ \ell^2 = -\ell^2 R_x \partial p/\partial x$, where ℓ^2 is the cross section and R_x is the x-component of the end-to-end vector. The friction to the free chain is given by $N\zeta v_c$, where N is number of segments, ζ is the friction constant for one Kuhn segment, and v_c is the chain's velocity along the reptation tube. The balance between the pressure gradient and the frictional force gives

$$v_c = -\frac{l^2}{\zeta N} R_x \frac{dp}{dx} \tag{14}$$

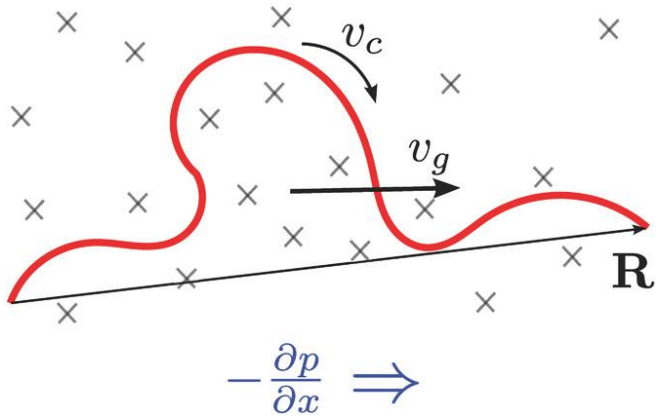

Figure 2. Schematics of reptation motion of a polymer chain under a pressure gradient.

The averaged velocity for the center of mass of the polymer is:

$$v_g = \frac{R_x}{L} v_c = -\frac{l^2 a_t}{3\zeta N} \frac{dp}{dx} \tag{15}$$

where L is the contour length of the tube, given by $L = (N/N_e)a_t$, N_e is the entanglement length, and $a_t = N_e^{1/2} b$ is the tube diameter. The average of R_x^2 is assumed to be ideal $\langle R_x^2 \rangle = (1/3)\, Nb^2$.

If the fraction of polymer chains participating the reptation is φ, the filling speed is then given by:

$$\dot{h} = \varphi \langle v_g \rangle = \varphi \frac{l^2 a_t}{3\zeta N} \frac{2\gamma \cos\theta}{hR} \tag{16}$$

where we averaged the pressure gradient along the whole fluid, $-\partial p/\partial x = \Delta P/h = 2\gamma \cos\theta_E$.

Complication arises when one needs to specify the crosssection ℓ^2. One natural choice is the cross-section of the reptation tube

$$l^2 = {a_t}^2 \Rightarrow \dot{h} = \varphi \frac{N_e^{3/2} b^3}{3\zeta N} \frac{2\gamma \cos\theta_E}{hR} \tag{17}$$

In reference[8], Johner *et al*. used

$$l^2 = N_e^{1/2} b^2 \Rightarrow \dot{h} = \varphi \frac{N_e b^3}{3\zeta N} \frac{2\gamma \cos\theta_E}{hR} \tag{18}$$

The only difference is in the scaling with respect to N_e. Here we shall assume a general form of

$$\dot{h} = \varphi \frac{N_e b^3}{3\zeta N} \frac{2\gamma \cos\theta_E}{hR} \tag{19}$$

where α is the exponent.

3.2.4. Summary of effective viscosity

In the case of $R_g << R$, the dead-zone effect is dominant and the filling dynamics is given by equation (12). In the other limit, $R_g >> R$, the reptation mode is important and the filling dynamics is governed by equation (19). A simple formula to interpolate these two limits is:

$$\dot{h} = \frac{\gamma cos\theta\, R_{eff}^4}{4\eta_o h R^3} + \varphi \frac{l^2 a_t}{3\zeta N} \frac{2\gamma \cos\theta}{hR} = \left[\frac{R_{eff}^4}{8\eta_o R^2} + \varphi \frac{N_e^\alpha b^3}{3\zeta N}\right] \frac{2\gamma \cos\theta}{hR} \tag{20}$$

We again define an effective viscosity by

$$\dot{h} = \frac{\gamma \cos\theta R}{4\eta_{eff} h} = \frac{R^2}{8\eta_{eff}} \frac{2\gamma \cos\theta}{hR} \tag{21}$$

Comparing equation (20) with equation (21), we obtain:

$$\frac{\eta_{eff}}{\eta_0} = \left[\left(\frac{R_{eff}}{R}\right)^4 + \varphi \frac{8N_e^\alpha b^3 \eta_0}{3\zeta N R^2}\right]^{-1} \tag{22}$$

In the limit of small pore, the first term in the square bracket vanishes because $R_{eff} \rightarrow 0$. The effective viscosity is then dominant by the second term

$$\eta_{eff} \sim \eta_0 \left(\frac{\eta_0}{N}\right)^{-1} \sim N^1 \tag{23}$$

This is quite different than the bulk scaling $\eta_0 \sim N^3$. Thus confined polymers show an enhanced mobility, consistent with the experiment findings in references[13,14] that have shown exponents of ≈ 1.4 and ≈ 0.9, respectively.

3.3. Comparison to the experiment and discussions

We compare our theoretical model with the capillary filling experiments in reference[14]. The bulk properties of PEO melts of different molecular weights are shown in Table 1. A fit to the viscosity gives $\eta_0 \sim N^{2.91}$, which indicates that we may use the standard formulation of Doi–Edwards model[19].

$$\eta_0 \approx \frac{\zeta b^2}{V_0} \frac{N^3}{N_e^2} \tag{24}$$

Table 1. PEO melt properties

Sample	γ (10^{-3} N/m)	θ_E (°)	η_0 (Pa.s)
PEO 50k	29.1	44.0	4.3×10^2
PEO 100k	27.8	44.5	3.9×10^3
PEO 280k	28.0	44.0	1.5×10^5
PEO 500k	28.1	40.7	4.6×10^5
PEO 1M	28.0	47.7	2.7×10^6

The effective viscosity in equation 22 can be written as:

$$\frac{\eta_{eff}}{\eta_0} = [f(\Delta R, R) + g(\phi, N, R)]^{-1} \tag{25}$$

where the first function, *f*, is related to the dead-zone,

$$f(\Delta R, R) = \begin{cases} \left(1 - \frac{\Delta R}{R}\right)^4 & if\ R > \Delta R \\ 0 & if\ R < \Delta R \end{cases} \tag{26}$$

The second function, *g*, is from the reptation model,

$$g(\phi, N, R) = \varphi \frac{8 N_e^{\alpha} b^3 \eta_0}{3\zeta N R^2} = \varphi \frac{8 N_e^{\alpha-2} b^5}{3 V_0} \frac{N^2}{R^2} = \phi \frac{N^2}{R^2} \tag{27}$$

where we have used Equation (24) and grouped parameters into one single factor φ. In the end, we have two free parameters: ΔR and φ. In principle, these two parameters may vary for different pore radii and molecular weights. As a first attempt, we neglect that dependence and assume ΔR and φ are constants.

Figure 3 shows the comparison between the experiment and theory. We plot the ratio of the effective viscosity to the bulk viscosity as a function of $1/R$, the inverse of the pore radius, for a polymer with various molecular weights. The fitting parameters are obtained by global fitting resulting to ΔR = 34.3 nm, $\phi = 3.21\times10^{-5}$ nm^2.

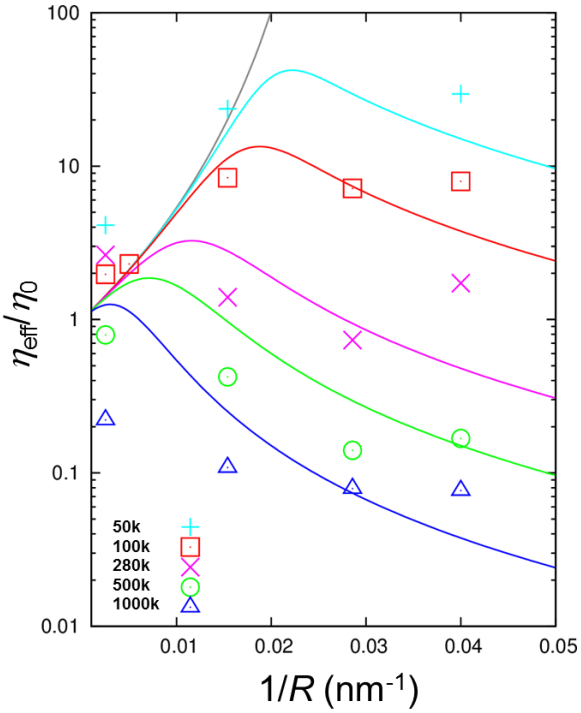

Figure 3. Comparison between the experiment and the theory. The symbols are shown for the experimental data taken from reference[14]. The lines are from theoretical prediction of equation (25).

The theoretic prediction is in qualitative agreement with the experimental data. Most importantly, the theory has captured the non-monotonic variation in the effective viscosity. The main reason for the non-monotonic behavior is that functions f and g vary differently with respect to 1/R. In the large pore limit, these two functions $f \to 1$ while $g \to 0$, and the effective viscosity approaches the bulk value, $\eta_{\text{eff}} \to \eta_0$. As the pore radius decreases ($1/R$ increases), the effect of the dead zone becomes important and eventually stops the macroscopic flow. Accordingly, the function f decreases. On the other hand, for small pores the reptation motion of the entangled polymer becomes effective and function g increases. It is the opposite trends in the functions f and g that lead to the non-monotonic variation of the effective viscosity as observed experimentally.

The inversion point, *i.e.*, the value of $1/R$ when the effective viscosity has its maximum, is a function of the molecular weight. For polymers of low molecular weight, the inversion point corresponds to a pore radius that is comparable with the thickness of the dead-zone, ΔR. Alternatively, for longer chains, the maximum shifts towards $1/R \rightarrow 0$, *i.e.*, to the very weak confinement limit.

3.4 Conclusion

We present a theoretical model for the imbibition dynamics of entangled polymer melts into nanopores. Experiments have demonstrated the validity of the $t^{1/2}$ scaling; however the Lucas–Washburn equation breaks down because of the prefactor. We have considered various effects that can affect the imbibition dynamics while preserving the $t^{1/2}$ scaling:

i) The effect of confinement. Biaxial confinement of polymer chains induces a penalty in the free energy, but the effect is too small to explain the slow-down in dynamics.

ii) The effect of adsorption. Strongly-adsorbed chains create a dead zone, reducing the pore radius, and leading to an increase in the effective viscosity.

iii) The effect of reptation under a pressure gradient: The reptation of polymer chains under strong confinement[8] enhances the mobility of confined chains, leading to faster imbibition.

The overall imbibition dynamics can be discussed by the competition of the latter two mechanisms. The theoretical predictions capture the main features of the experiment being in a qualitative agreement with the experiments.

3.5 References

1. R. Lucas, Kolloid-Z. 1918, 23, 15.
2. E. W. Washburn, Phys. Rev. 1921, 17, 273.
3. P.-G. de Gennes, F. Brochard-Wyart, D. Quéré, Capillarity and Wetting Phenomena, Springer, New York, USA 2004.
4. S. Ok, M. Steinhart, A. Sterbescu, C. Franz, F. V. Chávez, K. Saalwächter, Macromolecules 2010, 43, 4429.
5. F. Chauvet, S. Geoffroy, A. Hamoumi, M. Prat, P. Joseph, Soft Matter 2012, 8, 10738.
6. L. Mammen, P. Papadopoulos, K. Friedemann, S. Wanka, D. Crespy, D. Vollmer, H.-J. Butt, Soft Matter 2013, 9, 9824.
7. B.-Y. Cao, M. Yang, G.-J. Hu, RSC Adv. 2016, 6, 7553.

A. Johner, K. Shin, S. Obukhov, Europhys. Lett. 2010, 91, 38002.

8. N.-K. Lee, D. Diddens, H. Meyer, A. Johner, Phys. Rev. Lett. 2017, 118, 067802.
9. D. I. Dimitrov, A. Milchev, K. Binder, Phys. Rev. Lett. 2007, 99, 054501.
10. M. R. Stukan, P. Ligneul, J. P. Crawshaw, E. S. Boek, Langmuir 2010, 26, 13342.
11. W. Stroberg, S. Keten, W. K. Liu, Langmuir 2012, 28, 14488.
12. K. Shin, S. Obukhov, J.-T. Chen, J. Huh, Y. Hwang, S. Mok, P. Dobriyal, P. Thiyagarajan, T. P. Russell, Nat. Mater. 2007, 6, 961.
13. Y. Yao, S. Alexandris, F. Henrich, G. Auernhammer, M. Steinhart, H.-J. Butt, G. Floudas, J. Chem. Phys. 2017, 146, 203320.
14. M. Rubinstein, R. H. Colby, Polymer Physics, Oxford University Press, Oxford, UK 2003.

A. N. Semenov, S. P. Obukhov, J. Phys.: Condens. Matter 2005, 17, S1747.

15. N.-K. Lee, J. Farago, H. Meyer, J. P. Wittmer, J. Baschnagel, S. P. Obukhov, A. Johner, Europhys. Lett. 2011, 93, 48002.
16. S. Alexandris, G. Sakellariou, M. Steinhart, G. Floudas, Macromolecules 2014, 47, 3895.
17. M. Doi, S.F. Edwards, The Theory of Polymer Dynamics, Oxford, UK 1994.

Chapter 4. Capillary Imbibition of Polymer Mixtures in Nanopores

This chapter has been published as a research paper in Macromolecules. It is reprinted here with kind permission of American Chemical Society.

Yang Yao, Hans-Jürgen Butt, Jiajia Zhou, Masao Doi, and George Floudas
Macromolecules 51, 3059-3065 (2018).
DOI: 10.1021/acs.macromol.7b02724

Abstract

Capillary imbibition of homogeneous mixtures of entangled poly(ethylene oxide) melts in nanopores of self-ordered nanoporous alumina follows a $t^{1/2}$ dependence but contradicts the classical Lucas-Washburn equation. Herein we employ reflection microscopy and self-consistent field theory (SCFT) calculations to demonstrate the *faster* penetration of nanopores for the *shorter* chains. Combined results suggest on average a ~15% enrichment by the shorter chains. On top of that, SCFT shows an enrichment of the short chains near the pore surface. Possible applications in separating long and short polymer chains by the difference in imbibition speed - in the absence of solvent - are discussed.

4.1 Introduction

Squeezing a polymer chain in a thin tube can have several applications in fields such as membranes, gel chromatography, oil recovery etc.[1] Of particular interest is the case of a confining medium with sizes comparable to the molecular length scale. This is the case, for example, that the building blocks of life, *i.e.* DNA and proteins, are experiencing when migrating through a narrow passage with profound importance in cell biology.[2,3] When a polymer melt gets into contact with the opening of a thin pore the capillary force is strong and drags the chains into the pore. Recent experiments, however, have shown that capillary imbibition of polymer melts into narrow pores is anything but trivial.[4-6] Capillary penetration of a series of entangled poly(ethylene oxide) (PEO) melts within nanopores of self-ordered alumina followed an approximate $t^{1/2}$ behavior according to the classical Lucas-Washburn equation (LWE); t is time.[7,8] However, a reversal in dynamics of capillary rise has been reported with increasing polymer molecular weight.[6] Chains with 50 entanglements or less show a slower capillary rise than theoretically predicted as opposed to chains with more entanglements that display a faster capillary rise.

Insight on the imbibition process of polymer melts can be obtained by studying polymer blends. Here we study capillary imbibition in polymer mixtures consisting of short and long chains of the same polymer. By employing both experiment and self-consistent field theory (SCFT) calculations, we demonstrate that in a binary mixture composed of long and short chains of the same chemical identity, shorter chains penetrate consistently faster in narrow pores. By careful selection of the polymer molecular weights relative to the pore diameter, this procedure could be used in separating chains in a bimodal or polydisperse polymer melt in the absence of solvent.

4.2 Experimental section

Sample Preparation. Poly(ethylene oxide)s (PEOs) with molecular weights of 50k and 500k and their mixtures were employed (PEO 50k, synthesis by Wagner and Thiel (MPI-P); PEO 500k purchased from Polymer Standards Service). Both homopolymers were synthesized via anionic polymerization with *tert*-butyl ether and hydroxyl end groups. For the mixtures, homopolymers with different mass fractions (75/25, 50/50, 25/75) were dissolved in chloroform at a 10% polymer concentration. The solution was stirred for 24 h to ensure uniform mixing. Subsequently, the solvent was allowed to evaporate at ambient temperature for 5 days followed by heating at 90 ^{o}C for 3 days to completely remove any traces of solvent. As for the nanopores, we employ self-

ordered nanoporous aluminum oxide (AAO) that contains arrays of discrete-isolated, parallel cylindrical nanopores that are uniform in length and diameter. AAO templates with pore depth of 100 μm, pore diameters of 65 nm and 25 nm were prepared following methods reported in the literature.[9-11]

Method of Imbibition. Polymer films were hot-pressed (100 μm) at 100 ºC and placed above the AAO template at a fixed distance maintained by PEO pillars (diameter 1 mm; length 2 mm). The pillars were made of PEO ($M_w = 5\times10^3$ g/mol) and kept the nanopores open during the application of vacuum. The oven was subsequently brought to 85 ºC, *i.e.*, some 15 ºC above the equilibrium melting temperature of PEO. As the pillars melted, the polymer film got smoothly into contact with the AAO surface. Subsequently, the polymer melt was infiltrated into the nanopores under capillary force and the imbibition process was monitored for specific time intervals. Following imbibition the AAO templates were brought to ambient temperature and the imbibition height was determined from cross sections by reflection microscopy (Zeiss Axiotech vario). Several cross sections were examined at each time that revealed uniformity in capillary imbibition. In addition, for each cross section imbibition heights at 10 different positions were recorded, at each imbibition time (the uncertainties are presented as error bars in Figs 4 and 6).

Rheology. The viscosities of the two homopolymers and their mixtures were measured by a shear rheometer (ARES). Measurements were made with the environmental test chamber as a function of temperature. Samples were prepared on the lower plate of a 13 mm diameter parallel plate geometry. The upper plate was brought into contact, the gap thickness was adjusted and the sample was cooled. The storage (G') and loss (G'') shear moduli were monitored in different types of experiments. The linear and nonlinear viscoelastic ranges were identified from strain sweep experiments by recording the strain amplitude dependence of the complex shear modulus $|G^*|$ at selected temperatures. In subsequent experiments, frequency sweeps were performed at selected temperatures with strain amplitudes that correspond well within the linear viscoelastic range. The complex viscosity follows as $\eta^* = G''/\omega - iG'/\omega$, where ω is the angular velocity (in rad/s). Results for the viscosity of the homopolymers and their mixtures, all measured at 85 ºC, are shown in Figure 1. The extracted zero-shear viscosity values (η_o) are included in Table 1.

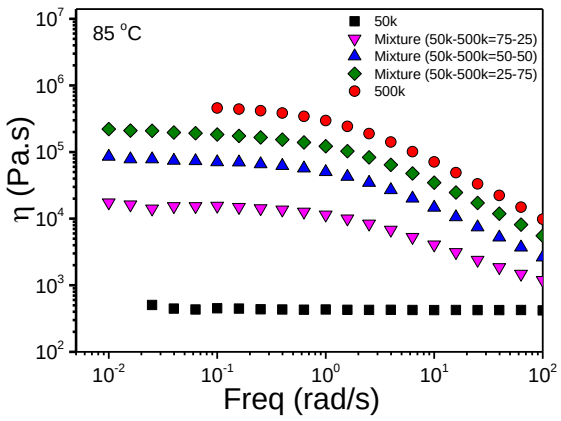

Figure 1. Measured viscosities for the two PEO homopolymers and their mixtures at 85 °C as a function of frequency.

Surface Tension. Surface tension of the homopolymers was measured by the Wilhelmy plate method using a tension meter (DCAT 11BC, Dataphysics). Values for the two homopolymers were in close proximity and the blend surface tension was obtained by a linear interpolation. **Contact Angle.** To measure advancing contact angles of the homopolymers and their mixtures we first formed spherical particles of 1 mm diameter by placing around 1 mg of sample on a soot-templated superamphiphobic surface at 85 °C for 96 h under vacuum.[12] Subsequently, the polymer sphere was slowly cooled below the melting temperature and transferred onto an electropolished Al disk coated by a thin native oxide layer. The latter comprises a flat model surface that mimics the AAO inner pore surface. Measurements of the advancing contact angles during spreading onto the substrate at 85 °C were made with a commercial goniometer (OCA35, Dataphysics).[13] While spreading, the contact angle was monitored as a function of time. In general, contact angles of highly viscous homopolymers need long times to equilibrate. Dynamic contact angles depend on the velocity of the three-phase contact line. To estimate the "static" advancing contact angles (θ_e) measurements of the dynamic contact angles were extrapolated to zero velocity (Figure 2). The thus obtained values are included in Table 1.

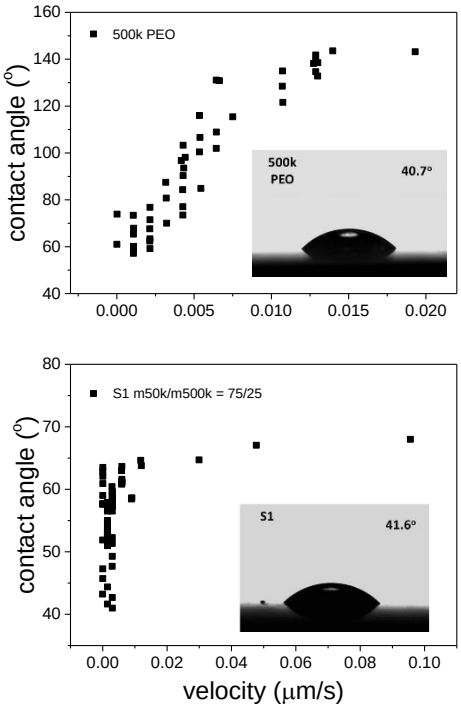

Figure 2. Dynamic contact angles of the homopolymer PEO 500k (top) and the symmetric mixture (bottom). The quasi-static advancing contact angles were estimated from the images shown as insets that correspond to the lowest contact line velocity measurements.

Gel Permeation Chromatography (GPC). The molecular weight distribution of the polymers located within AAO nanopores were measured with gel permeation chromatography (GPC) (Agilent Technologies 1260 infinity). Following imbibition at 85 ºC for 11 h, the surface polymer was totally removed and the polymer located within the nanopores was dissolved in chloroform. DMF was the eluent with elution rate of 1 ml/min at 60 °C. The samples were eluted through three SDV columns with a particle size of 10 μm and pore sizes of 10^6, 10^4, and 500 Å. UV-vis S-3702 (Soma) and DRI Shodex RI-101 (ECR) were used as detectors. Calibration was made using PEO standards provided by Polymer Standards Service.

4.3 Computational details

Self-consistent Field Theory. Self-consistent field theory (SCFT) for blends of homopolymer A or B (in bulk and in confinement) is based on the grand canonical ensemble. [13-19] Briefly, each polymer is built from N_α monomers of species α=*A*, *B*. We will use the homopolymer A as the

reference and write $N_A=\kappa_A N$ with $\kappa_A=1$. Polymers have the same associated Kuhn length, $b_A=b_B=b$. The monomers are assumed to have the same monomer density ρ_0. The average concentration is given by $\varphi_\alpha=n_\alpha\kappa_\alpha N/\rho_0 V$, where n_α is the total number of α-chains. We scaled all lengths by the end-to-end distance of a Gaussian chain $R_e=b\sqrt{N}$, and the chain arc length by the degree of polymerization N. For simplicity, we assume short-range interactions of Flory-Huggins type *i.e.*, $\chi=\chi_{AB}$.

A/B binary blends in the bulk. In the grand canonical ensemble, the controlling parameter is the chemical potential, μ_A and μ_B. As for the absolute energy scale we can set $\mu_A=0$. The chemical potential can also be expressed in terms of activities as $z_A=\exp(\mu_A)/\kappa_A=1/\kappa_A$ and $z_B=\exp(\mu_B)/\kappa_B$. The mean-field equations for A/B binary blends are

$$\varphi_A(\mathrm{r}) = z_A \int_0^{\kappa_A} ds\; q_A(\mathrm{r},s)\, q_A(\mathrm{r},\kappa_A - s)$$

$$\varphi_B(\mathrm{r}) = z_B \int_0^{\kappa_B} ds\; q_B(\mathrm{r},s)\, q_A(\mathrm{r},\kappa_B - s) \qquad (1)$$

$$\omega_\alpha(\mathrm{r}) = \chi N \varphi_\beta(\mathrm{r}) + \eta(\mathrm{r})$$

$\sum_{\alpha=A,B}\varphi_\alpha(\mathrm{r})=1$ where $\omega_\alpha(\mathrm{r})$ is the mean field experienced by α-species, $\eta(\mathrm{r})$ is the Lagrangian multiplier to enforce the incompressibility, and $q_\alpha(\mathrm{r},s)$ is the end-integrated propagator. The end-integrated propagator $q_\alpha(\mathrm{r},s)$ is the solution of the modified diffusion equation in the mean field $\omega_\alpha(\mathrm{r})$,

$$\frac{\partial}{\partial s} q_\alpha(\mathrm{r},s) = \frac{Nb^2}{6}\nabla^2 q_\alpha(\mathrm{r},s) - \omega_\alpha(\mathrm{r}) q_\alpha(\mathrm{r},s) \qquad (2)$$

with the initial condition $q_\alpha(\mathrm{r},0)=1$. The single-chain partition functions Q_α for $\alpha=A$ or B is given by

$$Q_\alpha(\{\omega_\alpha\}) = \frac{1}{V}\int d\mathrm{r} q_\alpha(\mathrm{r},\kappa_\alpha)\,. \qquad (3)$$

The free energy density is given by

$$g(\{\varphi\},\{\omega\}) = \frac{1}{V}\int d\mathrm{r}\{\chi N\varphi_A(\mathrm{r})\varphi_B(\mathrm{r}) - \sum_\alpha \omega_\alpha(\mathrm{r})\varphi_\alpha(\mathrm{r})\} - z_A Q_A - z_B Q_B \qquad (4)$$

Homogeneous phase. For the homogeneous phase all the concentrations and fields are constant. The propagators are easily obtained in this case as, $q_\alpha=\exp(-\omega_\alpha s)$, $Q_\alpha=\exp(-\omega_\alpha\kappa_\alpha)$. Hence, the mean-field equations now read

$$\varphi_A = Q_A = e^{-\omega_A \kappa_A} \quad \rightarrow \quad \omega_A \kappa_A = -\ln\varphi_A$$
$$\varphi_B = e^{\mu_B} Q_B = e^{\mu_B} e^{-\omega_B \kappa_B} \quad \rightarrow \quad \omega_B \kappa_B = \mu_B - \ln\varphi_B \tag{5}$$
$$\omega_\alpha = \chi N \varphi_\beta + \eta \, , \sum_\alpha \varphi_\alpha = 1$$

The chemical potential μ_B is related to φ_α by

$$-\frac{\mu_B}{\kappa_B} = \chi N(\varphi_B - \varphi_A) + \frac{\ln\varphi_A}{\kappa_A} - \frac{\ln\varphi_B}{\kappa_B} \tag{6}$$

The above equation is used to obtain the chemical potential, μ_B, from the bulk compositions φ_A and φ_B. The chemical potential, μ_B, is then used as an input parameter in the calculation of the cylindrical confinement. The free energy density for the bulk phase can be written in terms of φ_A:

$$g = \chi N \varphi_B^2 + \frac{\ln\varphi_A}{\kappa_A} - \frac{\varphi_A}{\kappa_B} - \frac{\varphi_B}{\kappa_B} \tag{7}$$

A/B binary blends under confinement. In the general SCFT framework, the total monomer density is unform everywhere, $\varphi_0(r)=\varphi_A(r)+\varphi_B(r)=1$. Under confinement, the hard surface is impenetrable, and the total monomer density has to vanish at the surface. A common method to solve this problem is to use a profile $\varphi_0(r)$ that decreases continuously from 1 to 0 in the proximity of the surface. For the detailed form of $\varphi_0(r)$, we use the one proposed by Meng and Wang. [20] In the cylindrical coordinates,

$$\varphi_0(\mathrm{r}) = \begin{cases} 1 & r < R - \tau \\ \tanh^2\left[\frac{2\tau(R-\tau)}{\tau^2-(R-r)^2}\right] & R - \tau < r < R \end{cases} \tag{8}$$

where R is the radius of the cylindrical pore, and τ is the characteristic length of the surface layer (Figure 3).

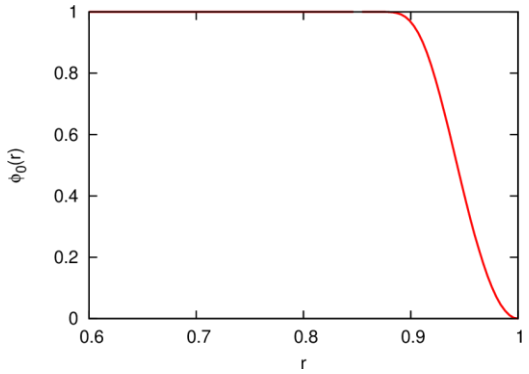

Figure 3. Total density profile near the hard wall. The characteristic length of the surface layer is τ=0.15$b\sqrt{N}$.

4.4 Results and discussion

Homopolymers. In general, for the homopolymers, the $t^{1/2}$ dependence is approximately valid.[6] Capillary rise in nanopores has been discussed in terms of the classical LWE[7,8, 21-23] applicable to Newtonian liquids penetrating a cylindrical capillary of radius *R*:

$$h(t) = (\frac{\gamma R cos\theta}{2\eta})^{1/2}\sqrt{t} \quad (9)$$

Here, $h(t)$ is the penetration length of the liquid meniscus, γ is the surface tension, θ is the advancing contact angle, η is the viscosity and t is the wetting time. The term $cos\theta$, makes penetrability a function of the nature of the material comprising the capillary. Thus both γ and $cos\theta$, need to be evaluated separately for each polymer on the same surface. Furthermore, different from Newtonian liquids one has to take into account that the contact angle depends on wetting speed. In the calculation of the theoretical imbibition length, *h*, the measured respective parameters for the PEO 50k and PEO 500k homopolymers were employed (Table 1). However, the experimental results for the homopolymers deviate substantially from the LWE predictions (Figure 4). For PEO 50k there is a slower capillary rise than theoretically predicted as opposed to chains with more entanglements (PEO 500k) that display a faster capillary rise. Results for other molecular weights and pore diameters were reported earlier.[6] The results demonstrate the breakdown of the LWE for non-Newtonian liquids.

Table 1. Parameters employed by the LWE, measured at 85°C

Sample	PEO 50k/PEO 500k	γ ($\times 10^{-3}$ N/m)	θ_e (deg)	η_0 (Pa.s)
PEO 50k	1	29.1±0.1	44±1	$4.3\pm0.1\times10^{2}$
PEO 500k	0	28.1±0.1	41±1	$4.6\pm0.2\times10^{5}$
S1	75/25	28.9	42±1	1.7×10^{4}
S2	50/50	28.6	42±1	8.5×10^{4}
S3	25/75	28.4	42±1	2.2×10^{5}

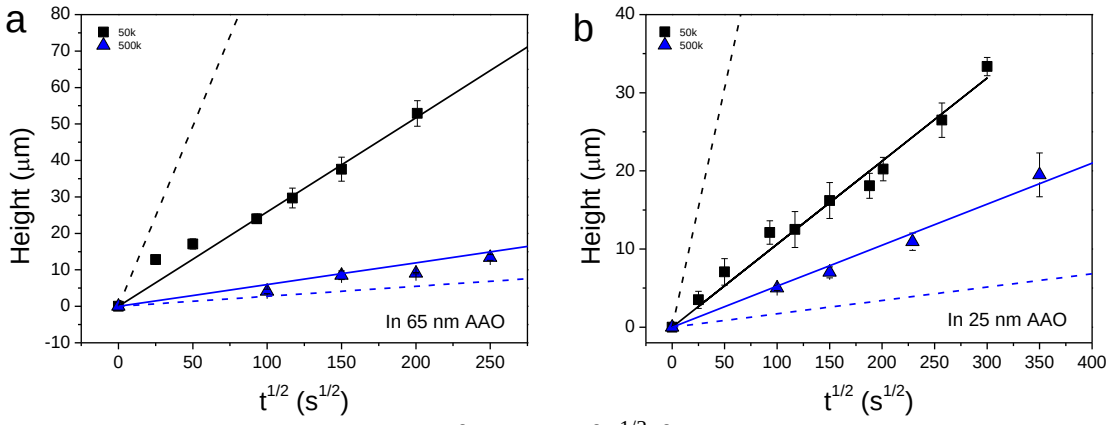

Figure 4. Imbibition heights as a fucntion of $t^{1/2}$ for the PEO homopolymers. Dashed lines give the predictions of the theoretical LWE for the PEO 50 k (black) and PEO 500k (blue) within AAO templates with diameters of 65 nm (a) and 25 nm (b). Note the slower (faster) imbibition for the shorter (longer) chains as compared to the theoretical predictions by the LWE.

These results on the dynamics of polymer imbibition under nanometer confinement can be discussed by the combination of two mechanisms: The first is the standard hydrodynamic flow, resulting in a parabolic flow profile. In the situation when the inner wall has a strong attraction to the polymer chains, a layer of immobile chains (called "dead zone") is created. In this case we define an effective radius as $R_{eff} = R - \Delta R$, where ΔR is the thickness of the dead zone. The flow velocity is given by

$$v_{flow} = \frac{R_{eff}^2}{8\eta_o h}\frac{2\gamma\cos\theta}{R} \tag{10}$$

Since only R_{eff}^2/R^2 portion of the polymer contributes to the flow

$$\dot{h} = v_{flow}\frac{R_{eff}^2}{R^2} = \frac{\gamma cos\theta\, R_{eff}^4}{4\eta_o h R^3} \tag{11}$$

This dead zone reduces the effective pore radius, leading to an increase of the effective viscosity.

The second mechanism is based on the reptation model, proposed earlier by Johner et al.[5] According to the model, material transport is achieved mainly by the reptation of free polymer chains in the network driven by the pressure gradient. Each free polymer feels a force

$$[-p(x + R_x) + p(x)]l^2 = -l^2 R_x \frac{dp}{dx} \tag{12}$$

where l^2 is the cross section, and R_x is the end-to-end vector along the pore axis. The polymer velocity along the tube is

$$v_c = -\frac{l^2}{\zeta N} R_x \frac{dp}{dx} \tag{13}$$

where ζ is the friction constant for one Kuhn segment. The averaged velocity of the center of mass of the polymer is

$$\langle v_g \rangle = \langle \frac{R_x}{L} v_c \rangle = -\frac{l^2}{\zeta N L} \langle R_x^2 \rangle \frac{dp}{dx} = -\frac{l^2 a_t}{3\zeta N} \frac{dp}{dx} \tag{14}$$

where L is the contour length of the tube, given by $L = (N/N_e)a_t$, N_e is the entanglement length and $a_t = \sqrt{N_e} b$ is the tube diameter. Moreover, $\langle R_x^2 \rangle$ is assumed to be ideal, *i.e.*, $\langle R_x^2 \rangle = Nb^2/3$. The filling speed is then given by

$$\dot{h} = \varphi \langle v_g \rangle = \varphi \frac{l^2 a_t}{3\zeta N} \frac{2\gamma \cos\theta}{hR} \tag{15}$$

where φ is the fraction of free polymers. This mechanism leads to a decrease of the effective viscosity. By varying the pore radius from large to small, initially the hydrodynamic mode dominates and the effective viscosity increases. As the pore radius gets smaller, the reptation mechanism takes over and the effective viscosity starts to decrease. Experiments have shown that the critical pore radius corresponding to the transition depends on the polymer molecular weight.[6] For shorter chains, the experiment revealed the non-monotonic behavior of the effective viscosity. For longer chains on the other hand, the critical radius is very small and only the decrease of the effective viscosity was observed. Overall the competition between the two mechanisms has as a result the reversal in the imbibition mechanism with increasing polymer molecular weight.[24]

Other effects that can influence the capillary imbibition are the surface roughness and the change of the liquid-to-glass temperature (T_g) at the surface. With respect to the surface roughness, recently we evaluated the internal pore surface roughness of AAO by atomic force microscopy.[25] It was found to be ≤0.6 nm, *i.e.* of the order of the statistical segment length for PEO. Under conditions that the statistical segment length is smaller than the AAO surface roughness certain repeat units can be entrapped within the corrugated surface and slow down capillary rise. On the other hand the changes in the T_g cannot account for the large changes in the effective viscosity under confinement. It was recently documented that there is a trend for a decreasing glass

temperature relative to the bulk with increasing interfacial energy for polymers located inside AAO nanopores.[26] However, for PEO the reduction of the glass temperature (~ 6 K) brings a decrease in viscosity of only 15% that cannot account for the experimental findings. We now turn our attention to the blend imbibition process.

Figure 5. Reflection microscope images of PEO mixtures located inside 65 nm AAO

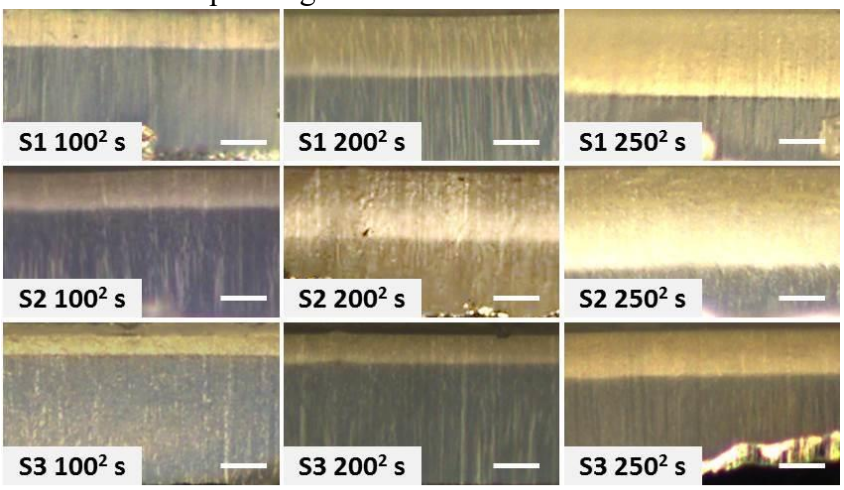

infiltrated for different times: (top) S1 (PEO 50k/PEO 500k = 75/25); (middle) S2 (50k/500k = 50/50); (bottom): S3 (50k/500k = 25/75). Scale bar indicates 20 μm (Times are shown as 100^2 s, 200^2 s, 250^2 s that correspond to approximately 2.8 h, 11.1 h, 17.4 h, respectively.)

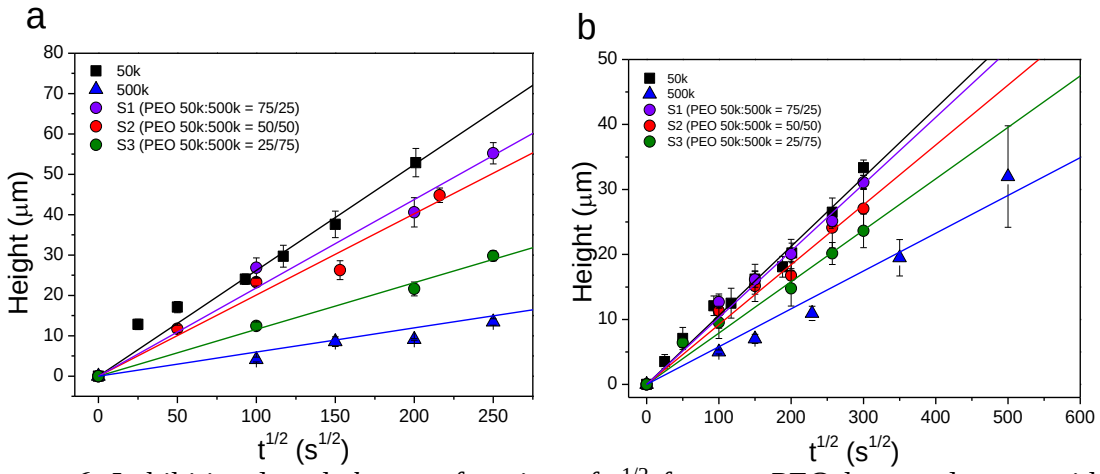

Figure 6. Imbibition length *h*, as a function of $t^{1/2}$ for two PEO homopolymers with molecular weights of 50k (squares) with 500k (triangles) and their mixtures with compositions: 50/50 (red spheres), 75/25 (magenta spheres) and 25/75 (green spheres) located inside AAO with pore diameters of (a) 65 nm and (b) 25 nm. Lines represent the result of a linear fit to the homopolymers and their mixtures.

Polymer Mixtures. Representative reflection microscopy images of the capillary imbibition process for the three blend compositions are depicted in Figure 5. Images show the rise of the imbibition front within the AAO capillaries with time. Notably the imbibition times are very slow for polymers but this is only partially due to the bulk viscosity.[6] The results with respect to the imbibition length, h, as a function of $t^{1/2}$ are summarized in Figure 6.

In the binary mixtures, the imbibition lengths follow approximate $t^{1/2}$ dependence in accord with the LWE. However, theoretical imbibition lengths, that are based on the measured viscosities (Figure 1), the measured quasi-static advancing contact angles (Figure 2 and Supporting Information section), and the surface tensions (Table 1), deviate strongly from the experimental values. Hence the LWE breaks down as with the homopolymers (Figure 4). In addition, imbibition lengths are biased towards the PEO 50k homopolymer (*i.e.*, the shorter chains) (Figure 6). This is evident for all blend compositions and both AAO pore diameters. For example, AAO pores with diameter of 65 nm are enriched by 20% in shorter chains. AAO templates with a pore diameter of 25 nm are enriched by ~10% in shorter chains. To further explore this effect, GPC was made on material extracted from the AAO pore interior. The result is presented in Figure 7 and confirms an enrichment of the pores by the shorter chains.

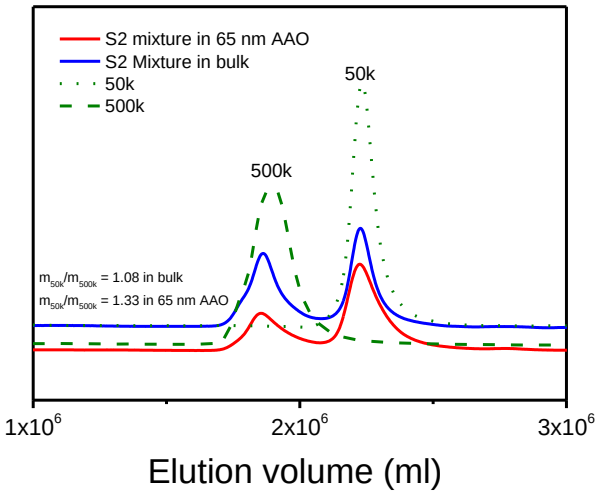

Figure 7. GPC traces of S2 symmetric mixture within AAO pores with a diameter of 65 nm (red line), compared with the same mixture in the bulk (blue line), and with the two homopolymers PEO 50k and PEO 500k. The mass ratio of PEO 50k to PEO 500k was obtained from the integration of the corresponding peaks.

With self-consistent field theory (SCFT)[14-20] we study a blend of the same chemical composition (*i.e.*, χ=0) and length ratio α=10. As with the experiments we consider three bulk compositions (A and B denote the polymer with the short and long chains, respectively) as follows (i) φ_A= 0.25, φ_B= 0.75, (ii) φ_A= φ_B= 0.50 and (iii) φ_A= 0.75, φ_B= 0.25 and the cylinder radius is varied from 0.5 $b\sqrt{N}$ to 8.0 $b\sqrt{N}$. Figure 8 summarizes the pertinent results of the numerical calculations. In general, shorter chains more easily penetrate the pores, and the effect becomes more pronounced with increasing degree of confinement ($R\rightarrow 0$). These results from SCFT calculations are in excellent agreement with experiment. For the symmetric blend located inside AAO with a pore diameter (2*R*) of 65 nm, the individual components have end-to-end distances of 1.7×*R* (PEO 50k) and 0.57×*R* (PEO 500k), respectively, suggesting on average a ~15% enrichment by the shorter chains. On the other hand, in the limit of increasing *R*, the bulk ratio is approached.

Subsequently, we study the density profiles inside the pore for a given pore radius (R=0.5$b\sqrt{N}$). The second row of Figure 8 depicts the spatial distribution of polymer chains as a function of r, the distance to the pore axis. In all cases the inner part of the pores are enriched by the shorter chains. For example, for the symmetric blend, the composition near the pore center is 55:45 and this persists to r=0.4 $b\sqrt{N}$. The local density ratio between the short and long chains is also of interest (third row of Figure 8). From an entropic point of view, ends of polymer chains have equal probability to be found near the pore surface. Consequently, there is an enrichment of the short chains near the pore surface.

Overall, SCFT calculations confirmed the faster imbibition of nanopores by the shorter chains. Furthermore they suggest the enrichment of the pore surface by the shorter chains. The importance of these findings is that they suggest a way of separating long from short chains in a polydisperse polymer mixture that is based on the difference in their imbibition speeds. A careful selection of the pore diameter relative to the polymer molecular weight can lead to the *fractionation* of a polydisperse melt in the absence of solvent.

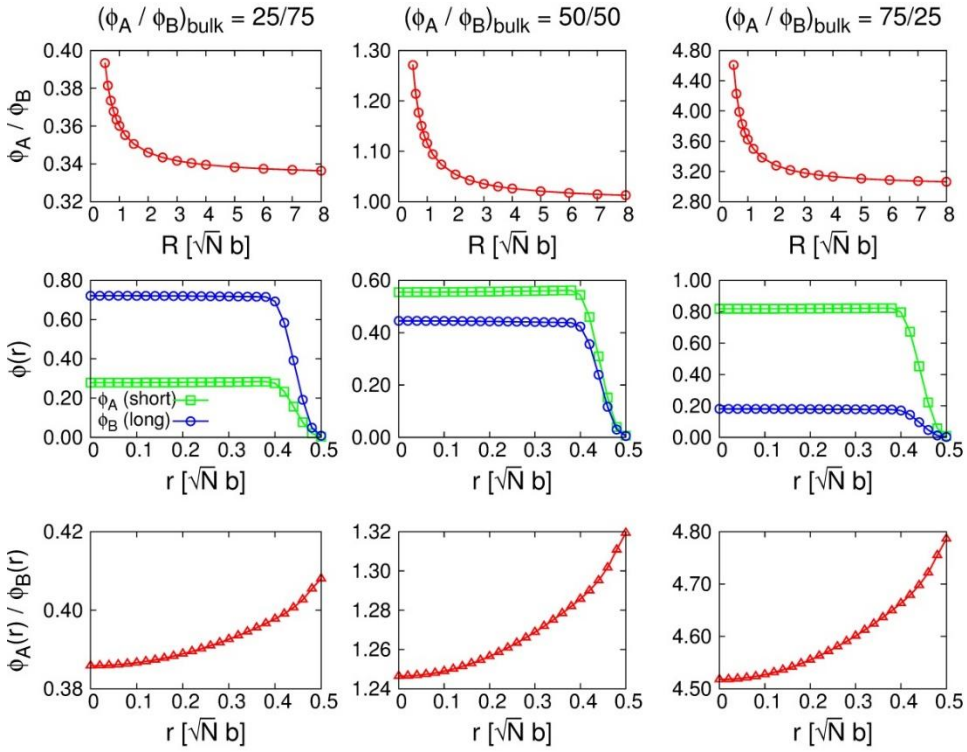

Figure 8. Self-consistent field theory calculations for three blend composisions; (left column) φ_A= 0.25, φ_B= 0.75, (middle) φ_A= φ_B= 0.50 and (right column) φ_A= 0.75, φ_B= 0.25. The results of the averaged φ_A/φ_B is shown in the first row as a fucntion of the cylinder radius R (in units of $b\sqrt{N}$). The spatial distribution of the polymers as a fucntion of r, the distance to the pore axis is shown in the second row. The local density ratio of short to long chains is plotted in the third row.

4.5 Conclusion

In summary, capillary imbibition in binary blends follows approximately $t^{1/2}$ dependence but contradicts the predictions of the classical LWE because of the pre-factor in the equation. Results from reflection microscopy demonstrate faster imbibition by the shorter chains. Results from SCFT calculations, performed on the same mixtures, are in excellent agreement with experiment suggesting on average a ~15% enrichment by the shorter chains. On top of that, SCFT shows an enrichment of the short chains near the pore surface. These results taken together suggest a way of separating long from short polymer chains in the bulk, namely, by the difference in imbibition speeds within narrow pores. Whereas in gel permeation chromatography (GPC) smaller polymer coils explore more pores and thus take longer to pass through a GPC column, in AAO, shorter chains penetrate faster purely for entropic reasons and in the absence of solvent.

4.6 References

1. de Gennes, P.G. Scaling Concepts in Polymer Physics, Cornell University Press, 1979.
2. Movileanu, L.; Cheley, S.; Bayley, H. Partitioning of individual flexible polymers into a nanoscopic protein pore. *Biophysical Journal* **2003**, *85*, 897-910.
3. Aksimentiev, A.; Heng, J.B.; Timp, G.; Schulten, K. Microscopic kinetics of DNA translocation through synthetic nanopores. *Biophysical Journal*, **2004**, *87*, 2086-2097.
4. Shin, K.; Obukhov, S.; Chen, J.-T.; Huh, J.; Hwang, Y.; Mok, S.; Dobriyal, P.; Thiyagarajan, P.; Russell, T.P. Enhanced mobility of confined polymers, *Nat. Mater.* **2007,** *6*, 961–965.
5. Johner, A.; Shin, K.; Obukhov, S. Nanofluidity of a polymer melt: Breakdown of poiseuille's flow model, *Europhys. Lett.* **2010,** *91*, 38002.
6. Yao, Y.; Alexandris, S.; Henrich, F.; Auernhammer, G.; Steinhart, M.; Butt, H.-J.; Floudas, G. Complex dynamics of capillary imbibition of poly(ethylene oxide) melts in nanoporous alumina, *J. Chem. Phys.* **2017**, *146*, 203320.
7. Lucas, R. "Ueber das zeitgesetz des kapillaren aufstiegs von flüssigkeiten," *Kolloid-Zeitschrift **1918**, 23*, 15–22.
8. Washburn, E.W. The dynamics of capillary flow, *Phys. Rev.* **1921**, *17*, 273–283.
9. Masuda, H.; Fukuda, K. Ordered metal nanohole arrays made by a two-step replication of honeycomb structures of anodic alumina. *Science* **1995,** *268* (5216), 1466.
10. Masuda, H.; Hasegwa, F.; Ono, S. Self-Ordering of Cell Arrangement of Anodic Porous Alumina Formed in Sulfuric Acid Solution. *Journal of the electrochemical society* **1997,** *144* (5), L127-L130.
11. Masuda, H.; Yada, K.; Osaka, A. Self-ordering of cell configuration of anodic porous alumina with large-size pores in phosphoric acid solution. *Japanese Journal of Applied Physics* **1998,** *37* (11A), L1340.
12. Deng, X.; Mammen, L.; Butt, H.-J.; Vollmer, D., Candle soot as a template for a transparent robust superamphiphobic coating. *Science* **2012,** *335*, 67-70.
13. See Supporting Information, Figure S1 for a video of the advancing contact angle during spreading of the homopolymers and the blend with the symmetric composition.
14. Schmid, F. Self-consistent-field theories for complex fluids, *J. Phys.: Condens. Matter* **1998**, **10**, 8105.
15. Matsen, M.W. The standard Gaussian model for block copolymer melts," *J. Phys.: Condens. Matter* **2002,** *14*, R21.
16. Shi, A.-C. Self-consistent field theory of block copolymers, in Developments in Block Copolymer Science and Technology, edited by I.W. Hamley (John Wiley & Sons, New York, 2004) Chap. 8.
17. Fleer, G.J.; Cohen Stuart, M.A.; Scheutjens, J.M.H.M.; Cosgrove, T.; Vincent, B. Polymer at Interfaces (Chapman & Hall, London, 1993).
18. Kawakatsu, T. Statistical Physics of Polymers (Springer, Berlin, 2004).
19. Fredrickson, G.H. The Equilibrium Theory of Inhomogeneous Polymers (Clarendon Press, Oxford, 2006).
20. Meng, D.; Wang, Q. Hard-surface effects in polymer self-consistent field calculations, *J. Chem. Phys.* **2007**, *126*, 234902.
21. Dimitrov, D.I.; Milchev, A.; Binder, K. Capillary rise in nanopores: Molecular dynamics evidence for the Lucas-Wahburn equation. *Phys. Rev. Lett.* **2007**, *99*, 054501.

22. Stukan, M.R.; Ligneul, P.; Crawshaw, J.P.; Boek, E.S. Spontaneous imbibition in naopores of different roughness and wettability. *Langmuir* **2010**, *26*, 13342-13352.
23. Stroberg, W.; Keten, S.; Liu, W.K. Hydrodynamics of capillary imbibition under nanoconfinement. *Langmuir* **2012**, *28*, 14488-14495.
24. Yao, Y.; Butt, H.-J.; Floudas, G.; Zhou, J.; Doi, M. in preparation.
25. Suzuki, Y.; Steinhart, M.; Kappl, M.; Butt, H.-J.; Floudas, G., Effects of polydispersity, additives, impurities and surfaces on the crystallization of poly(ethylene oxide)(PEO) confined to nanoporous alumina. *Polymer* **2016,** *99*, 273-280.
26. Alexandris, S.; Papadopoulos, P.; Sakellariou, G.; Steinhart, M.; Butt, H.-J.; Floudas, G., Interfacial Energy and Glass Temperature of Polymers Confined to Nanoporous Alumina. *Macromolecules* **2016,** *49* (19), 7400-7414.

Chapter 5. Effect of Poly(ethylene oxide) Architecture on the Bulk and Confined Crystallization within Nanoporous Alumina

This chapter has been published as a research paper in Macromolecules. It is reprinted here with kind permission of American Chemical Society.

Yang Yao, Takamasa Sakai, Martin Steinhart, Hans-Jürgen Butt, and George Floudas
Macromolecules 49, 5945 (2016).
DOI: 10.1021/acs.macromol.6b01406

Abstract

Polymer topology matters with respect to the structure, packing and dynamics of chains. Herein we investigate the impact of polymer architecture on the crystallization under rigid confinement provided by nanoporous alumina. We employ two poly(ethylene oxide) (PEO) star polymers and study the effect of (i) end groups and (ii) molecular weight on polymer crystallization in the bulk and under confinement. Functional end-groups have important consequences on the bulk crystallization process. Bulk end-groups reduce the crystallization/melting temperatures and the corresponding equilibrium melting point. Remaining catalyst in the polymer increases the nucleation density in the bulk. Under confinement, the role of catalyst is to enhance the propensity for heterogeneous nucleation, especially in the larger pores. In the absence of catalyst, homogeneous nucleation prevails as with linear PEOs. Long-range dynamics pertinent to star relaxation are affecting the homogeneous nucleation temperature. The homogeneous nucleation temperatures for the star polymers agree with that of linear ones provided that the arm molecular weight is used instead of the total molecular weight. On the other hand, the segmental dynamics speed-up on confinement.

5.1 Introduction

Polymers exist under nanoscale confinement in a range of applications including nanoporous membranes for gas separation, flow through nanopores as rheology modifiers in fracking fluids, and in nanoscale lithography for semiconductor manufacturing. In all these applications polymer conformation and dynamics at the segmental and chain length scales is of importance. With respect to linear polymers a variety of amorphous polymers have been investigated under 1D, 2D and 3D confinement.[1] Recent concerted efforts in this field have focused on the 2D confinement provided by self-ordered nanoporous aluminum oxide (anodic aluminum oxide, abbreviated as AAO).[2-10] AAO contains arrays of discrete-isolated, parallel, cylindrical pores that are uniform in length and diameter that have been employed as model confining systems.[11-13]

Similarly, semicrystalline polymers have been investigated under the uniform confinement provided by AAO.[14-21] Under confinement an interplay was found between *heterogeneous* and *homogeneous* nucleation. In bulk polymers, crystallization via homogeneous nucleation is a rare event. It reflects an intrinsic property that involves crossing a characteristic nucleation barrier. In the majority of cases polymers will crystallize by crossing a significantly lower energy barrier by a mechanism extrinsic to the polymer, known as heterogeneous nucleation. In the bulk, a single nucleus can in principle crystallize (heterogeneously) the whole sample. Recent studies of polymer crystallization demonstrated that by confining polymers to small isolated volumes of AAOs one can suppress heterogeneous nucleation in favor of homogeneous nucleation.[15, 19-21] In this respect, PEO is a model system as it best shows the transformation from heterogeneous to homogeneous nucleation upon confinement.[20,21,22] Indeed, confining PEO within self-ordered nanoporous aluminum revealed that heterogeneous nucleation is completely suppressed within pores with diameters below 65 nm. This resulted to the first phase diagrams for confined semicrystalline polymers.[20,21,16] The implication of this work is that heterogeneities are impurities extrinsic to polymers; by infiltrating chains within isolated nanometer size volumes effectively excludes these "impurities" and suppresses the propensity for heterogeneous nucleation.

Currently there is some understanding of the effect of confinement on polymer crystallization of linear polymers. However, the impact of confinement on *non-linear* polymers has not been investigated. Polymer topology matters with respect to the structure, packing and dynamics of chains. In the current work we investigate the impact of polymer architecture on the crystallization

by the rigid 2D confinement provided by self-ordered AAO. We employ two PEO star polymers[23,24] and study the effect of (i) end groups and (ii) molecular weight on crystallization in the bulk and under confinement. We address the questions: what is the role of star architecture and end-group functionality on confined polymer crystallization? What are the controlling parameters of the homogeneous crystallization temperatures as compared to linear PEOs confined within the same AAO templates? How is homogeneous nucleation influenced by the different time-scales involved in star polymers (e.g. arm retraction[25])? We find that confinement leads to a suppression of heterogeneous nucleation in favor to homogeneous nucleation in the smaller pores as with linear chains. The homogeneous nucleation temperature agrees with that of linear PEOs when the arm molecular weight is used instead of the total molecular weight. In addition, we investigate the segmental dynamics on confinement in comparison to linear PEOs.

5.2 Experimental section

Materials and method of infiltration. Tetra-Amine-Terminated PEO (TAPEO) and Tetra-NHS-Glutarate-Terminated PEO (TNPEO) were prepared from Tetrahydroxyl-Terminated PEO (THPEO) as described elsewhere in detail.[23,24] Briefly, THPEO was synthesized by successive anionic polymerization reaction of ethylene oxide from sodium alkoxide of pentaerythritol. The molecular structures are shown in Scheme I and the molecular characteristics and the

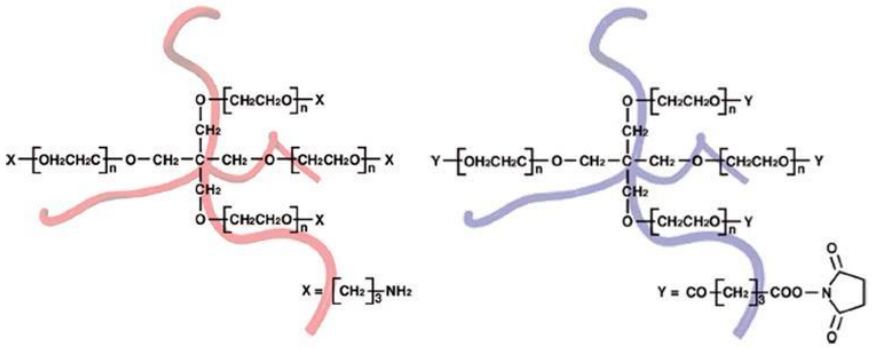

Scheme I. Molecular structures of TAPEO (left) and TNPEO (right)[22]

thermodynamic properties are shown in Table 1. The two series (TAPEO and TNPEO) differ not only on the end-group functionality but also on the amount of catalyst. For example, in TAPEO a Ni/carbon catalyst was employed whereas for TNMEO only traces of catalyst were used. Two

additional star-shaped PEOs were synthesized where the amount of catalyst was controlled to absolute minimum. The systems were tetra-NH_2-PEO (M_w=20k) and tetra-OH-PEO (M_w=20k).

Table 1. Molecular Characteristics and Thermodynamic Properties (Degree of Crystallinity and Equilibrium Melting Temperature)

Sample	M_w (g/mol)	M_w/M_n	X_c (%)[a]	T_m^o (^{o}C)
TAPEO 10k	9620	1.05	62	66
TNPEO 10k	11100	1.01	43	54
TAPEO 20k	20444	1.04	65	70
TNPEO 20k	19389	1.04	54	62

[a] based on a heat of fusion for the 100% crystalline linear PEO, namely 196 J/g.

Self-ordered nanoporous aluminum oxide (AAO) (pore diameters of 25, 35, 65, 200 and 400 nm; pore depth 100 μm) was prepared following the procedures reported in the literature.[11-13] Infiltration of samples was performed by different procedures: melt infiltration and solution infiltration. The former procedure is described in Figure 1. Typically, 20 mg of TAPEO/TNPEO were placed on a glass plate and heated to 80 ^{o}C to melt. The glass plate with the polymer film was placed above the AAO template at a fixed distance maintained by four pillars made of the same polymer. The pillars kept the polymer film at a close distance to the open AAO surface but at the same time allowing for application of vacuum. Subsequently, the oven was heated to 80 ^{o}C under vacuum. During heating, the PEO pillars melted bringing the polymer film in contact with the open AAO surface. Infiltration proceeded by capillary action at 80 ^{o}C for about 1day. Following this procedure the infiltrated AAO templates were brought to ambient temperature. In the latter procedure, 60 mg of PEO was dissolved in 8 ml chloroform (Sigma-Aldrich) and the solution was dropped on AAO template. Subsequently, the AAO template was kept under vacuum (200 mbar) at 100 ^{o}C for 2h to remove any remaining solvent. The infiltration procedure was repeated about 10 times. Typically, the sample mass was ~5 mg (400 nm), ~2 mg (200 nm), ~3 mg (65 nm), ~3 mg (35 nm) and ~3 mg (25 nm) independent of the infiltration method. Prior to DSC, excess amount of polymer was removed from the surface of the self-ordered AAO membranes with razor blades and soft polishing paper (Buehler Microcloth).

Figure 1. Schematic of the infiltration method under vacuum for bulk PEO.

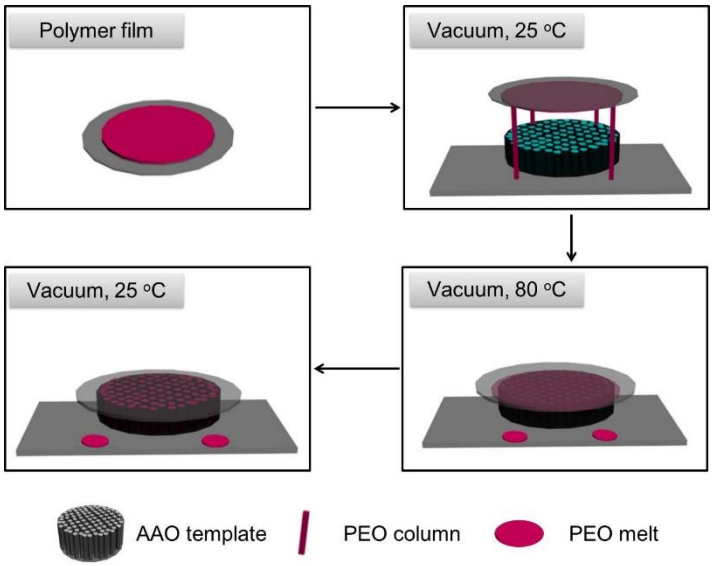

Differential Scanning Calorimetry. Thermal analysis was carried out using a Mettler Toledo differential scanning calorimeter (DSC-822). DSC traces of neat PEO were acquired using an empty pan as reference. The sample mass in the infiltrated AAO was estimated from the mass difference between PEO infiltrated AAO and empty AAO. Samples were weighed with a Mettler Toledo AX205 balance. AAO templates are formed on top of Al substrates. Prior to any DSC measurement, the Al substrates were etched with solutions containing 1.7 mg $CuCl_2 \bullet 2H_2O$, 50 ml deionized H_2O and 50 ml concentrated $HCl_{(aq)}$ under cooling with ice water. Subsequently, the samples were further milled to powder, and 3.0 – 5.5 mg sample material was sealed in aluminum pans (100 µl). DSC traces of infiltrated self-ordered AAO were recorded using reference pans containing empty AAO pieces of the same pore diameter. All samples were first cooled at a rate of 10 ^{o}C/min from ambient temperature to -100 ^{o}C and then heated to 120 ^{o}C at the same rate under a nitrogen atmosphere. The same cycle was repeated two times. Melting and crystallization points, as well as heats of fusion and of crystallization were determined from the second heating and cooling thermograms, respectively.

Polarizing Optical Microscopy. A Axioskope 40 FL optical microscope, equipped with a video camera and a fast frame grabber was used to follow the superstructure formation. A Linkam temperature control unit (THMS600), equipped with TMS94 temperature programmer, was employed for the temperature-dependent studies. Images were recorded following slow cooling (1 ^{o}C /min) from the melt state. In a second experiment the kinetics of superstructure formation were

investigated by performing *T*-jumps from high temperatures (*T*=80 °C) to different final crystallization temperatures where the growth of the crystalline complex was followed. Subsequently, the system was heated with 1 °C/min and the apparent melting temperature of the superstructure was recorded.

SEM. Scanning electron microscopy (SEM) images were obtained using a LEO Gemini 1530 SEM with acceleration voltages from 0.75 to 6 kV. Figure 2, shows top and cross-section images of AAOs infiltrated with the star-shaped PEOs.

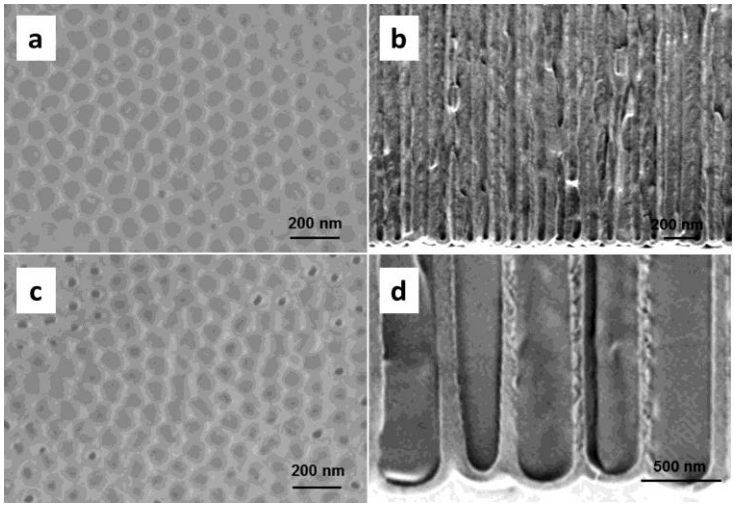

Figure 2. Scanning electron microscopy images of star-shaped PEO infiltrated in self-ordered AAO. (a) Surface of TNPEO 20k located inside AAO with a pore diameter of 65 nm, (b) cross-section of TAPEO 10k located inside AAO template with a pore diameter of 65 nm, (c) surface of TNPEO 20klocated inside AAO with a diameter of 35 nm, (d) cross-section of TAPEO 10k located inside AAO with pore diameter of 400 nm showing fully infiltrated pores to the bottom.

Some reports have shown the formation of polymer tubes rather than fully infiltrated pores.[2] This was not the case here. The cross sectional images show fully infiltrated pores down to the pore bottom (Fig. 2b,d).

X-Ray Scattering. Small-angle (SAXS) and wide-angle X-ray scattering (WAXS) measurements were made for the bulk samples using CuKα radiation (RigakuMicroMax 007 x-ray generator, Osmic Confocal Max-Flux curved multilayer optics). 2D diffraction patterns were recorded on an Mar345 image plate detector at a sample-detector distance of 2240 mm (SAXS) and of 311 mm (WAXS). Intensity distributions as a function of the modulus of the total scattering vector, q =

($4\pi/\lambda$) sin($2\theta/2$), where 2θ is the scattering angle, were obtained by radial averaging of the 2D datasets. Oriented fibers of 1.0 mm diameter from the bulk samples were prepared by a mini-extruder at 20 ^{o}C. SAXS experiments on the crystallization kinetics were made as follows: the sample was first heated to an initial temperature of 80 ^{o}C followed by fast cooling to different final crystallization temperatures. Sufficient time (typically 1-8 hours) was given at each temperature to allow for crystallization. Following this time interval, a 1h long measurement was made to obtain its crystalline structure. For the infiltrated samples WAXS measurements in the θ/2θ geometry was carried out with a D8 Advance X-ray diffractometer (Bruker) operated at a voltage of 40 kV and a current of 30 mA. An aperture (divergence) slit of 0.3 mm, a scattered-radiation (antiscatter) slit of 0.3 mm together with a monochromator slit of 0.1 mm and a detector slit of 1 mm were employed. Measurements were performed with Cu K_α radiation (a graphite monochromator was located between detector slit and detector) detected by a scintillation counter with 95% quantum yield for Cu K_α radiation.

Dielectric Spectroscopy (DS). Dielectric spectroscopy measurements were made as a function of temperature in the range from -110 ^{o}C to 30 ^{o}C using a Novocontrol Alpha frequency analyzer (frequency range from 10^{-2} to 10^{7} Hz). The measured dielectric spectra were corrected for the geometry by using two capacitors in parallel (composed of $\varepsilon^*_{Polymer}$ and ε^*_{AAO}, being the complex dielectric function of PEO and alumina, respectively). The measured total impedance was related to the individual values through $1/Z^*=1/Z^*_{PEO}+1/Z^*_{AAO}$. This equation allows calculating the real and imaginary parts of the dielectric permittivity as a function of the respective volume fractions by using: $\varepsilon^*_M=\varepsilon^*_{PEO}\varphi_{PEO}+\varepsilon^*_{AAO}\varphi_{AAO}$. Fig. S1, Supporting Information section, shows dielectric loss curves corresponding to empty and infiltrated nanopores. The complex dielectric permittivity $\varepsilon^*=\varepsilon'-i\varepsilon''$, where ε' is the real and ε'' is the imaginary part, is a function of frequency ω, temperature T, and in general pressure P, $\varepsilon^*=\varepsilon^*(\omega, T, P)$.[26-28] In the analysis of the DS spectra we have used the empirical equation of Havriliak and Negami (HN)[29]

$$\varepsilon^*_{HN}(\omega,T)=\varepsilon_\infty(T)+\frac{\Delta\varepsilon(T)}{\left[1+\left(i\omega\cdot\tau_{HN}(T)\right)^m\right]^n}+\frac{\sigma_0(T)}{i\varepsilon_f\omega} \quad (1)$$

where $\tau_{HN}(T,P)$ is the characteristic relaxation time, $\Delta\varepsilon(T,P)=\varepsilon_0(T,P)-\varepsilon_\infty(T,P)$ is the relaxation strength of the process under investigation, m, n (with limits $0 < m, mn \leq 1$) describe, respectively, the symmetrical and unsymmetrical broadening of the distribution of relaxation times, σ_0 is the dc-conductivity and ε_f is the permittivity of the free space. In the fitting procedure, we have used the

ε'' values at every temperature and in some cases the ε' data were also used as a consistency check. From, τ_{HN} the relaxation time at maximum loss, τ_{max}, is obtained analytically following:

$$\tau_{max} = \tau_{HN} \cdot \sin^{-1/m}\left(\frac{\pi m}{2(1+n)}\right) \cdot \sin^{-1/m}\left(\frac{\pi mn}{2(1+n)}\right) \quad (2)$$

In the temperature range where two relaxation processes contribute to ε^* there are two ways of representing the data. The first one, followed here, is based in a summation of two HN functions and assumes statistical independence in the frequency domain. The second one, proposed by Williams and Watts is a molecular theory for the dipole moment time-correlation function $C_\mu(t)$ (also known as "Williams ansatz"[30]). In addition to the measured ε'' spectra the derivative of ε' ($d\varepsilon'/d\ln\omega \sim -(2/\pi)\varepsilon''$) have been used in the analysis of the dynamic behavior.

5.3 Results and discussion

Bulk self-assembly and dynamics. The thermodynamics of the bulk Tetra-Amine-Terminated PEO (TAPEO) and Tetra-NHS-Glutarate-Terminated PEO (TNPEO) are discussed with respect to Figure 3. It can be seen that crystallization and melting depends on molecular weight as well as on end-group functionality. For TAPEO, the lower the molecular weight the lower the crystallization/melting temperatures. With respect to functionality, TNPEOs have a lower crystallization and apparent melting temperatures as compared to TAPEOs. The respective heats of crystallization and melting are also lower for TNPEOs; from a melting enthalpy (ΔH) of 122 J/g in TAPEO 10k to 84 J/g in TNPEO 10k and from 127 J/g in TAPEO 20 k to 106 J/g in TNPEG 20k. The thermodynamic results are reported in Table 1 and further discussed below with respect to the SAXS data.

The distinctly different crystallization/melting behavior is also demonstrated in Figure 4 for the lower molecular weight polymers by measuring the storage modulus and the dielectric permittivity as a function of temperature. Both are sensitive probes of crystallization/melting process. The latter, and especially the derivative of dielectric permittivity with respect to temperature (Fig. 4) was shown to be a sensitive probe of phase transitions in a number of soft materials including hydrogen bonded liquids and liquid crystals. Despite the different crystallization/melting temperatures (due to the different rates employed) the results from DSC, rheology and DS show the reduction in crystallization/melting temperatures (i) for the lower molecular weights at the same end-group functionality and (ii) in the tetra-NHS-glutarate-terminated (TNPEO) series as compared to tetraamine-terminated (TAPEG) at a fixed molecular weight.

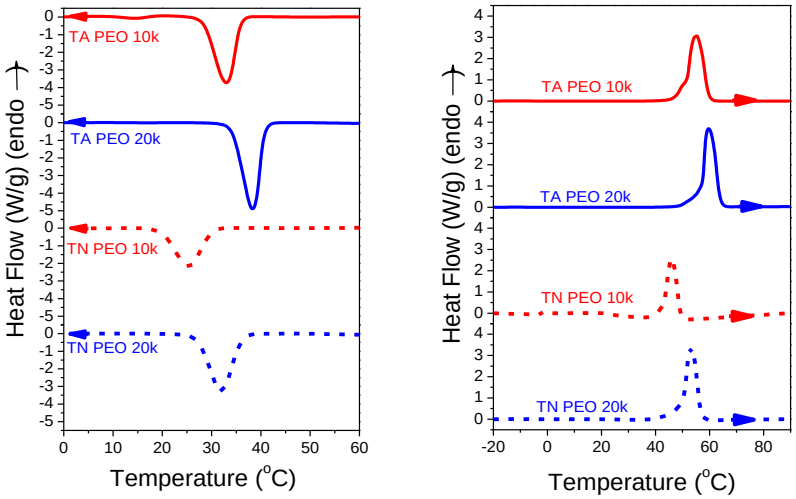

Figure 3. Cooling (left) and heating (right) thermograms of bulk TAPEO 10k, TNPEO 10k, TAPEO 20k, and TNPEO 20k (with cooling/heating rates of 10 °C/min).

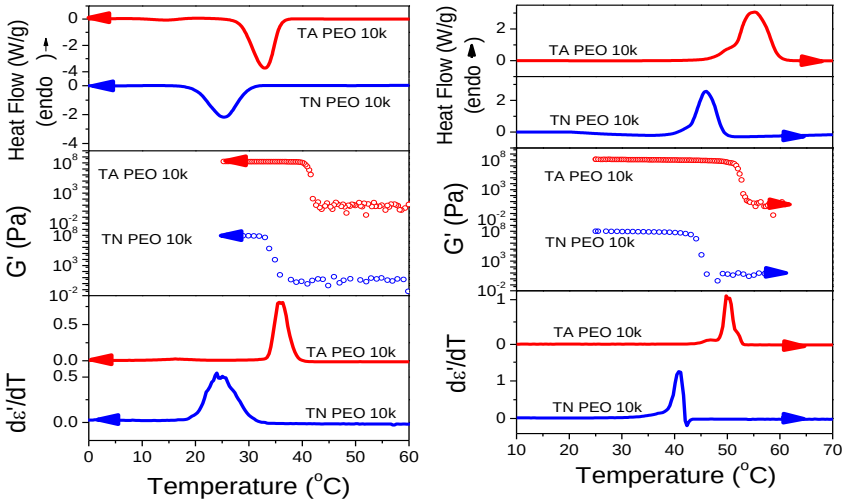

Figure 4. Heat flow, storage modulus and derivative of dielectric permittivity with respect to temperature obtained on cooling (left) and subsequent heating (right) for the TAPEO 10k and TNPEO 10k. The rate in DSC, rheology and dielectric spectroscopy experiments was 10 °C/min, 1 °C/min, and 5 °C/min, respectively.

POM images further revealed spherulitic superstructures in all star-shaped molecules, however with different number of spherulires indicative of a difference in nucleation density (Fig. S3, Supporting Information section). The number of spherulites, formed under isothermal conditions and compared under conditions of fixed undercooling, is higher in TAPEO as compared to TNPEO and linear PEOs. In addition, the spherulitic growth rates were measured at different temperatures (Fig. S4). Growth rates for TAPEO series are faster – for the 10k samples by some orders of

magnitude - with respect to TNPEO when compared at the same crystallization temperatures, implying a higher melting temperature for TAPEO. This is confirmed by measuring the apparent melting temperatures on slow heating (1^{o}C/min) following isothermal crystallization. By employing the Hoffman-Weeks approach[31] or better the nonlinear extrapolation using the MX approach[32,33] the TAPEO series exhibits consistently higher equilibrium meting temperatures (Fig. S5, Table 1). Data from the latter approach are included in Table 1.

The structure, at the level of the unit cell and crystalline lamellar, were investigated by WAXS and SAXS, respectively. The WAXS patterns of TAPEO 10k and TNPEO 10k are shown in Fig. S7 at ambient temperature together with a linear PEO (M_w=2460 g/mol). The scattering pattern of linear PEO exhibits the (021), (110), (120), (112), (032), (024), (131) and (114) Bragg reflections of the ordinary monoclinic PEO structure[34] with lattice parameters a=0.81nm, b=1.30 nm, c=1.95 nm and β=125.4^{o}. The pattern for both TAPEO and TNPEO reflects a less ordered structure with peaks corresponding to the (120), (032) and (024)/(131) reflections of the same monoclinic lattice. Hence, the star-shaped PEOs crystallize with an identical unit cell to linear PEO but with a lower degree of crystallinity.[35] The SAXS patterns indicate a lamellar structure with a long period that is 15.5 nm and 14.0 nm for TAPEO 10k and TNPEO 10k, respectively. These values of the long period are somewhat shorter than the expected from fully extended linear PEO[36] with a molecular weight that corresponds to the arm molecular weight of the stars. For example, the long period of $L=\lambda/(1+n)$, where λ is the crystalline chain length, $\lambda=M_n/\nu$=12.64 nm (ν=158.2 g/nm is the molar mass per unit length along c axis) and n is the number of folds, for extended chain conformation (no folds) is 15.2 nm and 17.5 nm for (arm) molecular weights of 2405 g/mol and 2775 g/mol corresponding to TAPEO and TNPEO, respectively. This suggests a nearly fully extended chain conformation of arms in TAPEO 10k and a more irregular configuration in TNPEO 10k resulting from the bulkier end groups that are excluded from the crystalline lamellar. The case with the 20k molecular weight is distinctly different. The domain spacing (Fig. S7b) is much shorter than the theoretical one corresponding to an extended chain configuration suggesting chain folding, *i.e.*, states away from equilibrium for the higher molecular weights.

The overall structural picture for the star-shaped PEOs as compared to their linear counterparts is of (i) reduced crystallinity albeit of identical unit cell, (ii) reduced long period as compared to fully extended chains, especially for the larger functionalized end-groups (in TNPEO) and (iii)

increased nucleation density in the TAPEO series. The latter reflects the type and amount of catalyst used (Ni/carbon catalysts was used in the TAPEO synthesis) and is expected to enhance the propensity for heterogeneous nucleation. Under the premise that nucleation density is the controlling parameter of heterogeneous nucleation, confinement within self-ordered AAOs should exhibit different crystallization behavior. In addition, at a fixed molecular weight, the bulkier end-group in TNPEO lowers the equilibrium melting temperature with respect to TAPEO by ~ 12 ^{o}C (10k) and 8 ^{o}C (20k).

Subsequently, we investigated the local dynamics of PEO within the amorphous PEO domains with DS. Two main relaxation processes were found that correspond to the segmental (α-) and local (β-) process. The former conforms to the Vogel-Fulcher-Tammann (VFT) equation:

$$\tau = \tau_0 exp(\frac{B}{T-T_0}) \quad (3)$$

where τ_0 is the relaxation time at very high temperatures, B is the activation parameter and T_o the "ideal" glass temperature located below the conventional glass temperature (taken at τ=100s). The latter process conforms to the Arrhenius equation:

$$\tau = \tau_0 exp(\frac{E}{RT}) \quad (4)$$

In eq. 4, E is the (single) activation energy. Figure 5, compares the dielectric loss curves at the same temperature (-30 ^{o}C) for all four star-shaped PEOs. It shows the fast β-process and a slower α-process corresponding to the segmental relaxation of dipoles located in the amorphous domains. In general, the loss curves of TNPEO exhibit higher dielectric strengths, reflecting the lower crystallinity and the more polar end groups. However, end group functionality does not alter significantly the location of the maxima in the dielectric loss curves.

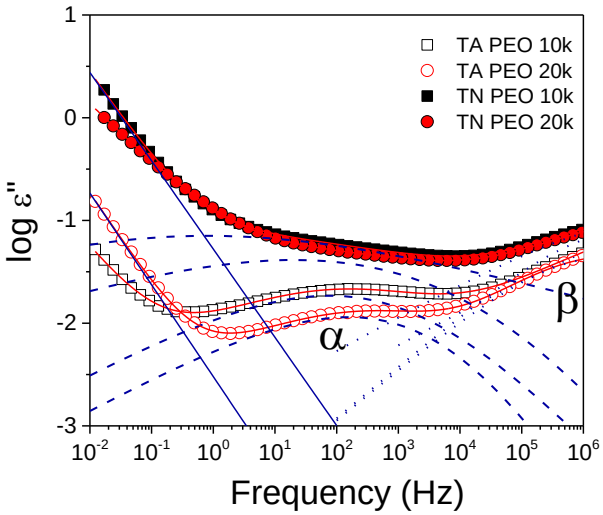

Figure 5. Comparison of the dielectric loss curves of TAPEO 10k, TNPEO 10k, TAPEO 20k, and TNPEO 20k at -30 ºC. The solid red lines are fits according to a summation of two HN functions with a conductivity contribution. The solid blue line gives the contribution from the ionic conductivity, and the dashed and dotted lines give the segmental (α-) and local (β-) processes, respectively.

This is demonstrated in Figure 6 where the relaxation times for the two processes are compared. The relaxation times at maximum loss display the usual VFT (α-) and Arrhenius (β-) dependencies and the parameters are summarized in Table S1. Segmental relaxation times for a linear PEO (M_w=2000 g/mol) are included for comparison.[37] The corresponding times of the latter have the following VFT parameters: $\tau_o = 10^{-12}$ s, B=1010 K, and T_o=182 K is the "ideal" glass temperature. The dynamic properties of branched polymers are, in general, different from their linear counterparts. In melts of entangled stars, the longest relaxation time and viscosity scale with the ratio (M^{arm}/M_e), where M_e is the entanglement molecular weight for PEO (M_e~1620 g/mol), as $\tau_{arm} \approx (M^{arm}/M_e)^{5/2}\exp((M^{arm}/M_e)$ and $\eta \approx (M^{arm}/M_e)^{3/2}\exp(M^{arm}/M_e)$.[25] This would result in a slowing-down of the longest time scales. However, at the segmental scale the effect is small; the main effect of the star-shaped structure being the increase in τ_o in the VFT equation.

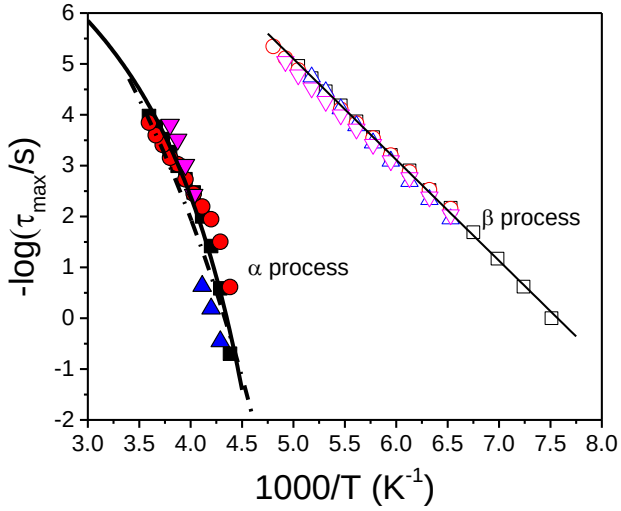

Figure 6. Relaxation times corresponding to the segmental (α) process (solid symbols) and the local (β) process (open symbols) of TAPEO 10k (squares), TNPEO 10k (triangles), TAPEO 20k (circles), and TNPEO 20k (down triangles). Solid lines are fits to the VFT (α) and Arrhenius processes (β), respectively. For the segmental process a fixed τ_o (= 10^{-9} s) value was used. Dashed-dotted line gives the segmental process for a linear PEO (M_w=2000 g/mol).[37]

Self-assembly and dynamics under confinement. Confinement affects the nucleation process, degree of crystallinity, crystal orientation and the local dynamics. To investigate the effect of confinement on the crystallinity and crystal orientation we show θ/2θ diffraction patterns for TAPEO and TNPEO in Figure 7. In the WAXS measurements the AAO surface was oriented perpendicularly and the AAO nanopore axes were oriented parallel to the plane of the incident and scattered X-ray beams. In this scattering geometry only sets of lattice planes oriented normal to the AAO pore axes and parallel to the AAO surface contribute to the scattered intensity. There are two main effects of confinement: first, a reduced scattered intensity for the crystalline part reflecting the reduced crystallinity in confinement and second, a dominating (120) reflection especially in the smaller pores. The direction normal to the (120) planes is parallel to the extended chain direction and is the direction of fastest crystal growth.[20] Therefore in TAPEO and TNPEO located within self-ordered AAO, the latter direction is aligned with the AAO pore axes. In some cases the (112) reflection is also evident suggesting that the direction normal to the (120) planes is not the only direction of crystal growth. The thus-formed crystals have their main growth direction not aligned with the pore axes, hence they will impinge on the pore walls.

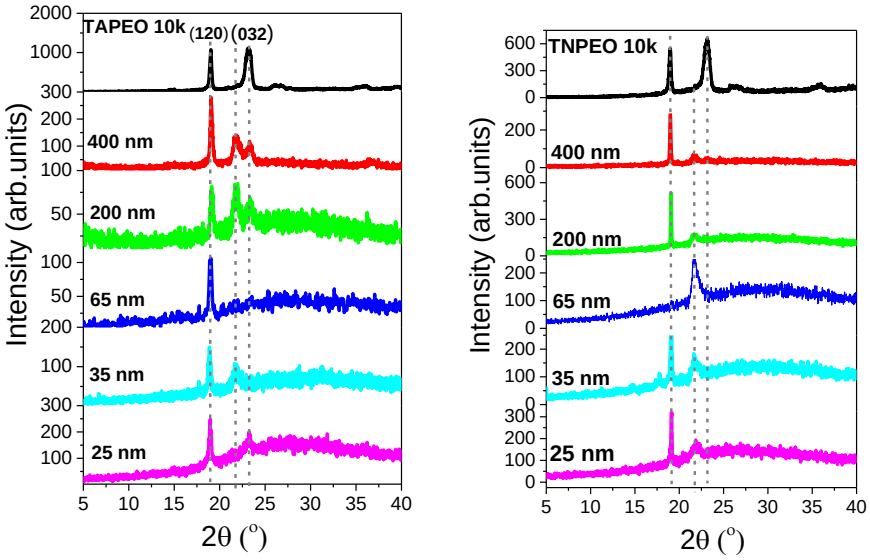

Figure 7. θ-2θ scans for TAPEO 10k and TN PEO 10k confined within AAO with different pore diameters as indicated. All samples following infiltration were first cooled to -80 °C and then measured at 25 °C following annealing (1 day). Dashed lines give the position and (*hkl*) indices of the main Bragg reflections corresponding to the monoclinic unit cell of TAPEO and TNPEO.

The DSC thermograms of the TAPEO 10k and TNPEO 10 k located inside self-ordered AAO on cooling and subsequent heating are compared in Figure 8. They show a distinctly different behavior. Bulk TAPEO 10k, with the applied cooling rate (10 °C/min) crystallizes at 33.1 °C. Upon confinement there is a progressive reduction in the crystallization temperature, from 19.0 °C within AAO templates with 400 nm pore diameter to -12.9 °C within AAO with 25 nm pore diameter. On subsequent heating (with the same rate), the apparent melting temperature shows a weaker dependence on pore size. The crystallization behavior of confined TNPEO 10k within the same AAO pores, also shown in Fig. 8, is distinctly different. Bulk TNPEO 10k crystallizes at 25 °C. Confined TNPEO 10k within AAO templates with pore diameter of 400 nm crystallize already at a low temperature of -20 °C whereas within 25 nm pores it crystallizes at -31 °C. As with the TAPEO 10 k, the apparent melting temperatures show only a weak dependence on pore size.

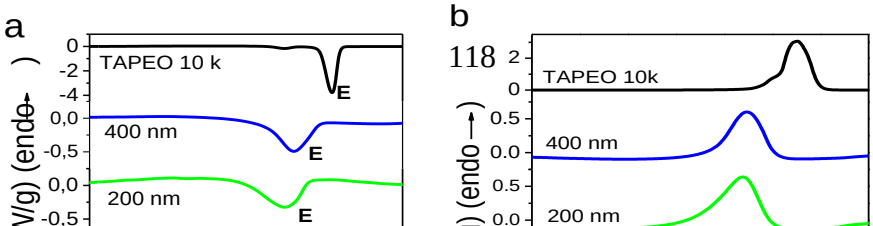

Figure 8. Cooling (left) and heating (right) thermograms of TAPEO 10k (a,b) and of TNPEO 10k (c,d) located inside self-ordered AAO with pore diameters ranging from 400 nm to 25 nm (heating/cooling rates of 10 ^{o}C/min). The letters, E and O, in (a) and (c) represent crystallization via heterogeneous and homogeneous nucleation, respectively.

These experimental findings can be summarized with respect to the pertinent phase diagram under confinement shown in Figure 9. Starting from higher temperatures, it shows apparent melting temperatures that are lower for TNPEO 10k as compared to TAPEO 10k and with a weak dependence on pore size. The dependence of the apparent melting temperatures can be parameterized as T_m'(in ^{o}C)=-310/d+51 (d in nm). The figure further shows the distinctly different crystallization behavior of TAPEO with respect to TNPEO. TAPEO crystallizes predominantly via *heterogeneous* nucleation at lower supercoolings, the latter defined as the temperature difference from the equilibrium melting temperature, $\Delta T=T_m^{o}-T_c$. This is especially the case for

the larger pores. It suggests the dominant role of Ni/carbon catalyst. TNPEO, on the other hand in the absence of the Ni/carbon catalyst, crystallizes at lower temperatures via *homogeneous* nucleation. To test this, two additional star-shaped PEOs were synthesized where the amount of catalyst was controlled to absolute minimum. The systems were tetra-NH_2-PEO (M_w=20k) and tetra-OH-PEO (M_w=20k) and the POM images in the bulk (**Fig. S3**) revealed a lower nucleation density in comparison to TAPEO. As has been reported in literature,[16,20,21] linear PEO in the bulk, crystallizes via heterogeneous nucleation whereas within the isolated nanopores of self-ordered AAO it crystallizes predominantly via homogeneous nucleation. The AAO templates act as filters that filter-out most of impurities.[38]

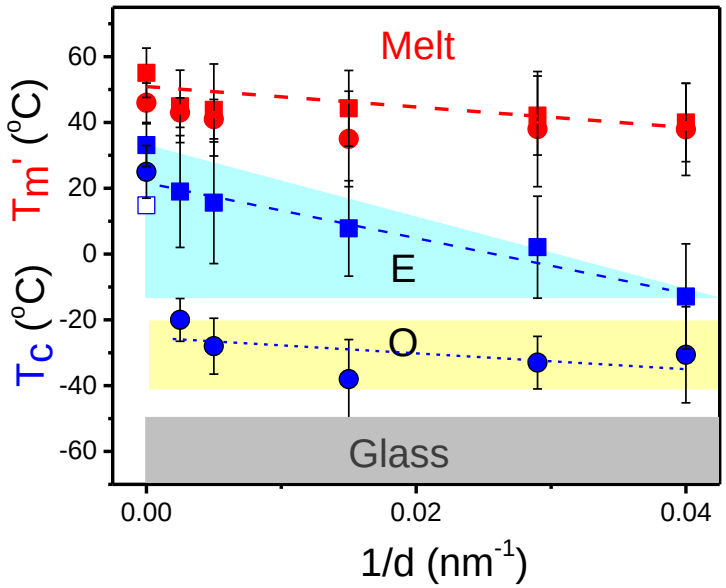

Figure 9. Apparent melting (red symbols) and crystallization temperatures (blue symbols) of TAPEO 10k (squares) and TNPEO 10k (circles) located inside AAO as a function of inverse pore diameter. The vertical bars do not indicate uncertainties but the temperature range corresponding to each crystallization/melting peak. Lines represent linear fits. Shadded areas indicate the (approximate) regions of heterogeneous nucleation (E), homogeneous nucleation (O) and glass states.

Before we comment on the effect of polymer architecture on the homogeneous nucleation temperature we address the dependence of homogenous nucleation on the pore volume. Earlier important contributions on PEO crystallization within confined space (within droplets[39,40] or within the spherical nanodomains of block copolymers[41]) demonstrated a correlation between the confining volume and the homogeneous nucleation temperature. Analytically, discrete PEO droplets (M_w=27000 g/mol) were formed by dewetting a thin film and studied by optical

microscopy.[39] Droplet crystallization was found in two discrete temperature regions corresponding to homogenous and heterogeneous nucleation. For the former mechanism it was shown that the probability of nucleation depended on the volume of droplets and not on the surface. This indicated that homogenous nucleation was indeed the origin of this mechanism. Similarly, homogeneous nucleation was observed when PEO (M_w=12000 and 40000 g/mol) crystallized within nanodroplets obtained by the miniemulsion process.[39] Lastly, homogeneous nucleation was observed for PEO crystallization in the spherical nanodomains of block copolymers.[41] It was argued that macroscopic impurities that served as heterogeneous nuclei could not be contained within the nanometer sized PEO domains. These findings were summarized earlier[42] and are depicted in Figure 10 (the plot contains data from a larger number of references therein). They show a correlation between the crystallization temperature of homogeneous nucleation and the PEO domain/droplet volume. In the same Figure the data for PEO crystallization within AAO templates are shown for two molecular weights (M_n=1070 g/mol and M_n=10^5 g/mol).[20] Note that only the PEO data inside AAO for the higher molecular weight agree with the miniemulsion and droplet experiments since they refer to molecular weights above 10^4 g/mol. On the other hand the homogeneous nucleation temperatures for the M_n=1070 g/mol (as well as those reported earlier by some of us[20] for PEOs of lower molecular weights that are not included in the figure for clarity) are substantially lower. The reason being the additional molecular weight dependence of the homogeneous nucleation temperature. The latter is associated with the reduced liquid-to-glass temperatures for the lower molecular weights.

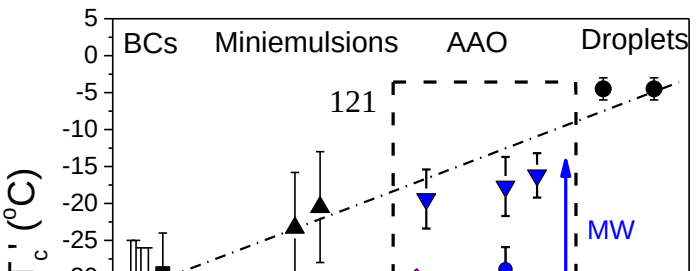

Figure 10. Dependence of the crystallization temperature T_c' of crystallization processes initiated by homogeneous nucleation of PEO within droplets (black rhombi), in miniemulsions (up triangles) and within the spherical domains of block copolymers (squares). The dash-dotted line is a guide for the eye. Data on PEO homogeneous crystallization within AAO templates are included for two molecular weights: M_n=1070 g/mol (blue spheres) and M_n=10^5 g/mol (down triangles). The blue dashed line is a guide to the eye for the lower molecular weight PEO. Another PEO sample from literature (M_n=41000 g/mol), is also shown (magenta rhombus). The vertical arrow shows the dependence of homogeneous nucleation temperature on polymer molecular weight.

We return to the homogeneous nucleation temperature (of TNPEO) and its dependence on molecular weight and polymer architecture. The dependence of the homogeneous nucleation temperature on molecular weight for linear PEO was recently established.[20] By studying the homogenous nucleation temperature for different PEOs (the temperature here is obtained for each molecular weight by following an extrapolation to $\rightarrow \infty$) a dependence similar to Fox-Flory equation was shown:

$$T_c^{hom} = T_c^{\infty} - \frac{A}{M_w} \quad (5)$$

where T_c^{∞} is the apparent crystallization temperature via homogeneous nucleation in the limit of very high molecular weight. In the present study we included the homogenous nucleation temperature from a high molecular weight PEO (M_w=10^5 g/mol)[38] resulting in a limiting value of -13.5 ^oC (Figure 11). The homogeneous nucleation temperatures for the star TNPEOs are in agreement with the linear ones once the arm molecular weight is used instead. This is understandable as long-range motions, such as arm-retraction and diffusion,[25] are controlled not by the total molecular weight but by the arm molecular weight.

The dynamics on a more local scale are also affected by confinement but in a fundamentally different way. The segmental dynamics of PEO with the star topology confined within self-ordered AAOs were subsequently investigated with DS. The dielectric loss curves of the confined star-shaped PEOs are shown in Fig. S2 for two pore diameters. They reveal (i) a broadening of the segmental α-process in both TAPEO and TNPEO and (ii) faster dynamics. With respect to (i) the low frequency shape parameter of TAPEO 20k it changed from a bulk value of m=0.5, to m=0.2 within AAO templates with 35 nm pore diameter (for TNPEO 20k the change is from a bulk value of m=0.4, to m=0.2 within 35 nm pores). A broader distribution of relaxation times results from a distribution of environments for the confined segments. Here we mention that a broad distribution of segmental relaxation times was found also for linear PEOs confined within the same AAOs.[20]

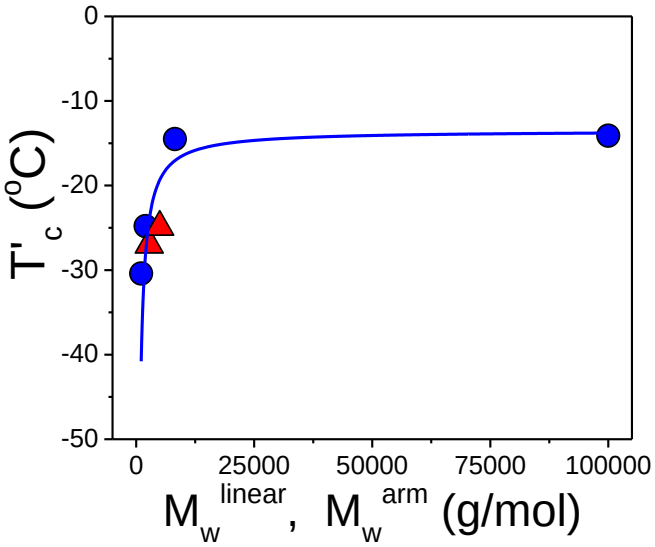

Figure 11. Dependence of the crystallization temperature T_c' of crystallization processes initiated by homogeneous nucleation on the molecular weight of PEO in the limit $d \rightarrow \infty$ (d = AAO pore diameter). (Spheres): The T_c' (d) profiles were obtained from DSC scans of linear PEO inside AAO at a cooling rate of 10 °C/min. (triangles): current investigation of star-shaped TNPEOs (in the limit $d \rightarrow \infty$) obtained from DSC at a cooling rate of 10 °C/min. The solid line is a fit using the Fox-Flory equation for linear PEOs located within self-ordered AAO templates.

The corresponding relaxation times at maximum loss are plotted in Figure 12 in the usual Arrhenius representation. In general, the segmental relaxation times become shorter on confinement leading to a lower glass temperature. Because of the small frequency/temperature range where data are available in the fitting procedure we fixed the value of the activation

parameter *B* to the bulk value. As an example, in TNPEO 20 k, the bulk T_g of 221±2 K is reduced to ~215±2 K within AAO templates with 400 nm pore diameter and to ~203±3 K within 65 nm pores. The speed-up of the segmental dynamics for confined PEO is anticipated from the earlier studies of linear PEO within the same AAO templates.[20] Interestingly, this is also the case in the star-shaped architectures where longer range dynamics are retarded.

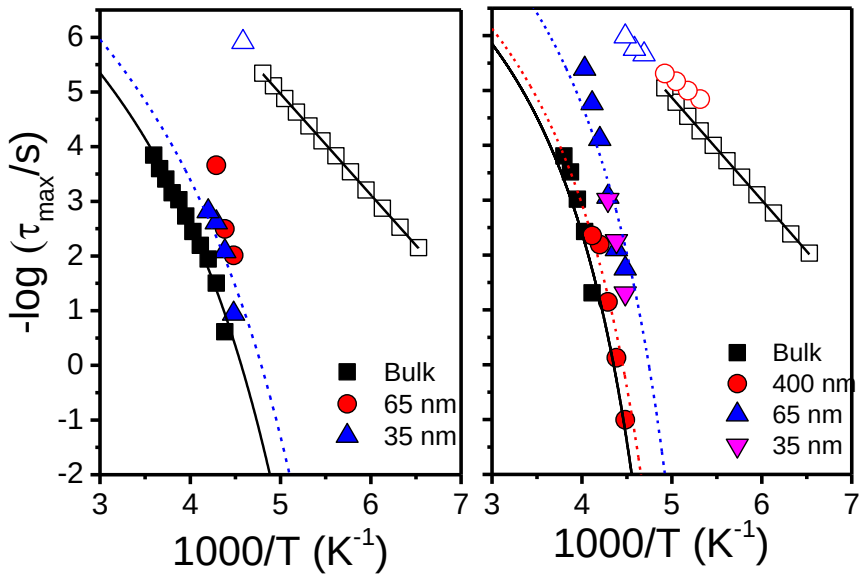

Figure 12. Relaxation times at maximum loss corresponding to the α-(filled symbol) and β- (open symbols) processes of TAPEO 20k (left) and TNPEO 20k (right) located inside self-ordered AAO pores with pore diameters ranging from 400 to 35 nm. Lines are fits to the VFT and Arrhenius equations.

5.4 Conclusion

The effect of star-shaped architecture on the crystallization behavior as a function of molecular weight and end-group functionality in the bulk and under nanometer confinement can be summarized as follows. In the bulk, star-shaped PEOs crystallize with the same unit cell but exhibit lower degree of crystallinity. They show unchanged local dynamics as compared to linear PEOs. End-group functionality has important consequences on the crystallization process. Bulk end-groups reduce the crystallization/melting temperatures and the corresponding equilibrium melting point by ~ 12 ºC (10k) and 8 ºC (20k). The presence of Ni/carbon catalyst is to increase the nucleation density in the TAPEO series. It also has consequences for the crystallization under confinement. The role of catalyst in TAPEO, is to enhance the propensity for heterogeneous

nucleation, especially in the larger pores. In the absence of catalyst (TNPEO), homogeneous nucleation prevails, as with linear PEO. The homogeneous nucleation temperatures for the star TNPEOs are in agreement with the linear ones once the arm molecular weight is used instead. Long-range dynamics pertinent to star relaxation are affecting the homogeneous nucleation temperature. On the other hand, the segmental dynamics speed-up on confinement, despite the expected slowing-down of longer-range dynamics by the star-shaped architecture.

5.5 References

1. Dynamics in Geometrical Confinement, F. Kremer, (Ed.). Berlin: *Springer* 2015.
2. Steinhart, M., Supramolecular organization of polymeric materials in nanoporous hard templates. In *Self-Assembled Nanomaterials II*, Springer: 2008; pp 123-187.
3. Shin, K.; Obukhov, S.; Chen, J.-T.; Huh, J.; Hwang, Y.; Mok, S.; Dobriyal, P.; Thiyagarajan, P.; Russell, T.P., Enhanced mobility of confined polymers. *Nature Mater.* **2007**, *6*, 961-965.
4. Krutyeva, M.; Wischnewski, A.; Monkenbusch, M.; Willner, L.; Maiz, J.; Mijangos, C.; Arbe, A.; Colmenero, J.; Radulescu, A.; Holderer, O.; Ohl, M.; Richter, D. Effect of Nanoconfinement on Polymer Dynamics: Surface Layers and Interphases. *Phys. Rev. Let.* **2013**, *110*, 108303.
5. Alexandris, S.; Sakellariou, G.; Steinhart, M.; Floudas, G. Dynamics of unentangled *cis*-1,4-Polyisoprene Confined to Nanoporous Alumina. *Macromolecules* **2014**, *47*, 3895.
6. Li, L.; Zhou, D.; Huang, D.; Xue, G. Double Glass Transition Temperatures of Poly(methyl methacrylate) Confined in Alumina Nanotube Templates. *Macromolecules* **2014**, *47*, 297-303.
7. Lange, F.; Judeinstein, P.; Franz, C.; Hartmann-Azanza, B.; Ok, S.; Steinhart, M.; Saalwächter, K., Large-Scale Diffusion of Entangled Polymers along Nanochannels. *ACS Macro letters* **2015**, *4*, 561-565.
8. Tung,W.-S.; Composto, R.J.; Riggleman, R.A.; Winey, K.I., Local Polymer Dynamics and Diffusion in Cylindrical Nanoconfinement. *Macromolecules* **2015**, *48*, 2324-2332.
9. Tan, A.W.; Torkelson, J.M., Poly(methyl methacrylate) nanotubes in AAO templates: Designing nanotube thickness and characterizing the Tg-confinement effect by DSC. *Polymer* **2016**, *82*, 327-336.
10. Kipnusu, W.C.; Elmahdy, M.M.; Mapesa, E.U.; Zhang, J.; Böhlmann, W.; Smilgies, D.-M.; Papadakis, C.M.; Kremer, F., Structure and Dynamics of Asymmetric Poly(styrene‑b‑1,4-isoprene) Diblock Copolymer under 1D and 2D Nanoconfinement. *ACS Appl. Mater. Interfaces* **2015**, *7*, 12328-12338.
11. Masuda, H.; Fukuda, K., Ordered metal nanohole arrays made by a two-step replication of honeycomb structures of anodic alumina. *Science* **1995,** *268* (5216), 1466-1468.
12. Masuda, H.; Hasegwa, F.; Ono, S., Self-Ordering of Cell Arrangement of Anodic Porous Alumina Formed in Sulfuric Acid Solution. *Journal of the electrochemical society* **1997,** *144* (5), L127-L130.
13. Masuda, H.; Yada, K.; Osaka, A., Self-ordering of cell configuration of anodic porous alumina with large-size pores in phosphoric acid solution. *Japanese Journal of Applied Physics* **1998,** *37* (11A), L1340.

14. Duran, H.; Gitsas, A.; Floudas, G.; Mondeshki, M.; Steinhart, M.; Knoll, W., Poly (γ-benzyl-L-glutamate) peptides confined to nanoporous alumina: Pore diameter dependence of self-assembly and segmental dynamics. *Macromolecules* **2009,** *42* (8), 2881-2885.
15. Duran, H.; Steinhart, M.; Butt, H.-J.; Floudas, G., From heterogeneous to homogeneous nucleation of isotactic poly(propylene) confined to nanoporous alumina. *Nano letters* **2011,** *11* (4), 1671-1675.
16. Michell, R. M.; Lorenzo, A. T.; Müller, A. J.; Lin, M.-C.; Chen, H.-L.; Blaszczyk-Lezak, I.; Martín, J.; Mijangos, C., The crystallization of confined polymers and block copolymers infiltrated within alumina nanotube templates. *Macromolecules* **2012,** *45* (3), 1517-1528.
17. Maiz, J.; Martin, J.; Mijangos, C., Confinement Effects on the Crystallization of Poly (ethylene oxide) Nanotubes. *Langmuir* **2012,** *28* (33), 12296-12303.
18. Guan, Y.; Liu, G.; Gao, P.; Li, L.; Ding, G.; Wang, D., Manipulating crystal orientation of poly (ethylene oxide) by nanopores. *ACS Macro Letters* **2013,** *2* (3), 181-184.
19. Suzuki, Y.; Duran, H.; Akram, W.; Steinhart, M.; Floudas, G.; Butt, H.-J., Multiple nucleation events and local dynamics of poly (ε-caprolactone)(PCL) confined to nanoporous alumina. *Soft Matter* **2013,** *9* (38), 9189-9198.
20. Suzuki, Y.; Duran, H.; Steinhart, M.; Butt, H.-J.; Floudas, G., Homogeneous crystallization and local dynamics of poly (ethylene oxide)(PEO) confined to nanoporous alumina. *Soft Matter* **2013,** *9* (9), 2621-2628.
21. Suzuki, Y.; Duran, H.; Steinhart, M.; Butt, H.-J.; Floudas, G., Suppression of Poly (ethylene oxide) Crystallization in Diblock Copolymers of Poly (ethylene oxide)-b-poly (ε-caprolactone) Confined to Nanoporous Alumina. *Macromolecules* **2014,** *47* (5), 1793-1800.
22. Michell, R.M.; Blaszczyk-Lezak, J.; Mijangos, C.; Müller, A. J. Confined crystallization of polymers within anodic aluminum oxide templates. *J. Polym. Sci. Polym. Phys.* **2014**, *52*, 1179-1194.
23. Sakai, T.; Matsunaga, T.; Yamamoto, Y.; Ito, C.; Yoshida, R.; Suzuki, S.; Sasaki, N.; Shibayama, M.; Chung, U.-i., Design and fabrication of a high-strength hydrogel with ideally homogeneous network structure from tetrahedron-like macromonomers. *Macromolecules* **2008,** *41* (14), 5379-5384.
24. Nomoto, Y.; Matsunaga, T.; Sakai, T.; Tosaka, M.; Shibayama, M., Structure and physical properties of dried Tetra-PEG gel. *Polymer* **2011,** *52* (18), 4123-4128.
25. Doi M., Edwards S.F. *The Theory of Polymer Dynamics*, Clarendon Press, 1994.
26. Kremer, F.; Schönhals, A., Broadband Dielectric Spectroscopy. *Berlin: Springer* **2002**.
27. Floudas, G., in Dielectric Spectroscopy. *Polymer Science: A Comprehensive Reference, Elsevier BV, Amsterdam, ed. K. Matyjaszewski and M. Möller*, **2012,** *2.32*, 825–845.
28. Floudas, G.; Paluch, M.; Grzybowski, A.; Ngai, K., *Molecular dynamics of glass-forming systems: effects of pressure*. Springer Science & Business Media: 2010; Vol. 1.
29. Havriliak, S.; Negami, S., A complex plane representation of dielectric and mechanical relaxation processes in some polymers. *Polymer* **1967,** *8*, 161-210.
30. Williams, G.; Watts, D. C. In *NMR Basic Principles and Progress*; Diehl, P., Flick, E., Kosfeld, E., Eds.; Springer: Berlin, 1971; Vol. 4, p. 271.
31. Hoffman, J. D.; Weeks, J. J. *J. Res. Natl. Bur. Stand.* **1962**, *A66*, 13.
32. Marand, H.; Xu, J.; Srinivas, S.; *Macromolecules*, **1998**, *31*, 8219.
33. Gitsas, A.; Floudas, G., Pressure dependence of the glass transition in atactic and isotactic polypropylene. *Macromolecules* **2008,** *41* (23), 9423-9429.

34. Takahashi, Y.; Tadokoro, H. Structural Studies of Polyethers, $(-(CH_2)_m-O-)_n$. X. Crystal Structure of Poly(ethylene oxide). *Macromolecules*, **1973**, *6*, 672-675.
35. Chen, E.-Q.; Lee, S.-W.; Zhang, A.; Moon, B.-S.; Mann, I.; Harris, F. W.; Cheng, S.Z.D. Isothermal thickening and thinning processes in low-molecular-weight poly(ethylene oxide) fractions crystallized from the melt. 8. Molecular shape dependence. *Macromolecules* **1999**, *32*, 4784-4793.
36. Buckley, C.P.; Kovacs, A.J. Melting Behavior of low Molecular Weight Poly(ethylene-oxide) Fractions 2. Folded Chain Crystals. *Colloid and Polym. Sci.* **1976**, *254*, 695-715.
37. Zardalidis, G.; Mars, J.; Allgaier, J.; Mezger, M.; Richter, D.; Floudas, G., Influence of Chain Topology on Polymer Crystallization: Poly(ethylene oxide) (PEO) Rings vs. Linear chains. Macromolecules (submitted).
38. Suzuki, Y.; Steinhart, M.; Kappl, M.; Butt, H.-J.; Floudas, G., Effects of polydispersity, additives, impurities and surfaces on the crystallization of poly(ethylene oxide) (PEO) confined to nanoporous alumina. *Polymer* **2016**, *99*, 373-280.
39. Massa, M.V.; Dalnoki-Veress, K. Homogeneous Crystallization of Poly(Ethylene Oxide) Confined to Droplets: The Dependence of the Crystal Nucleation Rate on Length Scale and Temperature. *Phys. Rev. Lett.*, **2004**, *92*, 255509-1.
40. Taden, A.; Landfester, K. Crystallization of Poly(ethylene oxide) confined in Miniemulsion Droplets. *Macromolecules* **2003**, *36*, 4037.
41. Chen, H.L.; Hsiao, S.-C.; Lin, T.-L.; Yamauchi, K.; Hasegawa, H.; Hashimoto, T. Microdomain-tailored crystallization kinetics in block copolymers. *Macromolecules* **2001**, *34*, 671-674.
42. Müller, A. J.; Balsamo, V.; Arnal, M.L. Nucleation and crystallization in diblock and triblock copolymers. *Adv. Polym. Sci.* **2005**, *190*, 1-63.

5.6 Supporting information

1. Dielectric Spectroscopy (DS)

Effect of AAO templates on dielectric properties of star-PEO:

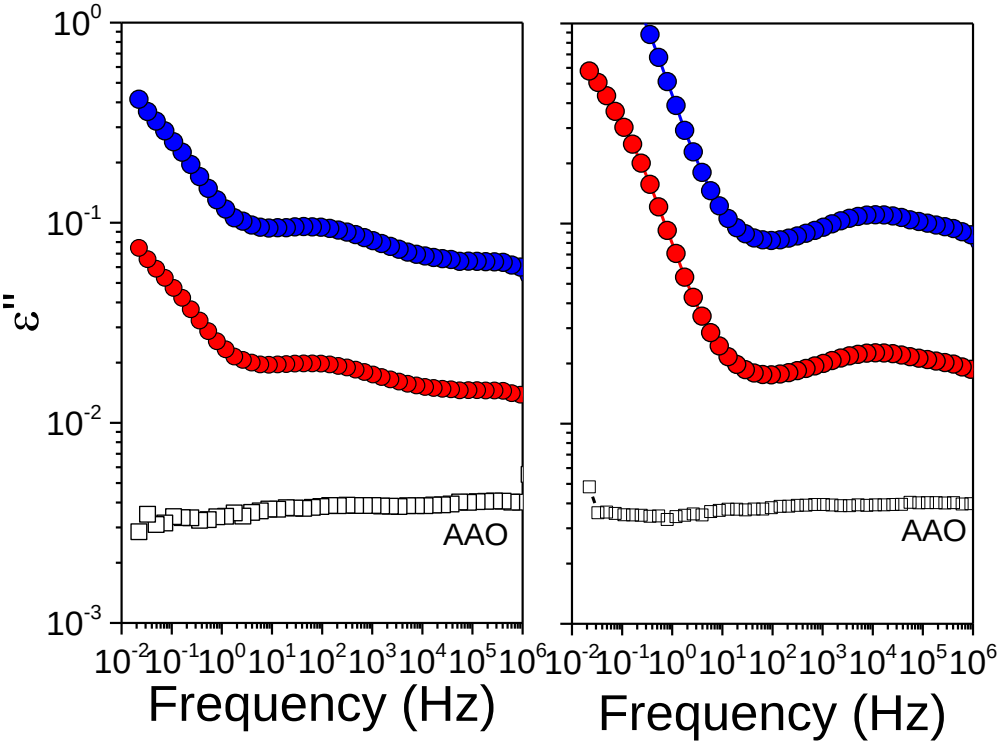

Figure S1. As measured dielectric loss curves of empty AAO templates (open squares), TAPEO 20k inside self-ordered AAO with pore diameter of 65 nm (red spheres) and bulk TAPEO 20 k (blue spheres) at two temperatures -50 ºC (left) and -40 ºC (right). The dielectric loss curves corresponding to the infiltrated polymer were calculated according to the mixing law: $\varepsilon''_M=\varepsilon''_{PEO}\varphi_{PEO}+\varepsilon''_{AAO}\varphi_{AAO}$. φ_{PEO} is 37% and 17.5% for 400 nm and 65 nm templates, respectively.

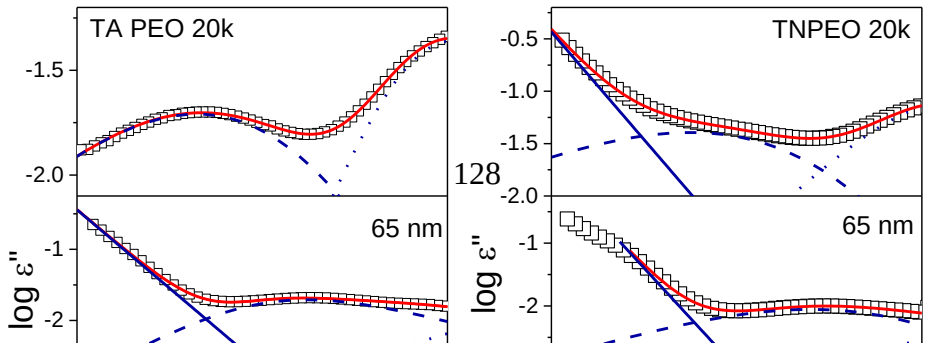

Figure S2. Comparison of dielectric loss spectra of bulk and confined TAPEO 20 k within self-ordered AAOs with pore diameters of 65 nm and 35 nm at -45 ºC (left) and bulk and confined TNPEO 20k at -35 ºC (right) within the same AAOs. The solid red lines are fits to a sum of two HN functions and to the ionic conductivity. Dashed and dotted lines give the individual contributions from the segmental (α-) and local (β-) processes, respectively.

2. Polarizing optical microscopy (POM)

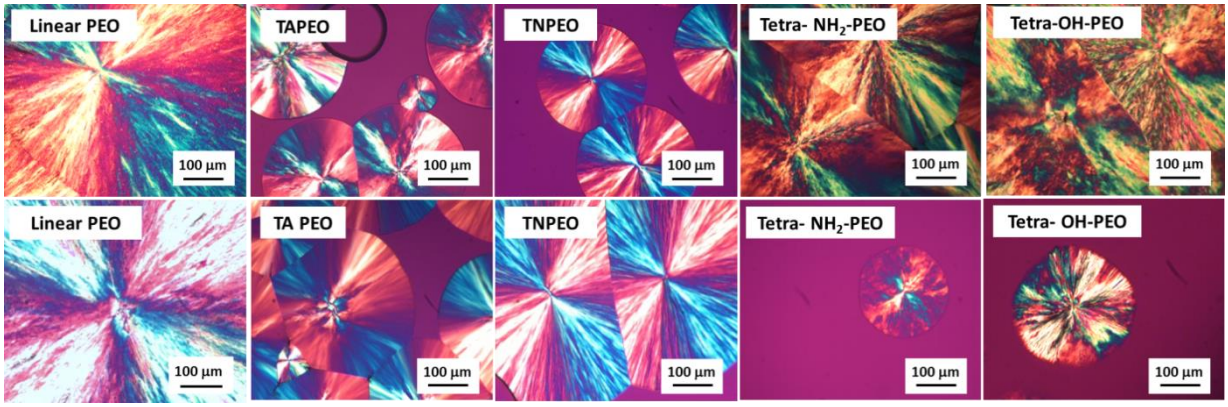

FigureS3. depicts POM images of linear PEO (with molecular weight of 2460 g/mol), TAPEO 10k and TNPEO 10k as well as star-shaped PEOs of tetra-NH_2-PEO (M_w=20k), and tetra-OH-PEO (M_w=20k) compared after the same isochronal cooling with rate of (top) and under conditions of same degree of undercooling (bottom).

The equilibrium melting temperatures were estimated from the MX procedure described on refs [1,2,3]. The obtained apparent melting temperature was plotted as a function of the crystallization temperature. In this approach, the temperature sets can be rewritten as

$$M = \gamma\left(\frac{\sigma_e^l}{\sigma_e}\right)(X + a)$$

where $M = T_m^0/(T_m^0 - T_m')$, $X = T_m^0/(T_m^0 - T_c)$, γ is the thickening coefficient, σ_e^l and σ_e refer to the fold surface free energies, and $a = \Delta H_f C_2/2\sigma_e^l$ where ΔH_f is the latent heat of fusion at the equilibrium melting temperature and C_2 is a constant. In the analysis, γ and σ_e^l/σ_e were taken equal to unity. Based on the fitting, equilibrium melting temperatures were obtained.

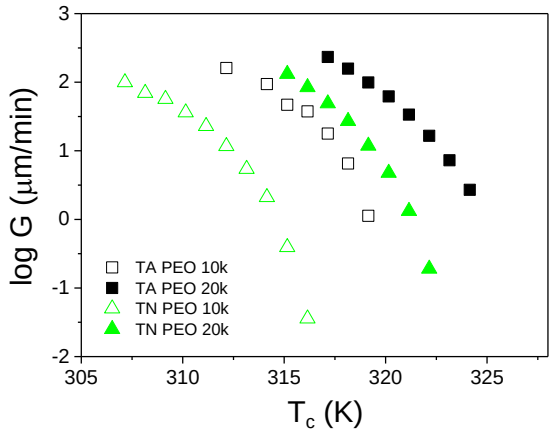

Figure S4. Spherulitic growth rates plotted as a function of crystallization temperature for bulk TAPEO 10k, TNPEO 10k, TAPEO 20k, and TNPEO 20k

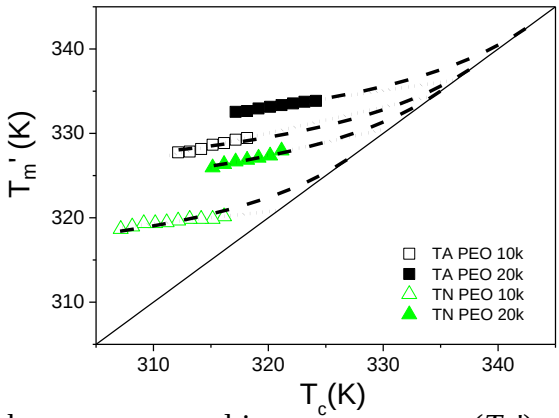

Figure S5. Plot of the apparent melting temperature (T_m') vs. the crystallization temperature (T_c). The solid line has slope unity, and the equilibrium melting point (T_m^o) is obtained in two ways; from a linear extrapolation following the Hoffman-Weeks equation (dotted line)[1], and a nonlinear extrapolation using the MX approach (dashed line).[2]

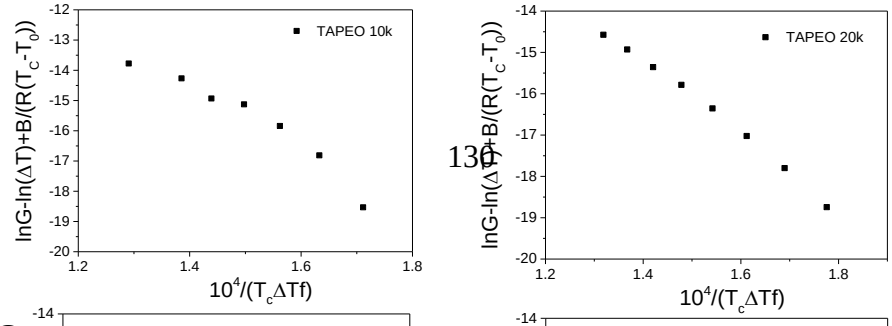

Figure S6. Spherulitic growth rates for TAPEO 10k, TAPEO 20k, TNPEO 10k, and TNPEO 20k as a function of reduced temperature. The values of B and T_{inf} used LH theory are taken from DS fitting (as shown in Table S1).

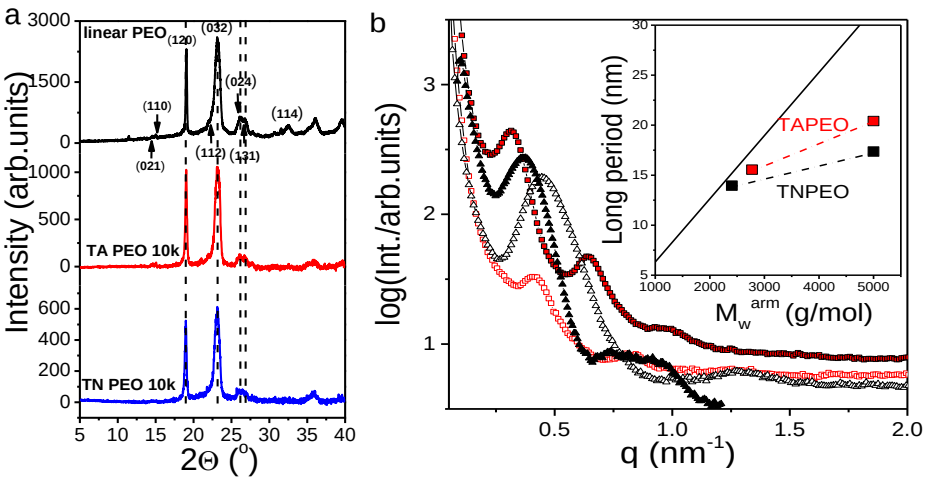

Figure S7. (a) X-ray scans for bulk linear PEO (M_w=2460 g/mol), TAPEO 10k and TNPEO 10k at ambient temperature. Arrows give the position and (*hkl*) indices of the Bragg reflections corresponding to the monoclinic unit cell of PEO. (b) SAXS patterns of bulk TAPEO 10k (open squares), TAPEO 20k (filled squares), TNPEO 10k (open triangles), and TNPEO 20k (filled triangles) at 30 °C. In the inset the long period is plotted as a function of arm molecular weight for the TAPEO (red symbols) and TNPEO (black symbols). Dashed lines are guides for the eye. The solid line gives the long period for an extended chain crystal.[4]

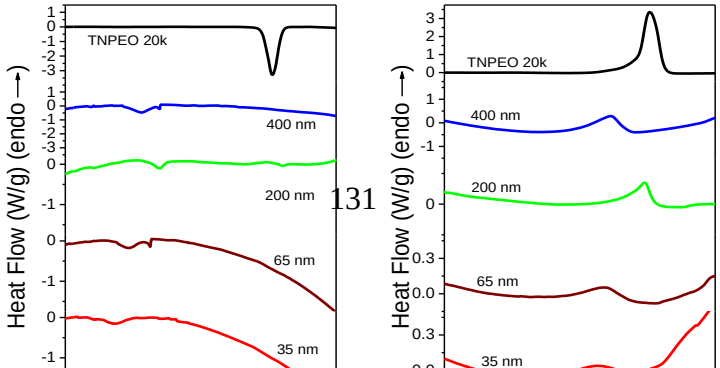

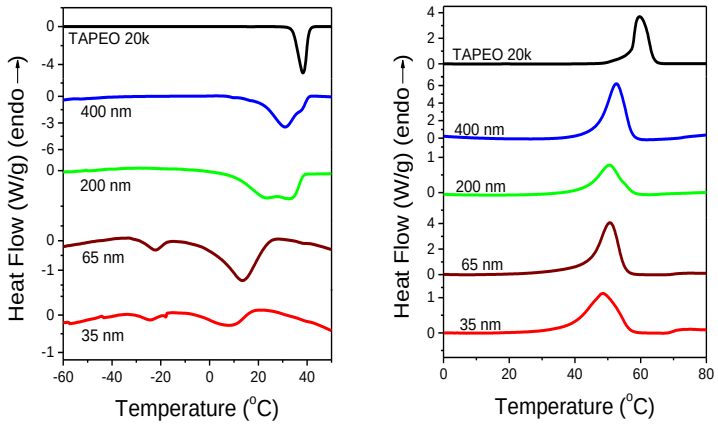

Figure S8. Cooling (left) and heating (right) thermograms of TNPEO 20k (top) and of TAPEO 20k (bottom) located inside self-ordered AAO templates with different pore diameters (heating/cooling rates of 10°C/min).

Table S1. Activation parameters for TAPEO 10k and TNPEO 20k

sample	τ_o (s) (β)	E (kJ mol^{-1})	T_m^o (°C)	τ_o (s) (α)	T_0 (K)	B (K)
TAPEO 10k	9.5×10^{-16}	38±0.4	66	10^{-9}	174±4	1160±60
TAPEO 20k	6.3×10^{-15}	35±0.1	70	10^{-9}	141±5	1620±70

References

1. Hoffman, J. D.; Weeks, J., Melting Process and the Equilibrium Melting Temperature of Polychlorotrifluoroethylene, *J. Res. Natl. Bur. Stand.* **1962**, *A66*, 13.
2. Marand, H.; Xu, J.; Srinivas, S., Equilibrium melting temperature and undercooling dependence of the spherulitic growth rate of isotactic polypropylene *Macromolecules*, **1998**, *1*, 8219.
3. Gitsas, A.; Floudas, G., Pressure Dependence of the Glass Transition in Atactic and Isotactic Polypropylene*Macromolecules* **2008**, *41* (23), 9423-9429.
4. Buckley, C.P.; Kovacs, A.J. Melting Behavior of low Molecular Weight Poly(ethylene-oxide) Fractions 2. Folded Chain Crystals. *Colloid and Polym. Sci.* **1976**, *254*, 695-715.

Chapter 6. Capillary Imbibition, Crystallization and Local Dynamics of Hyperbranched Poly(ethylene oxide) Confined to Nanoporous Alumina

This chapter has been published as a research paper in Macromolecules. It is reprinted here with kind permission of American Chemical Society.

Yang Yao, Yasuhito Suzuki, Jan Seiwert, Martin Steinhart, Holger Frey, Hans-Jürgen Butt, and George Floudas

Macromolecules 50, 8755 (2017).
DOI: 10.1021/acs.macromol.7b01843

Abstract

The crystallization and dynamics of hyperbranched poly(ethylene oxide) (*hb*PEO), obtained from the direct random copolymerization of EO and glycidol (PEO-*co*-PG), are studied both in bulk and within nanoporous alumina (AAO). Copolymerization decreases the degree of crystallinity and lowers the crystallization and melting temperatures as compared to linear PEO. The dynamics of capillary imbibition within AAO followed the $t^{1/2}$ prediction but is *slower* than predicted by the classical Lucas-Washburn equation. The most prominent effect of confinement is the change in nucleation mechanism; from heterogeneous nucleation in bulk to homogeneous nucleation inside AAO. The homogeneous nucleation temperatures for the hyperbranched PEOs agree with those of linear ones provided that the branch molecular weight is used instead of the total molecular weight. Confinement and interfacial effects further suppress the degree of crystallinity and speed-up the segmental dynamics.

6.1 Introduction

Polymers inside porous membranes have important applications in fields such as gel chromatography and heterogeneous catalysis. In the biological world, in particular, biomolecules exist in confined environments such as in proteinaceous pores and living cells.[1-4] In the former, the interactions between poly(ethylene glycol) (PEG) and the protein pores are of key importance. In the biomedical field, PEG (org poly(ethylene oxide) (PEO)) is the established reference polymer because of its biocompatibility, biodegradability and flexibility.[5,6] Understanding the conformational properties, the diffusion in solution, and the crystallization of bulk PEO under nano-sized confinement is of fundamental importance both in basic science and in biotechnology. From the academic point of view, there has been considerable interest in understanding the properties of linear polymers under 1D, 2D, and 3D confinement.[7] More recently, researchers in this field have focused on using self-ordered anodic aluminum oxide (AAO) as a confining medium. AAO contains arrays of discrete-isolated, parallel, cylindrical nanopores that are uniform in length and diameter.[8-10] AAO has been employed as *model* systems in studying the effect of 2D confinement on the dynamics of amorphous and semicrystalline polymers, including PEO.[11-27] Unlike small molecules, an inherent complication with the use of polymers in nanoporous membranes, is the need to consider the details of the imbibition process. It turns out that this is a highly non-trivial process – especially when the coil size approaches the pore radius (e.g. $R_g \sim d$). A recent study[24] reported on the dynamics of imbibition of linear PEOs with a range of molecular weights within AAO templates. Contrary to intuition, it was demonstrated that higher molecular weight PEOs exhibit a fast capillary rise, whereas lower molecular weights exhibit a slower capillary rise, as compared to the bulk. Furthermore, this observation is in sharp contrast to expectations born from classical theory applicable to Newtonian liquids. As a result in the limit, $R_g \geq d$, the effective viscosity under confinement, η_{eff}, had a weak molecular weight dependence as $\eta_{eff} \sim N^1$ as opposed to $\eta_{eff} \sim N^{3.4}$ in the bulk.[24] This result for linear PEOs naturally ignited our interest for studying capillary imbibition in other, non-linear PEO topologies.

Polymer crystallization under confinement can be substantially different from the bulk and this can have important technological applications for the design of polymeric nanofibers with tunable mechanical strength, processability and optical clarity. Previous studies of linear polymer crystallization within self-ordered AAOs demonstrated that by confining polymers to small

isolated volumes, the nucleation process, degree of crystallinity, and crystal orientation can be affected.[11-25] In bulk, the majority of polymers crystallize *via* heterogeneous nucleation, by crossing a significantly lower energy barrier. However, under confinement, one can largely or totally suppress heterogeneous nucleation in favor of homogeneous nucleation.[12,16,17,22] In addition, confinement and polymer-substrate interactions can affect the segmental dynamics. Up to date the majority of studies of confinement within cylindrical pores concerned linear polymers. One reason for this choice - other than availability - is the common perception about the imbibition processes been very slow for complex architectures. *Nonlinear* polymers on the other hand are of interest with a variety of applications ranging from catalysts[28] to drug carriers[29] as a result of their unique architectures.[30] In the first such study[23], star-shaped PEOs were successfully infiltrated within self-ordered AAOs. It was shown that – as with linear PEOs - confinement can lead to a suppression of heterogeneous nucleation in favor of homogeneous nucleation in the smaller pores and to a speed-up of segmental dynamics. However, a major difference from linear PEOs was that the homogeneous nucleation temperatures did not scale with the total molecular weight, but instead, with the arm molecular weight.

Hyperbranched polymers with their high functionality provide an extreme example of non-linear topology with interest in the biomedical world.[29-32] In the bulk, these systems are highly effective at frustrating crystallization.[33] Recently, the synthesis of random copolymers of EO and glycidol by anionic ring-opening copolymerization resulted in well-defined branch-on-branch PEO copolymers by random incorporation of glycerol units into the PEO backbone.[29-34] Recent kinetic studies provide detailed understanding of the respective reactivity ratios of ethylene oxide and glycidol.[30] The random poly(ethylene oxide)-*co*-poly(glycerol) copolymers, consisting only of ethylene glycol and glycerol units, are of interest for medical and pharmaceutical because they best combine high functionality with maximum biocompatibility.[33] Here, we report the effect of confinement within self-ordered AAO on the crystallization behavior of two hyperbranched PEOs (*hb*PEOs) with different glycerol content. The later tunes the degree of crystallinity and the associated mechanical and electrical properties. The work is organized as follows: first we study the dynamics of capillary imbibition, the first of this kind for a non-linear polymer topology. Subsequently, we report the main effects of confinement on *hb*PEO self-assembly and dynamics. These include (i) the change in the nucleation mechanism from heterogeneous to homogeneous

nucleation, (ii) the speed-up of the segmental dynamics and (iii) the lower temperatures for homogeneous nucleation reported for PEO as compared to all previous architectures. Although the first two were anticipated from linear PEOs, the lower temperatures of homogeneous nucleation in the hyperbranched polymers can be put in context with other PEO architectures (star-like and linear) by considering the average PEO molecular weight of linear segments between branching points.

6.2 Experimental section

Materials and Method of Infiltration. Hyperbranched PEOs (*hb*PEOs) were prepared as described elsewhere in detail.[33] Briefly, the synthesis was carried out in one step by random anionic copolymerization of ethylene oxide and glycidol using a partially deprotonated trifunctional core molecule and dimethyl sulfoxide as a solvent. The resulting poly(ethylene glycol)-*co*-poly(glycerol) random copolymers consisted exclusively of ethylene glycol and glycerol repeat units providing maximum biocompatibility. The degree of branching was controlled by varying the content of glycidol comonomer. Degrees of branching were determined by inverse gated (IG) ^{13}C NMR spectroscopy.[33] Two copolymers were studied, one with lower glycerol (G4 *hb*PEO) and one with higher glycerol fraction (G9 *hb*PEO) (Gx, x is the molar glycidol fraction determined by ^{1}H-NMR spectroscopy). On-line viscometry measurements of the molecular weights were performed at Polymer Standards Service GmbH using a PSS GRAM column (30/100/1000 Å porosity) equipped with a SECcurity GPC1260 Refractive Index detector and a SECcurity on-line viscometer DVD1260. DMF containing 5 g L^{-1} LiBr was used as a solvent. Samples and solvent were weighed in precisely to obtain exactly known sample concentrations of about 20 mg mL^{-1}. After eight hours, 100 µL solution were injected. The flow rate was 1 mL min^{-1}, and the temperature 70 °C. For each sample, the average over three injects was calculated. The universal calibration was based on poly(methyl methacrylate) standards. As we will see below, varying the glycidol comonomer content alters the degree of branching and this affects the degree of crystallinity. The molecular structure is shown in Scheme I and the molecular characteristics in Table 1.

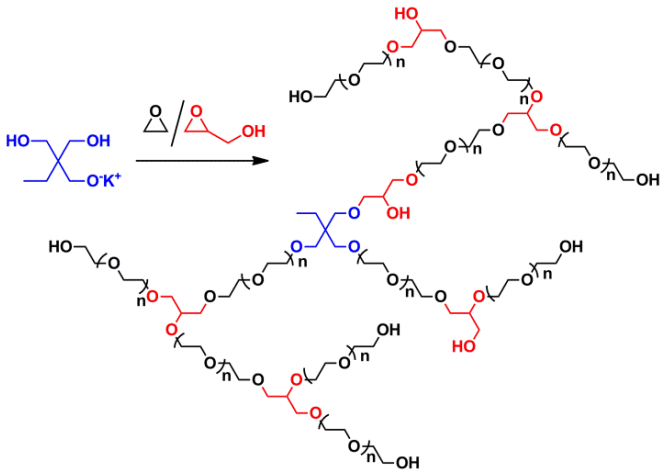

Scheme I. Molecular structure of hyperbranched PEO random copolymers (*hb*PEO) obtained from copolymerization of ethylene oxide and glycidol with glycerol branching units. The average linear segment length n depends on the comonomer ratio (EO:G).

Table 1. Molecular weights of *hb*PEOs used in the present investigation, equilibrium melting temperatures and heats of fusion.

Sample	Glycidol fraction	Degree of Branching	M_n (g/mol)	PDI (M_w/M_n)	$M_{branched}$[a]	T_m^o (^oC)	ΔH (J/g)
G4 *hb*PEO	0.04	0.08	2980	2.1	396	23	99
G9 *hb*PEO	0.09	0.11	2630	1.9	264	0	62

[a] The average branched molecular weight between two branching points.

Self-ordered AAO templates (pore diameters of 400, 200, 65, 35, and 25 nm, pore depth of 100 μm) were prepared as reported in literature.[8-10] Infiltration was performed directly from the melt; 20 mg of sample was placed uniformly on top of each AAO template and imbibition process was carried out under vacuum at 25 ^oC for different time intervals (see below). Subsequently, the excess amount of polymer on the template surface was removed with soft polishing paper (Buehler Microcloth). The templates were fully infiltrated based on (i) the dynamics of capillary imbibition (see below), (ii) the mass difference between empty and infiltrated templates (typically, 8 mg for 400 nm pores, 5 mg for 65 nm pores and 3-4 mg for the smaller pore sizes) and (iii) the SEM images below (Figure 1). Traces of solvent were removed by overnight drying under vacuum.

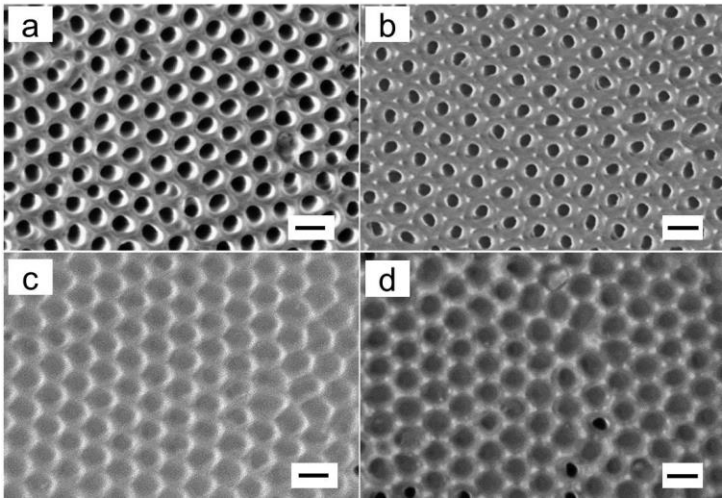

Figure 1. Scanning electron microscopy top views of (a) empty 65 nm AAO, (b) empty 35 nm AAO, (c) G4 *hb*PEO located inside AAO with pore dimeter of 65 nm, and (d) G4 *hb*PEO in 35 nm AAO template. The scale bar indicates 100 nm.

Scanning Electron Microscopy. Scanning electron microscopy (SEM) images were measured by LEO Gemini 1530 SEM with acceleration voltages of 1 kV. Figure 1 shows top views of empty AAOs and AAOs infiltrated with *hb*PEO.

Differential Scanning Calorimetry. A Mettler Toledo differential scanning calorimeter (DSC-822) was used for the thermal analysis. The sample mass in the infiltrated AAO was estimated from the mass difference between *hb*PEO infiltrated AAO and empty AAO. Samples were weighed with a Mettler Toledo AX205 balance. Before DSC measurement, the Al substrates to which the AAO layers had been connected were removed with solutions containing 1.7 mg $CuCl_2 \bullet 2H_2O$, 50 ml deionized H_2O and 50 ml concentrated $HCl_{(aq)}$ under cooling with an ice bath. The samples were further milled to powder; 3-7 mg polymer was sealed in aluminum pans (100 μl). DSC traces of infiltrated self-ordered AAO were recorded using reference pans containing empty AAO pieces of the same pore diameter. All samples were first cooled with a rate of 2 K/min from ambient temperature to -100 ^{o}C and then heated to 80 ^{o}C at the same rate under a nitrogen atmosphere to remove the thermal history. The same cycle was repeated two times. Melting and crystallization temperatures, as well as heats of fusion and of crystallization were determined from the second heating and cooling thermograms, respectively.

X-ray Scattering. Wide-angle X-ray scattering in the $\theta/2\theta$ geometry were carried out with a D8 Advance X-ray diffractometer (Bruker) operated at a voltage of 40 kV and a current of 30 mA. An aperture (divergence) slit of 0.3 mm, a scattered-radiation (antiscatter) slit of 0.3 mm together with a monochromator slit of 0.1 mm and a detector slit of 1 mm were employed. Measurements were performed with Cu K_α radiation (a graphite monochromator was located between detector slit and detector) detected by a scintillation counter with 95% quantum yield for Cu K_α radiation. Prior to measurements, samples were heated to 50 °C to ensure complete melting. Scans in the 2θ-range from 5-40° in steps of 0.01° were made at -50 °C for all templates following slow cooling from ambient temperature.

Dielectric Spectroscopy (DS). Dielectric spectroscopy measurements were carried out with respect of temperature in the range from -100 °C to 60 °C using a Novocontrol Alpha frequency analyzer (frequency range from 10^{-2} to 10^7 Hz). The measured dielectric curves were corrected for the alumina contribution by using a model of two capacitors in parallel with $\varepsilon^*_{Polymer}$ and ε^*_{AAO}, being the complex dielectric function of PEO and alumina, respectively. In this model, the measured total impedance is given by the individual values through $1/Z^*=1/Z^*_{PEO}+1/Z^*_{AAO}$. This equation allows calculating complex dielectric permittivity as a function of the respective volume fractions by using: $\varepsilon^*_M=\varepsilon^*_{PEO}\varphi_{PEO}+\varepsilon^*_{AAO}\varphi_{AAO}$. To obtain the porosity we have used water infiltrated membranes and $\varepsilon^*_M=\varepsilon^*_W\varphi_W+\varepsilon^*_{AAO}\varphi_{AAO}$. First, we employed this relation in obtaining the porosity φ_W. For this purpose the measured permittivity values of water infiltrated nanoporous alumina at 20 °C were used (ε'=16.3, 16.5, 8.4 and 11.4 for 400 nm, 65 nm, 35 nm and 25 nm pores, respectively) together with the AAO value of ε_A=2.6. This resulted in porosities of 17.3 %, 17.5 %, 7.3 % and 11.1 %, respectively for 400 nm, 65 nm, 35 nm and 25 nm pores. We note here that these values are substantially smaller than earlier estimates based on SEM images or by weighting. The complex dielectric permittivity $\varepsilon^*=\varepsilon'-i\varepsilon''$, where ε' is the real and ε'' is the imaginary part, is a function of frequency ω, and temperature T, $\varepsilon^*=\varepsilon^*(\omega, T)$.[35-37] In the analysis of the DS spectra we have used the empirical equation of Havriliak and Negami (HN)[38]

$$\varepsilon^*_{HN}(\omega,T) = \varepsilon_\infty(T) + \frac{\Delta\varepsilon(T)}{\left[1+\left(i\omega\cdot\tau_{HN}(T)\right)^m\right]^n} + \frac{\sigma_0(T)}{i\varepsilon_f\omega} \qquad (1)$$

where $\tau_{HN}(T,P)$ is the characteristic relaxation time, $\Delta\varepsilon(T,P)=\varepsilon_0(T,P)-\varepsilon_\infty(T,P)$ is the relaxation strength of the process under investigation, m, n (with limits $0 < m, mn \leq 1$) is the symmetrical and unsymmetrical broadening of the distribution of relaxation times, respectively, σ_0 is the dc-

conductivity and ε_f is the permittivity of the free space. In the fitting procedure, we have used the ε'' values at each temperature and in some cases the ε' data were also used as a consistency check. From, τ_{HN} the relaxation time at maximum loss, τ_{max}, is obtained analytically following:

$$\tau_{max} = \tau_{HN} \cdot \sin^{-1/m}\left(\frac{\pi m}{2(1+n)}\right) \cdot \sin^{-1/m}\left(\frac{\pi m n}{2(1+n)}\right) \quad (2)$$

In the temperature range where two relaxation processes contribute to ε^* we have employed a summation of two HN functions. Under confinement a third slower process appears that is discussed in terms of the Maxwell-Wagner-Sillars process of heterogeneous dielectrics (Supporting Information). In addition to the measured ε'' spectra the derivative of ε' ($d\varepsilon'/d\ln\omega \sim -(2/\pi)\varepsilon''$) was employed in the analysis of the dynamic behavior. Both bulk and confined samples were annealed overnight at 80 ^oC before the DS measurements.

Optical Microscopy. The superstructure formation of bulk *hb*PEO was observed by polarizing optical microscopy. A thin *hb*PEO film (thickness of 50 μm maintained by Teflon spacers) was placed between two glass plates and introduced to a Linkam THMS 600 temperature controller under an Axioskope 40 FL optical microscope, equipped with a video camera and a fast frame grabber. The images in Figure S2, Supporting information, depict polarization optical microscope (POM) images of linear and two hyperbranched PEOs under conditions of identical undercooling (ΔT = 15 K). Subsequently, samples were heated with 1 K/min and the apparent melting temperature (T_m') of the superstructure was recorded. For the imbibition process the polymer melt was infiltrated into the nanopores by capillary force at ambient temperature. The infiltration procedure was monitored for specific time intervals. Subsequently, the distance penetrated by the melt under capillary pressure (*i.e.*, the imbibition length) was determined from cross sections by reflection microscopy (Zeiss Axiotech vario). Different cross sections were examined for every time interval that revealed uniformity in capillary imbibition. In addition, for each cross section imbibition heights at 5 different positions were recorded, at each imbibition time, and the mean value is plotted in Fig. 4, below. The optical contrast originates from the change in the index of refraction between the polymer infiltrated part and the empty nanopores.

6.3 Results and discussion

We first discuss the effect of chain topology on the bulk self-assembly and dynamics. Subsequently, we explore the kinetics of capillary imbibition within nanoporous alumina. This study demonstrates the successful infiltration of non-linear polymers to nanoporous alumina. Lastly, we explore the phase behavior and segmental dynamics under 2D confinement.

Bulk Self-Assembly and Dynamics.

The thermal behavior of G9 *hb*PEO is distinctly different than G4 *hb*PEO and linear PEO (Figure 2). The crystallization and melting temperatures of G4 *hb*PEO shift to lower values as compared to bulk PEO. Glycerol branching units (glycerol units are incorporated exclusively as branched units for low amounts of glycerol) inhibit PEO crystallization and furthermore result in a broad distribution of crystal thicknesses reflected in the broad melting peaks. Strikingly, the crystallization temperature of G9 *hb*PEO shifts by more than 40 °C to -15 °C. The suppressed crystallization temperature is partially due to the increased glycerol units. In addition, it reflects the restricted crystallization of PEO segments by the branching points, especially in G9 *hb*PEO.

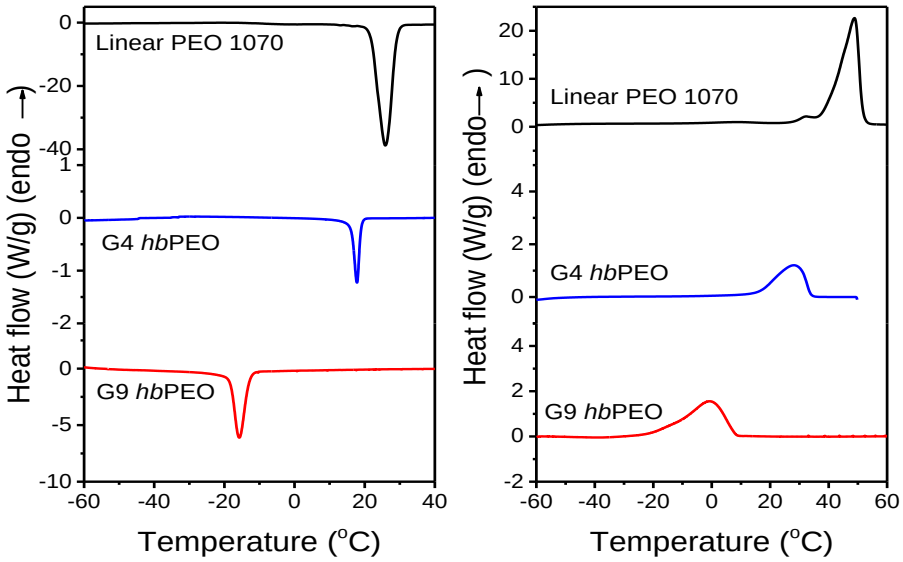

Figure 2. Cooling (left) and heating (right) thermograms of linear PEO (M_w=1070 g/mol), G4 *hb*PEO, and G9 *hb*PEO (with cooling/heating rates of 10, 2, and 2 K/min, respectively).

POM images of linear PEO, G4 *hb*PEO, and G9 *hb*PEO (Figure S2, Supporting Information) imaged for the same undercooling (ΔT = 26 K) indicate substantially different nucleation densities in the bulk of the materials. G9 *hb*PEO has a much higher nucleation density compared with G4 *hb*PEO and linear PEO (M_w=2460 g/mol). In addition, *hb*PEOs exhibit a large reduction in the equilibrium melting temperatures, as compared to linear PEO (Figure S3, Supporting Information).

The local dynamics of *hb*PEOs within the amorphous domains can be investigated by dielectric spectroscopy (DS). The dielectric loss spectra (Figure 3), reveal two main processes and a conductivity contribution at lower frequencies. These correspond to the slower segmental (α) and faster local process (β). The former process has a Vogel-Fulcher-Tammann (VFT) temperature dependence as

$$\tau = \tau_0 exp(\frac{B}{T-T_0}) \quad (3)$$

Here, τ_0 is the relaxation time at very high temperatures, B is the activation parameter and T_0 is the "ideal" glass temperature located below the conventional glass temperature (taken at τ=100s). For the G4*hb*PEO these parameters assume the following respective values: 10^{-12} s, 1060±15 K and 180±1 K. The latter process has an Arrhenius temperature dependence as

$$\tau = \tau_0 exp(\frac{E}{RT}) \quad (4)$$

where E is the (single) activation energy (E=31±1 kJ/mol for the G4*hb*PEO). Figure 3 compares the dielectric loss spectra of two samples at -50 ºC. Both processes originate from the weak dipole of PEO segments located mainly within the amorphous domains. Compared with G4 *hb*PEO, G9 *hb*PEO exhibits higher dielectric strength, reflecting the lower degree of crystallinity (Table 1). The difference in glycerol content only moderately affects the peak position, meaning that the relaxation times are largely unaffected.

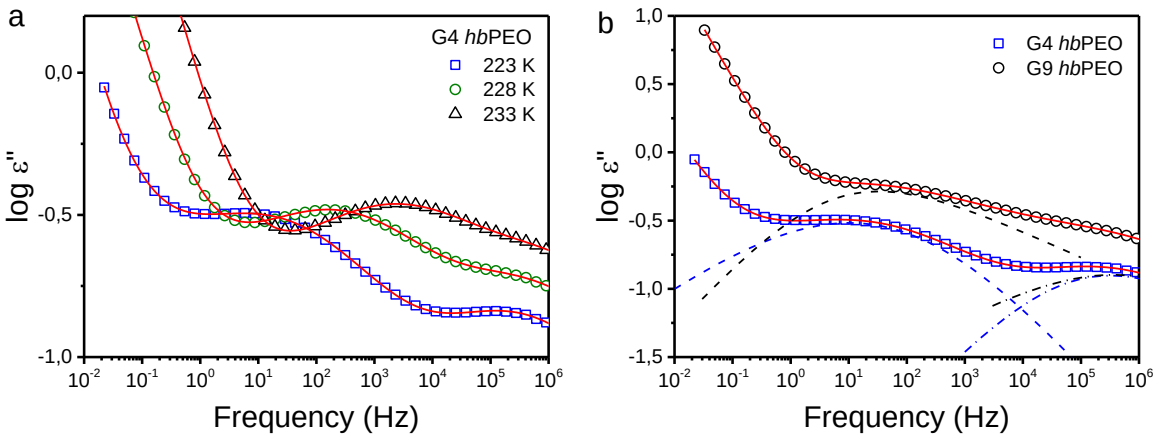

Figure 3. Dielectric loss curves of G4 *hb*PEO (a) at some temperatures as indicated. (b) Comparison of the dielectric loss curves for G9 *hb*PEO and G4 *hb*PEO at -50 °C. The solid red lines are fits according to a summation of two HN functions and a slower contribution. The dashed and dashed-dotted lines give the segmental (α-) and local (β-) processes, respectively.

Dynamics of capillary imbibition

Newtonian liquids penetrating a cylindrical capillary of radius *R*, follow the classical Lucas-Washburn equation (LWE):[39,40]

$$h(t) = (\frac{\gamma R cos\theta}{2\eta})^{1/2}\sqrt{t} \quad (5)$$

Here, $h(t)$ is the penetration length of the liquid meniscus, γ is the surface tension of the liquid, θ is the advancing contact angle, η is the viscosity and t is the wetting time. It was already discussed by Lucas and Washburn that the term, cosθ, makes capillary rise a function of the nature of the material comprising the capillary. According to LWE the degree of penetration is proportional to $t^{1/2}$ as well as to $(\gamma/\eta)^{1/2}$. For polymers, the dynamics of capillary imbibition is a non-trivial process as documented recently for linear PEOs in the same AAO templates.[24] A reversal in the dynamics of capillary rise with PEO molecular weight has been reported; chains with 50 entanglements (M_w≤100 kg/mol) or less showed a *slower* capillary rise than theoretically predicted. Chains with more entanglements (M_w≥500 kg/mol) displayed a *faster* capillary rise.

The penetration length, *h*, for the two hyperbranched polymers as a function of $t^{1/2}$ is depicted in Figure 4. Although the $t^{1/2}$ dependence is approximately valid, the results depict slower capillary rise than predicted by the LWE (dashed lines in Fig. 4). For the theoretical LWE - shown with dashed lines in the Figure - the following parameters were used; dynamic contact angle of 44°,

surface tension of 0.0376 N/m, zero-shear viscosities of 0.58 Pa·s and 0.88 Pa·s for G4 *hb*PEO and G9 *hb*PEO, respectively. Within the context of the LWE, this suggests a higher effective viscosity for *hb*PEOs infiltrated within AAO as compared to bulk. A way to reconcile the measured imbibition lengths with the LWE equation is by assuming a dead layer in contact with the pore walls, which does not participate in the flow. With the assumption of a dead layer we obtain thicknesses of ~19 nm and 17 nm for G4 *hb*PEO and G9 *hb*PEO, respectively.[41] Nevertheless, results shown in Fig. 4 demonstrate successful infiltration of AAO nanopores by the complex hyperbranched polymers. This facilitates an investigation of the effect of confinement on the crystallization process and on the molecular dynamics for a highly non-linear polymer topology.

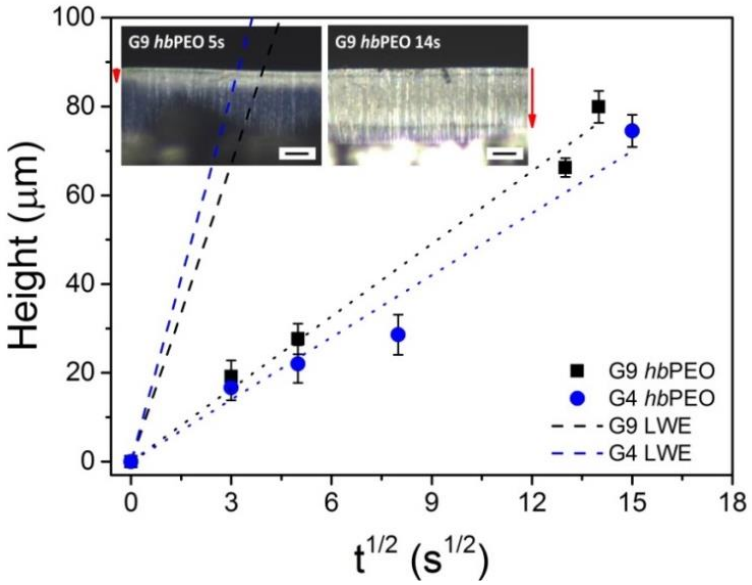

Figure 4. Imbibition length, h, as a function of $t^{1/2}$ for G4 *hb*PEO and G9 *hb*PEO within self-ordered AAOs with a pore diameter of 65 nm. Dashed lines give the predictions of the LWE equation. Solid lines are the results of a linear fit to the experimental data. The inset shows reflection microscopy images of G9 *hb*PEO located inside 65 nm AAO infiltrated for 5 s (left) and for 14 s (right) (scale bar is 20 μm). Vertical arrows indicate respective imbibition lengths.

Self-assembly and dynamics under confinement

Crystallization in confined space affects the nucleation mechanism, crystal orientation and degree of crystallinity.[11-25] Figure 5a compares the diffraction pattern of bulk PEO (M_w=1070 g/mol) with G4 *hb*PEO located within AAO with different pore diameters. Measurements refer to -50 ºC where all systems could crystallize (see below). Bulk PEO exhibits several peaks that correspond to the

(120), (032), (024) and (131) reflections belonging to a monoclinic unit cell with interplanar spacings, d_{hkl}, of the (*hkl*) lattice planes with unit cell parameters, a=0.81 nm, b=1.30 nm, c=1.95 nm and β=125.4°.[41] G4 *hb*PEO and G9 *hb*PEO within AAO with 400 nm pores exhibit a strong peak corresponding to the (120) reflection. The surface of the templates is oriented perpendicularly to the plane defined by the incident beam and the detector. In this geometry, only crystal lattice planes oriented normal to the AAO pore axes and parallel to the AAO surface contribute to the scattered intensity. The direction normal to the (120) planes is parallel to the extended chain direction that is known as the fastest crystal growth direction of PEO. We can assume therefore that in 400 nm pores the direction normal to the (120) planes is aligned with the pore axes. In smaller pores, G4 *hb*PEO and G9 *hb*PEO are still able to crystallize (see below), however, the scattered intensity is weak suggesting reduced crystallinity in agreement with the DSC results (below).

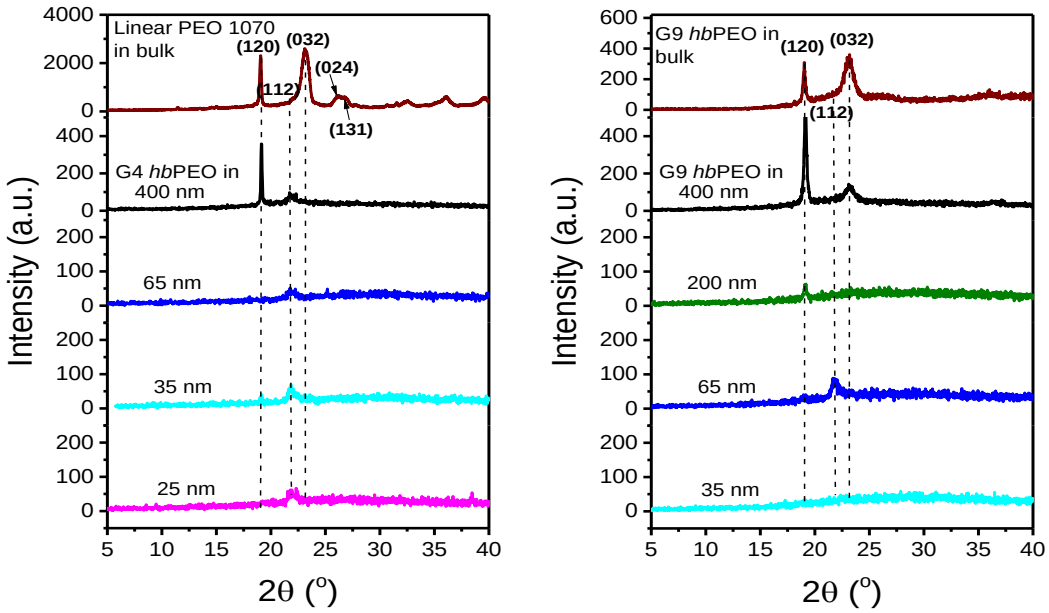

Figure 5. θ-2θ scans for G4 *hb*PEO and G9 *hb*PEO confined within AAO with different pore diameters as indicated all measured at -50 °C (e.g. below the crystallization temperature). Dashed lines give the position and (*hkl*) indices of the main Bragg reflections corresponding to the monoclinic unit cell of PEO.

The DSC thermograms of bulk G4 *hb*PEO and G4 *hb*PEO located inside AAO with different pore diameters obtained on cooling and subsequent heating (measured at 2 K/min) are shown in Figure 6. On cooling, bulk G4 *hb*PEO shows a strong exothermic peak due to heterogeneous nucleation at 17 °C. In G4 *hb*PEO located inside AAO with a pore diameter of 65 nm the

exothermic peak is shifted by some 58 °C to -41 °C. Furthermore, the crystallization temperature decreases slightly with decreasing pore diameter. The shift of the exothermic peak under confinement suggests crystallization via a different mechanism than in bulk. Bulk polymers crystallize at low supercoolings via heterogeneous nucleation initiated by impurities. We have recently shown that the impurities are "extrinsic" to the polymer.[22] Their origin can be traced back to the synthetic methods, like the use of catalyst, salts, etc.[22,23] Studies of polymer crystallization within nanometer size pores demonstrated that by confining polymers to small isolated volumes one can nearly completely suppress heterogeneous nucleation in favor of homogeneous nucleation.[12,16,17,22] This was explained by the AAO templates that offer a size exclusion mechanism for impurities. Under these conditions PEO can only crystallize by homogeneous nucleation at larger undercoolings. The DSC traces of G4 *hb*PEO obtained on cooling indeed show a transformation from heterogeneous nucleation in the bulk to homogeneous nucleation in the smaller AAO pores. Likewise the crystallization temperature in G9 *hb*PEO located within 400 nm pores shifts to lower temperatures as compared to the bulk. However, the higher glycerol content of G9 *hb*PEO, makes the identification of the nucleation mechanism in the smaller pores a difficult task (Figure S4, Supporting Information). The apparent melting temperatures (Figure 6b) also show a dependence on pore size and this will be discussed below with respect to Fig. 9.

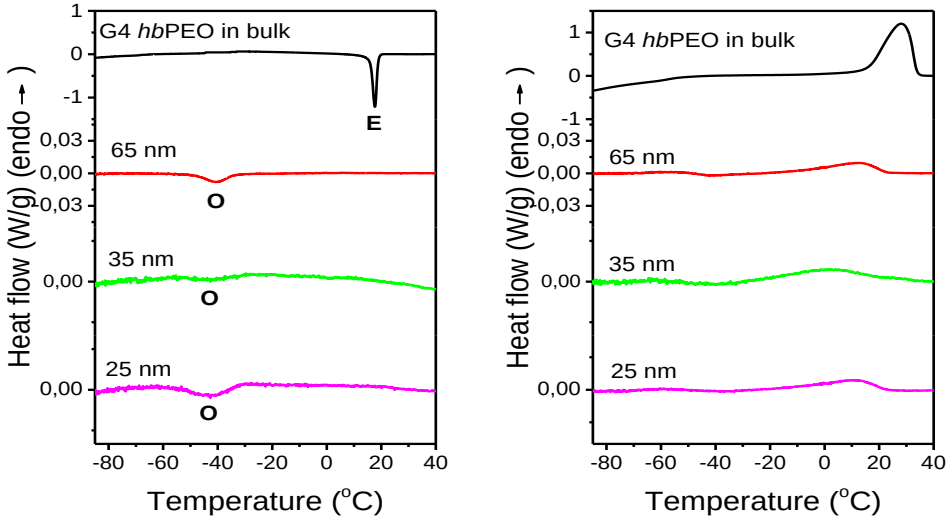

Figure 6. Cooling (left) and heating (right) thermograms of G4 *hb*PEO located inside self-ordered AAO with different pore diameters (heating/cooling rates of 2 K/min).

Next we explore the dipolar dynamics of the hyperbranched polymers under confinement. Dielectric permittivity, ε', and especially its absolute derivative with respect to temperature,

$|d\varepsilon'/dT|$, is a sensitive probe of phase transitions in a number of soft materials.[43,44] The temperature dependence of ε' and of $|d\varepsilon'/dT|$ of G4 *hb*PEO in bulk and within AAO - both at a frequency of 1 MHz - are shown in Figure S5, Supporting Information. On cooling, a dual step-like decrease in dielectric permittivity reflects the crystallization and glass temperatures, respectively.

Figure 7. Comparison of dielectric loss spectra of bulk and of hyperbranched PEOs located within self-ordered AAOs with pore diameters of 400 nm and 65 nm at -50 ºC for G4 *hb*PEO (left) and for G9 *hb*PEO (right). In the bulk the solid red lines are fits to a summation of two HN functions and a conductivity contribution, whereas under confinement to a summation of three HN functions. The dashed and dashed-dotted lines give the contributions of the segmental (α-) and local (β-) processes, respectively.

The assignment of the two processes is based on the frequency dependence (independence) of the latter (former). In confinement, the crystallization process is hidden by the broad glass temperature which also decreases with pore size. For this reason DS measurements were made as a function of frequency for a range of temperatures. Some representative loss curves of *hb*PEOs in the bulk and under confinement are shown in Figure 7. As it was discussed earlier, the dielectric loss spectra of *hb*PEOs in the bulk contain two main processes; a slower process associated with the segmental dynamics (α-process), and a faster more localized process (β-process). Under confinement, a third even slower process is necessary that is attributed to the Maxwell-Wagner-Sillars (MWS) polarization. The assignment is based on the contribution from a heterogeneous material composed from two phases (AAO and *hb*PEO) (Figure S6, Supporting Information). [35, 45-47]

The main effect of confinement on G4 *hb*PEO is to alter the segmental dynamics. The corresponding relaxation times at maximum loss for the α- and β- process are plotted in the usual activation representation in Figure 8 (The fitting parameters are shown in Figure S7, Supporting Information). The β-process, with an activation energy of E=31±1 kJ/mol, is unaffected by the confinement as indicated by the $\tau(T)$ dependence. In the contrary, the α-process speeds-up in confinement. The liquid-to-glass temperature (T_g) reduces from a bulk value of -50 ºC to -64 ºC within AAO with 65 nm pores. The change in T_g of the hyperbranced PEOs in confinement is similar, both in sign and magnitude (ΔT_g=-6 K), to the T_g change of linear PEOs within the same AAO templates.[16,22] The effect, however, is much smaller than for other polymers (poly(dimethyl siloxane) (PDMS), ΔT_g=-14 K; poly(butadiene) (PB), ΔT_g=-13 K). This reflects differences in interfacial energies (from ~0.2×10^{-3} N/m in PEO; to 7.4×10^{-3} N/m in PDMS and to 7.9×10^{-3} N/m in PB) between different polymers in contact with the AAO surface.[26] Lastly, the faster segmental dynamics within AAO templates is not in contradiction to the polymer dead-layer next to the pore walls.[48] The role of the latter is to reduce the dielectric strength, *i.e.* the fraction of mobile segments.

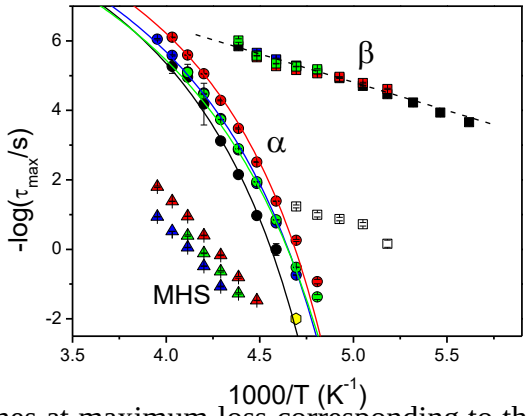

Figure 8. Relaxation times at maximum loss corresponding to the α-(filled circles) and β- (filled squares) and MWS (filled triangles) processes of bulk G4 *hb*PEO (black symbols) and G4 *hb*PEO located inside self-ordered AAO pores with pore diameters; 400 nm (red), 200 nm (blue) and 65 nm (green). Solid and dashed lines are fits to the VFT and Arrhenius equations, respectively. Open squares show the contribution of a small amount of water in the bulk sample. The yellow hexagon is the bulk T_g (obtained from DSC).

The results on the crystallization and melting temperatures (DSC) and on the freezing of the segmental process (DS) can be discussed together with respect to the pertinent phase diagram, *T vs* 1/*d*, shown in Figure 9. The Figure compares the glass/crystallization/melting temperatures of G4 *hb*PEO with the corresponding temperatures in linear[16,22] and star-shaped PEOs.[23] Starting from higher temperatures, the apparent melting temperatures show a dependence on pore size according to the Gibbs-Thompson equation, as T_m' (in ºC)=-500/*d*+27 (*d*, in nm).[49] In all cases, PEO crystallization within the smaller pores proceeds via homogeneous nucleation in sharp contrast to the bulk. Furthermore, homogeneous nucleation temperature has a weak dependence on confining volume, as demonstrated earlier by some of us.[23] Notably, homogeneous nucleation temperatures appear in the following sequence $T_{linear\ PEO} > T_{star\ PEO} > T_{G4\ hbPEO}$. At no surprise, homogeneous nucleation temperatures are in the vicinity of the glass temperatures of confined G4 *hb*PEO. This fact is anticipated by the classical Lauritzen and Hoffman theory of polymer crystallization.[50] It was further confirmed by adding small amounts of diluent to linear PEO that plasticized the polymer and reduced the temperature of homogeneous nucleation by precisely the same amount.[22]

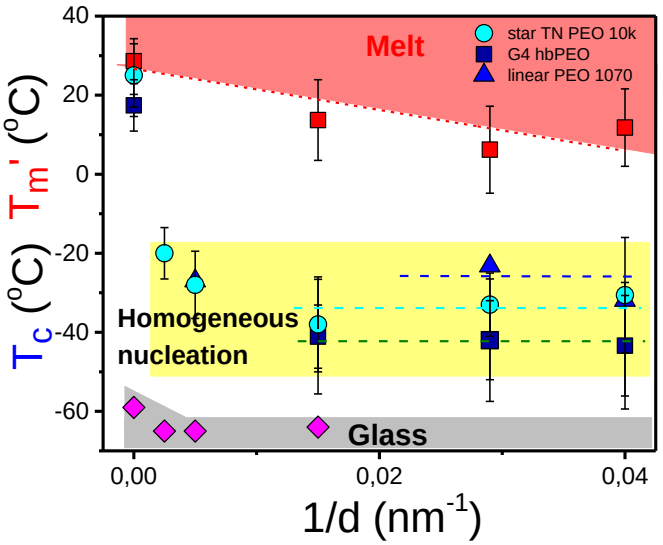

Figure 9. Apparent melting (red symbols) and crystallization temperatures (blue symbols) of star PEO 10000 g/mol (circles), G4 *hb*PEO (squares), and linear PEO (with molecular weight of 1070 g/mol) (triangles) located inside AAO as a function of inverse pore diameter. Glass temperatures from DS are shown with rhombi. The vertical bars indicate the temperature range corresponding to each crystallization/melting peak. Shadded areas indicate the (approximate) regions of melt state (red), homogeneous nucleation (yellow), and glass state (grey). Dashed lines are guides to the eye.

The systematic dependence of homogeneous nucleation temperature on polymer architecture suggests a possible governing law. For linear PEO, we have recently established[16,23] the dependence of the homogeneous nucleation temperature on molecular weight according to the Fox-Flory equation:

$$T_c^{hom} = T_c^{\infty} - \frac{A}{M_w} \tag{6}$$

where T_c^{∞} is the apparent crystallization temperature *via* homogeneous nucleation in the limit of very high molecular weight. We can discuss the homogenenous nucleation temperatures in the different polymer architectures (linear, star, branched) by comparing the arm (star)[23] or branched (*hb*PEO) molecular weight (396 g/mol), instead of the total molecular weight. The comparison is made in Figure 10 and reveals a single Fox-Flory dependence for the different PEO architectures. It further suggests that long-range motions, like arm-retraction and branched point fluctuations are controlling the chain diffusion mechanism involved in the process of homogeneous nucleation.

Figure 10. Dependence of the crystallization temperature T_c' initiated by homogeneous

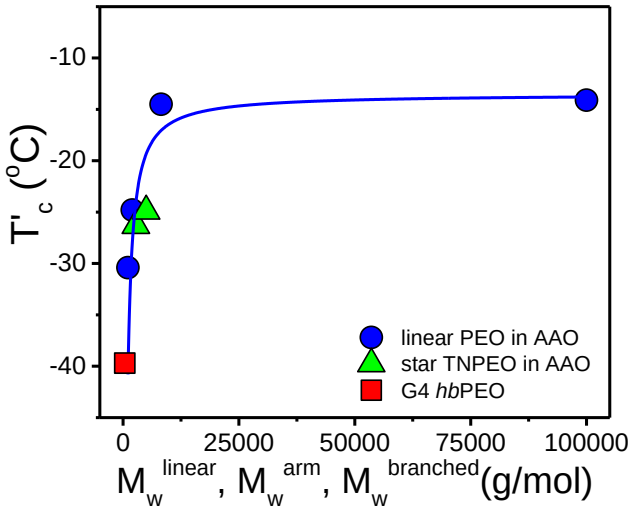

nucleation on the molecular weight of PEO in the limit $d \rightarrow \infty$ (d = AAO pore diameter). Spheres: the $T_c'(d)$ profiles were obtained from DSC scans of linear PEO inside AAO at a cooling rate of 10 K/min. Triangles: star-shaped PEOs (in the limit $d \rightarrow \infty$) obtained from DSC at a cooling rate of 10 K/min. Square: current studied G4 *hb*PEO (in the limit $d \rightarrow \infty$) obtained from DSC at a cooling rate of 2 ºC/min. The solid line is a fit using the Fox−Flory equation for linear PEOs located within self-ordered AAO templates.

6.4 Conclusion

The crystallization of PEO in hyperbranched poly(ethylene oxide)-*co*-poly(glycerol) random copolymers with different content of glycerol branching points is investigated both in the bulk and under confinement within self-ordered AAOs. In bulk, the increase of glycerol content results in lower crystallization and melting temperatures and to decreased crystallinity. In the case of G9 *hb*PEO, bearing the highest branching, additional confinement effects further suppress the crystallization temperature by some 40 ºC relative to G4 *hb*PEO. Hyperbranched polymers fully infiltrate AAO nanopores. However, the dynamics of capillary imbibition was *slower* than predicted by the Lucas-Washburn equation. This reduced imbibition velocity can be accounted for by a dead layer thickness of ~19 nm comprising immobilized polymer chains at the pore walls. Under confinement a transformation from heterogeneous nucleation in bulk G4 *hb*PEO, to homogeneous nucleation was observed. Furthermore, the homogeneous nucleation temperature of *hb*PEO agrees with that of linear and star PEOs once the branched molecular weight is used instead of the total molecular weight. It further indicates that in non-linear polymers long-range motions, like arm-retraction and branched point fluctuations are controlling the chain diffusion mechanism involved in the process of homogeneous nucleation. Besides, the segmental dynamics speed-up on confinement, reflecting a reduced glass temperature in *hb*PEO as compared to the bulk. The latter is in accord with the effects of interfacial energy of polymers in contact with alumina.

6.5 References

1. Movileanu, L.; Cheley, S.; Bayley, H., Partitioning of individual flexible polymers into a nanoscopic protein pore. *Biophysical journal* **2003,** *85* (2), 897-910.
2. Movileanu, L.; Bayley, H., Partitioning of a polymer into a nanoscopic protein pore obeys a simple scaling law. *Proceedings of the National Academy of Sciences* **2001,** *98* (18), 10137-10141.
3. Ellis, R. J.; Minton, A. P., Cell biology: join the crowd. *Nature* **2003,** *425* (6953), 27-28.
4. Knop, K.; Hoogenboom, R.; Fischer, D.; Schubert, U.S. Poly(ethylene glycol) in drug delivery: pros and cons as well as potential alternatives. *Angew. Chem. Int. Ed. Engl*. **2010,** *49*(36), 6288-308.
   (5) Herzberger, J. Niederer, K.; Pohlit, H.; Seiwert, J.; Worm, M.; Wurm, F.; Frey, H. Polymerization of Ethylene Oxide, Propylene Oxide and Other Alkylene Oxides: Synthesis, Novel Polymer Architectures and Bioconjugation. *Chem. Rev.* **2016**, *116* (4), 2170-2243.
5. Kainthan, R. K.; Gnanamani, M.; Ganguli, M.; Ghosh, T.; Brooks, D. E.; Maiti, S.; Kizhakkedathu, J. N., Blood compatibility of novel water soluble hyperbranched polyglycerol-based multivalent cationic polymers and their interaction with DNA. *Biomaterials* **2006,** *27* (31), 5377-5390.
6. Kremer, F., *Dynamics in geometrical confinement*. Springer International Publishing, 2014.
7. Masuda, H.; Fukuda, K., Ordered metal nanohole arrays made by a two-step replication of honeycomb structures of anodic alumina. *Science* **1995,** *268* (5216), 1466.
8. Masuda, H.; Hasegwa, F.; Ono, S., Self-Ordering of Cell Arrangement of Anodic Porous Alumina Formed in Sulfuric Acid Solution. *Journal of the Electrochemical Society* **1997,** *144* (5), L127-L130.
9. Masuda, H.; Yada, K.; Osaka, A., Self-ordering of cell configuration of anodic porous alumina with large-size pores in phosphoric acid solution. *Japanese Journal of Applied Physics* **1998,** *37* (11A), L1340.
10. Shin, K.; Woo, E.; Jeong, Y. G.; Kim, C.; Huh, J.; Kim, K.-W., Crystalline structures, melting, and crystallization of linear polyethylene in cylindrical nanopores. *Macromolecules* **2007,** *40* (18), 6617-6623.
11. Duran, H.; Steinhart, M.; Butt, H.-J.; Floudas, G., From heterogeneous to homogeneous nucleation of isotactic poly(propylene) confined to nanoporous alumina. *Nano letters* **2011,** *11* (4), 1671-1675.
12. Maiz, J.; Martin, J.; Mijangos, C., Confinement Effects on the Crystallization of Poly(ethylene oxide) Nanotubes. *Langmuir* **2012,** *28* (33), 12296-12303.
13. Michell, R. M.; Lorenzo, A. T.; Müller, A. J.; Lin, M.-C.; Chen, H.-L.; Blaszczyk-Lezak, I.; Martin, J.; Mijangos, C., The crystallization of confined polymers and block copolymers infiltrated within alumina nanotube templates. *Macromolecules* **2012,** *45* (3), 1517-1528.
14. Nakagawa, S.; Kadena, K.-i.; Ishizone, T.; Nojima, S.; Shimizu, T.; Yamaguchi, K.; Nakahama, S., Crystallization behavior and crystal orientation of poly (ε-caprolactone) homopolymers confined in nanocylinders: effects of nanocylinder dimension. *Macromolecules* **2012,** *45* (4), 1892-1900.
15. Suzuki, Y.; Duran, H.; Steinhart, M.; Butt, H.-J.; Floudas, G., Homogeneous crystallization and local dynamics of poly (ethylene oxide)(PEO) confined to nanoporous alumina. *Soft Matter* **2013,** *9* (9), 2621-2628.

16. Suzuki, Y.; Duran, H.; Akram, W.; Steinhart, M.; Floudas, G.; Butt, H.-J., Multiple nucleation events and local dynamics of poly(ε-caprolactone)(PCL) confined to nanoporous alumina. *Soft Matter* **2013,** *9* (38), 9189-9198.
17. Maiz, J.; Schäfer, H.; Trichy Rengarajan, G.; Hartmann-Azanza, B.; Eickmeier, H.; Haase, M.; Mijangos, C.; Steinhart, M., How gold nanoparticles influence crystallization of polyethylene in rigid cylindrical nanopores. *Macromolecules* **2013,** *46* (2), 403-412.
18. Guan, Y.; Liu, G.; Gao, P.; Li, L.; Ding, G.; Wang, D., Manipulating crystal orientation of poly (ethylene oxide) by nanopores. *ACS Macro Letters* **2013,** *2* (3), 181-184.
19. Suzuki, Y.; Duran, H.; Steinhart, M.; Butt, H.-J.; Floudas, G., Suppression of Poly (ethylene oxide) Crystallization in Diblock Copolymers of Poly (ethylene oxide)-b-poly (ε-caprolactone) Confined to Nanoporous Alumina. *Macromolecules* **2014,** *47* (5), 1793-1800.
20. Michell, R. M.; Blaszczyk-Lezak, I.; Mijangos, C.; Müller, A. J., Confined crystallization of polymers within anodic aluminum oxide templates. *Journal of Polymer Science Part B: Polymer Physics* **2014,** *52* (18), 1179-1194.
21. Suzuki, Y.; Steinhart, M.; Kappl, M.; Butt, H.-J.; Floudas, G., Effects of polydispersity, additives, impurities and surfaces on the crystallization of poly(ethylene oxide)(PEO) confined to nanoporous alumina. *Polymer* **2016,** *99*, 273-280.
22. Yao, Y.; Sakai, T.; Steinhart, M.; Butt, H.-J.; Floudas, G., Effect of poly(ethylene oxide) architecture on the bulk and confined crystallization within nanoporous alumina. *Macromolecules* **2016,** *49* (16), 5945-5954.
23. Yao, Y.; Alexandris, S.; Henrich, F.; Auernhammer, G.; Steinhart, M.; Butt, H.-J.; Floudas, G., Complex dynamics of capillary imbibition of poly(ethylene oxide) melts in nanoporous alumina. *The Journal of Chemical Physics* **2017,** *146* (20), 203320.
24. Li, L.; Liu, J.; Qin, L.; Zhang, C.; Sha, Y.; Jiang, J.; Wang, X.; Chen, W.; Xue, G.; Zhou, D., Crystallization kinetics of syndiotactic polypropylene confined in nanoporous alumina. *Polymer* **2017,** *110*, 273-283.
25. Alexandris, S.; Papadopoulos, P.; Sakellariou, G.; Steinhart, M.; Butt, H.-J.; Floudas, G., Interfacial Energy and Glass Temperature of Polymers Confined to Nanoporous Alumina. *Macromolecules* **2016,** *49* (19), 7400-7414.
26. Krutyeva, M.; Martin, J.; Arbe, A.; Colmenero, J.; Mijangos, C.; Schneider, G.J.; Unruh, T.; Su, Y.; Richter, D. Neutron scattering study of the dynamics of a polymer melt under nanoscopic confinement. *The Journal of Chemical Physics* **2009**, *131*, 174901.
27. Hajji, C.; Haag, R., Hyperbranched polymers as platforms for catalysts. *Dendrimer Catalysis* **2006**, *20*, 149-176.
28. Stiriba, S. E.; Frey, H.; Haag, R., Dendritic polymers in biomedical applications: from potential to clinical use in diagnostics and therapy. *Angewandte Chemie International Edition* **2002,** *41* (8), 1329-1334.
29. Leibig, D.; Seiwert, J.; Liermann, J.C.; Frey, H. Copolymerization Kinetics of Glycidol and Ethylene Oxide, Propylene Oxide and 1,2-Butylene Oxide: From Hyperbranched to Multi-Arm Star Topology. *Macromolecules* **2016**, *49*, 7767-7776.
30. Wurm, F.; Nieberle, J.; Frey, H., Double-hydrophilic linear-hyperbranched block copolymers based on poly (ethylene oxide) and poly (glycerol). *Macromolecules* **2008,** *41* (4), 1184-1188.
31. Wurm, F.; Klos, J.; Räder, H. J.; Frey, H., Synthesis and noncovalent protein conjugation of linear-hyperbranched PEG-poly(glycerol) α,ω_n-telechelics. *Journal of the American Chemical Society* **2009,** *131* (23), 7954-7955.

32. Wilms, D.; Schömer, M.; Wurm, F.; Hermanns, M. I.; Kirkpatrick, C. J.; Frey, H. Hyperbranched PEG by random copolymerization of ethylene oxide and glycidol. *Macromol. Rapid Commun.* **2010**, *31* (20), 1811–1815.
33. Perevyazko, I.; Seiwert, J.; Schömer, M.; Frey, H.; Schubert, U. S.; Pavlov, G. M. Hyperbranched Poly(ethylene glycol) Copolymers: Absolute Values of the Molar Mass, Properties in Dilute Solution, and Hydrodynamic Homology. *Macromolecules* **2015**, *48* (16), 5887–5898.
34. Kremer, F.; Schönhals, A., Broadband dielectric spectroscopy. *Berlin: Springer* **2002**.
35. Floudas, G.; Paluch, M.; Grzybowski, A.; Ngai, K., *Molecular dynamics of glass-forming systems: effects of pressure*. Springer Science & Business Media: 2010; Vol. 1.
36. Floudas, G., in Dielectric Spectroscopy. *Polymer Science: A Comprehensive Reference, Elsevier BV, Amsterdam, ed. K. Matyjaszewski and M. Möller*, **2012,** *2.32*, 825–845.
37. Havriliak, S.; Negami, S., A complex plane representation of dielectric and mechanical relaxation processes in some polymers. *Polymer* **1967,** *8*, 161-210.
38. Lucas, R. Ueber das Zeitgesetz des Kapillaren Aufstiegs von Flüssigkeiten. *Kolloid Z.* **1918**, *23*, 15-22.
39. Washburn, E.W., The dynamics of capillary flow. *Physical Review* **1921,** *17*, 273-283.
40. Yao, Y.; Butt, H.-J.; Zhou, J.; Doi, M.; Floudas, G. in preparation
41. Takahashi, Y.; Sumita, I.; Tadokoro, H. Structural studies of polyethers. IX. Planar zigzag modification of poly(ethylene oxide). *J. Polym. Sci., Polym. Phys. Ed.* **1973**, *11*, 2113-2122.
42. Suzuki, Y.; Duran, H.; Steinhart, M.; Kappl, M.; Butt, H.-J.; Floudas, G. Homogeneous nucleation in predominantly cubic ice confined in nanoporous aloumina. *Nano Lett.* **2015**, *15*, 1987-1992.
43. Duran, H.; Hartmann-Azanza, B.; Steinhart, M.; Gehrig, D.; Laquai, F.; Feng, X.; Müllen, K.; Butt, H.-J.; Floudas, G. Arrays of Aligned Supramolecular Wires by Macroscopic Orientation of Columnar-Discotic Mesophases. *ACS Nano* **2012**, *6*, 9359.
44. Sillars, R., The properties of a dielectric containing semiconducting particles of various shapes. *Institution of Electrical Engineers-Proceedings of the Wireless Section of the Institution* **1937**, *12* (35), 139-155.
45. Von Hippel, A. R., Dielectrics and waves. *New York: Wiley* **1954**.
46. Samet, M.; Levchenko, V.; Boiteux, G.; Seytre, G.; Kallel, A.; Serghei, A., Electrode polarization vs. Maxwell-Wagner-Sillars interfacial polarization in dielectric spectra of materials: Characteristic frequencies and scaling laws. *The Journal of Chemical Physics* **2015**, *142* (19), 194703.
47. Napolitano, S.; Wübbenhorst, M. Dielectric signature of a dead layer in ultrathin films of a non-polar polymer. *J. Phys. Chem. B* **2007**, *111*, 9197.
48. Hamilton, B.D.; Ha, J.-M.; Hillmyer, M.A.; Ward, M.D. Manipulating crystal growth and polymorphism by confinement in nanoscale crystallization chambers. *Accounts of Chemical Research* **2012**, *45*, 414-423.
49. Lauritzen, J.I.; Hoffman, J.D. Theory of formation of polymer crystals with folded chains in dilute solution. *J. Res. Nat. Bur. Std* **1960**, *64A*, 73.

6.6 Supporting information

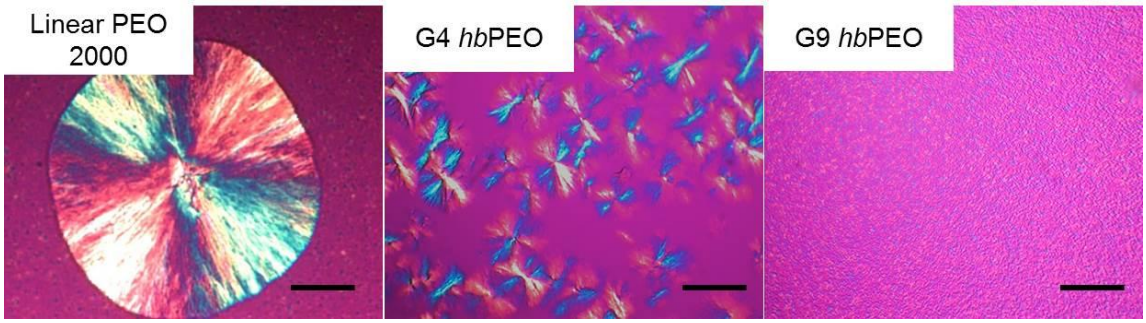

Figure S1. POM images of linear PEO (with a molecular weight of 2460 g/mol), G4 *hb*PEO, and G9 *hb*PEO compared at the same undercooling (ΔT = 26 ºC). The scale bar represents 100 μm

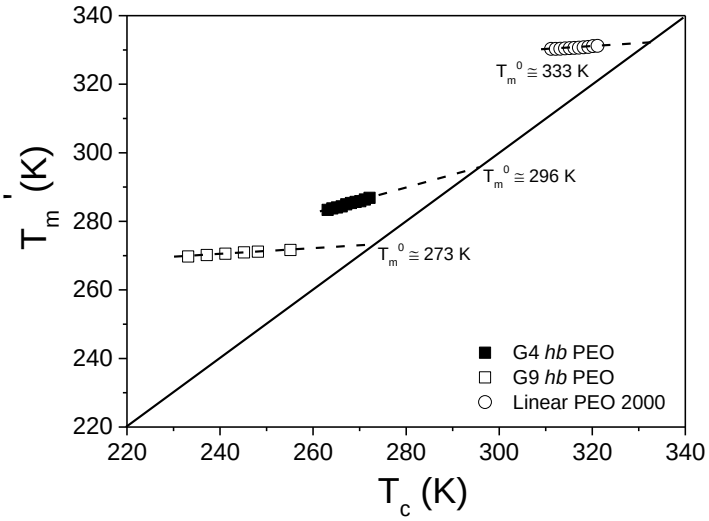

Figure S2. Plot of the apparent melting temperature (T_m') as a function of the crystallization temperature (T_c). The solid line has slope of unity, and the equilibrium melting temperature (T_m^o) is obtained from a linear extrapolation following the Hoffman-Weeks equation (dashed line). The different symbols correspond to (circles): linear PEO (M_w=2000 g/mol); (filled squares): G4 *hb*PEO and (open squares): G9 *hb*PEO.

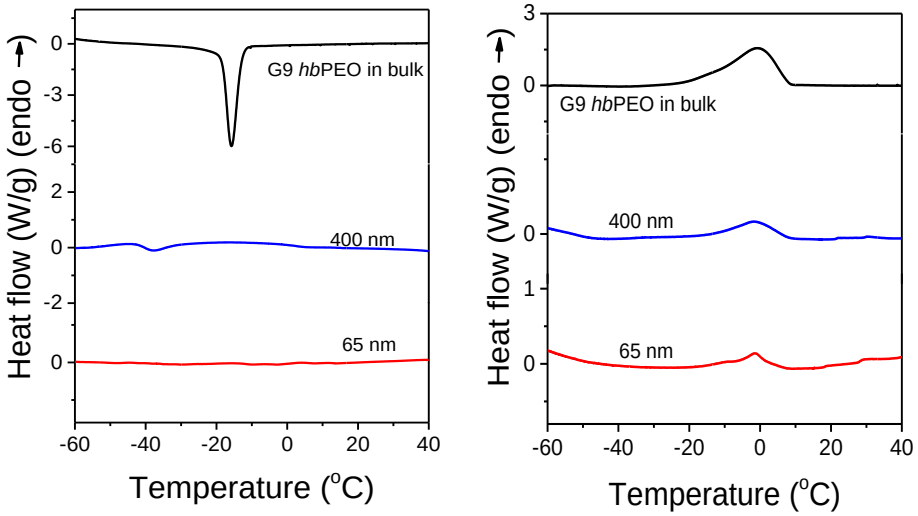

Figure S3. Cooling (left) and heating (right) thermograms of G9 *hb*PEO located inside self-ordered AAO with different pore diameters (heating/cooling rates of 2 °C/min).

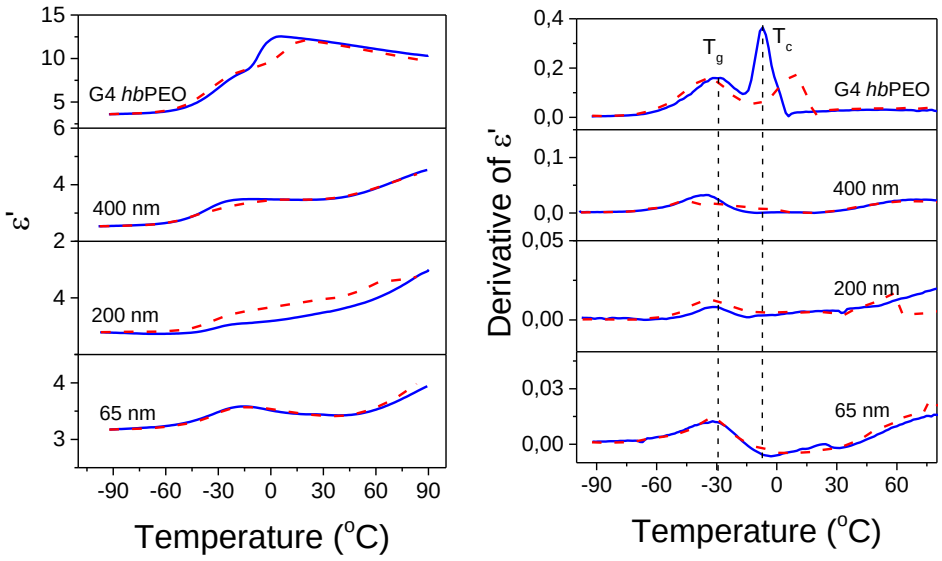

Figure S4. (Left) Temperature dependence of the dielectric permittivity of G4 *hb*PEO located within AAO with different pore diameters obtained on cooling (blue curves) and subsequent heating (red curves) with a rate of 5 °C/min. (Right) Derivative of dielectric permittivity, $|d\varepsilon'/dT|$, as a function of temperature for the data shown in the left.

Maxwell-Wagner-Sillars polarization

Inhomogeneous dielectrics exhibit an additional dielectric process whose magnitude, absolute time scale and temperature dependence reflect on the geometry of phases as well as differences in conductivities and permittivities of constituent phases.[1,2] Maxwell and Wagner first employed the simplest possible model of an inhomogeneous dielectric, consisting of plane sheets of two materials having different conductivities and permittivities.[3] Later, Sillars employed different geometries to show that the amplitude and time scale of this mechanism depends on the geometry of phases.[4,5] More recently, Serghei et al. obtained scaling laws for the characteristic frequencies of MWS polarization and of interfacial polarization of inhomogeneous dielectrics. [6]

The present geometry of uniform parallel channels filled with a conducting polymer embedded in a matrix of AAO where the electric field runs along the pore axes can be discussed in terms of an equivalent circuit composed of two layers connected in parallel (Scheme S1).

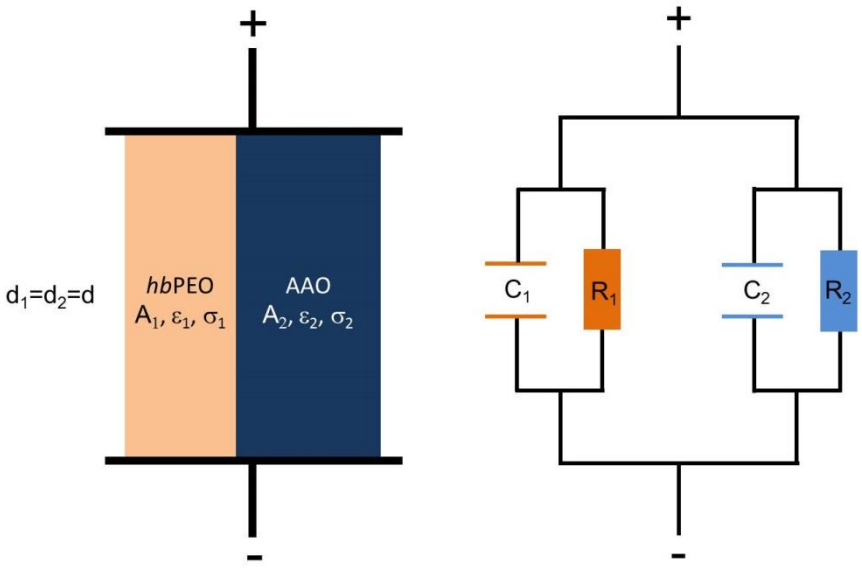

Scheme S1. (left) Two dielectric layers in parallel where D is the spacing, A_i, ε_i, and σ_i are the areas, permittivities, and conductivities of the layers. (right) The corresponding equivalent circuit.

Under these conditions,

$$V = V_1 = V_2 \tag{S1}$$

$$I = I_1 + I_2 \tag{S2}$$

$$I_1 = C_1 \frac{dV_1}{dt} + \frac{V_1}{R_1} \tag{S3}$$

$$I_2 = C_2 \frac{dV_2}{dt} + \frac{V_2}{R_2}$$

Solving these equations for I_1 and I_2 we obtain for the relaxation time

$$\tau = \frac{C_1 C_2}{C_1 + C_2}(R_1 + R_2) \tag{S4}$$

Using the geometrical characteristics

$$C_1 = \varepsilon_f \varepsilon_1 \frac{A_1}{d} \ , \ R_1 = \frac{d}{A_1 \sigma_1} \tag{S5}$$

$$C_2 = \varepsilon_f \varepsilon_2 \frac{A_2}{d} \ , \ R_2 = \frac{d}{A_2 \sigma_2}$$

results to the following expression for the characteristic relaxation time of the composite

$$\tau = \varepsilon_f \frac{\varepsilon_1 \varepsilon_2}{A_1 \varepsilon_1 + A_2 \varepsilon_2} \left(\frac{A_1 \sigma_1 + A_2 \sigma_2}{\sigma_1 \sigma_2} \right) \tag{S6}$$

Using typical permittivity and conductivity values for the polymer (ε_1=10, σ_1=10^{-6} S/cm) and AAO templates (ε_2=2.7, σ_2=10^{-13} S/cm) result in the data shown in Fig. S5 (open triangles). Although the model characteristic times are in the vicinity of the measured times their temperature dependence is different. In the parallel model (e.g. in contrast to the series model), the temperature dependence of MWS times is dictated by the AAO conductivity (as opposed to the polymer conductivity in the series model) giving rise to a weaker temperature dependence. Deviations from the experimental times can be the result of an additional contribution from the interface at the bottom of pores where AAO is connected in series with the polymer.

According to the series model:

$$\tau = \frac{R_1 R_2}{R_1 + R_2}(C_1 + C_2)$$

$$C_1 = \varepsilon_f \varepsilon_1 \frac{A}{d_1} \ , \ R_1 = \frac{d_1}{A \sigma_1} \tag{S7}$$

$$C_2 = \varepsilon_f \varepsilon_2 \frac{A}{d_2} \ , \ R_2 = \frac{d_2}{A\sigma_2}$$

giving rise to $$\tau = \varepsilon_f \left(\frac{d_2\varepsilon_1 + d_1\varepsilon_2}{\sigma_1 d_2 + \sigma_2 d_1}\right) \quad \text{(S8)}$$

With d_1=100 μm and d_2=0.07 nm it results to the inverted triangles shown also in Fig. S5.

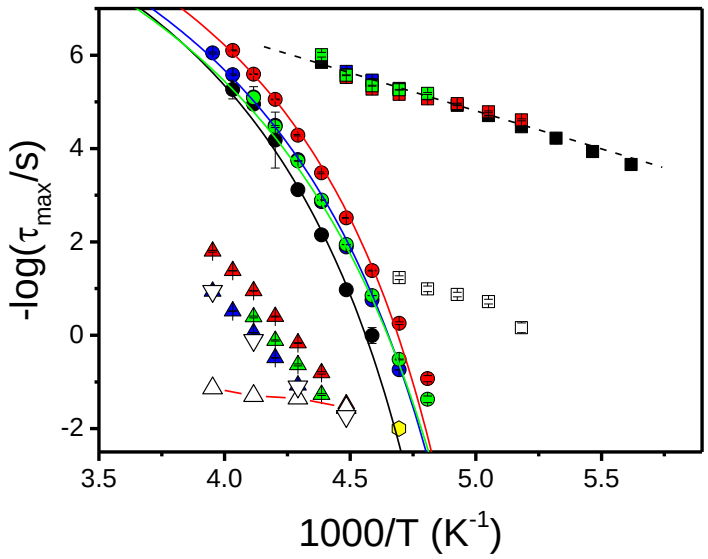

Figure S5. Relaxation times at maximum loss corresponding to the α-(filled circles) and β- (filled squares) and MWS (filled triangles) processes of bulk G4 *hb*PEO (black symbols) and G4 *hb*PEO located inside self-ordered AAO pores with pore diameters; 400 nm (red), 200 nm (blue) and 65 nm (green). Solid and dashed lines are fits to the VFT and Arrhenius equations, respectively. The yellow hexagon is the bulk T_g (obtained from DSC). MWS model predictions based on a two-layer model where the layers are connected in parallel (series) are shown by the open right (inverted) triangles (data applicable to 65 nm pores).

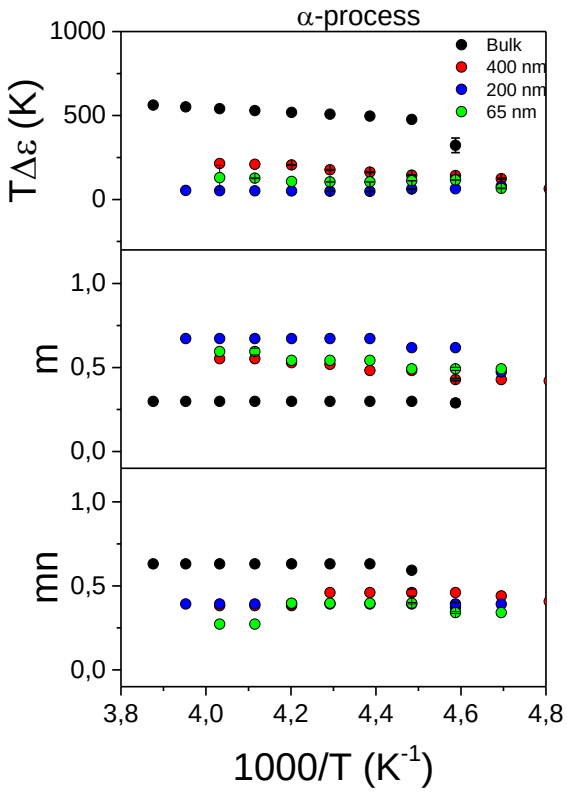

Figure S6. Summary of the Havrialiak-Negami fitting parameters obtained for the α-process of G4 *hb*PEO.

References

1. Kremer, F.; Schönhals, A., Broadband dielectric spectroscopy. *Berlin: Springer* **2002**.
2. Richert, R., Dielectric spectroscopy and dynamics in confinement. *The European Physical Journal-Special Topics* **2010**, *189* (1), 37-46.
3. Wagner, K. W., Erklärung der dielektrischen Nachwirkungsvorgänge auf Grund maxwellscher Vorstellungen. *Electrical Engineering (Archiv für Elektrotechnik)* **1914**, *2*(9), 371-387.
4. Sillars, R., The properties of a dielectric containing semiconducting particles of various shapes. *Institution of Electrical Engineers-Proceedings of the Wireless Section of the Institution* **1937**, *12* (35), 139-155.
5. Von Hippel, A. R., Dielectrics and waves. *New York: Wiley* **1954**.
6. Samet, M.; Levchenko, V.; Boiteux, G.; Seytre, G.; Kallel, A.; Serghei, A., Electrode polarization vs. Maxwell-Wagner-Sillars interfacial polarization in dielectric spectra of materials: Characteristic frequencies and scaling laws. *The Journal of chemical physics* **2015**, *142* (19), 194703.

Chapter 7. Homogeneous Nucleation of Ice Confined in Hollow Silica Spheres

This chapter has been published as a research paper in Macromolecules. It is reprinted here with kind permission of American Chemical Society.

Yang Yao, Pia Ruckdeschel, Robert Graf, Hans-Jürgen Butt, Markus Retsch, and George Floudas
The Journal of Physical Chemistry B 121, 306 (2016).
DOI: 10.1021/acs.jpcb.6b11053

Abstract

Ice nucleation is studied in hollow silica spheres. These hierarchical materials comprise ~3 nm pores within the silica network, which are confined to a ~20 nm shell of a hollow sphere (with diameters in the range ~190-640 nm). The multiple length scales involved in hollow silica spheres affect the ice nucleation mechanism. We find homogeneous nucleation inside the water filled capsules, whereas heterogeneous nucleation prevails in the surrounding dispersion medium. We validate our findings for a series of hollow sphere sizes and demonstrate the absence of homogeneous nucleation in case of polystyrene-silica core-shell particles. The present findings shed new light on the interplay between homogeneous and heterogeneous nucleation of ice with possible implications in undercooled reactions and the storage of reactive or biologically active substances.

7.1 Introduction

Water, the most important liquid, behaves differently under confinement.[1-5] Bulk water freezes due to impurities via *heterogeneous* nucleation. In contrast, confined water can be supercooled to -38 ^{o}C or even below, with an intrinsic process known as *homogeneous* nucleation. Understanding and eventually controlling supercooling via exerting control over the nucleation mechanism of ice is important in several fields: from atmospheric chemistry (by controlling cloud formation and precipitation) to anti-icing surfaces, to construction materials (avoiding ice formation is essential for the durability of building materials like cement) and to molecular biology (storage of biologically relevant substances). A common route towards supercooling is by confining water in micrometer to nanometer scales that limits the growth of crystals formed by heterogeneous nucleation and thus reduces the effect of heterogeneous nucleation. Of importance here have been measurements of ice nucleation in supercooled water microdroplets;[6-9] these experiments reported a freezing rate proportional to the droplet volume with a proportionality constant (*i.e.*, the nucleation rate) maximized at -38 ^{o}C.[6-8] However, despite fundamental importance in science and technology control of heterogeneous, and more importantly, of homogeneous nucleation of ice at atmospheric conditions remains a challenge. Recent efforts focused on confining water within the nanometer size cavities of porous silica materials, including sol-gel disordered silica, MCM-41 and SBA-15.[10-19] They have shown suppressed crystallization of water below the bulk freezing temperature -depending on the pore size- according to the Gibbs-Thomson equation. Furthermore, a fraction of molecules at the pore surface remained liquid-like through hydrogen bonding between water molecules and the silica surface. Other studies demonstrated the sensitivity of this interfacial water to details of surface chemistry by, e.g., inducing orientation order of water molecules in contact with the surface.[19,20]

In this work we employ a new confining medium composed of hollow silica spheres as the means to control the nucleation mechanism of ice. It is composed of monodisperse hollow silica (HS) spheres, which are dispersed in an aqueous phase. The hollow spheres can be regarded as capsules and represent a well-defined porous material with a number of interesting thermal, optical and mechanical properties.[21-23] These hierarchical materials exhibit structure over several length scales; they comprise micropores within the silica network (with a size of ~3 nm), which are then confined to a thin shell (~20 nm) of a hollow sphere (~190-640 nm). We hypothesize that these

multiple length scales may play a role on the nucleation mechanism of water and study ice nucleation within a series of HS having comparable microporous cavities and shell thickness but variable sphere radii resulting in different inner pore volumes. We provide clear evidences for well-separated nucleation mechanisms of ice at higher and lower supercoolings originating, respectively, from water molecules located inside and outside the spheres. Lastly, the results on the nucleation mechanism are compared to the mechanism of ice formation within another well-defined porous material, namely self-ordered anodic aluminum oxide (AAO), having a single pertinent length scale, the pore diameter. [24-26]

7.2 Experimental details

Materials. Styrene (≥ 99 %, Aldrich), 2,2'-Azobis(2-methylpropionamidine) dihydrochloride (AIBA; 97 %, Aldrich), 2-Methacryloxy-ethyltrimethylammonium chloride (MTC; 70 % solution in water, Polyscience), Polyvinylpyrrolidone K30 (PVP; M_w ~ 55 kg/mol, Aldrich), Tetraethyl orthosilicate (TEOS; ≥ 99 %, Aldrich) and Ammonium hydroxide solution (30 - 33 % in water, Aldrich) were used as received. 2,2′-Azobis(2-methylpropionitrile) (AIBN; ≥98.0%, Aldrich) was recrystallized from methanol. Ethanol (EtOH) was used in technical grade and water was taken from a *Millipore Direct Q3UV* unit for the entire synthesis and purification steps.

Synthesis of hollow silica spheres. The synthesis of hollow silica spheres comprises three steps: (1) Synthesis of polystyrene particles, (2) Coating of polystyrene template particles with a silica shell *via* a modified Stoeber process and (3) Calcination of the core-shell particles to remove the polystyrene core.

(1) Synthesis of polystyrene particles

Two different techniques were used to obtain monodisperse polystyrene particles. Smaller particles (140 – 275 nm) were obtained by emulsifier-free emulsion polymerization[103] and larger particles (495 – 580 nm) by dispersion polymerization. In the following, the synthesis of the smallest and largest particles is described.

Emulsifier-free emulsion polymerization: The synthesis was carried out in a three-necked flask, equipped with a reflux condenser and a gas inlet, which allows a slight argon flow during the synthesis. First, 100 mL water, 13 mL styrene, 300 µL MTC and 0.9 g PVP were heated to 70 °C at a stirring rate of 850 rpm with a magnetic stirrer egg. After an equilibration time of 30 min, 0.3

g AIBA, dissolved in 20 mL water, were added to initiate the polymerization. After nucleation, the stirring speed was reduced to 450 rpm and the reaction was carried out overnight.

Dispersion polymerization: The dispersion polymerization was carried out in a single-neck flask connected to a KPG stirrer rotating at a rate of 60 rpm. First, 130 mL ethanol (EtOH), 14 mL water, 10 mL styrene and 5 g PVP were purged with argon, while heating the reaction mixture to 75 °C. After an equilibration time of 30 min, the gas inlet was removed, 0.136 g AIBN, dissolved in 6 mL ethanol, were added to initiate the polymerization and the stirrer was set to 60 rpm. After 1.5 h, 400 µL MTC were added. The reaction was carried out overnight. For both polystyrene synthesis methods, different sizes can be obtained by adjusting the amount of comonomer, initiator and the ethanol/water ratio in the dispersion polymerization.

(2) Silica coating of the polystyrene particles

The silica coating was achieved by a Stoeber condensation process.[104] In the following, the coating process is exemplary described for the smallest particles: 84.8 vol.% EtOH, 6.7 vol.% aqueous polystyrene dispersion (8.4 wt.%) and 6.3 vol.% NH_4OH solution were stirred at 400 rpm in a single-neck flask. After stepwise addition of 2.2 vol.% TEOS the reaction was stirred overnight at room temperature. The core/shell particles were purified by repeated centrifugation and redispersed in water.

(3) Calcination of polystyrene-silica core-shell particles

In order to obtain hollow spheres, the samples were dried and calcined in a furnace (Nabertherm L5/11/P33) at 500 °C in air for 12 h. The hollow spheres were redispersed in water using mild sonication in a sonication bath.

Overall five different hollow silica nanoparticles and one core-shell particle as reference sample were synthesized. The concentration of the dispersions were adjusted between 2.5 and 10.7 wt.%. For sample HS-533, dispersions with a small (2.5 wt.%, HS-533-s) and a large (7.5 wt.%, HS-533-l) concentration were additionally prepared. The data for the synthesized particles and the concentrations are shown in Table 1.

Characterization. Transmission electron microscopy (TEM) images were taken on a Zeiss CEM 902 instrument in bright field imaging mode at an acceleration voltage of 80 kV. Nitrogen sorption measurements were carried out on a Quantachrome Autosorb AS-1 pore analyzer at 77 K. Prior to the measurements, all sample were preconditioned to remove water residues. The hollow silica

nanoparticle samples were preconditioned in a vacuum at 350 °C for 12 hours and the core-shell particle sample was preconditioned in a vacuum at 90 °C for 20 hours. For the analysis, the Quantachrome ASiQ v3.0 software was used. The specific surface areas were calculated using the BET method and the DFT method. Pore volumes and pore size distributions were obtained by applying the nonlocal density functional theory (NLDFT) adsorption model for silica materials with cylindrical or spherical pore geometry.

Table 1. Summary of the results obtained from TEM analysis and corresponding data based on individual hollow silica nanoparticle as well as data based on dispersion.

	TEM data[a]		Data based on individual hollow silica nanoparticle[b]		Data based on dispersion[c]	
	d [nm]	t [nm]	V_{pore} [nm³]	S_{pore}/V_{pore} [nm^{-1}]	V_{in}/V_{ex}	wt.% [%]
HS-185	185.1 ± 3.7	20.6 ± 1.3	$1.6 \cdot 10^6$	0.042	0.048	10.7
HS-257	256.2 ± 4.7	15.6 ± 1.0	$6.0 \cdot 10^6$	0.027	0.082	7.9
HS-341	340.7 ±7.5	20.1 ±1.2	$1.4 \cdot 10^7$	0.020	0.062	5.8
HS-533	533.4 ±12.5	23.5 ± 1.6	$6.0 \cdot 10^7$	0.012	0.071	4.8
HS-533-s	533.4 ±12.5	23.5 ± 1.6	$6.0 \cdot 10^7$	0.012	0.037	2.5
HS-533-l	533.4 ±12.5	23.5 ± 1.6	$6.0 \cdot 10^7$	0.012	0.116	7.5
HS-637	636.6 ±13.4	21.9 ± 1.8	$1.1 \cdot 10^8$	0.010	0.087	4.3
CS-261	260.8 ± 4.6	~16	0	0	0	10.8

[a] d: Diameter, t: Shell thickness, [b] V_{pore}: Inner pore volume of a single hollow silica nanoparticle, S_{in}: Inner surface area per particle, [c] V_{in}: Inner pore volume in 1 cm³, V_{ex}: Outer volume in 1 cm³, wt.%: Weight percentage.

Table 2. Summary of the results from nitrogen sorption analysis.

	N_2 sorption analysis		
	BET SA[a] [m²/g]	DFT SA[b] [m²/g]	V_{pore}[c] [cm³/g]
HS-185	170.3	151.1	0.137
HS-257	167.3	160.7	0.182
HS-341	170.6	161.1	0.166
HS-533	289.5	263.9	0.256
HS-533-s	289.5	263.9	0.256
HS-533-l	289.5	263.9	0.256
HS-637	189.3	179.6	0.213
CS-261	24.6	20.5	0.037

[a] BET SA: Surface area calculated by using BET method, [b] DFT SA: Surface area obtained from DFT analysis using NLDFT model on silica at 77 K, [c] V_{pore}: Pore volume obtained from DFT analysis using NLDFT model on silica at 77 K.

Differential scanning calorimetry (DSC). Thermal analysis was carried out using a Mettler Toledo differential scanning calorimeter (DSC-822). DSC traces of bulk water were acquired using an empty pan as reference. Samples were weighed with a Mettler Toledo AX205 balance. Subsequently, 10 mg of water/HS solution was sealed in aluminum pans (100 μl). All samples were first cooled at a rate of 50 °C/min from ambient temperature to -100 °C, and then heated to 30 °C at the same rate under a nitrogen atmosphere. In a second experiment, the rate dependence of the melting and crystallization temperatures was investigated for water/HS spheres with a diameter of 533 nm. In this experiment, samples were heated to 100 °C and DSC cooling/heating curves were obtained with rates of 30, 10, 5 and 2 °C/min.

Dielectric Spectroscopy (DS). Dielectric measurements were performed at temperatures in the range of -90 °C to 30 °C, at atmospheric pressure, under isochronal conditions (f=1 MHz) using a Novocontrol Alpha frequency analyzer (frequency range from 10^{-2} to 10^{6} Hz) as a function of temperature. For bulk water, the DS measurements were carried out with a Novocontrol cylindrical cell with electrodes of 10 mm in diameter and sample thickness of 1cm. In all cases, the complex dielectric permittivity $\varepsilon^*=\varepsilon'-i\varepsilon''$, where ε' is the real and ε'' is the imaginary part, was obtained at 1 MHz. The dielectric function of heterogeneous dielectric comprising a matrix (m) (e.g., water), an interfacial layer (l) (e.g., silica) and filler (f) (e.g., water) contributions are given by an effective medium approach as[3]:

$$\varepsilon_c^* = \frac{\varepsilon_f^*\varphi_f + \varepsilon_l^*\varphi_l R + \varepsilon_m^*\varphi_m S}{\varphi_f + \varphi_l R + \varphi_m S}$$

$$R = \frac{(1-n)\varepsilon_l^* + n\varepsilon_f^*}{\varepsilon_l^*}$$

$$S = \frac{\left[n\varepsilon_l^* + (1-n)\varepsilon_m^*\right]\left[n\varepsilon_f^* + (1-n)\varepsilon_l^*\right] + dn(1-n)(\varepsilon_l^* - \varepsilon_m^*)(\varepsilon_f^* - \varepsilon_l^*)}{\varepsilon_l^*\varepsilon_m^*} \quad (1)$$

Here $d=\varphi_f/(\varphi_f+\varphi_l)$, and n is the depolarization factor of the filler particle in the field direction. In the present case, n=1/3 and $\varepsilon_l^* = \varepsilon_l' = 3.8$. By further assuming $\varepsilon'_{water}=82$ and $\varepsilon'_{ice}=3.2$ we obtain for

the composite ε'_c=73 and 3.7 for water and ice, respectively. These values are very close to the experimentally measured values of permittivity at high and low temperatures.

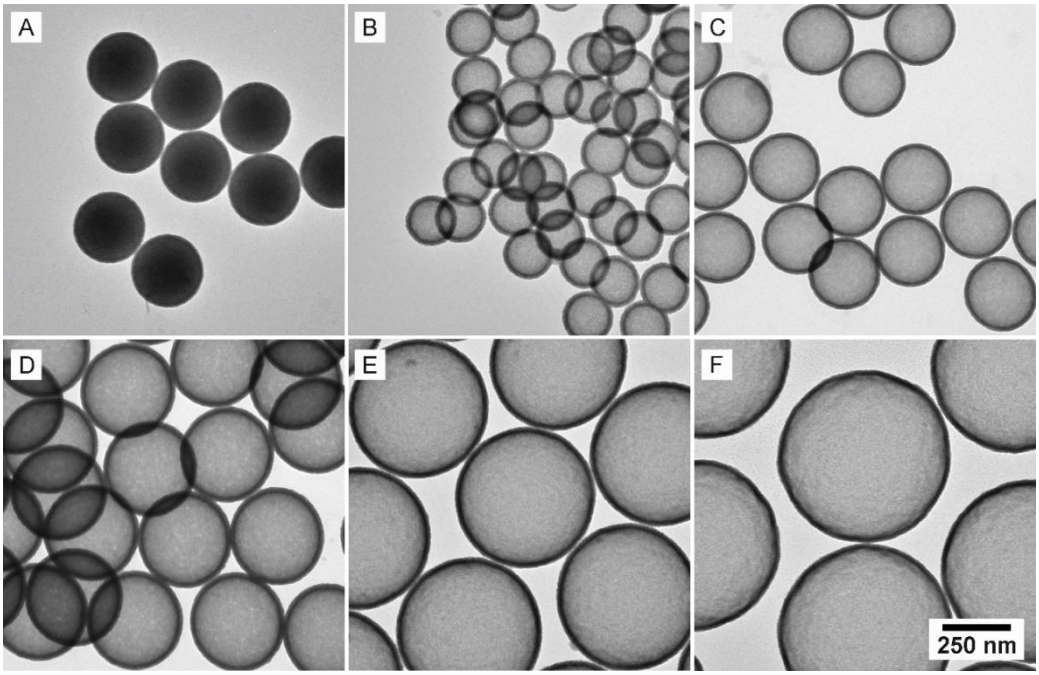

Figure 1. TEM images of polystyrene-silica core-shell particles (A) CS-261 and silica hollow spheres (B) HS-185, (B) HS-256, (C) HS-341, (D) HS-533 and (E) HS-637.

^{1}H MAS NMR Spectroscopy. ^{1}H MAS NMR spectroscopy measurements have been performed with a Bruker Avance III console operating at 850 MHz ^{1}H Larmor frequency in the temperature range between 230 and 290K at 20 KHz MAS spinning frequency. The measurements have been performed using a commercial MAS double resonance probe supporting 2.5 mm MAS rotors. The temperature has been calibrated using the temperature dependent ^{79}Pb chemical shift of lead nitrate as described in literature. A Bruker BCU II cooling unit has been used with a VT gas flow of 1500 l/h. The ^{1}H MAS NMR signals have been recorded using the EASY scheme, in order to suppress the ^{1}H probe back and the ringing artefacts of the rf coil.

7.3 Results and discussion

The synthesis of hollow silica spheres comprises three steps: synthesis of polystyrene particles, coating of polystyrene template particles with a silica shell *via* a modified Stoeber process and calcination of the core-shell particles to remove the polystyrene core.[21,27] With respect to

polystyrene particles two different techniques were used. Smaller particles (140 – 275 nm) were obtained by emulsifier-free emulsion polymerization and larger particles (495 – 580 nm) by dispersion polymerization. Silica coating of the polystyrene particles was achieved by a Stoeber condensation process followed by calcination. The characteristics of the hollow spheres (HS) are shown in Tables 1 and 2 and details are given in the methods section. As can be seen from transmission electron microscopy (TEM) measurements, the diameter, *d*, ranges from 185 nm to 637 nm whereas the shell thickness, *t*, is around 20 nm. TEM images of polystyrene-silica core-shell particles (CS) and hollow silica spheres (HS) are shown in Figure 1. They demonstrate nearly perfect uniformity. Characterization of the porous wall of HS spheres (pore volume and surface area) was made by nitrogen adsorption/de-sorption isotherms at 77 K. Pore volumes and pore size distributions were obtained by applying the nonlocal density functional theory (NLDFT) adsorption model for silica materials with cylindrical or spherical pore geometry (**Fig. S1**). The isotherms do not exhibit a pronounced hysteresis. Furthermore, microporous cavities with a diameter of about 2 - 3 nm were derived using the Fraissard model for cylindrical pore geometry.

DSC of ice formation in water/hollow spheres shows two exothermic peaks (Fig. 2): a major one in the temperature range from -19 to -22 ^{o}C and a smaller one in the range from -39 to -40 ^{o}C. For HS-637, the low temperature exothermic process appears at -24 ^{o}C. With the exception of HS-637, we assign the crystallization peaks at higher and lower temperatures to water crystallized outside/inside the HS spheres, respectively (see below). Water outside the HS spheres is the majority component and crystallization proceeds via heterogeneous nucleation at low supercooling. Naturally, the heat associated with heterogeneous nucleation is high (ΔH_E~271 J/g and 250 J/g, respectively, for HS-637 and HS-185). The respective heats for the homogeneous nucleation process are ΔH_O~4 J/g and 5 J/g. On the other hand, the melting process shows a broad featureless peak with heats of 319 and 274 J/g, respectively, for HS-637 and HS-185. These heats should be compared with the enthalpy of melting of bulk ice of 328 J/g.[28]

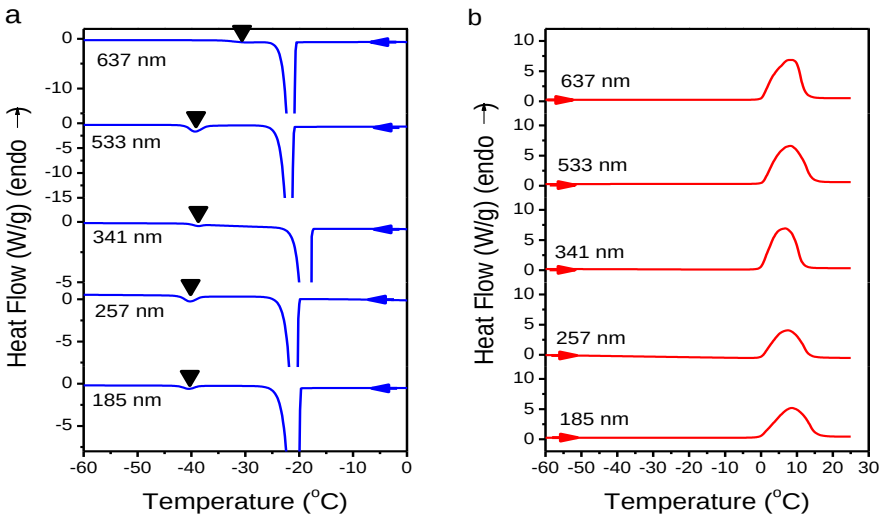

Figure 2. Differential scanning calorimetry traces of water/hollow silica spheres with different diameters obtained on (a) cooling and (b) heating with a rate of 10 °C/min. The vertical dashed line in (a) is a guide to the eye corresponding to the homogeneous nucleation temperature of confined water.

The higher crystallization temperature of HS-637 could be traced to less dense walls of this specific silica capsule. Furthermore, cracked spheres during dispersion via sonication and during repeated freeze-thawing have been more prominent in this case (the pressure-induced collapse of a thin spherical cell scales as Et^2/d, where E is the Young modulus).[23] This demonstrates that an intact and densely condensed silica shell is of paramount importance to support homogeneous nucleation in its interior. Such robust silica shells also withstand multiple freeze-thawing cycles without rupture or degradation.

Next the high dielectric permittivity of water and its temperature-dependence was employed as a fingerprint of the mechanism of ice nucleation. At a cooling rate of 5 °C/min, bulk water freezes at -7.9 °C. The bulk dielectric permittivity first increases on cooling and below freezing assumes a low value corresponding to the limiting high-frequency permittivity of hexagonal ice (ε'_∞~3.2) (Fig. 3). The dielectric permittivity of water/HS shows similar features: an increase on cooling and a discontinuous decrease within the temperature range from -7 to -11 °C to a permittivity value of ~4.5. Interestingly, on further cooling there exists another small step towards a permittivity value of ~3.7. The values of the dielectric permittivity at high and low temperatures are in agreement with the prediction of an effective medium theory for heterogeneous dielectrics.[29] As with the DSC

results, we assign these processes to ice formation via heterogeneous and homogeneous nucleation at low and high supercoolings, respectively. The temperature location of the two nucleation mechanisms can better be seen in the derivative representation, $d\varepsilon'/dT$, in Fig. 3c. On subsequent heating, there is a single melting process at 0 ^{o}C. Informative is the effect of increasing the HS content (from 2.5 wt. % to 7.5 wt. %) on the nucleation mechanisms (Fig. 3 d-f). The figure depicts dielectric permittivity measurements on cooling and subsequent heating of water/HS samples with increasing weight fraction of hollow silica spheres (HS-533) with a diameter of 533 nm. There is a clear increase in the step of dielectric permittivity ($\Delta\varepsilon_O$) for the low temperature mechanism in comparison to the step at higher temperatures ($\Delta\varepsilon_E$). Moreover, the ratio $\Delta\varepsilon_O/\Delta\varepsilon_E$ increases from 0.006 to 0.024 with increasing HS content as expected from the ratio of inner to outer volumes (Table 2). These results on the effect of HS content are supported by DSC measurements made on the same dispersions (**Fig. S2**). The DSC results show an increasing heat of crystallization via the homogeneous nucleation mechanism ($\Delta H_E/\Delta H_O$~29, 13, and 7 for 2.5 wt. %, 4.8 wt. % and 7.5 wt. % of HS-533) with increasing HS content.

To further verify that homogeneous nucleation prevails in the HS we studied the crystallization of water in dispersions with polystyrene-silica core-shell particles (CS-261). This test is expected to differentiate between the two mechanisms as CS particles do not contain water and water exists only in one environment, *i.e.*, bulk-like water. Results on the dielectric permittivity and heat flow are depicted in **Fig. S3** and **Fig. S4**, respectively. They both reveal crystallization via a *single* mechanism at low supercoolings (ΔT~-20 K). These findings suggest two well–resolved nucleation mechanisms correspond to two different water environments; a bulk-like water crystallizing via heterogeneous nucleation at low supercoolings and a confined water within the HS spheres crystallizing via homogeneous nucleation at higher supercoolings. The likelihood of finding a heterogeneous nucleus inside a HS is low. The walls do not seem to be efficient nuclei. Of importance here is the role of the microporous cavities on the HS spheres (see below).

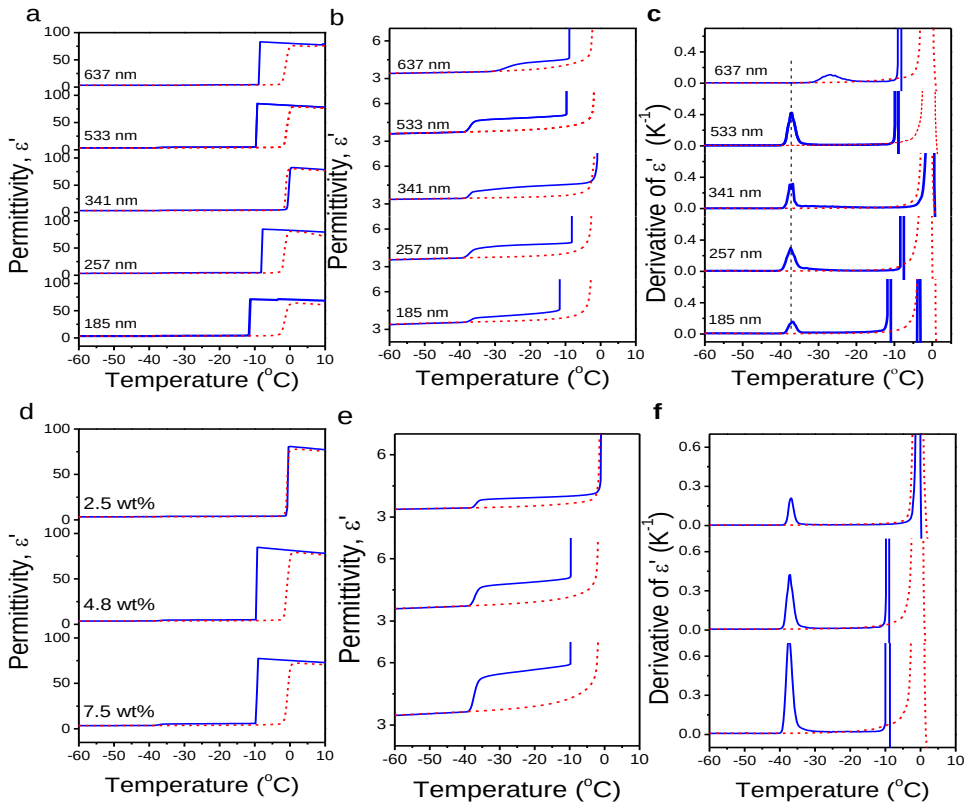

Figure 3. (a) Temperature dependence of the dielectric permittivity of water/hollow silica spheres with different diameters obtained on cooling (blue curves) and subsequent heating (red curves) with a rate of 5 °C/min. (b) Magnification of (a) in the region of low permittivity. (c) Derivative of dielectric permittivity, $d\varepsilon'/dT$, as a function of temperature for the data shown in (a). (d) Temperature dependence of the dielectric permittivity of water/hollow silica spheres with a diameter of 533 nm for different weight fractions of hollow silica spheres as indicated. (e) Magnification of (d) in the region of low permittivity. (f) Derivative of dielectric permittivity as a function of temperature for the data shown in (d). In all cases the frequency is 1 MHz.

The results of water crystallization in hollow silica spheres can be summarized in a pertinent "phase diagram". In Figure 4, the crystallization/melting temperatures are depicted as a function of the surface-to-volume ratio of spheres. This plot facilitates the comparison with water crystallization inside self-ordered AAO investigated earlier by some of us.[24-26] The temperatures of homogeneous nucleation, in the two -distinctly different- systems are in remarkable coincidence. In contrast, the temperatures of heterogeneous nucleation in HS spheres are independent of the surface-to-volume ratio whereas a strong dependence was found for water crystallized inside AAO. In addition, the temperature of crystallization via heterogeneous nucleation is identical to the crystallization temperature in dispersions of polystyrene-silica core-

shell particles. In the latter system, bulk-like heterogeneous nucleation is the only possible crystallization mechanism, hence the high temperature crystallization process in HS spheres has the same origin, *i.e.*, crystallization initiated via heterogeneous nuclei. Note that differences in crystallization temperatures by DSC and DS reflect the different cooling rates (see also Fig. S5). The mechanism at lower temperatures deserves some attention. It is assigned to homogeneous

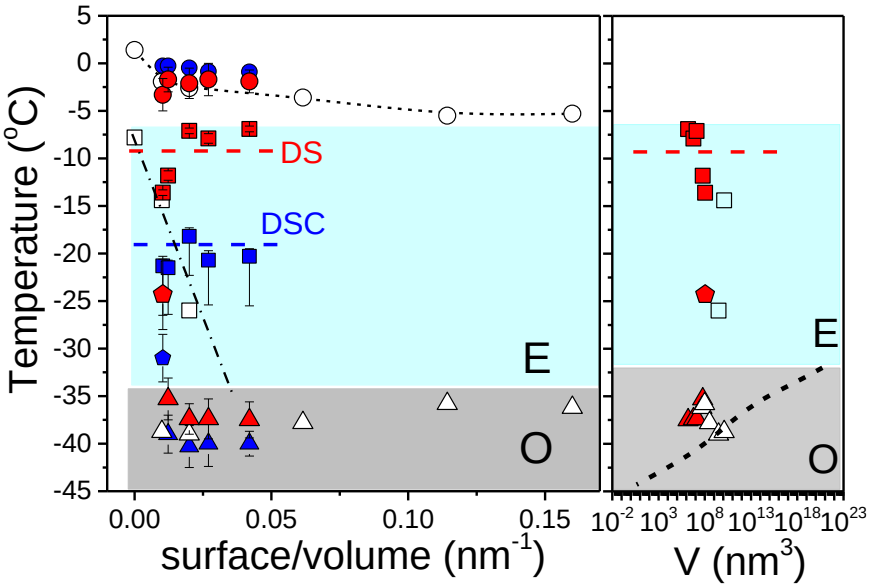

nucleation since water molecules are infiltrated through the microporous cavities in the silica

Figure 4. (Left) Phase diagram of water in hollow silica spheres (filled symbols) compared to water located inside self-ordered AAO (open symbols)[24] as a function of the surface-to-volume ratio. Red and blue symbols represent results from DS and DSC, respectively. The circles indicate the melting temperatures. The squares indicate the process of heterogeneous nucleation. The triangles indicate crystallization via homogeneous nucleation. Grey and blue areas correspond to ice formation via homogeneous (O) and heterogeneous (E) nucleation, respectively. The dash-dotted line gives the heterogeneous nucleation of ice in self-ordered AAOs.[24] The horizontal dashed line gives the temperature of heterogeneous nucleation in polystyrene-silica core-shell particles (CS-261) from DS (red) and DSC (blue). (Right) Dependence of the homogeneous nucleation temperature on volume. The black dashed line gives the reported lowest temperatures for homogeneous nucleation of water droplets as a function of their volume (cooling rate of ~1 °C/min).[7] The symbols and shaded areas have the same meaning.

shell. Effectively, this filters away all heterogeneities above a size of ~3 nm, leaving homogeneous nucleation as the sole nucleation mechanism for water located inside HS spheres. The assignment of the low temperature process in the smaller HS spheres to homogeneous nucleation (and of the

low temperature feature of HS-637 to heterogeneous nucleation) becomes more evident by comparison with the onset of homogeneous ice nucleation in supercooled water microdroplets as a function of the droplet volume (Fig.4).[7] Overall, our results support the notion that nucleation of ice is volume-dominated. On the other hand, the possibility that the low temperature process originates from nucleation within the micropores of the silica network (and not in the HS interior) can be excluded as the corresponding nucleation temperatures (Fig. 4) for such volumes is well below -40 ^{o}C.

Valuable information on the state of supercooled water/ice in the confined environment of HS spheres can be obtained from ^{1}H MAS NMR measurements. Figure 5 gives the MAS spectra of water/HS spheres with a diameter of 533 nm at -20 ^{o}C. The spectrum is composed from a narrow and a broad component associated, respectively, with a small fraction of undercooled water and a larger fraction of ice. In general, the linewidth of liquid water is determined by the chemical shift distribution of all populated states of water molecules in the liquid state, as well as from the exchange rate of the molecules between those different states. Moreover, differences in the dipolar dephasing efficiency of water, typically expressed as T2 relaxation time, will contribute to the linewidth of liquid water.

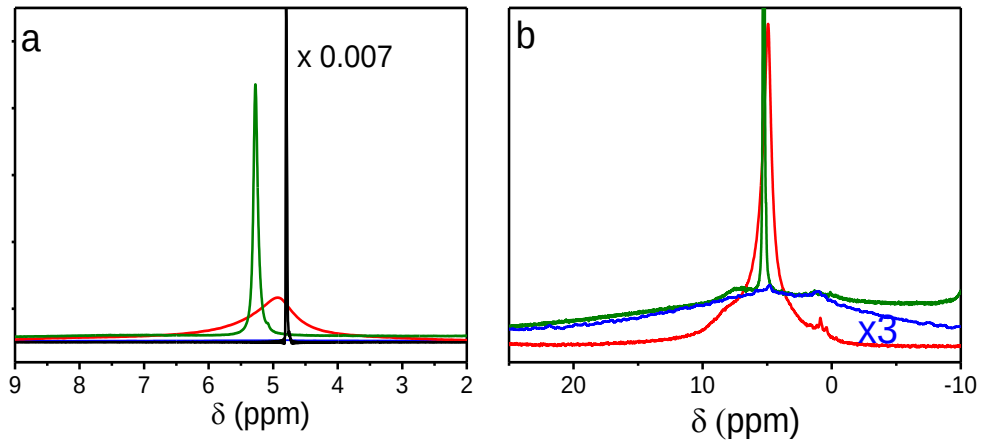

Figure 5. MAS spectra at a Larmor frequency of 20 kHz for (i) water/HS spheres with diameter of 533 nm at -20 ^{o}C (green line), (ii) water located inside AAO with pore diameter of 400 nm at -20 ^{o}C (red line), (iii) bulk water at 1 ^{o}C (black line), and (iv) bulk hexagonal ice at -20 ^{o}C (blue line), and in the regions of (a) liquid and (b) solid components. Bulk water and bulk ice spectra in (a) and (b), respectively, have been scaled (respective factor x0.007 and x3).

By comparing the linewidth of the broader component with that of bulk hexagonal ice recorded at the same temperature (Fig. 5b) we conclude that ice in water/HS spheres at -20 ^{o}C has the same characteristics (broadening, chemical shift) as bulk hexagonal ice.[26] This is understandable as at this temperature ice formation takes place via heterogeneous nucleation at the bulk of the dispersion, *i.e.*, outside the HS spheres. The narrower component associates with a small fraction of undercooled water, that based on DS and DSC, will freeze only at a lower temperature (-37 ^{o}C) via homogeneous nucleation. A quantitative analysis comparing the signal intensity of the ice and water signals -by peak deconvolution- is not feasible (the background suppression sequence will suppress some very broad contributions to the ice spectrum and therefore lead to a systematic overestimation of supercooled water). Interestingly, this fraction of supercooled water is much more mobile than water located inside AAO pores with a diameter of 400 nm and measured at the same temperature (Fig. 5b)[26] but slower than bulk water measured at 1 ^{o}C (Fig. 5a).

7.4 Conclusion

Ice nucleation was studied in monodisperse hollow silica spheres dispersed in an aqueous phase. These capsules, with hierarchical structures over several length scales (3 nm to 640 nm), provide a well-defined porous material where the nucleation mechanism of ice can be precisely controlled. Increasing the hollow silica sphere content engenders ice nucleation via homogeneous nucleation as opposed to the expected heterogeneous nucleation found in water located outside polystyrene-silica core-shell particles. These results, when examined together with ice nucleation in nanoporous alumina, support the notion that heterogeneous nucleation is suppressed in small volumes irrespective of the geometry of confinement. The present findings shed new light on the interplay between homogeneous and heterogeneous nucleation of ice with possible implications in the storage of reactive or biologically active substances. As an example, we refer to supercooled micro flow in microchannels of an aqueous/organic two-phase reaction with a chiral phase-transfer catalyst. There enantiomeric selectivity was found to increase with decreasing temperature of supercooled water.[30]

7.5 References

1. Mishima, O.; Stanley, H.E. The relationship between liquid, supercooled and glassy water. *Nature* **1998**, *396*, 329-335.
2. Debenedetti, P.G. Supercooled and glassy water. *J. Phys.: Condens. Matter.* **2003**, *15*, R1669-R1726.
3. Russo, J., Romano, F., Tanaka, H. New metastable form of ice and its role in the homogeneous crystallization of water. *Nature Mater.* **2014**, ***13***, 733-739.
4. Angell, C.A. Supercooled water. *Ann. Rev. Phys. Chem.* **1983**, *34*, 593-630.
5. Alba-Simionesco, C.; Coasne, B.; Dosseh, G.; Dudziak, K.E.; Gubbins, R.; Radhakrishnan, R.; Sliwinska-Bartkowiak, M. Effects of confinement on freezing and melting. *J. Phys. Condens. Matter* **2006**, *18*, R15.
6. Huang, J.; Bartell, L.S. Kinetics of homogeneous nucleation in the freezing of large water clusters. *J. Phys. Chem.* **1995**, *99*, 3924-3931.
7. Pruppacher, H.R. A new look at homogeneous ice nucleation in supercooled water drops. J. Atmos. Sci. 1995, 52, 1924-1933.
8. Manka, A.; Pathak, H.; Tanimura, S.; Wölk, J.; Strey, R.; Wyslouzil, B.E. Freezing water in no-man's land. *Phys. Chem. Chem. Phys.* **2012**, *14*, 4505-4516.
9. Stan, C.A.; Schneider, G.F.; Shevkoplyas, S.S.; Hashimoto, M.; Ibanescu, M.; Wiley, B.J.; Whitesides, G.M. A microfluidic apparatus for the study of ice nucleation in supercooled water droplets. *Lab Chip* **2009**, *9*, 2293-2305.
10. Steytler, D.C.; Dore, J.C.; Wright, C.J. Neutron diffraction study of cubic ice nucleation in a porous silica network. *J. Phys. Chem.* **1983**, *87*, 2458-2459.
11. Morishige, K.; Kawano, K. Freezing and melting of water in a single cylindrical pore: The pore-size dependence of freezing and melting behavior. *J. Chem. Phys.* **1999**, *110*, 4867-4872.
12. Dore, J. Structural studies of water in confined geometry by neutron diffraction. *Chemical Physics* **2000**, *258*, 327-347.
13. Rault, J.; Neffati, R.; Judeinstein, P. Melting of ice in porous glass: why water and solvent confined in small pores do not crystallize? *Eur. Phys. J. B.* **2003**, *36*, 627-637.
14. Findenegg, G.H., Jähnert, S., Akcakayiran, D., Schreiber, A. Freezing and melting of water confined in silica nanopores. *ChemPhysChem* **2008**, *9*, 2651-2659.
15. Johari, G.P. Origin of the enthalpy features of water in 1.8 nm pores of MCM-41 and the large C_p increase at 210 K. *J. Chem. Phys.* **2009**, *130*, 124518:1-6.
16. Tombari, E.; Johari, G.P. On the state of water in 2.4 nm cylindrical pores of MCM from dynamic and normal specific heat measurements. *J. Chem. Phys.* **2013**, *139*, 064507:1-9.
17. Limmer, D.T.; Chandler, D. Phase diagram of supercooled water confined to hydrophilic nanopores. *J. Chem. Phys.* **2012**, *137*, 044509.
18. Seyed-Yazdi, J.; Dore, J.C.; Webber, J.B.W.; Farman, H. Structural characteristics of water and ice in mesoporous SBA-15 silica IV: partially filled case for 86 Å pore diameter. *J. Phys.: Condens. Matter.* **2013**, *25*, 465105.
19. Alabarse, F.G.; Haines, J.; Cambon, O.; Levelut, C.; Bourgogne, D.; Haidoux, A.; Granier, D.; Coasne, B. Freezing of water confined at the nanoscale. *Phys. Rev. Lett.* **2012**, *109*, 035701.
20. Giovambattista, N.; Rossky, P.J.; de Benedetti, P.G. Effect of temperature on the structure and phase behavior of water confined by hydrophobic, hydrophilic, and heterogeneous surfaces. *J. Phys. Chem.* **2009**, *113*, 13723.

21. Ruckdeschel, P.; Kemnitzer, T.W.; Nutz, F.A.; Senker, J.; Retsch, M. Hollow silica sphere colloidal crystals: insights into calcination dependent thermal transport. *Nanoscale* **2015**, *7*, 10059.
22. Retsch, M.; Schmelzeisen, M.; Butt, H.-J.; Thomas, E.L. Visible Mie scattering in nonabsorbing hollow sphere powders. *Nano Lett.* **2011**, *11*, 1389.
23. Yin, J.; Retsch, M; Thomas, E.L.; Boyce, M.C. Collective mechanical behavior of multilayer colloidal arrays of hollow nanoparticles. *Langmuir* **2012**, *28*, 5580.
24. Suzuki, Y.; Duran, H.; Steinhart, M.; Kappl, M.; Butt, H.-J.; Floudas, G. Homogeneous nucleation of predominantly cubic ice confined in nanoporous alumina. *Nano Lett.* **2015**, *15*, 1987-1992.
25. Suzuki, Y.; Steinhart, M.; Butt, H.-J.; Floudas, G. Kinetics of ice nucleation confined in nanoporous alumina. *J. Phys. Chem. B.* **2015**, *119*, 11960-11966.
26. Suzuki, Y.; Steinhart, M.; Graf, R.; Butt, H.-J.; Floudas, G. Dynamics of ice/water confined in nanoporous alumina. *J. Phys. Chem. B* **2015**, *119*, 14814-14820.
27. Zhang, L., M. D'Acunzi, M. Kappl, A. Imhof, A. van Blaaderen, H.-J. Butt, R. Graf, D. Vollmer. Tuning the mechanical properties of silica microcapsules. *Physical Chemistry Chemical Physics* **2010,** *12*, **15392-15398.**
28. Sugisaki, M.; Suga, H.; Seki, S. Calorimetric study of the glassy state. IV. Heat capacities of glassy water and cubic ice. *Bull. Chem. Soc.* Japan **1968**, *41*, 2591-2599.
29. Kremer, F.; Schoenhals, A. *Broadband Dielectric Spectroscopy*, Ch. 13: Dielectric properties of inhomogeneous media; Steeman, P.A.M.; van Turnhout, J. Springer: Berlin, 2002.
30. Matsuoka, S.; Hibara, A.; Ueno, M.; Kitamori, T. Supercooled micro flows and application for asymmetric synthesis. *Lab Chip* **2006**, *6*, 1236-1238.

7.6 Supporting information

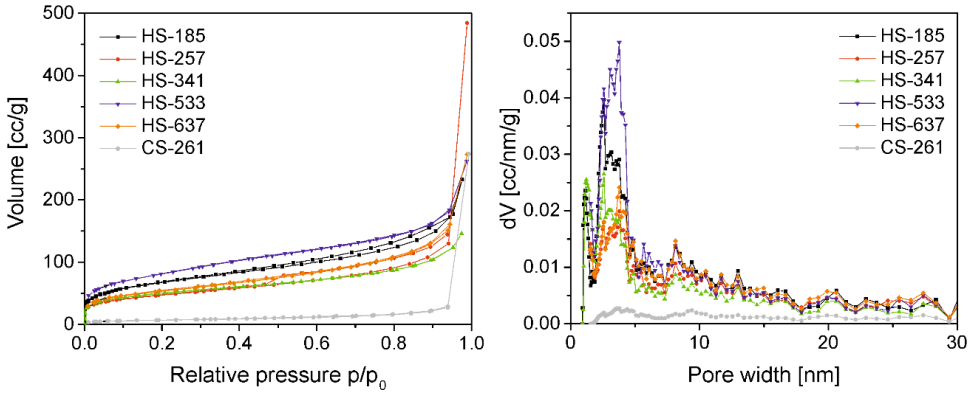

Figure S1. Characterization of the internal structure of hollow silica spheres: (a) Nitrogen adsorption/de-sorption isotherms at 77 K used in determining the pore volume and surface area. (b) Pore radius distribution. Pore volumes and pore size distributions were obtained by applying the nonlocal density functional theory (NLDFT) adsorption model for silica materials with cylindrical or spherical pore geometry

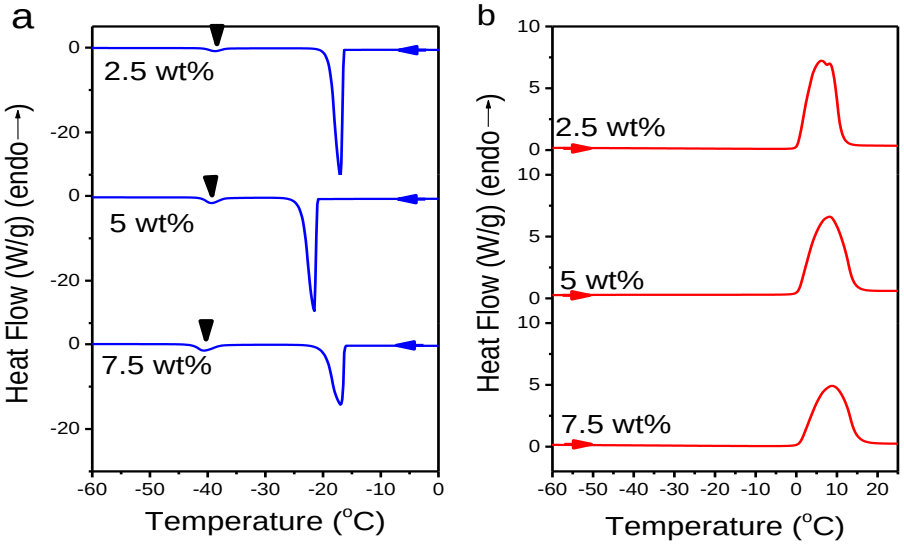

Figure S2. Differential scanning calorimetry traces of water/hollow silica spheres with different weight fractions of hollow silica spheres (diameter 533 nm) as indicated obtained on (a) cooling and (b) heating with a rate of 10 °C/min.

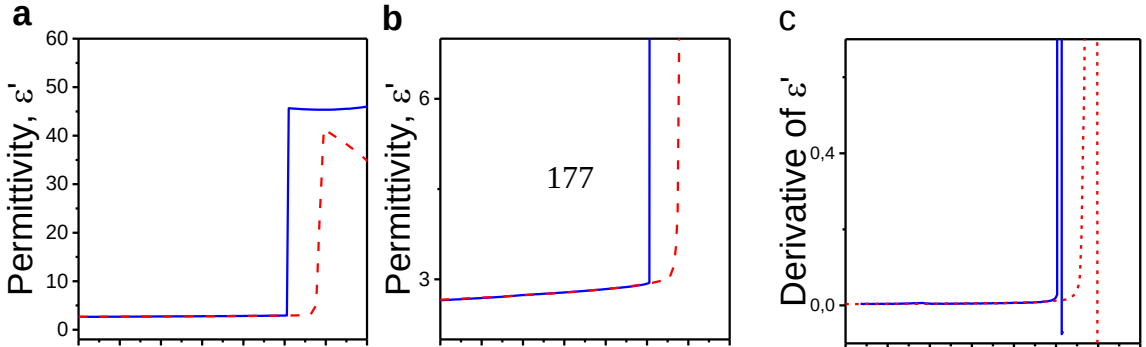

Figure S3. (a) Temperature dependence of the dielectric permittivity of water/polystyrene-silica core-shell particles (CS-261) with a diameter of 261 nm obtained on cooling (blue curves) and subsequent heating (red curves) with a rate of 5 °C/min. (b) Magnification of (a) in the region of low permittivity. (c) Derivative of dielectric permittivity, $d\varepsilon'/dT$, as a function of temperature for the data shown in (a). In all cases the frequency is 1 MHz.

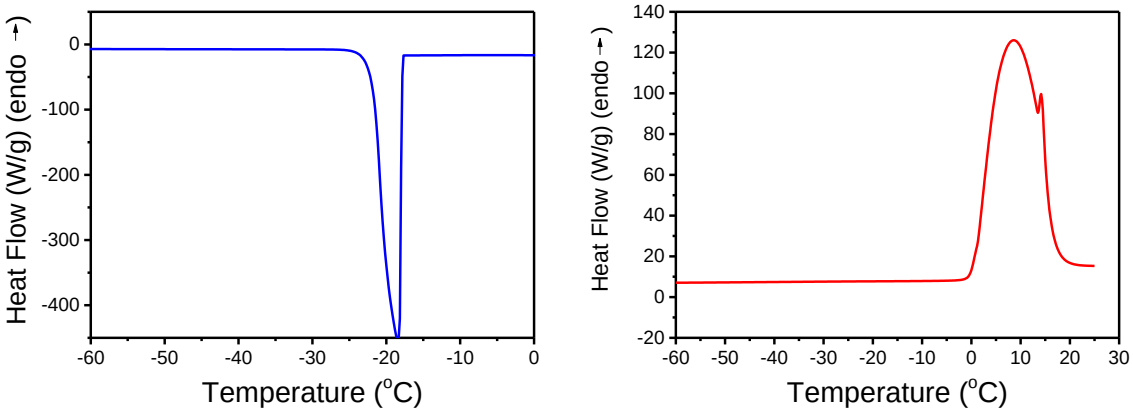

Figure S4. Differential scanning calorimetry traces of water/polystyrene-silica core-shell particles (CS-261) with a diameter of 261 nm obtained on cooling (blue curve) and heating (red curve) with a rate of 10 °C/min.

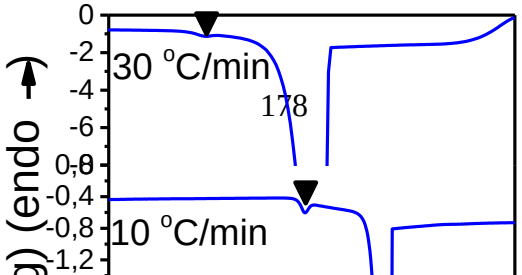

Figure S5. Differential scanning calorimetry traces of water/hollow silica spheres (diameter 341 nm) with different cooling rates as indicated.

References

1. Y. Chung-li, J. W. Goodwin and R. H. Ottewill, 1976, **60**, 163-165.
2. W. Stöber, A. Fink and E. Bohn, *J. Colloid Interface Sci.*, 1968, **26**, 62-69.
3. Kremer, F.; Schoenhals, A. *Broadband Dielectric Spectroscopy*, Ch. 13: Dielectric properties of inhomogeneous media; Steeman, P.A.M.; van Turnhout, J. Springer: Berlin, 2002.

Conclusion

Within this Thesis we examined how polymers penetrate into thin pores and once within nanopores, how they crystallize. Of particular interest to us was the crystallization of complex polymer topologies, such as stars, hyperbranched, or block copolymers structures. As earlier studies have shown that water crystallizes with nanopores with a similar mechanism to polymers, we further examined water crystallization under moderate and severe confinement conditions.

First, we studied the imbibition of linear PEO melts within self-ordered nanoporous alumina over a broad range of degree of confinement ($0.06 < 2R_g/d < 3$) that have not been explored before. The capillary rise followed an approximate $t^{1/2}$ behavior according to the Lucas-Washburn equation. However, for the first time a reversal in the capillary filling speed was found with increasing molecular weight. Shorter chains (with 50 entanglements or less) exhibited a slower imbibition than theoretically predicted, while longer chains with more entanglements showed a faster imbibition. The complex imbibition of polymer melts was discussed in terms of two mechanisms. One mechanism was due to the adsorption of polymer chains on the pore wall creating a "dead zone", which resulted in a slower imbibition. The other was due to the reptation of free chains through a network under a pressure gradient, giving a faster imbibition. The competition between the two mechanisms resulted to a non-monotonic dependence of the effective viscosity on inverse of pore diameter. Subsequently, inspired by the dependence of molecular weight on filling speed, we studied the imbibition of bimodal polymer blends (composed of long and short PEO chains) in nanopores. An enrichment of shorter chains was observed during the capillary filling. The result suggested a new method of separating long from short chains and in the absence of solvent (contrary to GPC).

Secondly, we investigated the imbibition, crystallization, and dynamics of *non-linear* polymer chains located within AAO. Polymers with three different topologies were employed; star-PEOs, hyperbranched PEOs (*hb*PEO), and a diblock copolymer (PI-*b*-PEO). The imbibition height of *hb*PEO followed a $t^{1/2}$ dependence but the speed was slower than theoretically predicted. Surprisingly, imbibition of PI-*b*-PEO in AAO could be achieved at a temperature far below the order-to-disorder transition temperature (T_{ODT}), *i.e.*, well within the ordered state. The imbibition speed of PI-*b*-PEO was found to depend on the pore diameter. In 65 nm pores, the imbibition

was faster than for a linear PEO 35k (of approximately the same molecular weight as for the diblock copolymer). However, in smaller pores (35 nm and 25 nm), the imbibition was similar to that of linear PEO 50k (having twice the molecular weight of the block copolymer). The mechanism of reversal in imbibition is presently not understood. One possible explanation lies in the various morphologies of block copolymers formed within nanopores. The latter depend on the ratio of the domain spacing to the pore diameter, the volume fraction, and the polymer/surface interactions. Subsequently, the crystallization and dynamics of polymers with the three topologies were investigated under confinement. In the absence of heterogeneities/impurities/catalyst, homogeneous nucleation was observed. The molecular weight dependence of homogeneous nucleation temperatures of non-linear polymers agreed with linear ones provided that the arm (star), branched (*hb*PEO), or the block (PI-*b*-PEO) molecular weight was used, instead of the total molecular weight. It suggests that the chain diffusion mechanism involved in the process of homogeneous nucleation is controlled by long-range motions, like arm retraction and branched point fluctuations. In addition, segmental dynamics of non-linear polymers speeded-up under confinement reflecting a reduced glass temperature.

Lastly, the crystallization and dynamics of water were investigated under moderate confinement (within hollow silica spheres) and under severe confinement (within mesoporous silica). For water in HS spheres, impurities present in bulk water were filtered out through the ~ 3 nm channels on the shell of hollow silica spheres. Thus, water in the interior crystallizes via homogeneous nucleation at large supercooling (-39 ^{o}C), whereas water in the surrounding dispersion crystallizes via heterogeneous nucleation at lower supercooling. A phase diagram (*T vs.* 1/*d*) covering a broad range of pore diameters was established that includes nanoporous alumina and mesoporous silica. The dependence of the homogeneous and heterogeneous nucleation temperatures on pore diameter was established. The two lines coincide at a pore diameter of ~ 2.6 nm below which no crystallization could be obtained. This provided an estimate for the critical nucleus size required for ice formation. In addition, a liquid-like surface water layer (thickness 0.3 nm) was obtained according to a modified Gibbs-Thompson equation. The dynamics of ice and water were investigated by employing DS and solid state NMR techniques. For the first time, two states of *liquid* water under confinement were identified and their dynamic features were explored.

Overall we have clarified the dynamics of polymer imbibition in nanopores by employing theory and experiment. We further investigated the way that semicrystalline polymers of complex topologies crystallize under confinement. Lastly, the pertinent phase diagram for confined polymers bears similarities to confined water.

Appendix: Details of the imbibition method by reflection optical microscopy

Prior to infiltration, PEO powder was pressed into a 150 μm thick film. First, ~300 mg PEO was placed in a frame sandwiched between two metal plates covered by Teflon film. The whole system was then moved to a preheated (100 ^{o}C) hot press set-up and maintained for 5 min, followed by fast release and increase of pressure for three times (in order to avoid air bubbles). Subsequently, the sample was pressed at 100 ^{o}C with 50 kN pressure for 12 min followed by cold pressing for 10 min at room temperature to allow the polymer to crystallize.

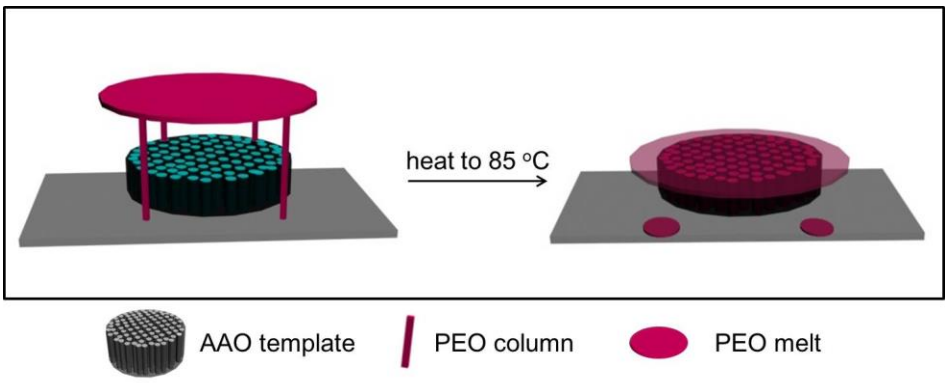

Figure A1. Schematic of the infiltration method.

The infiltration process is shown in Figure A1. The polymer film with thickness of 150 μm was placed on top the AAO template at a fixed distance maintained by a pillar made also of PEO (with M_w=5×10^3 g/mol). The pillar kept the polymer film at a close distance from the open end of AAO templates so as to keep the nanopores open before the application of vacuum. Subsequently, the oven was heated under vacuum. The pillar started to melt at ~48 ^{o}C and it slowly brought the polymer film into contact with the AAO surface. The temperature reached 56 ^{o}C when the pillar melted completely, signifying the start of the imbibition process. PT 100 was placed closed to the AAO template to record the real-time temperature. To obtain a faster contact between polymer film and AAO, the vacuum was vent for 0.5 s. At the end of the imbibition, the temperature reached 79.3 ^{o}C. Then the oven was slowly vented and the template together with

the top polymer layer was immediately transported to a metal plate at room temperature. It took 13 s for the surface PEO melt to crystallize. Then the sample was sealed and put in the fridge (-26 ^{o}C) for 4 hours to confirm the complete crystallization before measurement.

Two videos were taken simultaneously recording the melting of pillar and the corresponding temperature, respectively. The screenshots are shown in Figure A2.

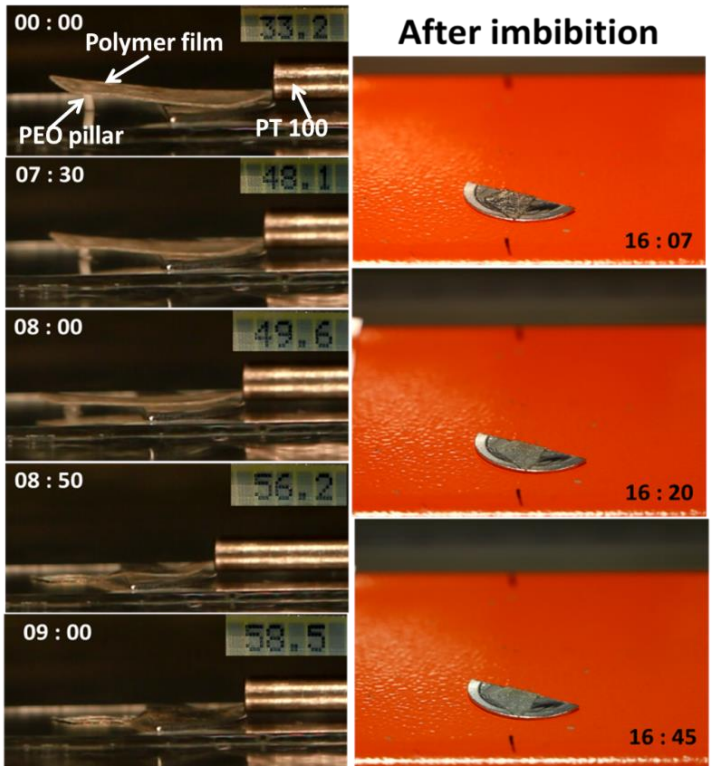

Figure A2. (left) The melting of PEO pillar during the heating of the oven. Insets show the realtime temperature of the sample in ^{o}C. (right) The crystallization of PEO after imbibition. The number in each image records the corresponding time (mm:ss) since the heating starts.

Figure A3 shows the temperature as a function of heating time during the short imbibition of PEO 50k (30^2 s, 50^2 s) and the long imbibition (200^2 s) of PEO 500k. For long time imbibition, the effect of a temperature gradient within the oven is negligible. However, the temperature gradient for short time imbibition cannot be ignored since the zero shear viscosity is changing with temperature. The temperature dependence of viscosity for PEO 50k is shown in Figure A4. The effect of a temperature gradiant during imbibition can be minimized by using a PEO of higher molecular weight (M_w > 100 kg/mol) as the pillar.

Overall, it took ~ 900 s for the oven to reach a stable temperature (79.3 °C). It is the temperature gradient during heating that results in the non-linearity at short times. Overall, this method is applicable for measurements with imbibition times longer than 35^2 s.

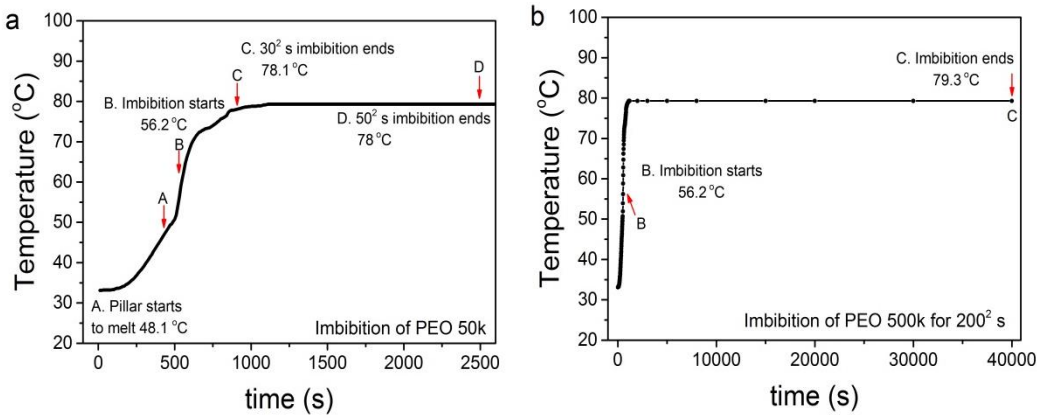

Figure A3. Temperature as a function of heating time during (a) the imbibition of PEO 50k for 30^2 s, 50^2 s and (b) imbibition of PEO 500k for 200^2 s.

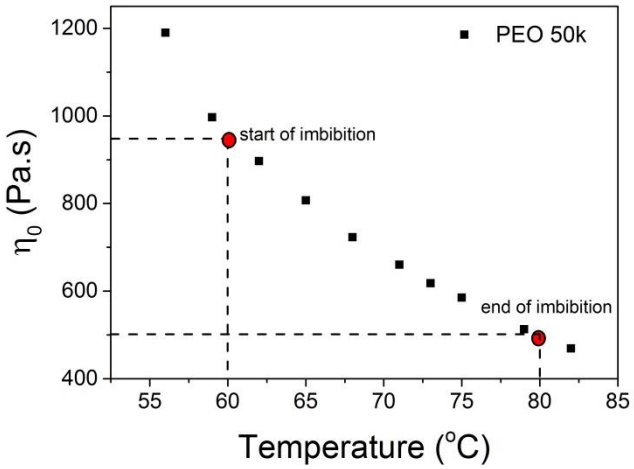

Figure A4. Zero-shear viscosity of PEO 50k as a function of temperature.